

Abstract

Regulation of Microtubule Nucleation and Repair by an Abl Family Kinase

Daisy Duan

2024

Abl family kinases serve as hubs for signaling cues and cytoskeletal rearrangement to regulate cell morphogenesis and migration. Loss of Abl2 in mice leads to a significant decrease in neuronal dendrite branch complexity accompanied by learning and memory behavioral deficits. Previous studies reveal that Abl2 interacts with microtubules to promote plus-end elongation both *in vitro* and in cells. However, the mechanisms underlying Abl2 regulation of MT dynamics and organization remain understudied. Here, I report that Abl2 interacts with both the MT lattice and tubulin dimers to regulate dynamics. For the first time, I show that Abl2 can undergo phase separation and form coacervates with tubulin, both mediated by its cytoskeleton-binding C-terminal half. I demonstrate that Abl2 promotes MT nucleation, which is facilitated by co-condensation of Abl2 and tubulin dimers. A naturally occurring splice-isoform is tubulin-binding deficient, which underlies its inability to promote MT nucleation. Additionally, my findings reveal that knockout of Abl2 in COS-7 cells inhibits recovery of the MT network after nocodazole treatment. Only Abl2, but not the tubulin-binding deficient Abl2 isoform, can promote MT reassembly. I also discovered that Abl2 mediates repair of damaged MT lattices *in vitro* and increases MT rescue frequency and lifetime. Collectively, I have shown that Abl2 has two novel regulatory functions that involve the recruitment and addition of tubulin dimers to MTs in different functional scenarios in the cell.

Regulation of Microtubule Nucleation and Repair by an Abl Family Kinase

A Dissertation

Presented to the Faculty of the Graduate School

Of Yale University

In Candidacy for the Degree of

Doctor of Philosophy

By

Daisy Duan

Dissertation Director: Anthony J. Koleske, Ph.D.

May 2024

© 2024 by Daisy Duan

All rights reserved.

Acknowledgements

Throughout my graduate school journey, I received substantial professional, scientific, and emotional support from my mentors, mentees, colleagues, lab mates, friends, and family. I want to first thank my dissertation advisor, Anthony J. Koleske, PhD. Tony took me into the lab and put me under his wing knowing I had little benchwork experience. I knew I had a lot to learn, and he did too. I was – and still am – very lucky to have Tony's support both inside and outside of the lab. Tony always provided me advice, which was sometimes hard but was needed for me to hear. I was given so much space to grow, to make mistakes, and to pursue my curiosities freely. Thank you, Tony, for always being there for me. I am eternally grateful for your mentorship and could not have asked for a better scientific mentor. I also want to thank my thesis committee members, Mark Mooseker, PhD, Mark Solomon, PhD, and Yong Xiong, PhD; and my outside reader, Mark Peifer, PhD. They have always made my semi-annual thesis committee meetings enjoyable because our discussions were often filled with troubleshooting advice for experiments and their help in developing my professional development plan for the upcoming year.

Thank you to my previous and current lab mates, especially Josie Bircher, PhD, Kuanlin Wu, PhD, Ellen Corcoran, PhD, Yevheniia Ischenko, PhD, Amanda Jeng, Nicolas Stuardo, Alyssa Blaise, Wanqing Lyu, PhD, and Noële Certain, PhD. When I had rotated in the lab, I was extremely impressed by how intellectually rigorous science was being done. It wasn't until I officially joined the lab I really understood what that meant. My lab mates challenged me in the best way possible by not only providing me troubleshooting advice but taught me through example the importance of designing and conducting collaborative, mechanism-driven experiments. I want to give special thanks to Wanqing Lyu and Noële Certain, who both sat in the bench adjacent to mine, making every day a truly enjoyable workday that I looked forward to. Wanqing was not only a Koleske Lab colleague, but my close collaborator throughout my PhD and someone I looked up to as an older sister. She and I constantly read papers and exchanged ideas daily. I will always be fortunate to have had the opportunity to start and complete a project with a partner whose drive and work ethic I admire and respect. Noële is someone who I consider to be one of my very good friends. Noële has been by my side through some of the toughest moments towards the end of my PhD. I am so

blessed to have a friend who I get to see nearly every day, someone who gives me the space to share all the good and bad moments with. Thank you Noële for teaching me how to be a more emotionally aware person and friend and providing me tools to lead a more fulfilling life.

Thank you to the current junior and senior lab technicians, Andrew Boulton, and Xiaoyuan Li, and special thanks to the previous sole lab technician (A.K.A. the OG Koleske Lab member) Xianyun Ye. Thank you, Andrew, Xiaoyuan, and Xianyun for being the backbone of the lab. No science could have been completed without your support making stock solutions, purifying DNA, genotyping, cleaning glassware, among so many other tasks. Thank you to the previous and current financial lab assistants, Elizabeth Vellali and Amber Thammavongsa, for without them, no experiment could have been completed in the lab, and no social event could have been planned without their top-notch organizational skills. I want to give a very special thank you to Anthony DeSimone, the sole medical campus machine shop specialist who can fix anything and create anything anyone asks of him to do. Tony DeSimone is the backbone of the Yale School of Medicine, for without him, no centrifuge, incubator, shaker could be fixed, nor prototypes or special electronics hardware could have been curated without his expertise. Thank you, Tony, for being there whenever my experiments called for you, and teaching me exciting things about your current projects whenever I stopped by.

I want to thank my Científico Latino (CL) community. I have not met most of the CL team members in person, but our friendships have been born through our countless Slack conversations and Zoom team meetings due to our strong commitment to service. Of the ones I have met are Robert W. Fernandez, PhD and Olivia Goldman, PhD. They are the CL co-founders who greeted me with welcome arms and brought me into the organization in April 2019 before my graduate school journey began (and even before the birth of our national Graduate School Mentorship Initiative). I was able to navigate the first several years of my PhD because I felt a sense of belonging within the CL community which actively promotes networking, open-access resources, and peer mentorship. Thank you, Rob and Olivia, for showing me what strong, positive leadership looks like and for allowing me to help grow the CL team to what it is today. Throughout the years, I was able to interact and become friends with several other team members who helped strengthen

my character and inspired me within the DEI space. I especially want to thank CL team members Aníbal Tornes Blanco, Dennisha King, Cathy Amaya, PhD, Melissa Cadena, and Carlos A. Rico, PhD. I've had the privilege to work with these talented, brilliant minds through webinars that I've co-developed and/or facilitated throughout the years.

I want to also express immense gratitude for Faye Rogers, PhD, and Barbara Kazmierczak, MD, PhD for bringing me into the Yale BioMed Amgen community. Through Rob, I was made aware of the Yale BioMed Amgen Scholars Program, in which I was determined to participate as a peer mentor from year 1. This didn't happen until the transition into my third year of the PhD program when summer undergraduate research opportunities were operating in person since the onset of COVID. From Summer 2021 to Summer 2023, I was extremely privileged to have served as a peer mentor to three wonderful cohorts of peer mentees: Shamauri Rivera, Deandra Simpson, Tristian Wiles (2021); Joshua Lazaro, Emily Afriyie, and Sushma Gude (2022); and Ta'Aliyah Jones, Isaiah Diggs, and Isabela Fuentes (2023). My mentees held so much passion, excitement, drive, and curiosity that always found its way seeping into my research. Every single one of them reminded me why all the tough, long nights in the lab and struggles as a person of color were worth going through. The completion of my graduate school journey mattered not only to me and my family, but also to them, and to all the other people of color and those coming from minoritized backgrounds in academe. Thank you especially to Sushma and Deandra for constantly reminding me of this to this very day. Special shoutout to Faye for showing me what a true superwoman is like in STEM. After having known Faye for over three years now, I am still constantly in awe of all the things she manages to juggle effortlessly: serving as the Vice Chair for Yale School of Medicine DEI, to Associate Director of the Yale MD/PhD Program, to Director of the Yale BioMed Amgen Program, and serving all the roles as a PI – all the while being a mother. Thank you, Faye, for always keeping it real, making space for all of us in a place like Yale, and for showing us that we, too, can make it out here.

I especially want to thank everyone outside of the New Haven community. I am so blessed for the friends who visited me and those who hosted me in their homes throughout the country, who I consider my family only separated by blood. These people visited me throughout the years,

making New Haven feel more like home. Thank you to my for-lifers Celine Shanosky, Stephanie Klaskin, Sarah Helen Braver, and Karina Polanco for all the Broadway shows, fun Boston trips, Austin hangouts, and NYC museum visits; to my soon-to-be-lawyer Jessica Shyong; my middle school homies Jocelyn Yeung, Fiona Chen, Calvin Sun, Jessica Ma; my soon-to-be-doctor Maxine Derrick; my cousin Edward Liu; and my high school friends Nelly Lin, and Juno Lee, for making so many memories in New Haven with me. Thank you, Nathan Magalit, Ruchita Kothari, Max White, Nicole Pagane, Melissa Mai, Sophie Shoemaker, Yiben Fu, PhD, Jessica Rose Schlotfeldt, Maya Drzewicki, Alejandra Casanova, and Chris Jones for the unforgettable Baltimore, Chicago, Seattle, and San Diego visits; and for having deep meaningful conversations with me through all the ups and downs of life. Special thank you to the Casanova-Sepúlveda family for hosting me in Puerto Rico and making me feel like a member. Thank you to Gabriela Casanova for trying out new restaurants and being a foodie with me in New Haven and NYC, especially for all the dinners where we shared laughs and cries and vented about our science struggles. Thank you for your unwavering support through some of the toughest times of 2023 with me.

Lastly, I want to thank my family. I could not have gone through graduate school without my parents. My mom was, is, and will always be the person who reminds me it is okay to fail, and that it is far more important that I learn from my mistakes. She has always shown me grace and taught me through example that kindness towards oneself and others goes a long way in life. Thank you, Mom, for teaching me how to learn to forgive, to let go, to never give up, and to be kind. Thank you most of all for being my best friend. Thank you, Dad, who always reminded me to take breaks, who always indulged me with my favorite foods whenever I visited home, and who always said yes whenever I needed someone to go on a walk with. I cannot thank my parents – especially my mom – enough for visiting Grandpa, 爺爺, whenever I think of him and for showing him love and care through food and quality time. Thank you to my brother, Devon, who continues to support my parents and looked out for them when I could not be there. Though he is not one to be considered most patient, Devon has always been one of the most kind and giving Duan family members. Lastly, I want to thank 爺爺. There are no words to describe how eternally grateful I am to have him as my grandpa, how lucky I am to be his granddaughter, and how blessed I am to have learned what

resilience, sacrifice, and unconditional love meant from none other than him. 爺爺 is someone who has always demonstrated kindness, even to others who did not treat him the same. When his initial experiences in America were wrought with struggle, he did not waver and remained resilient in finding a home that could house an entire family. And 爺爺 did just that. The same home he purchased with my grandma, 嫲嫲, is the same home I was raised in. To 爺爺 and 嫲嫲, I will always remember to pay it forward, for it was their bravery, strive for a better future, and loyalty to family that paved forward my future for a better life in America. To my entire village, I could not have done this without you. To all my other first-generation low-income high school and college students, Chinese-American children of immigrants—this one's for you.

Table of Contents

Chapter 1: Introduction into Abl family kinases and microtubule dynamics

1.1 Abl family kinases and their roles in regulation of cytoskeletal dynamics.....	12
1.1.1. Structure and function of Abl family kinases.....	12
1.1.2. Tissue and cellular expression levels of Abl family kinases.....	16
1.1.3. Abl family kinases in cytoskeletal regulation.....	17
1.1.3.1. Abl2 regulation of actin dynamics.....	17
1.1.3.2. Abl2 regulation of microtubule dynamics.....	21
1.2. Microtubule dynamics and structure.....	24
1.2.1. Microtubules are dynamic polymers.....	24
1.2.2. Microtubule dynamics are regulated by microtubule-binding proteins.....	25
1.2.3. Structures of microtubule polymers in various nucleotide states and recognition by microtubule-binding proteins.....	27
1.2.4. Regulation of microtubule lattice repair.....	33
1.2.5. Existing models for MT nucleation in neurons.....	36
1.3. Contributions of phase separation behavior of microtubule-binding proteins to cellular and neuronal function.....	41
1.3.1. Emerging role of MBP phase separation in MT dynamics revealed by <i>in vitro</i> studies....	42
1.3.1.1. Liquid-liquid phase separation of MBPs in lattice stabilization and regulation of cargo-trafficking.....	43
1.3.1.2. LLPS of MBPs in formation of +TIP bodies to promote MT dynamics.....	45
1.3.1.3. LLPS of MBPs in MT nucleation.....	48
1.3.2. LLPS of MBPs in neurons.....	50
1.3.2.1. Phase separation of MBPs in axons.....	51
1.3.2.2. Emerging roles of LLPS in dendritic spine maintenance.....	54
1.3.3. LLPS of kinases in cytoskeletal regulation.....	61

Chapter 2: Regulation of microtubule nucleation and rescue by Abl2

2.1. Abl2 binds tubulin dimers <i>in vitro</i>	63
2.2. Abl2 undergoes LLPS and co-condense with tubulin <i>in vitro</i>	70
2.3. Abl2 promotes nucleation and rescue <i>in vitro</i>	78
2.4. Abl2 preferentially binds expanded over compacted MT lattices.....	87
2.5. Abl2 mediates repair in damaged MT lattices.....	93
2.6. Abl2 increases rescue frequency to prolong MT lifetimes.....	98
2.7. Materials and Methods.....	103

Chapter 3: Evolutionary differences between Abl2 and Abl2 Δ 688-791

3.1. Single-cell and bulk RNA-seq transcriptomics reveal differential Abl2 transcript levels between mice and humans.....	125
3.2. Ongoing work to generate CRISPR mouse model.....	131
3.3. Materials and Methods.....	134

Chapter 4: Regulation of Abl2 on the tubulin code

4.1. Crosslinking mass spectrometry to identify the Abl2:tubulin binding interface.....	137
4.2. Structure of Abl2:tubulin complex.....	142
4.3. Post-translational modifications of tubulin in whole brain lysates.....	147
4.4. Materials and Methods.....	153

Chapter 5: The Abl2 interactome and phosphoproteome in mouse brain tissue

5.1. Co-immunoprecipitation of Abl2 in mouse brain lysates.....	156
5.2. Using BioID as a proximity labeling technique to capture Abl2 interactions in cells.....	167
5.3. Abl2 whole brain proteomics.....	170
5.4. Abl2 phospho-proteomics.....	174
5.5. Materials and Methods.....	188

Chapter 6: Ongoing work and future directions

6.1. Abl2 mediates F-actin-MT crosstalk.....	191
6.2. Function of phase separated Abl2 <i>in cellulo</i>	195
6.3. Visualizing F-actin and microtubule crosstalk under the regulation of Abl2 <i>in cellulo</i>	199
6.4. Determining whether, and if so how, Abl2 kinase impacts F-actin and MT cytoskeletal organization under hyperosmotic stress.....	202
6.5. Materials and Methods.....	207

7. Conclusions and future perspectives

7.1. Abl2 binds tubulin using two distinct C-terminal regions.....	209
7.2. Abl2 interacts with MTs and tubulin to promote MT nucleation, growth, and lattice repair....	209
7.3. Abl2 localizes to expanded lattices via multiple binding patterns.....	210
7.4. Phase separation contributes to Abl2 function in regulating MT nucleation.....	211
7.5. The tubulin-binding Abl2 splice isoform is more predominant in human tissues than in mouse tissues.....	212

Chapter 1: Introduction into Abl family kinases and microtubule dynamics

1.1. Abl family kinases and their roles in regulation of cytoskeletal dynamics

1.1.1. Structure and function of Abl family kinases

Abelson (Abl) proteins belong to a family of nonreceptor tyrosine kinases. Abl family kinases were first identified from Abelson murine lymphosarcoma virus that induced transformation of fibroblasts and lymphoid cells *in vitro* and lymphomas *in vivo* (Abelson & Rabstein, 1970; Goff et al., 1980). Product of the oncogene, *v-abl*, demonstrated tyrosine kinase activity and was later determined to be a mutant form of c-Abl. In 2001, a number of groups revealed that chronic myeloid leukemia (CML) patients share an activated fusion oncoprotein BCR-ABL that can be treated with imatinib mesylate – a small molecule type II inhibitor that competitively inhibits tyrosine kinase phosphorylation via binding to ATP/drug binding cleft (Azam et al., 2003; Druker, Sawyers, et al., 2001; Druker, Talpaz, et al., 2001; Shah et al., 2002; Wong & Witte, 2004). Since then, Abl tyrosine kinases have been highly studied due to the mutant forms of Abl identified as determinants for both Abelson murine leukemia virus and CML. The family of Abl kinases include vertebrate Abl and Arg (also known as Abl1 and Abl2, respectively), *Drosophila melanogaster* dAbl, and *Caenorhabditis elegans* Abl. Since its discovery of the virus in 1970, many studies have demonstrated that Abl kinases (paralogs Abl1 and Abl2 in vertebrates and Abl in invertebrate metazoans) regulate diverse cellular processes for development and homeostasis (Brasher & Van Etten, 2000; Chislock & Pendergast, 2013; Finn et al., 2003; Fox & Peifer, 2007; Greuber et al., 2013; Grevengoed et al., 2001; Hoj et al., 2020; Kain & Klemke, 2001; Khatri et al., 2016; Luttmann et al., 2021; Moresco & Koleske, 2003; Plattner et al., 1999; Plattner et al., 2004; Rogers et al., 2016; Wang et al., 2001; Z. Wills et al., 1999; Zandy & Pendergast, 2008; Zandy et al., 2007).

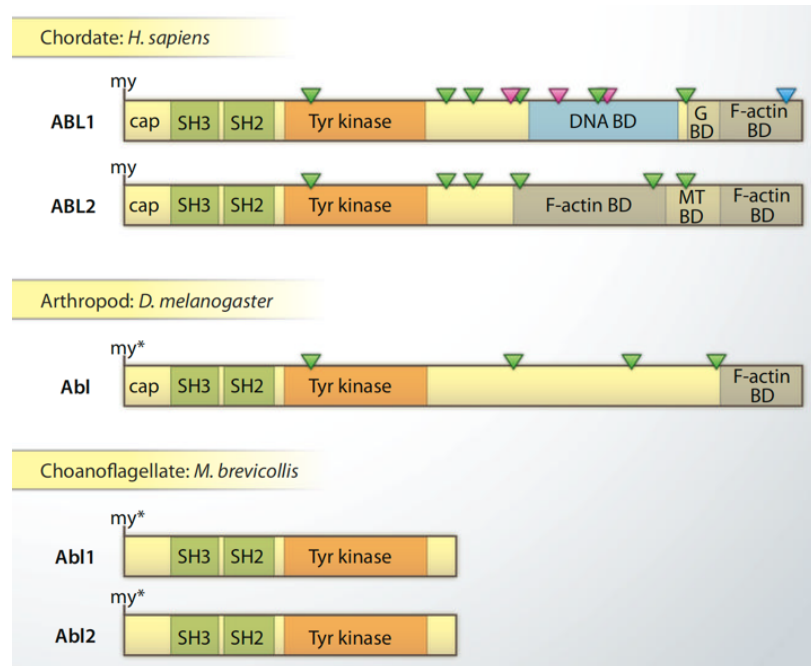


Figure 1.1. Domain architecture of Abl tyrosine kinases across species. Blue triangle, NES; magenta triangle, NLS; and green triangle, proline-rich motif that has ability to bind SH3 domains. Adapted from (Colicelli, 2010).

The catalytic activity of Abl family kinases is tightly regulated through intra- and intermolecular interactions. Each Abl protein contains a cassette consisting of Src-homology 3 (SH3), Src-homology 2 (SH2), and tyrosine kinase (or SH1) domains residing in the N-terminus (**Figure 1.1**). The cassette undergoes a coordinated regulatory mechanism like the autoinhibitory regulation of the SH3-SH2-SH1 cassettes of Src and Hck (Figure 2) (Harrison, 2003; Nagar et al., 2003). Like Src, Abl1 and Abl2 remain in an autoinhibited closed conformation. The SH3 and SH2 domains are packed against both lobes of the kinase domain such that SH3 interacts with a proline residue in the SH2-kinase linker region and SH2 via hydrogen bonding interactions (Nagar et al., 2003), thereby clamping it to maintain a kinase inactive state (**Figure 1.2A**). The N-terminal myristoyl group, only present in Abl1 isoform 1b and Abl2 isoform 1b (but not in splice form 1a in human Abl1 and Abl2, equivalent to isoform I in mice), serves as the “cap” to stabilize the SH3-SH2 clamp (**Figure 1.2**) (Bradley & Koleske, 2009; Harrison, 2003). Truncation of the first 80 amino acids including the N-myristoyl cap domain leads to enhanced catalytic activity and tyrosine phosphorylation levels *in vitro* and *in vivo* (Pluk et al., 2001). The C-lobe of the kinase domain

contains a hydrophobic pocket that presents itself for the myristoyl cap to dock into, which induces a sharp bend in the C-terminal helix of the kinase domain thereby allowing SH2 domain to dock (Nagar et al., 2003). However, the solved X-ray crystallographic N-terminal Abl structure contained a myristoyl group. It is likely that endogenous lipids in the cell may contribute to kinase inhibition by also binding into the hydrophobic pocket of the kinase domain. Indeed, it was discovered that PIP2, an abundant phosphoinositide known to regulate cytoskeletal and membrane proteins, can inhibit Abl1 and Abl2 kinase activity both *in vitro* and in cells (Plattner et al., 2004).

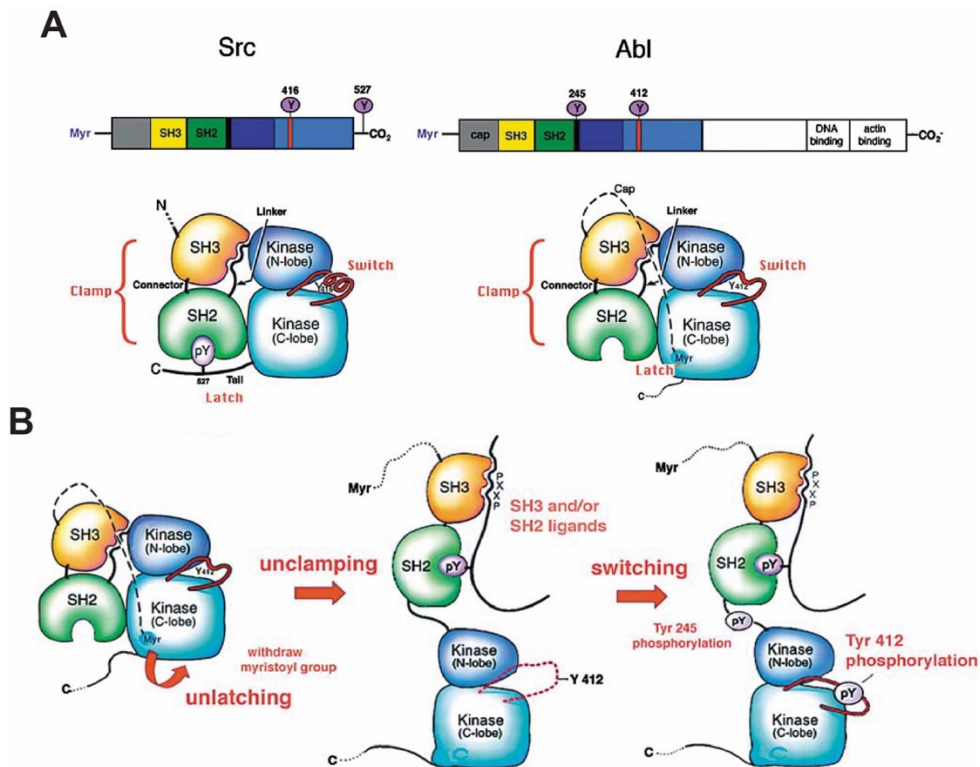


Figure 1.2. Activation mechanisms for Src and Abl. Adapted from (Harrison, 2003).

Abl kinases become activated with the initial release of the cap, followed by the unclamping of SH3-SH2 from the kinase domain. The lobes of the kinase domain can adopt various orientations, as the catalytic cleft must open and close to release ADP and allow ATP to bind (Harrison, 2003). However, the clamp assembly inhibits the catalytic cycle by protecting Tyr 412 in Abl1 and Tyr 439 in Abl2, which resides within the activation loop or “switch” within the C-lobe of the kinase domain, from phosphorylation, as this would trigger rearrangement of the activation loop. The release of the cap and unclamping is followed by the switch. Phosphorylation of Tyr 245 in

Abl1 and Tyr 272 in Abl2 in the SH2-kinase linker region (thereby dislodging from the kinase domain) and Tyr 412 in Abl1 and Tyr 439 in Abl2 *in trans* (either by Src-family kinases or by a neighboring Abl1 or Abl2 molecule) causes Abl1/Abl2 to “switch” into its active conformation or its fully activated state (Brasher & Van Etten, 2000; Nagar et al., 2003; Tanis et al., 2003). It is worth noting that both Abl1 and Abl2 can self-associate and exist as oligomers.

A recent study reveals novel tyrosine phosphorylation sites, where the upstream regulator platelet-growth derived growth factor receptor β (PDGFR β) phosphorylates and activates Abl2 via phosphorylation of Tyr 116, Tyr 161, Tyr 272, Tyr 310 which are all located near the SH3-SH2 linker interface that is essential for autoinhibition (Wu et al., 2021). In fact, PDGFR β is just one of the various upstream stimuli that engage in the activation of Abl family kinases. Among them include growth factor receptors (Plattner et al., 1999; Plattner et al., 2004), and integrin and cadherin adhesion receptors (Hernández et al., 2004; Lewis et al., 1996; Moresco et al., 2005; Simpson et al., 2015; Zandy et al., 2007). These cell surface receptors and other cytoplasmic factors or those containing phospho-tyrosine ligands can partially open the autoinhibited conformation.

Downstream of the SH3-SH2-kinase cassette, all Abl family members contain an intrinsically disordered region (IDR), but this region varies widely in sequence. In vertebrates, IDRs of Abl1 and Abl2 consists of the cytoskeletal-binding C-terminal half that binds to F-actin and/or microtubules (MTs). Their extended C-terminal halves make Abl family kinases unique amongst the larger family of tyrosine kinases. There is only ~29% sequence identity between the C-termini/IDRs of Abl1 and Abl2 (Kruh et al., 1990). Abl1 contains 4 PxxP motifs following the kinase domain, whereas Abl2 has only 3 that allow for interactions with other cellular binding partners that contain SH3 domains (Lapetina et al., 2009). Whereas Abl1 contains an extreme C-terminal calponin homology (CH) domain that binds to filamentous (F)-actin and globular (G)-actin (Van Etten et al., 1994), Abl2 has both a C-terminal F-actin domain and another [I/L]WEQ F-actin binding domain internally (**Figure 1.1**) (Wang et al., 2001). Both Abl1 and Abl2 bundle F-actin *in vitro*. Unpublished co-sedimentation data by Dr. Wanqing Lyu, a previous member of the Koleske Lab, revealed that Abl1 also binds to MTs, with a MT-binding region that has yet to be precisely localized. Abl2 also contains a MT-binding region that has recently been identified to likely encompass amino acids

688-1090 (to be discussed in Chapter 2). Additionally, Abl1 has been reported to contain DNA-binding region and has a nuclear-localization and -export sequences (NLS, NES, respectively) that allow for shuttling between the nucleus and cytosol (Miao & Wang, 1996; Wen et al., 1996). Abl2 contains a leucine-rich NES motif that is conserved in Abl1. Both Abl1 and Abl2 predominantly reside in the cytoplasm (see Section 1.1.3 for discussion on how Abl2 regulates the cytoskeleton via its C-terminal half) (Koleske et al., 1998; Peacock et al., 2010). Collectively, these functional and structural studies demonstrate that Abl1 and Abl2 share a highly conserved kinase-domain containing N-terminal half, whose kinase activities are carefully regulated in cells. It is their C-terminal halves that share low conservation that distinguishes these two paralogs from one another in cytoskeletal regulation (Colicelli, 2010).

1.1.2. Tissue and cellular expression levels of Abl family kinases

Mammalian Abl1 and Abl2 are differentially expressed in humans and mice. Though both are widely expressed in fetal and adult tissues, Abl2 expression is significantly higher than Abl1 expression in the brain (Koleske et al., 1998; Pendergast, 2002). Koleske and others discovered that Abl2 protein is primarily enriched in synapse-rich brain regions, such as that adjacent to the granular layer of the hippocampus; and can be found in synaptosomes and dendritic spines (Koleske et al., 1998; Lin et al., 2013; Moresco et al., 2003; Wang et al., 2001). Abl2 localization in synapse-rich regions suggests that Abl2 plays an essential role in synaptic plasticity. Indeed, Abl2 has since been discovered to regulate neurotransmitter vesicle release at presynaptic termini and acts in the postsynaptic compartment to regulate spine size and stability and neurotransmitter receptor subunit composition (Moresco et al., 2003; Xiao et al., 2016).

Mammalian Abl1 protein is expressed at low levels in various tissues and cell types but found highest in cartilage and adipocytes within adult human tissues. However, it is in human fetal tissue that Abl1 protein levels can be found highest in muscle, endothelial cells, and osteoblasts (O'Neill et al., 1997). Mammalian Abl1 and Abl2 proteins are both present in the apical actin latticework in the developing neuroepithelium (Koleske et al., 1998). However, they localize

differentially in subcellular compartments – contributing to their unique cytoskeletal regulatory functions, to be discussed in the next section.

1.1.3. Abl family kinases in cytoskeletal regulation

Abl-family nonreceptor tyrosine kinases play essential roles in key cytoskeletal processes for cell adhesion, motility, and morphogenesis (Boyle et al., 2007; Bradley & Koleske, 2009; Hernández et al., 2004; Zandy et al., 2007). Of the known mammalian tyrosine kinases, only Abl1 and Abl2 are only known to interact with the cytoskeleton directly. Activated forms of Abl localize to the cytoplasm, plasma membrane, and focal adhesions (Kruh et al., 1990). Cytoplasmic c-Abl can be activated by cell adhesion and growth factors and localizes to F-actin-rich protrusions, membrane ruffles, and leading edge of spreading fibroblasts (Woodring et al., 2003). Much like cytoplasmic Abl1, Abl2 also localizes to dynamic F-actin structures to mediate cellular morphogenesis, cell migration, ruffling, and filopodia formation through kinase-dependent and -independent mechanisms. Both Abl1 and Abl2 kinase activities for mediating these processes are stimulated by growth factor and adhesion receptor, and upstream effector engagement (Boyle et al., 2007; Courtemanche et al., 2015; Gifford et al., 2014; Lapetina et al., 2009; MacGrath & Koleske, 2012; Miller et al., 2004; Miller et al., 2010; Moresco et al., 2005; Plattner et al., 1999; Shaw et al., 2021; Wang et al., 2001; Zhang et al., 2018). Despite overlapping roles in development likely due to the similarity in structure of their kinase-domain containing N-termini, Abl2 protein is predominantly cytoplasmic. Across the span of over two decades, biochemical studies have emerged that elucidated the various cytoskeletal remodeling capabilities of Abl2 that are both dependent and independent of its kinase activity. For the rest of this dissertation, I will primarily focus on Abl2, specifically on its regulatory functions on actin and microtubule dynamics.

1.1.3.1. Abl2 regulation of actin dynamics

Abl2 has N-terminal SH3, SH2, and kinase domains for phosphorylating multiple substrates to control cellular processes including motility and morphogenesis (Boyle et al., 2007; Hernández et al., 2004; Lapetina et al., 2009; Miller et al., 2010; Peacock et al., 2007). These cellular processes

require changes in cell shape that are powered by forces from F-actin cytoskeletal remodeling. Polymerization of F-actin promotes cell edge protrusions while contractility to provide traction force for translocation is powered by the actomyosin network (Gupton & Waterman-Storer, 2006; Pollard & Borisy, 2003). Early work by Wang and others revealed that Abl2 bundles F-actin *in vitro* via two distinct F-actin-binding domains, which are necessary and sufficient to induce formation of actin-rich structures at the lamellipodia of fibroblasts (Wang et al., 2001). It has been shown in subsequent studies that cells deficient in Abl2 exhibit significantly reduced membrane ruffling, but this phenotype is rescued by re-expression of the kinase (Boyle et al., 2007), and that Abl2 localizes to and promotes dynamic cell edge protrusions during adhesion and spreading on fibronectin (**Figure 1.3**) (Lapetina et al., 2009; Miller et al., 2004; Peacock et al., 2007). Importantly, Abl2 phosphorylation of and binding interactions with cortactin are necessary for dynamic cell edge protrusions in fibroblasts (Boyle et al., 2007; Lapetina et al., 2009; Miller et al., 2004; Miller et al., 2010) and for lamellipodial formation in COS-7 cells (Zhang et al., 2018) upon growth factor treatment and adhesion on fibronectin.

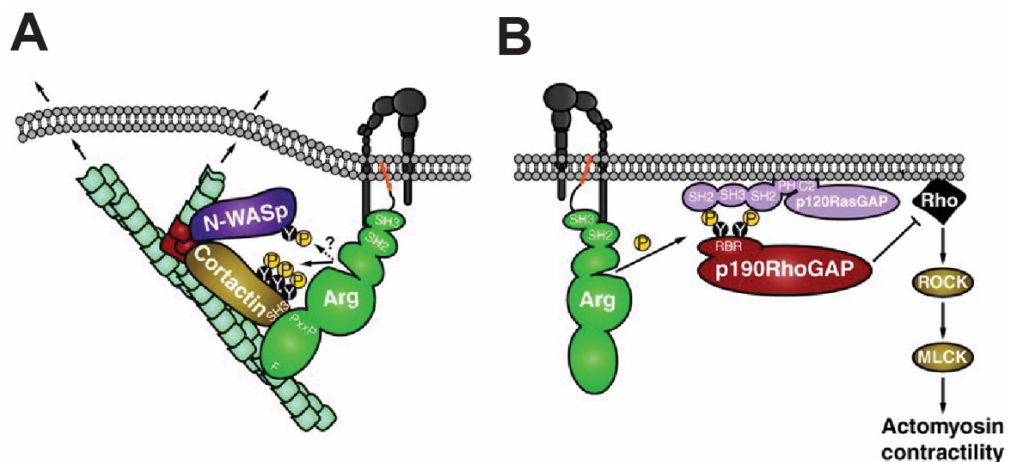


Figure 1.3. Abl family kinases regulate actin cytoskeleton dynamics through various signaling pathways. Adapted from (Bradley & Koleske, 2009).

For cell edge protrusions to form, actin polymerization requires the nucleation of actin filaments by the Arp2/3 complex or by formins. Cortactin, which binds to and activates the Arp2/3 complex (Urano et al., 2001), becomes tyrosine phosphorylated by Abl2 at 3 tyrosine residues (Tyr 421, 466, 482) in fibroblasts upon PDGF treatment and adhesion to fibronectin (**Figure 1.3, A**)

(Boyle et al., 2007; Lapetina et al., 2009; Mader et al., 2011). It was later revealed that both Abl2 and cortactin co-localize at the cell periphery at these protrusive structures in fibroblasts; and that knockdown of cortactin eliminates adhesion-dependent cell edge protrusions (Lapetina et al., 2009). Additional experiments reveal that the Abl2 N-terminal half does not bind to unphosphorylated cortactin, but binds with high affinity to phosphorylated cortactin, and that adhesion stimulates Abl2-dependent cortactin phosphorylation to present a novel binding site for the Abl2-SH2 domain (Lapetina et al., 2009). Retroviral expression of phospho-null cortactin (three Y-to-F point mutations in cortactin) or of Abl2 with a binding-defective SH2 point mutant in *abl2*^{-/-} fibroblasts reduces cell edge dynamics, which demonstrates that both phosphorylation of Y421 and Y466 and Abl2:cortactin binding interactions are required for adhesion-dependent cell edge protrusion. Phosphorylated cortactin also serves as a scaffolding protein to recruit additional SH2-domain containing proteins, e.g. Nck1, to modulate actin polymerization (Lapetina et al., 2009). Previous work from the Koleske Lab has revealed that Abl2-deficient dendritic spines are also deficient in cortactin and exhibit loss of stability in culture and *in vivo* (Lin et al., 2013). A recent study by Shaw and others also shows that Abl2 kinase activity and phospho-tyrosine binding via its SH2 domain to cortactin is necessary for Abl2 localization in dendritic spines for supporting normal spine density. Importantly, both cortactin phosphorylation by Abl2 and Abl2:cortactin binding interactions are required to maintain a stable actin pool in dendritic spines (Shaw et al., 2021).

Abl2 also phosphorylates (Burton et al., 2005; Miller et al., 2010) and directly binds to N-WASp (Miller et al., 2010), a member of the Wiskott-Aldrich Syndrome protein (WASp) and the WASp-family verprolin-homologous (WAVE) protein family (**Figure 1.3, A**). WAVE and WASp proteins contain a C-terminal verprolin-connecting acidic (VCA) domain that interacts with actin monomers and the Arp2/3 complex. The SH3 domain of Abl2 binds directly to N-WASp and phosphorylates N-WASp at Tyr 256, which increases its affinity of Abl2 for N-WASp – an interaction that does not require the Abl2 SH2 domain. The SH3 domain of Abl2 promotes N-WASp-dependent actin polymerization *in vitro* and has been shown to both colocalize at adhesion-dependent cell edge protrusions in 3T3 fibroblasts upon adhesion to fibronectin. Retroviral-mediated re-expression of Abl2 – but not an Abl2-SH3-point mutant that is defective in binding N-WASp – restores adhesion-

dependent cell edge protrusions (Miller et al., 2010). A later study by Courtemanche and others reveals that Abl2 stimulates filament severing by cofilin, but this is attenuated by cortactin. This is likely due to structural changes to the actin filament as Abl2 and cortactin do not compete for the same F-actin binding sites. Abl2 stabilizes F-actin with cortactin in a cooperative manner, and promotes actin filament branching by the Arp2/3:cortactin:N-WASp complex (Courtemanche et al., 2015).

Two additional phosphorylation substrates of Abl2 are a Rho-specific GTPase-activating protein p190RhoGAP (p190), which regulates cell motility and contractility (Bradley et al., 2006; Hernández et al., 2004). Cell motility is regulated by Rho family GTPases RhoA (Rho) and Rac1 (Rac) by coordinating F-actin cytoskeletal rearrangements (Spiering & Hodgson, 2011). Phosphorylation by Abl2 localizes p190 to the cell periphery where it forms a complex with p120RasGAP (**Figure 1.3, B**) (Bradley et al., 2006; Bradley & Koleske, 2009). Rho is membrane-bound protein and Abl2 controls the ability of p190 to inhibit Rho by modulating its localization. *abl2*^{-/-} fibroblasts exhibit high Rho activity, leading to high contractility with the formation of F-actin stress fibers (Peacock et al., 2007). Because Abl2 is required for p190:p120 complex formation at the cell periphery and phosphorylated p190 inhibits Rho activity for actomyosin contractility, it is postulated that Abl2 regulates Rho activity during cell adhesion and initial cell spreading for cells to sample their new environment (Bradley et al., 2006).

However, despite it being a kinase, Abl2 has the ability to directly interact with the cytoskeleton to regulate cell edge protrusions independently of its kinase domain, using only its C-terminal half (Lapetina et al., 2009; Zhang et al., 2018). Re-expression of the C-terminal half alone (Abl2-557-C) can restore cell edge dynamics upon adhesion in *abl2*^{-/-} fibroblasts up to 70% of WT levels (Miller et al., 2004). As noted above, a 2009 study revealed that Abl2 phosphorylates cortactin and phosphorylated cortactin enhances Abl2 binding (Lapetina et al., 2009). Additionally, the SH3 domain of cortactin binds to a PxxP motif within the C-terminal half of Abl2 (located within aa. 557-688). The binding interaction between the SH3 domain of cortactin and the first PxxP motif of Abl2-557-C is essential because re-expression of Abl2-688-C in *abl2*^{-/-} (lacking the three PxxP motifs) did not rescue adhesion-dependent cell edge protrusion, even though it localized to the cell

periphery (Lapetina et al., 2009). Additionally, Abl2 utilizes its extreme C-terminal calponin homology (CH) domain to increase cortactin:actin stoichiometry, from one cortactin per four actin subunits to one cortactin per two actin subunits. The binding of Abl2-CH on F-actin likely induces a twist, leading to a level of dissociation in actin subdomain 2. This structural re-arrangement by Abl2 binding may modify the cortactin binding site on the filament or eliminate steric hindrance thereby allowing cortactin to bind with increased density (MacGrath & Koleske, 2012). A seminal study by Miller and others revealed for the first time that Abl2 not only localizes to F-actin rich cell edge protrusions in cells, but also to the MT cytoskeleton (Miller et al., 2004).

1.1.3.2. Abl2 regulation of microtubule dynamics

The first clue into whether Abl2 regulated MT dynamics was from genetic studies in *Drosophila* that suggested functional interactions between Abl and the CLASP ortholog *orbit*. These interactions are required for proper axonal growth cone guidance which is mediated by dynamic MT reorganization (Lee et al., 2004; Lowery et al., 2010). In a 2004 study by Lee *et al.*, loss of function in *orbit* or Abl caused ectopic midline crossings in stage 17 *Drosophila* embryos. In contrast, homozygous loss of function in both *orbit* and Abl showed increased ectopic midline crossings at axon fascicles (**Figure 1.4**). These genetic data suggest that Abl and *Drosophila* CLASP cooperate at the midline for ensuring accurate growth cone orientation to avoid Slit. In *Drosophila* and *Xenopus* growth cones, it was shown from the same study that CLASP primarily localizes at the growth cone where many guidance cues occur to impact cytoskeletal remodeling. The authors proposed a model in which Abl locally phosphorylates CLASP as to impede MT growth in the direction nearest the source of Slit, a repulsive axon guidance cue.

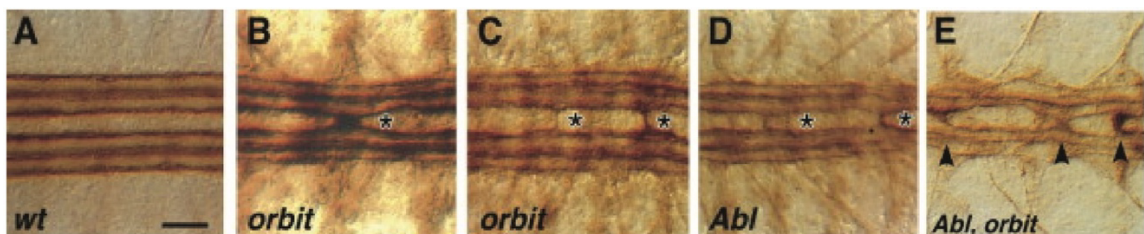


Figure 1.4. Abl kinase and *Drosophila* CLASP coordinate to ensure proper midline crossings at axon fascicles. Adapted from (Lee et al., 2004).

A biochemical study from the Koleske Lab revealed that Abl2 crosslinks F-actin and MTs. In *arg*^{-/-} 3T3 fibroblasts re-expressing Abl2-YFP, Abl2-YFP was found to co-localize with F-actin and MT structures at the cell periphery (**Figure 1.5**) (Miller et al., 2004). Abl2:actin:MT interactions were abolished upon treatment with latrunculin A or nocodazole in these cells. The authors determined that Abl2 C-terminal half containing both the F-actin and MT-binding domains is required to localize Abl2 to the cell periphery.

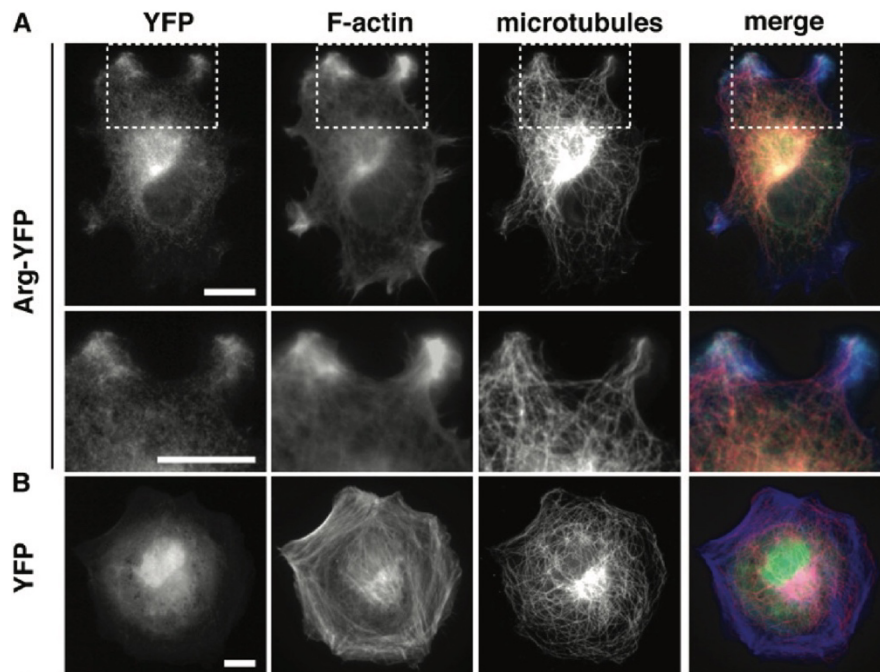


Figure 1.5. Abl2 co-localizes with both MT and F-actin structures at the cell periphery. Re-expression of Abl2-YFP in *abl2*^{-/-} 3T3 fibroblasts promotes lamellipodial dynamics (**A**), not YFP alone (**B**). Figure adapted from (Miller et al., 2004).

A follow-up biochemical study in 2014 by Engel and others demonstrated that Abl2 phosphorylation modifies the association of CLASP2 with microtubules (Engel et al., 2014). MYC-tagged CLASP2 α purified from HEK293T cells associated more with MTs, as assessed by co-sedimentation densitometric analysis, when incubated with Abl2 relative to CLASP2 α alone. Upon adding STI571 inhibitor (imatinib), which locks Abl2 in the kinase inactive conformation, CLASP2 α associated with MTs at similar levels relative to the condition in absence of Abl2. In *Xenopus* growth cones co-expressing GFP-CLASP2 with hyperactive Abl, the population of CLASP2 comets

significantly decreased compared to control. This phenotype was rescued upon treatment of STI571 indicating that the reduction in comet formation is an Abl phosphorylation-induced change in CLASP2:MT association. Interestingly, CLASP2 re-localized to large adhesion plaques within the central domain of hyperactive Abl-expressing growth cones. These actin-rich plaques also have an accumulation of Abl. Though this study additionally reveals that Abl2 kinase activity in spinal cord growth cones play a role in CLASP association with MTs and F-actin, it remains unclear whether Abl2 can directly bind MTs.

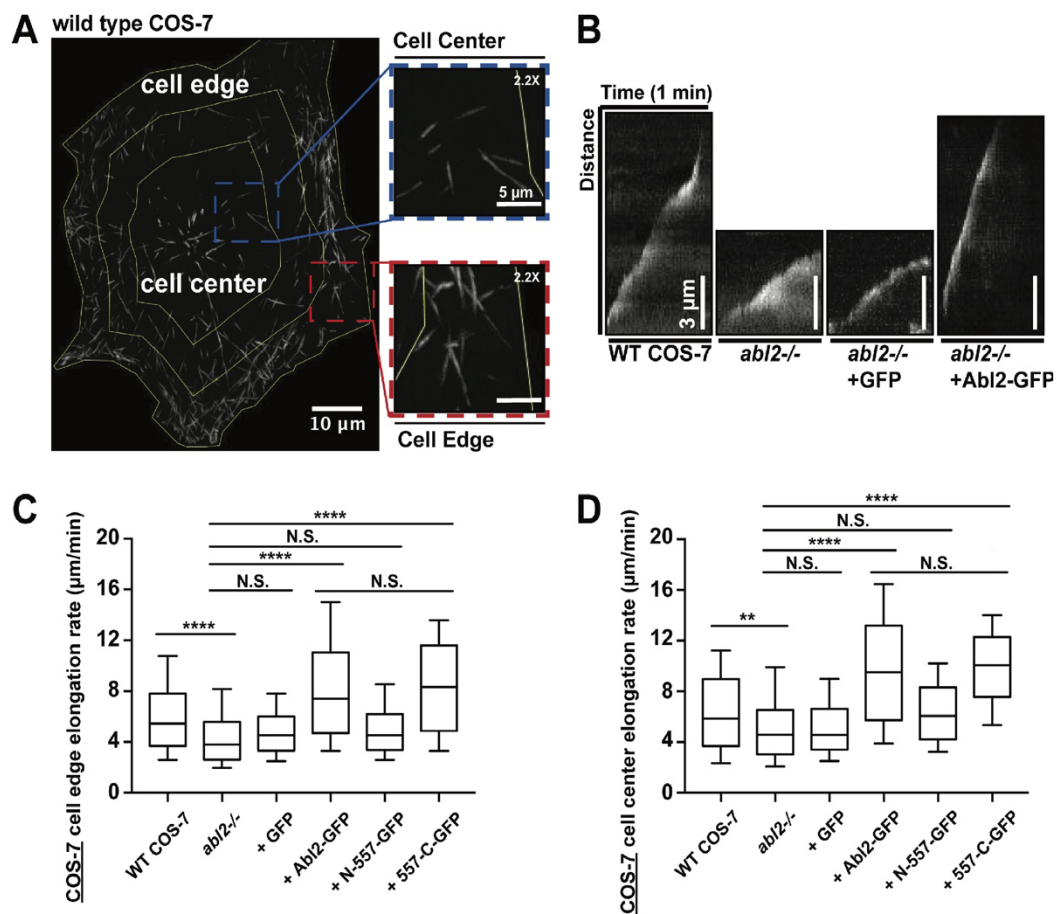


Figure 1.6. Abl2 promotes MT dynamics at the cell center and cell edge. (A) Scoring of MT dynamics in *abl2*^{-/-} COS-7 cells re-expressing MACF43 at the cell center and cell edge. (B-D) *abl2*^{-/-} COS-7 exhibit a reduction in MT dynamics at the cell edge and center (representative kymographs shown in B). Only the re-expression of Abl2-GFP or Abl2-557-C-GFP restores elongation rate, not the kinase-domain containing N-terminal half, Abl2-N-557-GFP at the cell edge (C) and cell center (D). Figure adapted from (Hu et al., 2019).

It was not until much later it was determined that the C-terminal half of Abl2, Abl2-557-C, is necessary and sufficient for binding to MTs, elongate polymers, and suppress catastrophe (**Figure 1.6, C**) (Hu et al., 2019). From the same study, it was demonstrated that Abl2 is necessary for normal MT growth in COS-7 cells. In Abl2-deficient COS-7 cells, MT growth rate was reduced by ~25% at the cell periphery (**Figure 1.6, A, D**). Expression of Abl2-557-C-GFP complemented this deficit, suggesting that Abl2 plays a crucial regulatory role in MT dynamics (**Figure 1.6, B-D**) (Hu et al., 2019). How the C-terminal half regulates microtubule dynamics remains unclear. Chapter 2 will further define novel microtubule cytoskeleton regulatory properties of Abl2: a) Abl2 binds to tubulin dimers via two binding interfaces; b) Abl2 promotes MT nucleation; and c) Abl2 promotes rescue frequency and lattice repair. See Sections 1.2.3 and 1.2.4 for discussion on lattice repair and nucleation. The next section will be focused on elaborating MT dynamics and structures elucidated from biochemical and structural studies.

1.2. Microtubule dynamics and structure

1.2.1. Microtubules are dynamic polymers

Microtubules (MTs) are one of the major cytoskeletal components that are present in all mammalian cell types. They are cylindrical hollow tubes assembled by laterally adjacent protofilaments polymerized from GTPase tubulin subunits. Tubulin subunits are comprised of α - and β -tubulin heterodimers that longitudinally bind in a head-to-tail manner (Brouhard & Rice, 2018; Desai & Mitchison, 1997; Lasser et al., 2018). MTs are polymers that undergo nonequilibrium behavior called dynamic instability, a phenomenon discovered by Mitchison and Kirschner in 1984 (Mitchison & Kirschner, 1984) to describe the stochastic interconversion between states of MT growth and shrinkage via cycles of GTP hydrolysis (**Figure 1.7**) (Erickson & O'Brien, 1992; Hyman et al., 1992). The transition from growth to shrinkage phases is called catastrophe and is a key feature of dynamic instability (Desai & Mitchison, 1997; Erickson & O'Brien, 1992; Hyman et al., 1992; Walker et al., 1988). Though a stochastic process, MT growth is biased: GTP-tubulin heterodimers are added at the growing plus-ends to form a stabilizing GTP-cap (Desai & Mitchison, 1997), which is generated and maintained depending on cellular needs, while local concentrations of microtubule-

binding proteins (MBPs) regulate MT dynamics (Brouhard & Rice, 2018; Kirschner & Mitchison, 1986; Lansbergen & Akhmanova, 2006). As more studies on MBPs are conducted to study their impact on MT dynamics, the GTP-hydrolysis model is evolving to capture the complexity of their behavior (Bowne-Anderson et al., 2015; Bowne-Anderson et al., 2013; Erickson & O'Brien, 1992; Vandecandelaere et al., 1999).

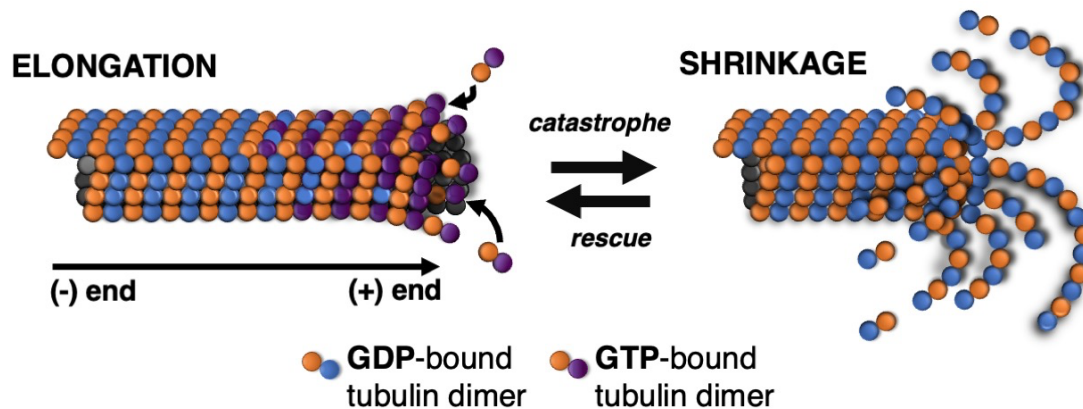


Figure 1.7. Dynamic instability of MTs. Length of MTs fluctuates at steady state. MTs elongate with addition of GTP-tubulins that cap at plus-ends and shorten when GTP hydrolysis and dimer addition events occur at similar rates. In the absence of a GTP-tubulin cap, GDP-tubulin protofilaments (PFs) curve, causing dissociation of dimers and rapid shortening of MTs.

1.2.2. Microtubule dynamics are regulated by microtubule-binding proteins

MT dynamics are regulated by microtubule-binding proteins (MBPs). Though both ends of MTs are capable of undergoing growth *in vitro*, plus ends experience greater dynamic instability than minus ends (Howard & Hyman, 2009). Plus ends serve as hubs for proteins to bind, including those that lie within a subset of MBPs called plus end tracking proteins (+TIPs) (Akhmanova & Steinmetz, 2008; Nogales, 2000). Recently, minus end tracking proteins (-TIPs) were discovered to tightly regulate minus-end dynamics and stabilize the MT filament (Akhmanova & Hoogenraad, 2015). +TIPs and -TIPs impact different parameters that govern dynamic instability. +TIPs such as End-Binding (EB) protein, a master regulator of the +TIP network that recruits other MBPs to growing ends (Akhmanova & Steinmetz, 2008), prefers to bind to a specific region within the MT lattice (**Figure 1.8**). EB proteins prefer to localize at the ends where polymerized tubulin is in its GDP·Pi state, and they stimulate the rate of GTP hydrolysis, increasing both MT growth rate and catastrophe frequency (Akhmanova & Steinmetz, 2011; Duelberg et al., 2016; Maurer et al., 2011;

Maurer et al., 2014; Rickman et al., 2017; Zanic et al., 2009; Zhang et al., 2015). However, the XMAP215 polymerase binds to soluble tubulin in solution and can diffuse along the lattice until it reaches the MT tip for processive plus-end loading, increasing growth rate without impacting catastrophe frequency (**Figure 1.8**) (Brouhard et al., 2008). -TIPs including CAMSAP2/3 proteins within the CAMSAP/Nezha/Patronin family autonomously bind and cap the minus ends, stabilize the MT lattice, and restrict minus end growth and shortening (**Figure 1.8**) (Akhmanova & Hoogenraad, 2015; Akhmanova & Steinmetz, 2015, 2019).

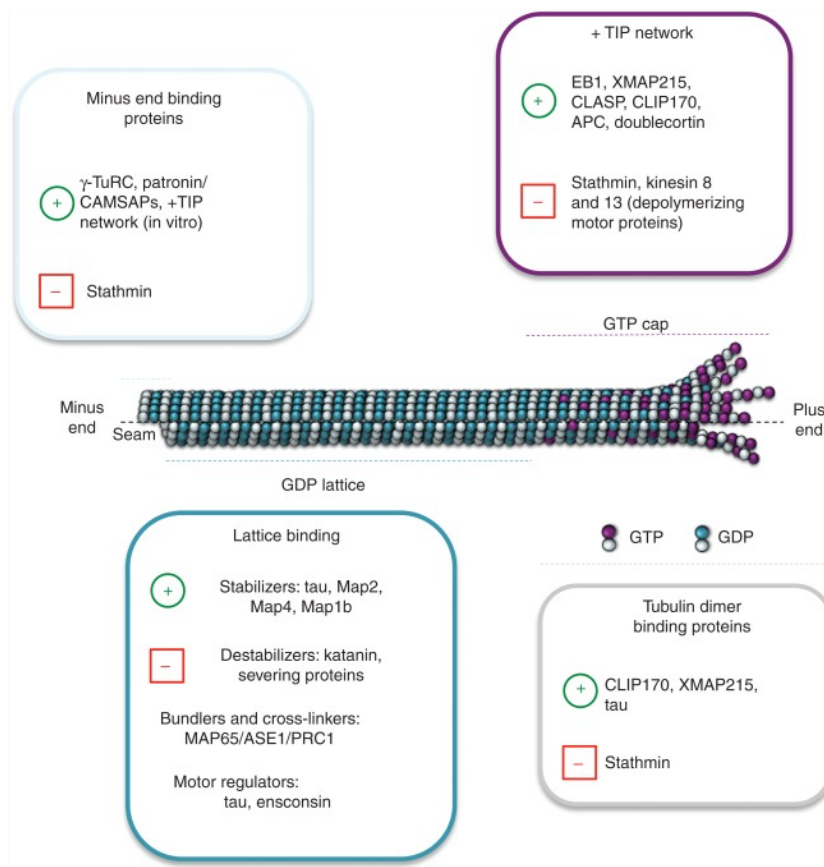


Figure 1.8. Landscape of the MT lattice harboring different binding sites for various classes of MBPs. Adapted from (Goodson & Jonasson, 2018).

A subset of MBPs are microtubule-associated proteins (MAPs) including tau and MAP2. Tau and MAP2 are structural MAPs that exert stabilizing effects on MT assembly by binding the MT lattice (**Figure 1.8**) (Al-Bassam et al., 2002). Tau, like EB and XMAP215 proteins, can diffuse along the lattice, but instead increases MT growth rate and suppresses catastrophe (Bodakuntla et al., 2019;

Castle et al., 2020; Drechsel et al., 1992; Hinrichs et al., 2012; McVicker et al., 2014). However, there are lattice-binding destabilizing MBPs such as severing proteins katanin and spastin that increase shrinkage rate, and kinesin-13 that decreases the number of steps a MT takes towards catastrophe (Bailey et al., 2015; Bowne-Anderson et al., 2015; Hertzler & Walczak, 2008). This evidence demonstrates that though dynamic instability is stochastic, in the presence of MBPs, the growth and shrinkage of MTs can be modulated (Kirschner & Mitchison, 1986). Remodeling the MT network under MBP regulation is critical for cell polarity, development and response to environmental cues, such as the process of neuronal morphogenesis (Baas et al., 2016; Hoogenraad & Bradke, 2009; Kapitein & Hoogenraad, 2011; Koleske, 2013).

1.2.3. Structures of microtubule polymers in various nucleotide states and recognition by MBPs

There are many types of single-protofilament models developed to explain how dynamic instability is tightly coupled to GTP hydrolysis, often focusing on the presence and loss of a stabilizing cap of terminal GTP-bound tubulin subunits (O'Brien et al., 1987; Odde et al., 1995; Walker et al., 1988). GTP hydrolysis is triggered by the glutamate residue in the incoming α -tubulin (E254) that is adjacent to the GTP nucleotide in the β -subunit at the longitudinal interface between dimers. Hydrolysis has a destabilizing effect because polymerization can only proceed in the presence of GTP-tubulin at the most terminal end of the tip. It is thought that GTP-cap must remain to prevent depolymerization (Drechsel & Kirschner, 1994). There are four types of GTP hydrolysis models to describe the switch-like behavior from MT growth to catastrophe: 1) vectoral hydrolysis; 2) random hydrolysis; 3) coupled random hydrolysis; and 4) stabilizing GTP-cap (**Figure 1.9**). For this dissertation, I will solely focus on the GTP cap model as it pertains to understanding the structural states of both the MT lattice and growing tips.

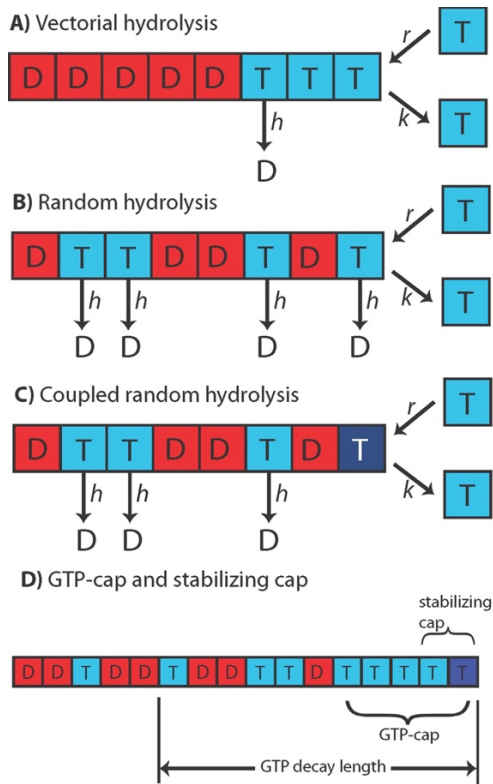


Figure 1.9. Schematic of single-protofilament models that explain the relationship between GTP hydrolysis and dynamic instability. (A) Vectorial hydrolysis. GTP hydrolysis only occurs at the GDP-tubulin:GTP-tubulin dimer interface in the lattice. This model presents challenges as growth rate can be lower than the hydrolysis rate so MTs undergo catastrophe almost immediately upon nucleation. If growth rate is larger than the hydrolysis rate, the GTP-cap becomes large such that catastrophes rarely occur. (B) Random hydrolysis. Any tubulin dimer that has incorporated into the lattice has the same probability of undergoing hydrolysis. Though this model allows for existence of GTP islands, it fails to predict dynamics over a large range of tubulin concentrations. (C) Coupled random hydrolysis. GTP hydrolysis can also occur randomly as in (B), but it is only the terminal dimer that cannot undergo hydrolysis. This model fails to account for the multi-step catastrophe process (Odde et al., 1995). (D) GTP-cap and stabilizing cap. There is a distinction between the GTP-cap, which consists of the entire length of the terminal end of the MT in the GTP-bound state, and the stabilizing cap which consists of 2 GTP-bound dimers. The most terminal tubulin dimer cannot undergo hydrolysis. Adapted from (Bowne-Anderson et al., 2013).

The GTP cap model has undergone many variations in the past five decades. The GTP-tubulin cap model suggests that at least one layer of tubulin dimers in the GTP-bound state is required to prevent the microtubule from undergoing catastrophe, which initiates upon solvent exposure of GDP-tubulin at the plus-ends (Walker et al., 1989; Walker et al., 1991). This was determined from an early study that revealed microtubules grown with the slowly hydrolysable analog GMPCPP does not undergo dynamic instability (Hyman et al., 1992). Most of the earlier single-protofilament models have their shortcomings, one of them being the inability to capture the multistep catastrophe

process. Thus, multiple-protofilament models have been developed, with the latest one being the coupled-random hydrolysis model which postulates that the GTP-cap is distinct from the most terminal two-layer stabilizing cap (Bowne-Anderson et al., 2013; VanBuren et al., 2002).

The evolving GTP-cap model serves as the foundation for our understanding of dynamic instability because the nucleotide state of polymerized tubulin within the lattice determines the recruitment of MT effectors. Along with the development of many theoretical models stemming from experimental observations and measurements of dynamic instability rate parameters, many biochemical and structural studies have focused on understanding the mechanism and resolving structures of MT polymers undergoing these nucleotide state transitions. MTs in these nucleotide states are: 1) the GDP-lattice; 2) the immediate post-hydrolysis GDP·Pi state at the growing ends; and 3) the terminal GTP-cap. Seminal biochemical studies led by Carlier and Pantaloni show that both AlF_4^- and BeF_3^- can serve as inorganic phosphate analogs to mimic kinetic intermediate states of MT-GDP-Pi (Carlier, Didry, Melki, et al., 1988; Carlier, Didry, Simon, et al., 1988). In 2020, Estevez-Gallego *et al.* found that not $\text{GTP}\gamma\text{S}$ but GDP- AlF_4^- bound MTs best mimic MTs in the immediate post-hydrolysis state, and that MTs exhibit expanded lattices transiently to release the inorganic phosphate, transitioning between GDP-Pi and the eventual GDP-state (Estévez-Gallego et al., 2020).

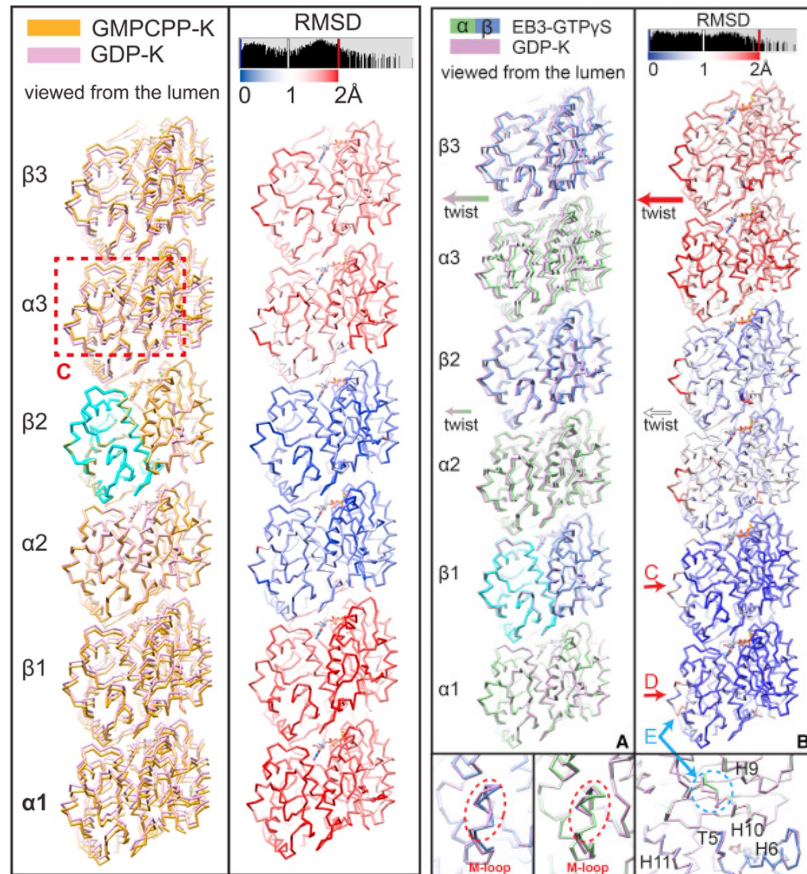


Figure 1.10. EB3-bound GTP γ S-MT reveals that EB3 induces a lattice twist and compaction. Adapted from (Zhang et al., 2015).

In addition to solving structural architectures of MT polymers undergoing each stage of GTP hydrolysis, it is equally important to determine where along the MT polymer an MBP binds, as it is linked to the molecular mechanisms underlying protein function. A study by Alushin and others demonstrated that GTP hydrolysis is accompanied by a ~ 2.5 Å longitudinal compaction of the interdimer interface within the tubulin lattice (Alushin et al., 2014), and the compacted GDP-lattice can be expanded with MT stabilizing agents including taxanes (Prota et al., 2023). +TIPs like EBs recognize polymerized tubulin at the growing ends of MTs and mark the GTP-cap (Rickman et al., 2017; Roostalu et al., 2020; Seetapun et al., 2012). Many biochemical and biophysical studies have shown that EBs likely recognize a particular MT lattice structure (Vitre et al., 2008; Zanic et al., 2009). It was not until Maurer and others in the Surrey Group found that Mal3 or fission yeast homolog of EB1 likely recognizes the immediately post-hydrolyzed state of MTs using non-

hydrolysable GTP analog GTP γ S (Maurer et al., 2011). The mechanism by which EB proteins bind to MT lattices was first structurally determined by the Nogales Group by using reconstituted MTs grown in the presence of either GMPCPP or GTP γ S (**Figure 1.10**) (Zhang et al., 2015). Compared to the expanded lattice of GMPCPP-MT, the EB3-bound GTP γ S-MT has a compacted lattice with a difference in lattice twist compared to that of GDP-MT and reveals highest EB3 occupancy compared to GMPCPP-MTs and GDP-MTs. However, it is worth noting that buffer supplemented with GTP and kinesin was used to dilute dynamic GDP-MTs because recent studies demonstrate that kinesin binds GDP-MTs and expands them, making structural comparisons inaccurate. Nonetheless, Zhang and others in the Nogales Group show that even EB3-bound GMPCPP-MT exhibit missing Mg²⁺ and γ -phosphate, suggesting that EB3 stimulates hydrolysis and release of the inorganic phosphate (**Figure 1.10**) (Zhang et al., 2015). Another 2018 cryo-EM study revealed that by taking advantage of the nucleation efficiency of doublecortin—a MAP that promotes MT nucleation—to immediately generate 13 pf-MTs in their GDP-Pi state, it was revealed that these polymers undergo GTP hydrolysis and consequentially, longitudinal interdimer compaction (Manka & Moores, 2018).

Despite resolving structures using GTP and inorganic phosphate analogs in the presence or absence of MBPs, the GTP-cap model is insufficient to explain for the dynamics of the MT minus end. After eliminating the small GTP-cap via UV microbeam and microneedle cutting experiments (Tran et al., 1997; Walker et al., 1989), the minus end resumes elongating whereas the newly severed plus end quickly depolymerizes. The Zanic Group challenges this model by demonstrating that not only is the GTP hydrolysis at either end the same, the GTP-tubulin off rate at minus ends is lower than that of the plus end, suggesting that the GTP-cap at minus ends are more stable (Farmer & Zanic, 2022; Strothman et al., 2019). Thus, the GTP-cap size is not the only determining factor that prevents MT from undergoing catastrophe.

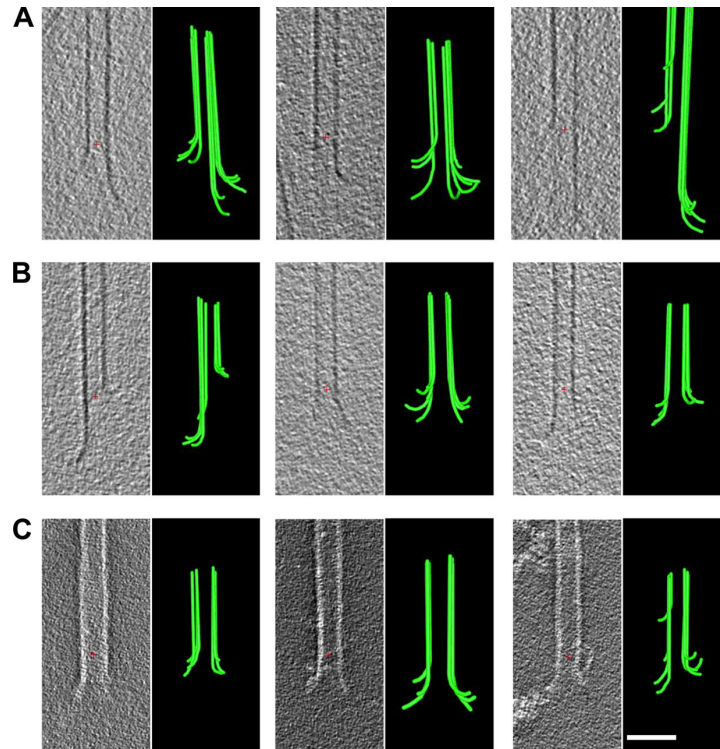


Figure 1.11. Representative cryo-electron tomographic slices of growing MT ends under various stabilizing conditions. Shapes of growing ends shown in slides (left) with models (right). **(A)** MTs plunge frozen while still growing in GMPCPP. **(B)** MTs fixed isothermally in 0.2% then 2% glutaraldehyde prior to plunge freezing. **(C)** MTs fixed in 0.2% first followed by 2% glutaraldehyde, then negatively stained in uranyl acetate. Despite the different stabilizing conditions, growing MTs still reveal various flared conformations. Adapted from (McIntosh et al.,

Cryo-electron tomography (cryo-ET) studies challenge the notion that GTP-tubulin polymerized in the lattice is straight, but rather suggest it mimics curling, flared protofilament ends in disassembling MTs (**Figure 1.11**) (Höög et al., 2011; McIntosh et al., 2018). As these structural studies began to emerge, there is a shift away from the notion that MT effectors recognize polymerized tubulin in a nucleotide-bound state, but rather recognize conformation polymerized tubulin adopts due to lattice spacing (LaFrance et al., 2022). For example, human full-length tau 2N4R recognizes the compacted GDP-lattice (Castle et al., 2020; Siahaan et al., 2022; Tan et al., 2019). Likewise, kinesin-1 prefers to bind to compacted GDP-like lattices and expands them for stabilization (Shima et al., 2018). On the other hand, a recent study has shown that CAMSAP3, an indispensable non-centrosomal MT nucleator, prefers to bind the expanded MT lattice which mimics the GTP-bound state at the minus ends (Liu & Shima, 2023). EB1 exhibits similar binding preference for the expanded lattice as steric hindrance prevents EB1 binding at the interface

between four adjacent tubulin dimers at +TIPs (Reid et al., 2019). However, these transitions in the MT polymer owing to GTP hydrolysis are complex (Estévez-Gallego et al., 2020). EB proteins have been found in another study to bind to both the straight and curved portions of the MT lattice (Guesdon et al., 2016). Although CAMSAP3 can expand MT lattices, the lattice expansion returns to its original state upon CAMSAP3 dissociation (Liu & Shima, 2023). The notion that regions all along a dynamic MT lattice undergo different structural transitions has altered the way the field looks at local MT regulation. In particular, seminal studies have revealed that for the first time, tubulin dimers can self-repair by localizing to sites of damage along the MT lattice (Aumeier et al., 2016; de Forges et al., 2016; Gazzola et al., 2023; Schaedel et al., 2015; Triclin et al., 2021). The next section elaborates on how the MT polymer not only undergoes dynamic instability but contains an intrinsic self-repair mechanism to mediate lattice replenishment, and how MBPs promote this self-repair mechanism.

1.2.4. Regulation of microtubule lattice repair

Farmer and Zanic state that the size of the GTP-cap is not the sole factor in determining MT stability or predicting lifetime, but rather it is the structure of the growing end that ultimately dictates the fate of the polymer (Farmer & Zanic, 2022). An example MBP that challenges this notion of the GTP-cap size being a primary determinant of MT fate is the cytoplasmic linker-associated protein (CLASP). CLASP proteins contain tubulin-binding TOG domains and promote MT nucleation at the centrosome and the Golgi apparatus. CLASPs do not increase GTP-cap size, as experiments using an EB1 mutant lacking the C-terminal CLASP2-binding domain revealed no change to the density of EB1 proteins at the growing ends (Lawrence et al., 2018). CLASP2 also does not impact growth nor shrinkage rates, but rather the catastrophe and rescue frequencies (Aher et al., 2018; Lawrence et al., 2018). It is likely CLASP recognizes a specific inter- or intra-dimer interface within a protofilament to stabilize the MT, potentially using even a single TOG domain (**Figure 1.12**). Additionally, in experiments that include both EB and CLASP proteins, the number of repair events for EB-positive comets increase, suggesting that CLASP stabilizes polymers with incomplete lattices so that the MT can repair itself (Aher et al., 2018). This was one of the earlier studies that

reveal MBPs has a structural recognition feature that may allow these macromolecules to exert their function based on their loci along these dynamic polymers.

1.2.4.

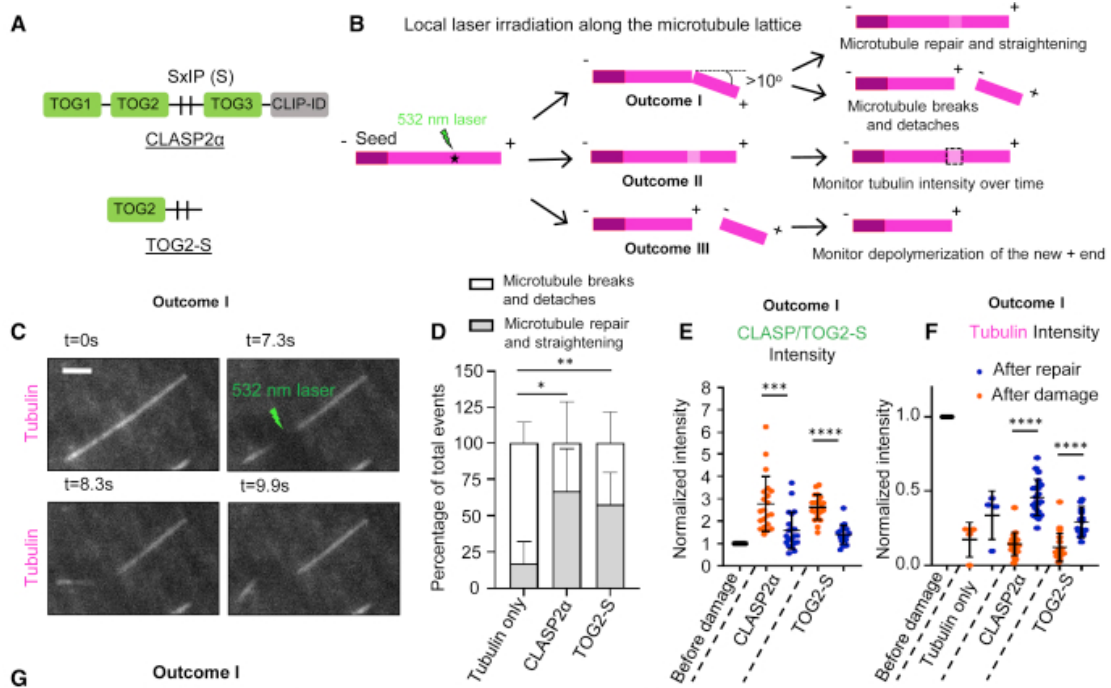


Figure 1.12. CLASP2 α stabilizes newly severed ends and promotes repair by directly recruiting to laser irradiated sites. (A) Domain architecture of CLASP2 α and its TOG2S fragment. **(B)** Schematic to monitor outcomes of a 532 nm pulsed laser induced damage at a site in a dynamic MT lattice. MTs can bend at site of damage that may lead to straightening of the lattice, or MT breakage. Tubulin will also reduce in intensity. MT severing may result also in the appearance of two novel ends. **(C)** Photodamage of a MT growing, undergoing bending, followed by complete breakage and detachment. **(D)** Quantification of total MT photodamage events in absence or presence of CLASP2 α or TOG2-S. Adapted from (Aher et al., 2020).

The idea of aged MT lattices exhibiting vacancies or missing dimers and undergoing transitions in lattice periodicity is not new (Chrétien & Fuller, 2000; Chrétien et al., 1992). However, with the advent of single-molecule TIRF microscopy and antibodies that recognize the GTP-bound polymerized tubulin, it was discovered that MTs not only harbor GTP-bound polymerized tubulin at growing ends, but contain GTP islands within the aged lattice (Dimitrov et al., 2008; Tropini et al., 2012). Several subsequent experimental and computational studies have shown the tubulin dimer itself can promote rescue by replenishing MT lattices at sites of structural defects (Alexandrova et

al., 2022; Aumeier et al., 2016; de Forges et al., 2016; Gazzola et al., 2023; Schaedel et al., 2015; Schaedel et al., 2019; Triclin et al., 2021).

MT lattice defects induced by mechanical stress, severing enzymes, or fast polymerization impact MT dynamics by triggering shrinkage or precluding rescue from catastrophe (Andreu-Carbó et al., 2022; Arellano-Santoyo et al., 2017; de Forges et al., 2016; Reid et al., 2017; Schaedel et al., 2015; Schaedel et al., 2019; Triclin et al., 2021). These defects are detected by tubulin itself (Aumeier et al., 2016; Gazzola et al., 2023; Schaedel et al., 2015; Triclin et al., 2021) and/or by MBPs such as SSNA1 via a readout mechanism for localization on the MT (Lawrence et al., 2021); and are repaired via incorporation of new tubulin dimers, which is stimulated by MBPs such as CSPP1 (van den Berg et al., 2023) and CLASP2 (Aher et al., 2020; Al-Bassam et al., 2010). It is thought that the physiological context underlying lattice repair may complement “wholesale” turnover of MTs to maintain the integrity of the microtubule network in homeostasis. Self-repair may be mediated and regulated by recruitment of MBPs at specific subcellular regions, especially when exposed to mechanical stress or in the process of cell polarization (Portran et al., 2017; Xu et al., 2017). Additionally, it is also known that molecular motors can induce lattice damage, either by pulling dimers from the lattice or having already walked along and disassembled unstable regions of the MT polymer (Théry & Blanchoin, 2021). But in doing so, motor activity also promotes repair as soluble tubulin can replenish the MT shaft (Andreu-Carbó et al., 2022). Though the exact mechanisms by which motors induce damage and promote rescue remains unclear, there is likely a feedback loop by which motor proteins undergo intracellular trafficking through modulation of MT dynamics (Théry & Blanchoin, 2021). Motor recruitment, pausing, and motility along the MT shaft is likely a response to the conformation changes it induces on the MT shaft (Andreu-Carbó et al., 2022; de Jager et al., 2022; Shima et al., 2018). The heterogeneity that exists within MT subnetworks—and at the single MT level shown by kinesin motor track selectivity (Cai et al., 2009)—allows for fine tuning local stabilization and density of MTs underlying cell polarity (Lavrsen et al., 2023; Mehidi & Aumeier, 2023). MT dynamics are necessary for supporting various cellular processes, thus the initial formation or nucleation of MTs must carefully regulated and finetuned *in vivo* to support local cellular needs.

1.2.5. Existing models for MT nucleation in neurons

Most cells and young neurons have a centrosome, which serves as the primary microtubule organizing center (MTOC). The centrosome contains the γ -tubulin ring complex (γ TuRC), which is a large multi-protein complex that serves as the template for MT formation in eukaryotes and anchors the radial MT network (**Figure 1.13, A**). γ TuRC contains 14 γ -tubulin proteins that organizes into a cone-like structure via γ -tubulin complex proteins 2-6 (GCP2-6) and is thought to form a stable cap for nucleation by interfacing with α -tubulin subunits at minus ends. γ TuRC alone is not sufficient to support MT assembly *in vitro* nor *in vivo*, as other proteins are required to synergize and stimulate nucleation. One of these stimulators is XMAP215, which promotes MT polymerization and synergizes with γ TuRC to promote MT nucleation (Brouhard et al., 2008; Thawani et al., 2018; Widlund et al., 2011). γ TuRC-mediated nucleation activator (γ TuNA) or CDK5RAP2 also promotes nucleation by synergizing with the γ TuRC *in vitro*, and depletion of endogenous CDK5RAP2 impairs both centrosomal and acentrosomal MT nucleation (Choi et al., 2010). In fission yeast *S. pombe*, cytosolic Mto1 and Mto2 form the Mto1/2 complex, activating γ -TuRC without localizing to the MTOC. Instead, they multimerize into a higher-order complex to drive assembly of multimeric γ -TuRC (Lynch et al., 2014). Though many genetic studies focus on understanding how MT nucleation is activated and regulated in cells, still very little is known about the assembly of the critical nucleus or the smallest stable intermediates formed at the onset of MT nucleation.

To visualize structural intermediates during nucleation and understand how the critical nucleus is formed, structural and biochemical studies made use of reconstituted microtubules from bovine or porcine brain tissue undergoing spontaneous nucleation. Spontaneous nucleation is the process in which MTs can nucleate *in vitro* in the presence of GTP and magnesium ions in an appropriate buffered solution (Brinkley Renaturing Buffer 80, BRB80). It is a kinetically restrained process as there exists a high activation energy barrier, and the efficiency increases nonlinearly with the concentration of free tubulin (Kuchnir Fygenon et al., 1995). Without a template, at least 20 μ M tubulin is required for nucleation (Voter & Erickson, 1984). From turbidity assays (“bulk

experiments”) which measure the optical density throughout time, there is a characteristic lag phase prior to the onset of nucleation and later for elongation, which is often thought to be attributed to the formation of the critical nucleus – the rate-limiting step of the MT nucleation-elongation pathway (Flyvbjerg et al., 1996). Negative-stain EM has directly visualized these nascent oligomers, with some studies noting that the MT intermediates are sheet-like with various curvatures or ribbon-shaped structures (Roostalu & Surrey, 2017). Roostalu and Surrey note that the energy barrier for MT nucleation can be reduced to stabilize both longitudinal and lateral tubulin-tubulin contacts in these intermediates, which is mediated by MBPs. A recent theoretical model developed by Rice and others explains the kinetics of spontaneous MT assembly, elaborating that steps towards polymer formation are energetically favorable but kinetically frustrated with addition of new layers (Rice et al., 2021). The rates for layer additions depend on how fast tubulin docks onto the growing sheet, and increasing this rate should enhance the initiation of layer formation and zippering of the nascent MT tube. Proteins that increase this rate include XMAP215 which accelerates the delivery of tubulin dimers to the layer (Ayaz et al., 2014); and Targeting protein for Xklp2 (TPX2) and doublecortin that bridge neighboring subunits together to enhance longitudinal and lateral contacts (“molecular stapling”) (Bechstedt et al., 2014; Fourniol et al., 2010; Zhang et al., 2017).

In cells, there are MBPs such as CAMSAP/Patronin (Goodwin & Vale, 2010; Jiang et al., 2014; Yau et al., 2014), CLASPs (Aher et al., 2018; Aher et al., 2020; Al-Bassam et al., 2010; Efimov et al., 2007; Girão et al., 2019; Lawrence et al., 2018; Majumdar et al., 2018), and p150^{Glued} (Lazarus et al., 2013) that enhance unstable longitudinal and lateral contacts in an open tube/sheet-like structure to stabilize formation of the critical nucleus. Spastin/Op18 and katanin can harness energy from ATP hydrolysis to sever existing MT lattices, thereby generating new minus ends in cells which serve as new nucleation templates (**Figure 1.13, B**) (Kuo & Howard, 2021; Kuo et al., 2019; Roll-Mecak & Vale, 2006). In mature neurons, the centrosome loses its role as the MTOC as γ -tubulin becomes delocalized during differentiation (Stiess et al., 2010). MTs serve as the structural backbone for axons and dendrites in neurons, and also serve as tracks for mediating retrograde and anterograde transport of cargoes. Axons, however, span millimeters in length with dendrites adopting highly polarized branch morphologies. Though it remains elusive how specific sites of

neuronal acentrosomal MT nucleation are determined, there have been strides made towards understanding how dendritic and axonal MT nucleation occurs.

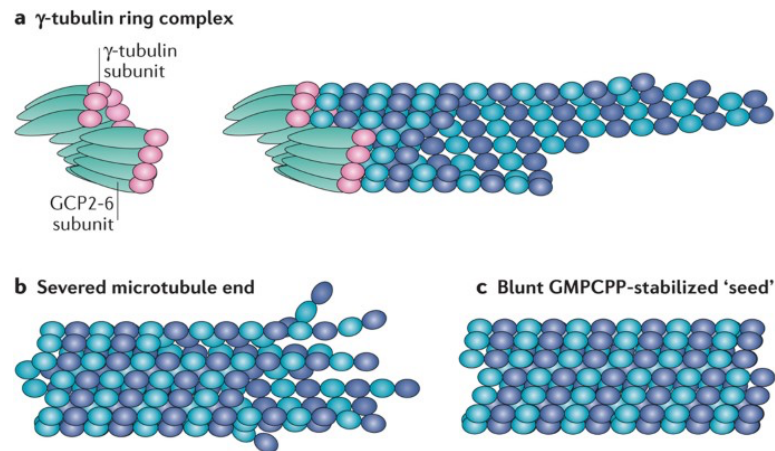


Figure 1.13. Different templates for microtubule nucleation *in vitro* and in cells. Adapted from (Roostalu & Surrey, 2017).

Non-templated and branching nucleation are two types of nucleation found in cells and neurons. Non-templated nucleation refers to nucleation that occurs independent of a template, whereas branching nucleation refers to daughter MTs that are nucleated from pre-existing MTs. In axons, the HAUS/augmin complex binds to the side of a MT and recruits γ TuRC which is stimulated by RanGTP and TPX2 (Kraus et al., 2023; Petry et al., 2013). Puncta of colocalized γ -tubulin and HAUS are found at excitatory synapses, which suggest pre-synaptic localization of nucleation sites whose nucleation function can be regulated by neuronal activity (Qu et al., 2019). A later study reveals that at axon branch sites, augmin is less likely to be involved in mediating branched MT networks but rather, it determines MT orientation (Sánchez-Huertas et al., 2016). Another MT-binding protein SSNA1 mediates MT nucleation and promotes branching of new MTs from existing ones (Basnet et al., 2018). SSNA1 localizes at axon branching sites in primary neurons and promotes the formation of fork-like structures as visualized by cryo-electron tomography (cryo-ET, **Figure 1.14**). Cryo-ET reconstructions reveal that newly assembled protofilaments are not connected to the mother MT, but rather, there is a clear discontinuity, that is, there exists a splitting point of the branch (**Figure 1.14**). Interestingly, SSNA1 oligomerizes to form condensates—mediated by its two N-terminal acidic residues and three basic C-terminal consecutive residues—

as to increase its local concentration to promote aster-like formation of MTs and nucleation from the sides of pre-existing MTs. Swapping the two acidic residues to lysines and three basic residues to glutamic acid residues (resulting in net charge of +1 to -1) eliminated MT branching. Upon transfection of a MT-branching deficient 5A mutant (both acidic residues and all three basic residues mutated into alanines) abolished axon branch formation in mouse hippocampal neurons. Basnet and others reveal that SSNA1 independently promotes MT branching at branch sites to promote axon growth via self-multimerization.

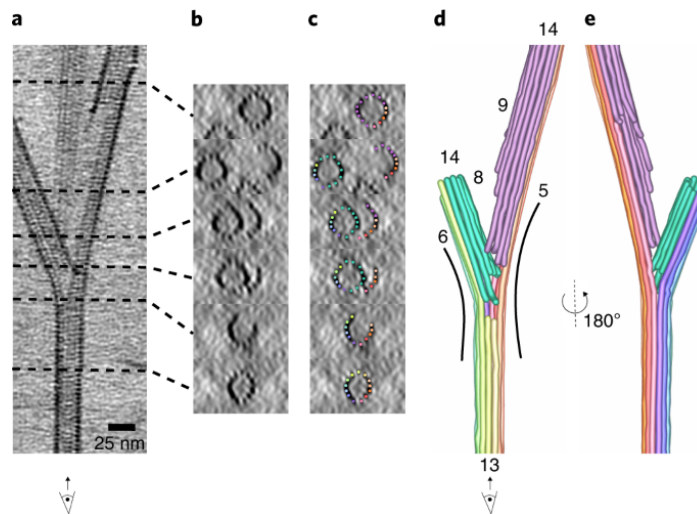


Figure 1.14. Cryo-ET reconstructions reveal branching of new microtubules under regulation of SSNA1. (A-C) Cross-sections of 14-pf branched microtubules from a 13-pf mother microtubule. **(D-E)** Individual protofilaments are traced in 3D density map of MT shown in (A). Newly formed MTs are shown in green (left) and pink (right). Adapted from (Basnet et al., 2018).

Currently, there is still little known how γ -tubulin is localized in dendrites, but sites of dendritic nucleation have been elucidated from *Drosophila* and *C. elegans* studies (Weiner et al., 2021). Non-templated nucleation is mediated by AAA-ATPase severing proteins such as stathmin/Op18 and minus-end stabilizers CAMSAP/Patronin which function synergistically. One of the original neuronal MT nucleation models posits that though the arrangement of neuronal MTs is non-centrosomal, neuronal MTs destined for the axon and dendrites are preassembled in the soma and delivered via an active transport mechanism by combination of severing and motor proteins (Baas & Yu, 1996). A seminal 1995 study revealed that MTs are severed away by katanin and released from the γ TuRC at the centrosome to be transported into the axon in cultured rat ganglion

neurons (Ahmad & Baas, 1995). Microinjection of an antibody that targets and inactivates katanin inhibited axon outgrowth and caused an accumulation of MTs at the centrosome. Followed by generation of freed minus ends from the centrosome, CAMSAP/Patronin decorates, and form stretches along the minus ends to ensure proper dendrite development (Yau et al., 2014).

Curiously, it was postulated that nucleation hotspots originate from Golgi outposts which serve as mini-MTOCs at branch points in *Drosophila* sensory neurons (Mukherjee et al., 2020; Ori-McKenney et al., 2012). However, this is now being reconsidered as removing the dendritic Golgi outposts did not delocalize γ -tubulin at branch points (Nguyen et al., 2014). These initial studies brought into light that organelles can serve as nucleation sites, bringing forth another neuronal MT nucleation model that comes from the observation that centrosomal γ -tubulin decreases over time, so MTs must be generated locally in axons and dendrites (Stiess et al., 2010). From combined studies in *Drosophila* and developing *C. elegans* neurons, it is becoming more widely accepted MTs are likely not originated from Golgi outposts but from early endosomes. In developing *C. elegans* sensory neurons, the anterior dendrite minus-end out polarity is determined via positioning of an MTOC within the growth cone (Liang et al., 2020). γ TuRC also localizes to the growth cone region during development, co-localizing with endosome marker Rab11 in primary dendrites. Liang et al. found that depletion of Rab11 in *C. elegans* neurons impaired γ TuRC localization, which parallels similar phenotypes in non-neuronal cells (Hehnlly & Doxsey, 2014) and in *Drosophila* dendrites (Weiner et al., 2020). Rab11 endosomes play a role in mitotic spindle organization in U2OS and HeLa cells via dynein-mediated endosome transport. In a *Drosophila* study by Weiner et al., using EB1-GFP as a readout of nucleation, authors observed new comets initiating from puncta labeled with Rab5, an early endosomal marker, which co-localized with Wnt signaling markers located at dendritic branch points (a conserved signal transduction pathway that dictates developmental processes and tissue homeostasis in metazoans). This revealed that endosomes carry MT nucleating and regulatory proteins to the spindle poles, and mediate high order branch related MTOC assembly. Additionally, in *Drosophila* neurons, the tethering of a Wnt signalling player, Axin, to mitochondria increased MT dynamics in dendrites by recruiting and positioning γ -tubulin and centrosomin, Cnn, at branch points. Depletion of Wnt signaling proteins phenocopied

the loss of γ -tubulin which resulted in changes in dendritic MT polarity and reduced ability to nucleate following axon injury. Collectively, these data suggest that Wnt signaling proteins directly recruit nucleation complexes at branch points. Future studies include determining whether Axin plays a similar role in localizing γ -tubulin at specific non-centrosomal nucleation sites in the endosomal Wnt signaling pathway in mammalian cell types. Together, from *in vitro* and *in vivo* studies, it is clear there exists various modes of γ -TuRC-dependent and -independent MT nucleation mechanisms that occur depending on the neuronal differentiation stage.

Many questions remain as to whether other γ -TuRC localization platforms exist within dendrites. Additional studies are required to dissect the cellular control mechanisms that dictate where γ -tubulin should be transported for local MT nucleation and how re-localization impacts neuronal activity and development at the systems level. It is interesting that following axon injury, the endosomal Wnt signaling pathway is activated to recruit γ -tubulin in mature neurons to promote dendritic MT nucleation, which parallels a similar phenotype in neurons depleted of receptor tyrosine kinase-like orphan receptor, Ror (Nye et al., 2020). Ror acts upstream of Wnt signaling proteins by localizing scaffolding protein Axin at dendrite branch points for MT nucleation in dendrite regeneration. It is known that initial injury response involves a nucleation-dependent increase in MT dynamics for dendrite stabilization (Chen et al., 2012). However, the molecular mechanism underlying Ror interactions with Wnt signaling proteins *e.g.* Axin to localize them at branch points remains elusive. Nonetheless, there is a paradigm that has become increasingly popular to explain how local concentration of MT regulators and nucleators at specific cellular and neuronal compartments promote nucleation: biomolecular phase separation. The following section will elaborate on ways phase separation of cytoskeletal regulators has contributed to understanding MT dynamics *in vitro* and in cells.

1.3. Contributions of phase separation behavior of microtubule-binding proteins to cellular and neuronal function

Biomolecular phase separation (PS) in cells was first described for P granules in *C. elegans* (Brangwynne et al., 2009), a term for the formation of membraneless compartments. The PS

paradigm proposes that membraneless compartments are typically liquid-like, resulting from a phenomenon analogous to the thermodynamically driven separation of oil from water (Musacchio, 2022). Proteins with intrinsically disordered regions (IDRs) or multivalent proteins (MVPs) display the tendency to undergo droplet formation *in vitro*, and it has been suggested that these MVPs or proteins with IDRs serve as scaffolds that drive PS via weak homotypic interactions. Other macromolecules entering these compartments are associated via heterotypic interactions and are termed clients. Compartment assembly often involves a primary scaffold, a primary client, and a secondary client as to locally concentrate components and control biochemical reactions within a cell (Musacchio, 2022). For example, the centromere serves as a primary scaffold because it recruits the primary client, Chromosomal Passenger Complex (CPC), kinase, which can undergo coacervation via multivalent interactions and recruits additional cellular components during mitosis, e.g. histone H3pT3, Sgo1, and HP1 α , as a cooperative means to control the assembly and disassembly of phase-separated bodies (Trivedi et al., 2019). Interestingly, LLPS has evolved as a paradigm to also describe the spatiotemporal regulation of cytoskeletal dynamics. This section serves to summarize the ways in which LLPS of MBPs contributes to microtubule dynamics through *in vitro* and *in cellulo* studies.

1.3.1. Emerging role of MBP phase separation in MT dynamics revealed by *in vitro* studies

A growing list of MT-binding proteins has been shown to regulate MT dynamics through LLPS, which is associated with regions of disorder (Hernández-Vega et al., 2017; King & Petry, 2020; Lin et al., 2017; Maan et al., 2022; Meier et al., 2022; Song et al., 2022; Tan et al., 2019). Protein condensation is often driven by IDRs and multivalent binding regions (Alberti et al., 2019; Boeynaems et al., 2018; Feng et al., 2019; Lin et al., 2017; Wang et al., 2018), and is a common feature of diverse MT regulators (Hernández-Vega et al., 2017; King & Petry, 2020; Maan et al., 2022; Meier et al., 2022; Miesch et al., 2023; Safari et al., 2021; Song et al., 2022; Tan et al., 2019). Three distinct classes of MBPs are defined based on their LLPS behavior to regulate the following mechanisms: 1) MT stabilization; 2) MT dynamics; 3) MT nucleation.

1.3.1.1. LLPS of MBPs in lattice stabilization and regulation of cargo-trafficking

The MT stabilizer tau is implicated in neurodegenerative disorders including Alzheimer's Disease and is known to accumulate in neurofibrillary tangles. Tau is an MBP that contains MT-binding intrinsically disordered repeat regions that form the core of the neurofibrillary tangle and can undergo LLPS both *in vitro* and *in cellulo* (Ambadipudi et al., 2017; Hernández-Vega et al., 2017; Zhang et al., 2020). In axons, tau can stabilize MTs, and biochemical assays reveal it utilizes its MT-binding repeats to govern its spacing on GDP-lattices (Siahaan et al., 2019; Siahaan et al., 2022; Tan et al., 2019). Under hydrodynamic flow, tau oligomerizes and forms envelopes (previously referred to as islands and condensates) are sensitive to lattice extension, as buffer flowed into the TIRF chamber induced a drop in tau density at site of fissure in the envelope (Siahaan et al., 2022). Using elegant optical trapping experiments to further validate that tau was sensitive to the mechanical state of MTs, these authors show that tau envelopes disassemble when GMPCPP-capped GDP-lattices were extended. These data suggest that tau envelope formation is mechanosensitive to MT lattice compaction. Prior to addition of taxol, tau remains bound on MT lattices in U2OS cells, but upon 0.01 μM taxol treatment, the tau envelope quickly disassembles. Tau also co-localizes with MAP2c, another MAP found in axons, which undergoes similar envelope formation. Both tau and MAP2c form islands on GDP-lattices, serving as protective and regulatory means of gating severing enzymes (spastin, katanin) and cytoplasmic dynein and kinesin motors, respectively (**Figure 1.15**) (Siahaan et al., 2019; Tan et al., 2019). Whereas highly processive dynein-dynactin complexes bound to Hook3 and Rab11-FIP3 (adaptors that recruit two dynein dimers) were able to traverse and pass through cohesive tau islands, diffusive dynein-dynactin-BicD2 (adaptor that only recruits only one dynein dimer) and p150^{Glued} molecules could not (**Figure 1.15**) (Tan et al., 2019). These data suggest that adapter-dependent variations in the number of dynein dimers per dynactin scaffold impact the ability of the complex to navigate tau condensates, and that tau islands can modulate motor protein velocity and run lengths in a cargo-dependent manner. The question remains whether these observations for tau to utilize LLPS as a gating

strategy against specific motor proteins can be recapitulated in neurons, and how phase separation behavior impacts axonal trafficking.

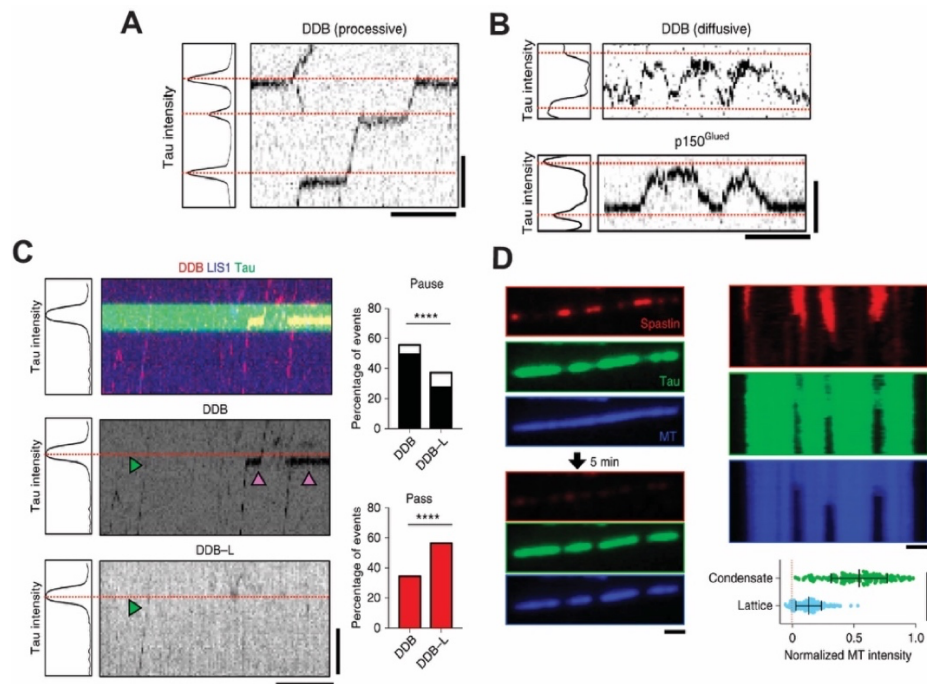


Figure 1.15. Tau condensates form selective gates to regulate MAPs and MBPs. (A-B) Tau condensates allow processive DDB to pass through gates (A), while preventing diffusive DDB and p150^{Glued} (B) from traversing along the MT lattice bound by tau envelopes. **(C)** Distribution of diffusive DDB molecules that have paused or passed tau condensates. **(D)** Tau envelope formation protects local sites from spastin-mediated severing. Adapted from (Tan et al., 2019)

Additionally, both MAP2c and tau envelopes served as gates for KIF1A, a neuronal cargo transporter, which could not traverse through the islands (Siahaan et al., 2022). A study by Tymanskyj and others using the reconstituted MT system under TIRF microscopy revealed that MAP7 also affects MT motors, as MAP7 reduces the amount of kinesin-3 KIF1A bound on the MT and kinesin-3 landing rates, while having no effect on cytoplasmic dynein and even displacing tau from the MT. In fact, MAP7 directly recruits kinesin-1 to the same sites on the lattice and promotes the ATPase activity of kinesin-1 in vitro, whereas tau inhibits kinesin-1 ATPase activity and transport (Monroy et al., 2018). Collectively, these data suggest that formation of MBP envelopes on MT lattices differentially regulates spatial distribution of selective motors on lattices and activation of motor-mediated cargo transport in cells.

Aside from MT lattice stabilization, a motor protein that has a high affinity for GDP-lattices is kinesin-3 (KIF1A, (Guedes-Dias et al., 2019). A recent study demonstrates that another member of the family, variant KIF1C, undergoes LLPS via its disordered C-terminal tail (Geng et al., 2023). KIF1C delivers and localizes mRNA to protrusions in 3T3 fibroblasts via direct binding interactions at the 3' UTR sequence. It was also shown that deletion of the IDR abolishes KIF1C ability to undergo LLPS and disrupts the delivery of *Rab12* mRNA to the cell periphery. However, it remains unclear when within the RNA transport cycle and where within neurons KIF1C undergoes LLPS to mediate this process. Collectively, these data reveal that classical MAPs tau and MAP2 can undergo LLPS to promote envelope formation on stable lattices, and that these envelopes can selectively gate processive motors undergoing cargo trafficking. Though most regulatory functions and signaling occurs at growing ends, it was not until recently there are proteins that condense with other MBPs to modulate dynamic instability parameters at MT tips.

1.3.1.2. LLPS of MBPs in formation of +TIP bodies to promote MT dynamics

In 2022, a series of papers have shown that +TIP End-Binding Protein (EB) family and its associated MT regulators undergo condensation at MT plus ends (**Figure 1.16**). Song and others show that in COS-7 cells, EB1 clusters and forms comets that exhibit liquid-like properties, while a separate study by Meier *et al.* revealed that EB3 and CLIP-170 undergo LLPS in cells with tubulin as their client protein to promote MT growth (Miesch et al., 2023). K/R residues are essential for EB1 LLPS behavior, which underlies EB1 concentration of tubulin dimers (**Figure 1.16, A**) (Song et al., 2022). EB1 LLPS is required for mediating MT dynamics, as LLPS-deficient IDR mutant, EB1-KR6Q failed to tip-track MTs *in vitro* and in COS-7 cells (**Figure 1.16, A, i**). It was also demonstrated that liquid-like property of EB1 comets is directly linked to its effect on MT dynamics to promote growth rate *in cellulo* and reduce catastrophe frequency *in vitro*, as fusion to hnRNPA1^{D262V} caused chimeric EB1-hnRNPA1^{D262V} to undergo the 'liquid-to-gel' transition thereby significantly attenuating EB1 regulation of MT dynamics. LLPS deficient EB1-KR6Q mutant also failed to recruit other MT plus end trackers like MCAK, p150Glued, and TIP150 *in vitro* and to the spindle in HeLa cells undergoing mitosis. These data strongly support that EB1 LLPS is critical for

Interestingly, Tip1 accumulates at the MT tip ends in a nonstoichiometric manner relative to Tea2 density, indicating that accumulation of Tip1 is not limited to one-on-one interactions with motor proteins. Abolishing the IDRs of Mal3 and EB homology domain eliminates comet formation, further demonstrating that tip tracking requires Mal3 to oligomerize with itself, bind the MT lattice, and co-localize with the motor track using its IDRs (**Figure 1.16, B, i**). Stochastic simulations confirm that motor-driven end accumulation could only be achieved if motors slow down at the MT end and cargo clusters are stabilized by lateral interactions. The MT ends may serve as platforms to promote multivalent interactions for MBPs to condense into large complexes. However, it remains a question from this study whether multivalency of Mal3 drives the accumulation of Tea2 and Tip1 to form condensed structures at MT ends can be recapitulated *in vivo*.

The last of the last three seminal MBP LLPS studies published in 2022 provides strong evidence for MBP multivalency contributing to MT function. Meier and others demonstrate that *S. pombe* MT-actin crosslinking factor homolog Kar 9, Bim1 (orthologous to EB1), and Bik1 (orthologous to CLIP-170) form a network that undergoes condensation *in vitro* and in yeast cells (**Figure 1.16, C**) (Meier et al., 2022). Together, the macromolecules form a +TIP body that accumulates at MT plus ends, persists on both growing and shrinking MT ends and can couple both MTs and F-actin. Multivalency contributes to Kar9 self-association, underlying LLPS behavior *in vitro* and modulating its localization to few MTs in yeast. Kar9 does not form stoichiometric structures in yeast, but rather forms a condensed structure that can undergo fusion into a single entity. It is postulated that Ostwald ripening of the condensate (i.e. the largest condensate continuing to collect smaller materials in surrounding) explains why there is typically one Kar9 +TIP body in budding yeast. Progressive reduction in the multivalency of the Kar9 network impacted cell viability. While deletion of *bik1* or introduction of three self-association interface mutations in Kar9 yielded little effects on mitosis, the combination induced a substantial accumulation of late-anaphase cells with spindles that remained in the mother cell that failed to segregate to the bud (**Figure 1.16, C, ii**). Persistence of the condensed Kar9 +TIP body at shrinking MT ends reveal that the wetting promotes the +TIP body persistence, likely facilitating the linking of MTs and actin cables during nuclear positioning.

1.3.1.3. LLPS of MBPs in MT nucleation

Lastly, a final class of MBPs specifically concentrates tubulin dimers to promote non-templated nucleation. In cells and young neurons, the centrosome serves as the primary microtubule-nucleating structure, which contains the γ -tubulin ring complex (γ -TuRC) and recruits additional macromolecules to the centrosome (Roostalu & Surrey, 2017). There exist MBPs that promote microtubule nucleation via branching, like TPX2, and γ -tubulin independent nucleation, like CAMSAP2, which decorates nascent non-centrosome MTs at minus ends. TPX2 is an effector of MT nucleation in spindles but the underlying mechanism remained unclear. It was only recently TPX2 was shown to undergo LLPS *in vitro* and co-condense with tubulin dimers at physiologically relevant concentrations in meiotic *Xenopus* egg cytosol (King & Petry, 2020). TPX2 utilizes its disordered N-terminus to efficiently partition tubulin, which underlies its ability to locally concentrate clients to promote nucleation. As one of the definitive assays to test that it was the TPX2 N-terminus that stimulated branching MT nucleation, this region was replaced with various heterologous regions to generate chimeras that harbored distinct functions, i.e. with the intrinsically disordered N-terminal region of FUS (can phase separate but does not bind tubulin), and with the ordered TOG1 and TOG2 domains of XMAP215 (does not phase separate but can bind tubulin). Neither chimera can efficiently co-condense with tubulin to form condensates and mediate MT nucleation efficiency.

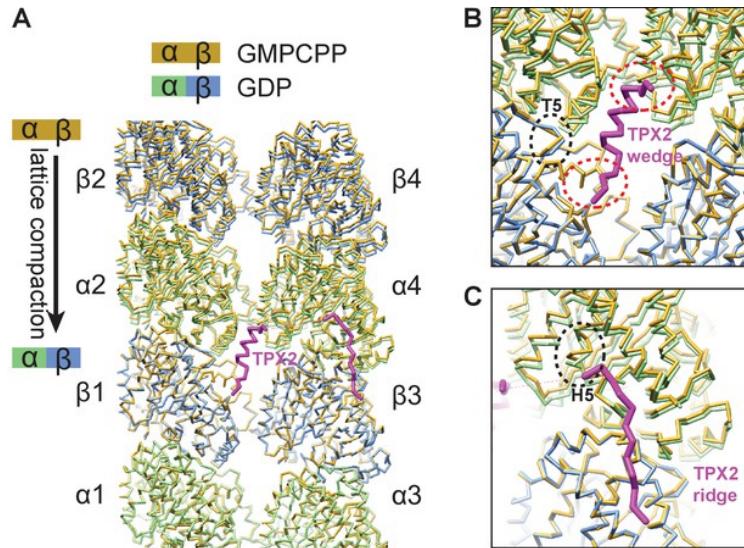


Figure 1.17. TPX2 binds at interdimeric interfaces (“wedge” in B and “ridge” in C) that alter during MT lattice compaction in GTP hydrolysis (A). Adapted from (Zhang et al., 2017).

A follow-up study from the Petry Lab focused on investigating the structural basis of protein condensates using a combination of magic-angle-spinning NMR and molecular modeling (Guo et al., 2023). A TPX2 ^{$\alpha 5-\alpha 7$} construct—carrying the minimal C-terminal active domain for stimulating branching MT nucleation—bound to MTs and assembled condensates on the lattice, exhibiting rigid and folded regions flanked by IDR stretches that contribute to its transient, dynamic binding MT interactions. This was also confirmed by an earlier 2017 cryo-EM study that revealed TPX2 bound to GMPCPP-MTs via a novel type of MT interaction mode, revealing two small structural elements (termed wedge and the ridge) connected by a flexible linker. This mediates TPX2 interaction across both the longitudinal and lateral tubulin interfaces (**Figure 1.17**) (Zhang et al., 2017). Interestingly, MAS NMR spectroscopy reveals that TPX2 is intrinsically disordered in solution, but transitions from unfolded to folded upon binding to MTs at two adjacent protofilaments. Interaction with spindle assembly factors importins α/β can independently suppress TPX2 LLPS and its regulation of branching MT nucleation during cell cycle until the onset of mitosis (Safari et al., 2021). Though it remains a question whether TPX2 undergoes LLPS in vivo and how it is spatiotemporally regulated at each stage of mitosis, these biochemical and structural studies collectively demonstrate that TPX2 likely utilizes its intrinsically disordered region to self-organize and concentrate tubulin dimers for spindle assembly.

In polarized cells such as neurons that are non-mitotic, the centrosome loses the ability to nucleate MTs. Vertebrate CAMSAP1-3 proteins and *Drosophila* Patronin are involved in non-centrosomal MT assembly by stabilizing the minus ends. Imasaki, Kikkawa and others demonstrated using *in vitro* assays that CAMSAP2, a member of the minus-end MT binding CAMSAP family, interacts with tubulin and undergoes LLPS to stimulate spontaneous nucleation of MTs independent of the γ -TuRC complex (Imasaki et al., 2022). The authors find that upon incubation of CAMSAP2 with tubulin, the co-condensates form aster-like structures, with nascent MTs radially polymerizing from the coacervates. However, it is worth noting that the physiological concentration of CAMSAP2 is tens of nanomolar, whereas the concentrations of CAMSAP2 used to form asters is nearly 25-fold higher, at 0.25 μ M. Nonetheless, the authors were able to observe ring-like structures formed during MT nucleation with CAMSAP2 under negative stain and cryo-electron microscopy, likely resembling MT nucleation intermediates. A subpopulation of the rings exhibited ends of MTs or tubulin sheets that had partially curved sheet-like structures, again resembling polymerizing MTs. These data suggest that CAMSAP2 and tubulin co-condense to function as its own MTOC, thereby increasing nucleation efficiency and promoting MT polymerization.

These studies so far have demonstrated that LLPS of MBPs serve a functional role in MT dynamics through *in vitro* studies. However, it remains a question of whether and when MBP LLPS driving nucleation occurs in cells and mature neurons to exert their function; and what factors (*i.e.* post-translational modifications (PTMs) on tubulin dimers/MTs, PTMs of MBP itself, structural cues along the MT, signaling cues) control LLPS in a cellular context; and how disruption in these regulatory mechanisms for LLPS give rise to neurodevelopmental disorders.

1.3.2. LLPS of MBPs in neurons

Cellular compartmentalization has been recognized as a paradigm for regulating many cellular processes, from cell polarization to mitosis. Recently, LLPS of macromolecules has been used to describe how young neurons develop their polarization into a single axon and multiple dendrites, and how mature neurons maintain their highly polarized morphology to support functional plasticity

throughout brain development (Wu et al., 2020). To mediate connections for synaptic function, axons and dendrites in mature neurons must solve the challenge in localizing various molecular components in distinct compartments.

It is believed that if inappropriately regulated, LLPS—widely considered a physiological process for influencing reaction kinetics, buffering, and adaptive filtration—can evolve into protein aggregation underlying neurodegenerative diseases (Zbinden et al., 2020). For example, tau droplets can become pathogenic upon hyperphosphorylation and harden into aggregations in neurofibrillary tangles—a hall mark of Alzheimer’s Disease (Wegmann et al., 2018; Zbinden et al., 2020). Hence, though there is a fast-growing list of studies that strongly suggest LLPS of MBPs plays a role in MT dynamics through *in vitro* studies, there is a greater need for *in vivo* studies that demonstrate how MBP condensation contributes to biological function throughout neuronal development. In doing so, dissecting the molecular mechanisms underlying the ability of MBP LLPS and what function it may contribute in neurons will elucidate how neurodevelopmental and neurodegenerative disease arises. This section focuses on the studies that incorporate *in cellulo* and *in vivo* assays to demonstrate how phase separation of MBPs contributes to axonal and dendritic processes; and highlights potential MBP candidates that may undergo phase separation to exert function.

1.3.2.1. Phase separation of MBPs in axons

In axons, microtubules are densely packed with their plus ends oriented away from the soma (Baas et al., 1988; Kapitein & Hoogenraad, 2011). Tau is abundant in axons where it modulates assembly, dynamics, and spatial organization of MTs, and these processes are tightly regulated by post-translational modifications of the tau molecule. Indeed, squid axoplasm assays to assess vesicle motility reveal that tau is closely linked to both kinase and phosphatase signaling pathways to regulate motor-based organelle and mRNA transport along axons (Morfini et al., 2004). Pathologically modified tau perturbs MT function and organization, thereby impeding axonal transport. Wegmann and others revealed that disease-relevant and aberrant hyperphosphorylation of tau leads to tau LLPS, which forms into aggregates in neurons (Wegmann et al., 2018). The

PP1-GSK3 pathway involves activation of PP1 and subsequent dephosphorylation of GSK3 β for activation which is required for phosphorylating kinesin light chains for release from transported cargo in fast axonal transport. Pathological modifications of tau, such as hyperphosphorylation that increases exposure of its phosphatase-activating domain, disrupt this anterograde transport by affecting this signaling cascade (Kanaan et al., 2011).

Tau can utilize phase separation to increase its density and decrease mobility of motor proteins where it predominates in axons. Interestingly, tau has been shown to switch its localization from the axon to the presynapse to selectively control mobility of recycling synaptic vesicles through phase separation (Longfield et al., 2023). Longfield and others reveal that formation of tau nanoclusters is necessary to control the presynaptic clustering of recycling pool of synaptic vesicles, likely mediated by its phosphorylation status as LLPS-deficient tau mutants reveal increased mobility at the axon and presynapse. From *in vitro* studies, tau and MAP2 envelope formation has been shown to spatially regulate KIF1A motor on the MT, greatly affecting its landing rate (Monroy et al., 2018; Siahaan et al., 2022). As KIF1A is also an axonal transporter of synaptic vesicles to the presynapse (Guedes-Dias et al., 2019; Yonekawa et al., 1998), it will be interesting to see in future studies whether and how axonal tau condensates regulate KIF1A-mediated synaptic vesicle precursor transport to selectively control mobility of recycling vesicles at the presynapse under neuronal stimulation.

The novelty and difficulty in monitoring cellular LLPS has limited the number of *in vivo* studies of the importance of phase separation behavior of MBPs (Alberti et al., 2019; Musacchio, 2022), but there are potential MBP candidates that could exhibit phase separation to exert specific functions in axons. For example, MAP7 is a largely intrinsically disordered non-motor MBP that has 4 isoforms encoded by genes MAP7, MAP7D1, MAP7D2, and MAP7D3 in mammals. MAP7, MAP7D1, and MAP7D2 are expressed in neuronal tissues: MAP7 and MAP7D1 localize specifically to somatodendritic compartments whereas MAP7D2 localizes to primary axons (Pan et al., 2019). All four mammalian MAP7 family members bind to kinesin-1, with MAP7, MAP7D1, and MAP7D3 exhibiting redundant functions in mediating kinesin-1 transport and MT recruitment (Hooikaas et al., 2019). Various studies utilized cell-based assays to demonstrate that MAP7 members recruit

kinesin-1 to microtubules for modulating organelle transport in COS-7 and HEK293 cells, and dorsal rat ganglion neurons (Hooikaas et al., 2019; Tymanskyj et al., 2018). MAP density on MTs can impact motor-mediated cargo transport (Dixit et al., 2008; Monroy et al., 2018; Siahaan et al., 2019; Tan et al., 2019). Thus, MAP7-bound MTs may recruit kinesin-1 from neighboring MTs to redirect kinesin-bound cargos in axons via direct binding interactions. At axonal branch junctions, MAP7 may undergo envelope formation along parts of a MT; and promote branch formation using its N and P domains to facilitate kinesin track switching, thereby diverting kinesin-bound organelles into those branches. A recent cryo-EM structural study reveals a biphasic mechanistic regulation of kinesin-1 by MAP7, where the projection domain of MAP7 enables kinesin-1 motor to diffuse to available MT sites partially decorated by MAP7, thereby increasing run length (Ferro et al., 2022). The projection domain of MAP7 is required for kinesin-1 motility as it tethers the motor to the MT surface, allowing for its transient detachment and reattachment. However, higher concentrations (>100 nM) of MAP7 on MTs decrease kinesin run frequency, as kinesin-1 competes for binding on the same tubulin dimer as MAP7, suggesting that density of MT-bound MAP7 is tightly regulated in axons to tune motor processivity in mitochondrial/ER/peroxisome transport. Tymanskyj and others conducted *in cellulo* FRAP analysis on full-length MAP7-transfected COS-7 cells to quantify disassociation kinetics of MT-bound MAP7 (Tymanskyj et al., 2018). They found that its half-life on MTs was longer by nearly 43-fold and a 44-fold slower dissociation rate relative to the N-terminus of MAP7. These data suggest that MAP7 is not dynamic nor liquid-like on MTs. However, these are overexpression experiments, thus concentrations of exogenous MAP7 likely exceeds endogenous levels of protein found in COS-7. An extensive study is required to determine whether MAP7 undergoes phase separation, and if so, under what physiological context. As MAP7 and tau compete for binding to the same MT sites (Monroy et al., 2018), it will be interesting to determine in future studies whether MAP7 undergoes phase separation on a MT; and how condensation of tau and/or MAP7 on lattices determines correct distribution and balance of motor activity in axons.

Another potential MBP candidate that may undergo LLPS is CAMSAP3, which is another member of the CAMSAP family that binds to MT minus ends. CAMSAP3 preferentially localizes along axons and mutations in CAMSAP3 promoted a supernumerary axon phenotype

(Pongrakhananon et al., 2018). In contrast, loss of CAMSAP2 in hippocampal neurons has no effect, suggesting that CAMSAP3 is required for neuronal polarity. It has recently been shown through an *in vitro* study that CAMSAP3 strongly prefers to bind expanded MT lattices and decorate minus ends via its CKK domain (Liu & Shima, 2023). It is possible that CAMSAP3 undergoes LLPS, analogous to its paralog CAMSAP2, on MT minus ends *in vivo* to promote non-templated MT nucleation in axons.

1.3.2.2. Emerging roles of LLPS in dendritic spine maintenance

Unlike axons, MTs in dendrites exhibit mixed polarity (Baas et al., 1988). While there is limited *in vivo* evidence for LLPS of MBPs in dendritic spines or shafts, the literature supports the hypothesis that MBP condensates may form at MT plus ends and recruit F-actin binding proteins to exert function. For example, as noted in Section 1.3.1, EB proteins exhibit LLPS behavior to concentrate at growing MT ends and in a separate study, have been shown to bind directly to the F-actin binding protein drebrin both *in vitro* and in growth cones—an interaction that is essential for growth-cone pathfinding (Geraldo et al., 2008). MBPs like kinesin and dynein may also be captured at F-actin filaments where other postsynaptic proteins are condensed. Cargos that these motor proteins carry throughout the dendritic shaft include synaptic vesicle precursors, mRNAs, membrane proteins, and organelles, which are delivered to actin-rich postsynaptic sites where they exert function or in the case of mRNAs, are locally translated. There are key regulatory mechanisms in place that control what cargos motor proteins bind, how cargo specificity is defined depending on local needs within the dendritic compartment, and where and when motor proteins are targeted. One potential mechanism that may regulate these dendritic processes is the phase separation behavior of macromolecules that concentrate at dendritic spines and shafts. This section will focus on the contributions of LLPS of macromolecules in dendrites from *in vivo* studies, and how LLPS promotes MT:actin crosstalk to regulate synaptic activity.

Though it has not been directly shown *in vitro* that MAP2c undergoes LLPS, an early study by Roger *et al.* reveals that MAP2c, which is located within dendritic shafts, can bind and bundle F-actin via its MT-binding domain (Roger et al., 2004). MAP2 and tau have similar MT-stabilizing

activities. However, MAP2 is enriched in the cell body and dendrites, with tau residing primarily in the axon. MAP2c is indeed an intrinsically disordered protein that exhibits large differences in flexibility within its individual regions, with lowest flexibility in the known binding sites revealed by small-angle X-ray scattering and NMR relaxation enhancement measurements (Melková et al., 2018). Neuro-2a cells transfected with GFP-tagged MAP2c, but not with GFP alone nor GFP-tagged tau, exhibited an accumulation of large interphase bundles. Due to its actin-bundling activity, expression of MAP2c in Neuro-2a cells promoted neurite initiation. A study by Siahaan and others revealed that MAP2c is diffusive on MTs at picomolar concentrations, but forms envelopes with dwell times that are threefold higher than tau 2N4R (Siahaan et al., 2022). Like tau, the MAP2c envelope formation is sensitive to the mechanical state of the MT lattice and selectively gates motor proteins, such as dynein-dynactin-Hook3 complexes by inducing pausing at the MAP2c envelope boundary. Additionally, in a seminal study, Kapitein and others showed that upon calcium-dependent NMDA receptor activation in rat hippocampal neurons, EB3 comets are lost from MT plus ends, and become redistributed along MTs in the dendritic shaft via direct MAP2:EB3 interactions (**Figure 1.18**) (Kapitein et al., 2011). These dendritic MAP2-bound MTs are stable, and the authors postulated that MAP2 serves as a “sink” on these MT bundles to locally reduce EB3 concentration available for tip tracking and promoting MT growth into dendritic spines. NMDA-receptor activation prevents EB3-mediated MT spine entry, which consequentially decreases MT content in neighboring spines. This is likely done so that their response to NMDA receptor stimulation is enhanced via clustered plasticity for long-term depression. Future studies should be aimed at understanding how MAP2c LLPS and envelope formation gates kinesin- and dynein-adaptor complexes during neurogenesis, and other MBPs like EB3 for synaptic plasticity; and whether and how other alternatively spliced MAP2 isoforms, MAP2a and MAP2b, utilize LLPS as a gating strategy to regulate motor transport on MTs in dendritic shafts.

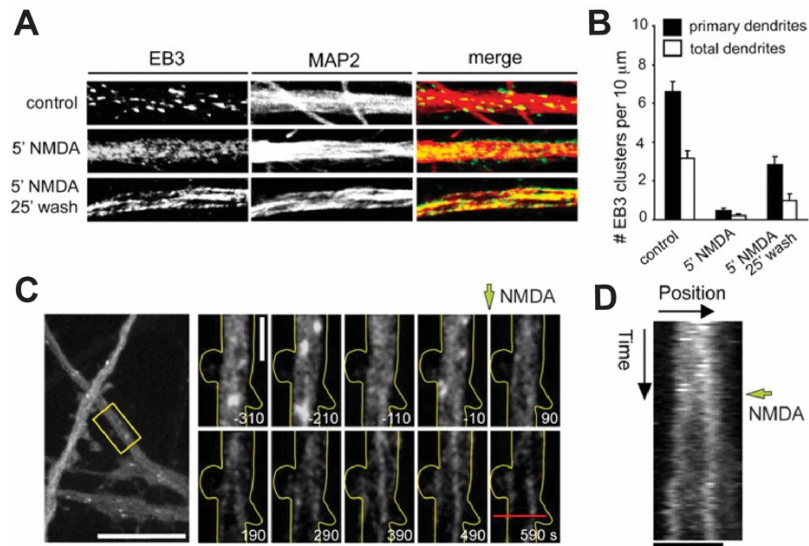


Figure 1.18. Stimulating DIV17 hippocampal neurons with 50 μ M NMDA suppresses EB3 comet formation in dendrites. Adapted from (Kapitein et al., 2011; Zhang et al., 2017).

Though MTs are often found in axons, MT dynamics are important for regulating dendritic spine morphology and synaptic function via polymerization into spines from the shaft for transient invasions (Dent, 2017; Dent, 2020; Gu et al., 2008; Hu et al., 2011; Hu et al., 2008; Jaworski et al., 2009). A recent study confirms MT entry of spines requires actin filament remodeling at base of dendritic spines (Schätzle et al., 2018). Actin remodeling for MT spine entry and spine activation is dependent on NMDA receptor activation and calcium influx. Direct MT invasion of spines allows for efficient cargo transport, and is believed that they may also serve as intermediate platforms for macromolecules and cargo to “hitchhike” on, with their eventual destination being actin filaments at spine heads (Dent, 2020). For example, during transient MT polymerization into spines, kinesin-3 member KIF1A recruits its associated cargo, synaptotagmin-IV (synt-IV), along MTs into spines, and this is activity-dependent (McVicker et al., 2016). Knockout of KIF1A in neurons led to random diffusion of synt-IV into spines, decreased mobility, and aberrant trafficking of synt-IV vesicles throughout the dendritic shaft, suggesting that there is an underlying mechanism that selectively targets KIF1A-bound MTs with dendritic cargo into spines. Actin filaments are essential for dictating spine shape, as periodic actin structures define spine necks (Bär et al., 2016). It remains an attractive hypothesis that actin-mediated phase separation of macromolecules at dendritic spine

heads and bases of spines serve as hotspots to capture dynamic MBP-bound MTs for selective entry and cargo transport. This will be the focus of the following section.

The post-synaptic density (PSD) of the synapse is extremely dense, formed by hundreds of proteins via LLPS-mediated assembly (Chen et al., 2023; Cohen et al., 1977). F-actin filaments form three types of pools that underlie spine structure and plasticity: a dynamic pool, enlargement pool, and stable pool (Honkura et al., 2008). The actin cytoskeleton directly contacts the PSD and can nucleate at the PSD to support spine growth (Chazeau et al., 2014). Indeed, from a recent study, Chen and others reveal that a PSD condensate that lacks any known actin-binding regulators can promote actin polymerization, co-partitioning SynGAP, PSD-95, Shank3, and Homer3 (Chen et al., 2023). The guanylate kinase-associated protein or GKAP can also partition into PSD condensates. GKAP is another PSD scaffolding protein that links PSD95 to Shank/Homer complexes and reduces synaptic activity at excitatory synapses by interacting with motor proteins myosin Va and dynein (Naisbitt et al., 2000). It was discovered recently that kinesin motor Kif21b localizes at actin-enriched spine protrusions in cultured hippocampal neurons, colocalizing with PSD-95, indicating that Kif21b enters postsynaptic sites (Gromova et al., 2023). Kif21b binds to myosin motor MyoVa, and live-cell imaging in COS-7 cells confirms that Kif21b concentrates at actin-rich cellular cortex, with mobile kinesin molecules at MTs and static puncta accumulating at +TIPs. Inhibition of MyoVa in COS-7 cells induces Kif21b re-localization from the actin-rich cell periphery to MT-enriched regions. In cultured neurons, chemical inhibition of MyoVa significantly reduced colocalization of Kif21a at actin-rich spine protrusions. Additionally, chemical induction of long-term depression with NMDA or DHPG revealed a significant reduction in Kif21b:MyoVa interaction in co-IP experiments. These biochemical experiments also revealed a direct binding interaction between GKAP and Kif21b in a complex independent of submembrane proteins Shank and Homer. Using FRAP imaging to assess actin dynamics in wildtype and Kif21b KO neurons, the authors determined that GKAP:Kif21b:MyoVa interactions contribute to homeostatic synaptic downscaling, as actin recovery rates in wildtype neurons subjected to chemical MyoVa inhibition mimicked those of Kif21b KO neurons. These data suggest that Kif21b, which is normally associated with MTs, likely “hitchhikes” on MyoVa-bound actin filaments via direct binding

interactions, and is brought into the PSD at dendritic spines via GKAP:Kif21b binding interaction. Kif21b:MyoVa interactions are present upon inclusion of phosphatase inhibitors, suggesting that direct binding is phosphorylation-dependent. Thus it is likely that the phase separation behavior of GKAP is phosphorylation dependent. Indeed, for another PSD-associated protein, Homer3, phosphorylation by CaMKIIa attenuated its propensity to undergo condensation, weakening actin bundling (Chen et al., 2023). It remains a question when and where GKAP undergoes phase separation in dendritic spines for actin bundling during homeostatic synaptic downscaling; and whether and how MT:actin capture at contact sites of GKAP:Kif21b:MyoVa is attributed to GKAP:actin rich condensates.

EB3 is another interactor of PSD-95, an abundant organizer of AMPA and NMDA receptors at the PSD (Sweet et al., 2011). In this early study, the PSD-95 SH3 domain binds a proline-rich region of EB3. The lifetime of EB3 comets in cultured hippocampal neurons decreased when PSD-95 was overexpressed, in contrast to neurons overexpressing a PSD-95 Δ SH3 mutant lacking the EB3-binding domain. PSD-95 alters EB3 comet and MT dynamics by modulating the time EB3 spends on MT plus-ends. Interestingly, PSD-95 also reduces the comet velocity of EB3-bound polymerizing MTs. As the study focuses on developing neurons, it remains unclear whether PSD-95:EB3 interactions were studied in dendrites. However, these data suggest that PSD-95 likely recruits additional factors that suppress growth of MTs, specifically ones that enter spines. It will be interesting to explore how PSD-95 attenuates potentiation of spines invaded by EB3-bound MTs, and whether synaptic activity can modulate phase separation behavior of PSD-95 and other PSD proteins to modulate F-actin dynamics. Future studies include investigating whether and how these PSD condensate “hotspots” at the actin-rich spine heads play a role in capturing motor-protein bound MTs from dendritic shafts.

In neurons, there are various modes of trafficking to ensure proper formation and dynamics of both presynaptic and postsynaptic structures and processes. Delivery of organelles and synaptic vesicles in axons and dendrites primarily depends on motor proteins. Transport of these cargoes is controlled by regulatory molecules and signaling pathways that provide additional layers of specificity for cargo delivery and directional movement. Liprin- α serves as a core synaptic scaffold

important for the assembly of synapses in presynaptic and postsynaptic processes and is required for trafficking of synaptic vesicles (Miller et al., 2005; Xie et al., 2021). Liprin- α contains N-terminal coiled coils that mediate its self-assembly, interacting with active zone protein ELKS, kinesin-3 member KIF1A, and PSD-95-interacting protein, TANC2. A recent *C. elegans* study by McDonald and others demonstrated that assembly of synaptic active zones in axons requires liprin- α and ELKS-1 to undergo LLPS that would later mature into a solid structure (McDonald et al., 2020). The formation of synaptic active zones in axons is essential for long-term plasticity as they cluster ion channels and synaptic vesicle docking machinery, priming for its exocytosis and release of neurotransmitters (Südhof, 2012). By introducing Δ IDR mutations into endogenous liprin- α and ELKS-1 into *C. elegans*, authors observed that protein expression nor recruitment was impacted by the mutation. However, mutant nematodes displayed a marked decrease in the number of docked vesicles, suggesting that phase separation behavior of both liprin- α and ELKS-1 is required for active-zone assembly, recruiting other active zone components to ensure proper localization and formation of the synapse. Another study showed that ELKS1 can capture cargo by binding to axonal cargo Rab6, a small GTPase that is used as molecular switch for cargo motility and as a recognition signal for tethering complexes. The authors postulate that LLPS may be the underlying mechanism by which ELKS1 can undergo LLPS to tether vesicles and capture Rab6 cargo for presynaptic compartment assembly and delivery to release sites. Given that KIF1A can undergo anterograde transport of dense core vesicles from the Golgi apparatus to axons and dendrites with liprin- α as a “signpost” for synaptic vesicle transport (Hummel & Hoogenraad, 2021), it is possible that cargo-bound (*i.e.* containing Rab6, syt-IV cargoes) KIF1A is recruited to specific synapses via phase-separated liprin- α and ELKS-1 condensates. It will also be interesting to explore how post-translational modifications impact the propensity for liprin- α and ELKS-1 to form condensates, as phosphorylation by protein kinase C at S760 of liprin- α 3 directly attenuates liprin- α 3 phase separation for regulating active zone structure and function in live-cell STED and FRAP imaging in cultured mouse hippocampal neurons (Emperador-Melero et al., 2021).

In addition to its roles in the presynaptic compartment, liprin- α isoforms play a crucial role in KIF1A-mediated dense core vesicle transport at dendritic spines (Stucchi et al., 2018). Both

TANC2 and liprin- α are enriched at dendritic protrusions and co-localize with PSD markers PSD-95 and Homer. Interestingly, KIF1A co-clusters with both TANC2 and liprin- α 2 in spines. From the same study, live-cell imaging revealed that KIF1A was highly mobile along the shaft, whereas TANC2 and liprin- α 2 remained immobile at spines. Dense core vesicles (DCVs) often paused near TANC2 and liprin- α clusters, and the frequency of pausing correlated with the age of neurons which had higher density of TANC2 and liprin- α . Upon knockdown of TANC2 and liprin- α , there was a reduction in KIF1A and syt-4 density at spines. These data suggest that TANC2 and liprin- α recruit KIF1A-bound DCVs to dendritic spines. Future studies are needed to determine whether TANC2 and liprin- α co-condense with other PSD proteins at spine heads to capture specific motor-cargo complexes.

Lastly, a putative MBP candidate for LLPS is doublecortin-like kinase 1, DCLK1, which is a homolog of doublecortin that was identified as a causative gene for lissencephaly (Gleeson et al., 1999). Human DCLK1 has 2 MT-binding domains, DC1 and DC2, with a C-terminal kinase domain (Lipka et al., 2016). DCLK1 is localized to dendrites and regulates dense-core vesicle transport into dendrites by directly interacting with kinesin-3 KIF1 via its N-terminal region. DCLK1-KIF1-dependent DCV trafficking controls dendritic outgrowth, and it is likely that the DCLK1 MTBD associates with both KIF1A and KIF1C motor domains, thereby directing KIF1-bound vesicles on MTs into dendrites. Though it has not been directly determined whether DCLK1 phase separates *in vitro* nor *in vivo*, a structural study reveals that the microtubule-binding property of DCLK1, whose C-terminus contains a serine/threonine kinase domain and unstructured tail, is autoregulated via intramolecular interactions with its tail. DCLK1 auto phosphorylates residue T688 within its tail to modulate its MT-binding affinity, and removal of the tail or mutation of T688 significantly decreases MT-binding. Autophosphorylation is likely a mechanism to prevent aberrant DCLK1 hyperphosphorylation at DC1 and DC2 domains. Biochemical studies using reconstituted dynamic MTs for TIRF experiments reveal punctate-like morphology of sfGFP-DCLK1 bound on MTs, reminiscent of tau and MAP2c envelope formation. Future studies are needed to determine whether DCLK1 can indeed undergo phase separation *in vivo*, whether phase separation behavior on MTs

is mediated by its phosphorylation state, and if so, how phase separated DCLK1 regulates kinesin-3 mediated vesicle-trafficking in dendrites.

1.3.3. LLPS of kinases in cytoskeletal regulation

There are spatiotemporal mechanisms in place that carefully control enzyme activity in the cell. Kinases must find their intended substrates in a densely packed cytoplasm, and their interaction partners need to find these kinases to limit off-target activity. These events are fine-tuned based on ligand competition, distances between substrates, differential compartmentalization of substrates in the cell, and conformational barriers. The phase separation paradigm allows us to understand how kinases find their intended substrates, and how phosphorylation or addition of other PTMs control the timely assembly and disassembly of condensates that include kinases, which act as either the scaffold or client in LLPS. This section will focus solely on LLPS of kinases that are involved in cytoskeletal regulation.

The integrin adhesion cluster (IAC) is specialized compartment in the cell that exhibits characteristics of phase separation. IACs are enriched with adaptor proteins that are multivalent, containing protein-protein interaction domains such as SH2/SH3 and proline-rich motifs for binding other IAC-associated proteins. Focal adhesion kinase (FAK) is a substrate for Src and is a highly tyrosine-phosphorylated protein that localizes to cell adhesion sites to act as a signaling-protein scaffold for the assembly of focal contacts (Mitra et al., 2005). In migrating cells, cell protrusions are mediated by changes in the actin and MT cytoskeletal organization due to the FAK-Rho GTPase signaling cascade. Using recombinant purified proteins, it was shown that upon binding to phospholipid bilayers, FAK undergoes phase separation and forms micron-sized clusters with its interaction partners pCas, Nck, N-WASP, paxillin, and kindlin which are all membrane-associated (Case et al., 2022). Interestingly, FAK contains an IDR situated between its kinase and FAT domains. The FAK fragment containing IDR, though, does not undergo phase separation *in vitro*, revealing that FAK phase separation is driven not by its IDR but by its FERM-FAT domains that mediate higher order oligomerization. From the same study, Case and others reveal that knockdown of FAK in mouse embryonic fibroblasts significantly decreased nascent adhesion

assembly and fewer IACs. However, it remains a question how FAK LLPS scaffolds contribute to IAC assembly in cells.

LLPS is also a paradigm used to explain how oncogenic kinase fusions are activated in the context of disease (López-Palacios & Andersen, 2023). Kinase gene fusions often include the coiled-coil (CC) domain of its fusion partner to drive oligomerization, leading to aberrant kinase activation and activity in cancer. The oncogenic fusion protein Bcr-Abl has been shown to oligomerize via its CC domains. Fusion of BCR to the c-Abl kinase introduces the CC domain and removes the N-terminal myristoylation site, thereby removing the autoinhibitory function of the SH3 and SH2 domains, thereby making it a hyperactive oncogenic kinase. Recently, it has been shown that Bcr-Abl forms liquid-like granules, and Bcr-Abl-positive granules localize to stress granules (Kashiwagi et al., 2019). Granule formation requires both the Abl kinase activity and the CC domain of Bcr. Interestingly, as regulation of signaling molecules depends on specificity of binding partners in the signaling cascade and cellular localization, it has been shown that Bcr-Abl exerts its function via enhanced localization to F-actin, inducing redistribution of actin filaments into punctate aggregates adjacent to the nucleus. This enhanced association with F-actin contributes to the efficient Bcr-Abl transforming activity (McWhirter & Wang, 1993; Wertheim et al., 2003). Its paralog, Abl2, is altered in various cancers, in particular breast carcinomas (Khatri et al., 2016). It has not yet been shown whether Abl2 oligomerizes with and/or without its N-terminal fusion partners. The work presented in my thesis is the first biochemical study that investigates the propensity for Abl2 to undergo condensation and how its phase separation behavior contributes to its regulation of MT dynamics.

Chapter 2: Regulation of microtubule nucleation and rescue by Abl2

Data presented in this chapter have been published (Duan et al., 2023). I collaborated with Wanqing Lyu who conceptually designed the entire project with me. She co-purified Abl2 and Abl2 fragments from Hi5 insect cells and tubulin from porcine brains, conducted the BLItz assays, and MT co-sedimentation assays. She also performed turbidity experiments and spontaneous MT nucleation assays; as well as two of the three SEC-MALS experiments (6XHis-cleaved Abl2 and 557-C). SEC-MALS experiments were conducted alongside Charlie Wu from Yong Xiong's lab who oversaw instrument use. Wanqing also generated lentiviruses for the stable cell line generation. Cell-based MT reassembly experimental design was developed by Kuanlin Wu. Pengxin Chai conducted cryo-electron microscopy analysis of Abl2-557-1090-bound GMPCPP-MT single particles. Tony Koleske designed the Abl2-mCherry-Cry2 plasmids and purified 6XHis-mCherry for Abl2-mCherry-Cry2 quantification.

2.1. Abl2 binds tubulin dimers *in vitro*

A 2019 study from members of the Koleske Lab showed that Abl2 promotes MT elongation *in vitro* and knockout of Abl2 in COS-7 cells significantly impacts MT growth rates at the cell edge and cell center (Hu et al., 2019), it was initially hypothesized that Abl2 diffuses to growing ends and recruits tubulin dimers to stabilize the GTP-cap. The first experimental observation that confirmed Abl2 binds to tubulin dimers was an *in vitro* tubulin:MT competition TIRF assay using GMPCPP-stabilized rhodamine-labeled MTs.

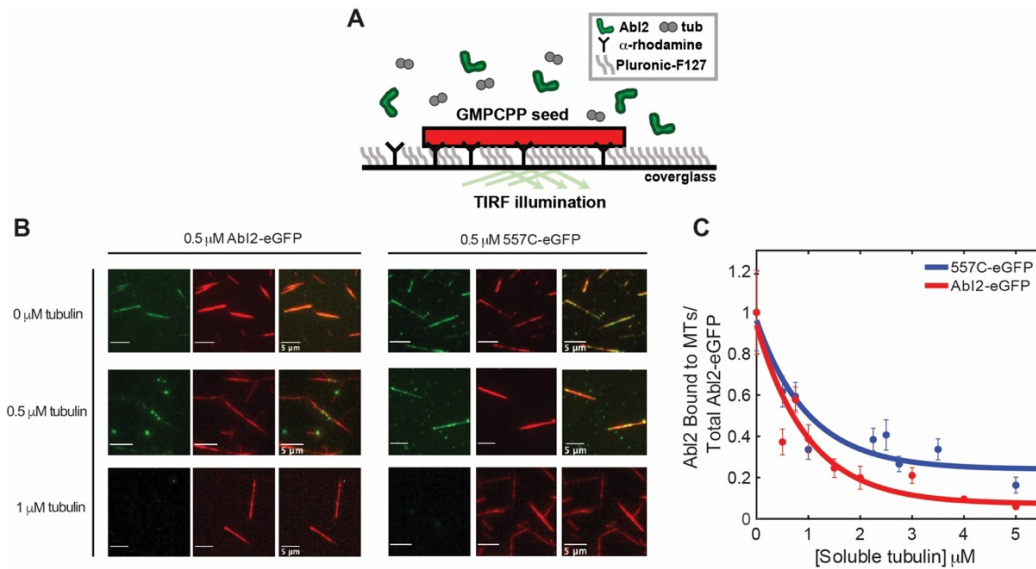


Figure 2.1. Abl2 preferentially binds soluble tubulin dimers. (A) TIRF experimental setup. GMPCPP-stabilized biotinylated 10% rhodamine MT seeds were bound onto Pluronic-F127 and biotin-neutravidin coated coverslips. **(B)** 0.5 μ M Abl2-eGFP and Abl2-557-C-eGFP were incubated with increasing concentrations of non-fluorescent tubulin dimers. The mixture was introduced into the TIRF chamber that was functionalized as shown in (A). **(C)** The population of Abl2-eGFP and Abl2-557-C-eGFP molecules that remained on the MT per condition was quantified and the final binding curves were fitted to a negative exponential.

Increasing concentrations of dark tubulin dimers were incubated with 0.5 μ M Abl2-eGFP or 0.5 μ M Abl2-557C-eGFP and flowed into TIRF flow chambers containing stabilized MTs (**Figure 2.1, A, B**). Upon titrating in increasing concentrations of tubulin, increasingly less density of Abl2 was bound on stabilized MTs after a 5 min incubation period (as to ensure the binding reaction reached equilibrium (Pollard, 2010)). Negative exponential fits reveal that the tubulin concentration required to sufficiently sequester 557C-eGFP is 1.02 μ M, whereas the amount of tubulin dimers for Abl2-eGFP is 0.71 μ M (**Figure 2.1, C**). This information led us to wonder whether Abl2 directly binds to tubulin dimers, and also generated the hypothesis that the C-terminal half may contain 2 tubulin-binding sites.

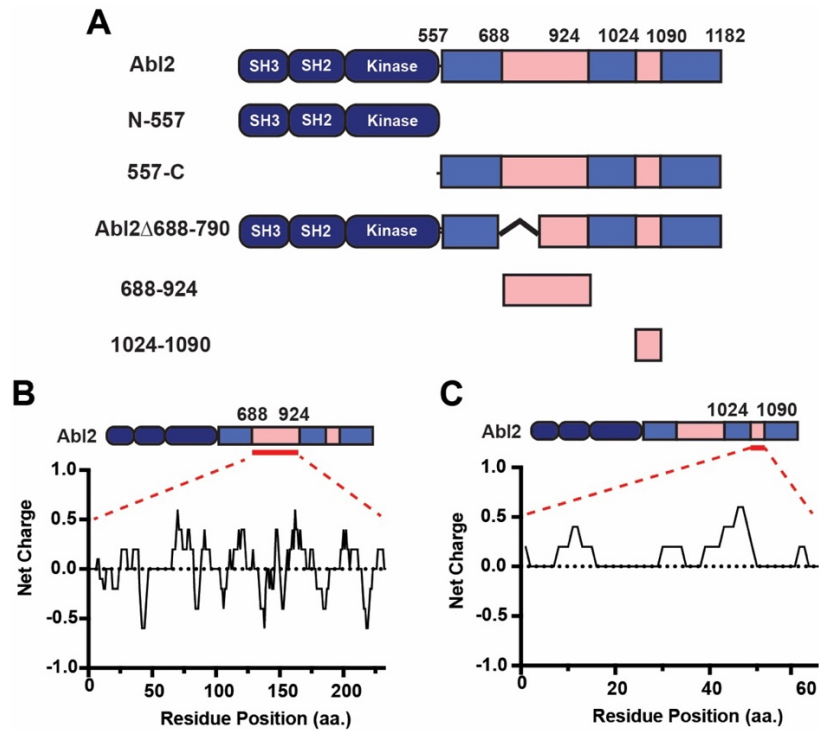


Figure 2.2. Abl2 contains a MT- and tubulin-binding C-terminal half. (A) Domain architecture of Abl2, Abl2-74-557 (N-557), Abl2-557-1182 (557-C), Abl2 Δ 688-790, Abl2-688-924, and Abl2-1024-1090. **(B-C)** Abl2-688-924 and Abl2-1024-1090 bind to tubulin dimers, not to MTs. Net charges of every 5-residue block within Abl2-688-924 **(B)** and Abl2-1024-1090 **(C)**. The residue charge distribution was calculated with EMBOSS to indicate positively-charged clusters.

To definitively test whether Abl2 binds tubulin dimers *in vitro*, I purified Abl2 and generated Abl2 truncation mutants to identify the region that binds to tubulin and/or MTs (**Figure 2.2, A; 2.3**). Alongside collaborator Wanqing Lyu, I purified 557-C and porcine tubulin dimers were applied, separately or after mixing, to a size exclusion column, and monitored their elution profiles. Purified 557-C (68 kDa) eluted with an estimated Stokes radius (R_s) = 68 Å, corresponding to a globular protein of 350 kDa (**Figure 2.4, A**). This revealed that 557-C likely adopts an elongated, unstructured form.

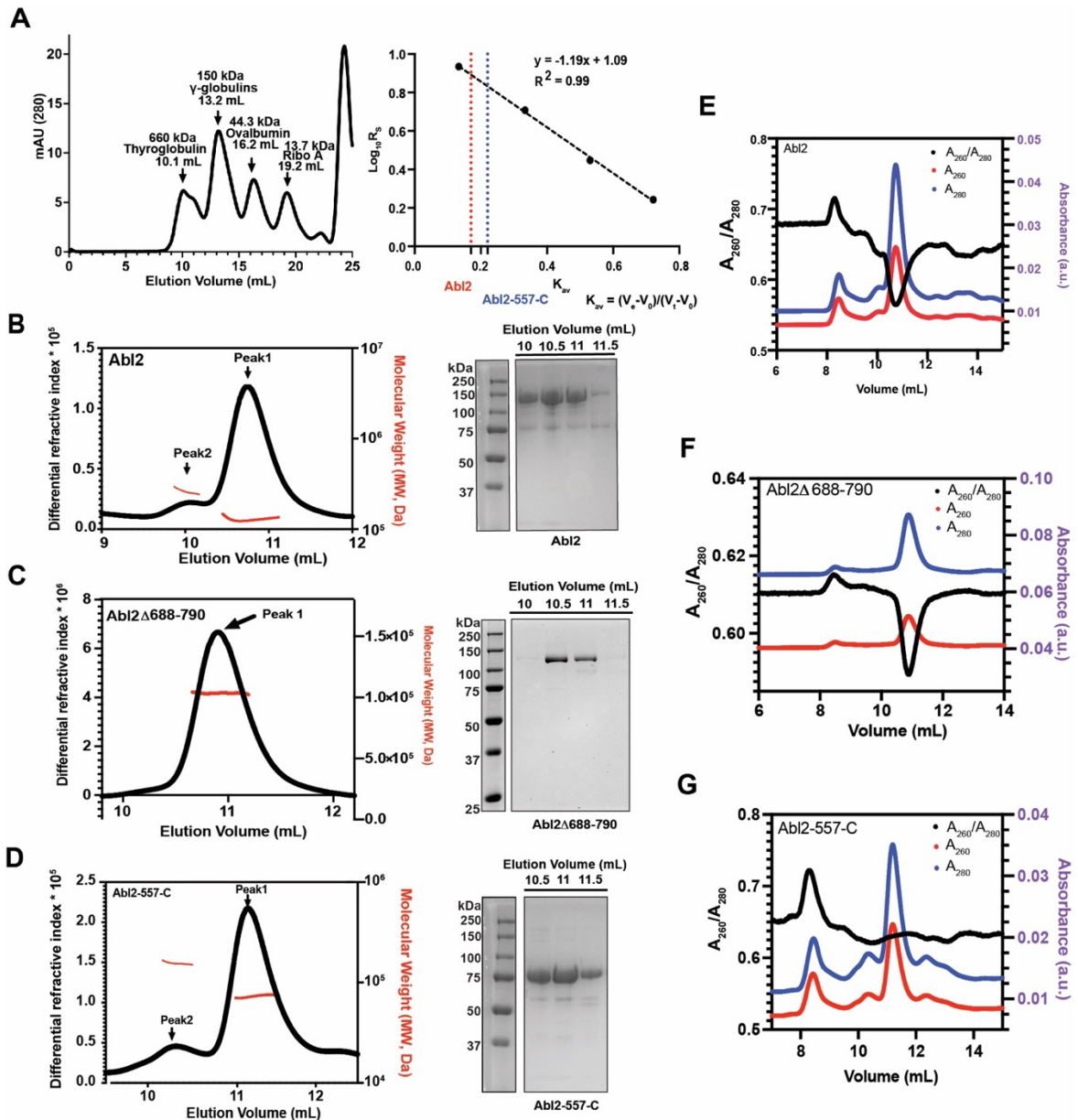


Figure 2.5. Characterization of the physical properties of Abl2 and interactions with tubulin and MTs, related to Figure 1. (A) SEC analysis of standard proteins as indicated using the Superdex 200 increase 10/300 GL column (top). The standard linear plot of the standard proteins $\log_{10}R_s$ and K_{av} (bottom), with R_s = Stokes radius and $K_{av} = (V_e - V_0) / (V_t - V_0)$, in which V_e represents the elution volume of the protein peak, V_0 represents the column void volume (8 ml), and V_t represents the total column volume (23.562 ml). Stokes radii of Abl2 (10.7 ml), 557-C (11.4 ml), and tubulin (14.2 ml) were calculated from the fitted equation. SDS-PAGE gels of the SEC samples are shown in the right panels. **(B-G)** SEC-MALS analysis of Abl2 in **(B)**, Abl2 Δ 688-790 **(C)**, and 557-C in **(D)** showed that Abl2, Abl2 Δ 688-790, and 557-C mainly exist as monomers in solution despite the large Stokes radius. In **(B, D)**, Peak1 represents the predominant monomer peak; Peak2 represents a small amount of dimer formation. Absorbance curves taken at $\lambda = 260$ nm (in red), 280 nm (in blue) reveal that the ratios (in black) are approximately 0.6 at the peak elution fraction corresponding to the monomeric population of Abl2 **(E)**, Abl2 Δ 688-790 **(F)**, and 557-C **(G)**.

Size exclusion chromatography coupled with multi-angle light scattering (SEC-MALS) analysis revealed an estimated molecular weight of 73 kDa for the peak, corresponding to a monomer of 557-C (**Figure 2.5, D**). Similarly, SEC-MALS revealed full-length Abl2 to be a monomer of ~127 kDa, with $R_s = 78 \text{ \AA}$, corresponding to a globular protein of 480 kDa (**Figure 2.5, B**) while Abl2 Δ 688-790, which closely mimics the alternatively spliced Abl2 Δ 688-791 isoform found in both humans and mice, was a monomer of ~104 kDa (**Figure 2.5, C**). Peak elution fractions of Abl2, Abl2 Δ 688-790, and 557-C had $A_{260\text{nm}}/A_{280\text{nm}}$ ratios ≈ 0.6 , indicating a lack of nucleic acid contamination (**Figures 2.5, E-G**).

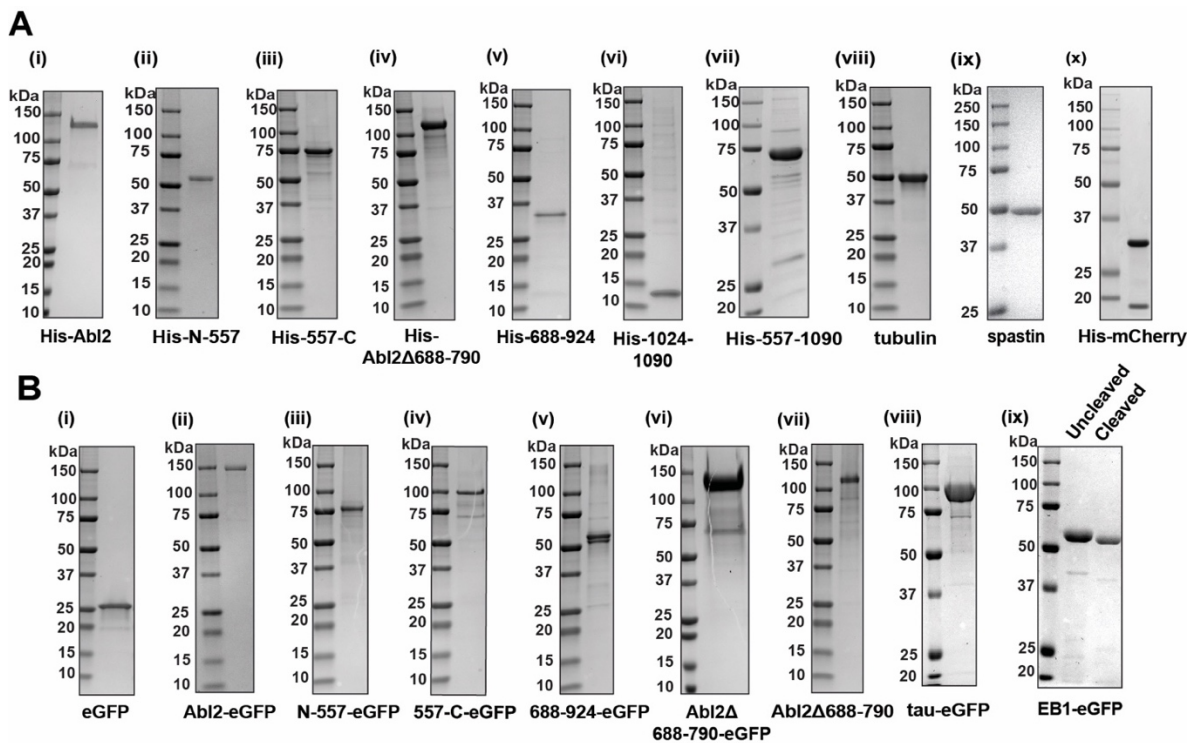


Figure 2.6. Purity of His-tagged and His-cleaved proteins used in this study. All purified proteins used in this work were analyzed by SDS-PAGE and stained with Coomassie Blue G250 to assess purity. **(A) (i-vii)** Purified 6XHis-tagged Abl2 proteins; **(viii)** purified porcine brain tubulin; **(ix)** purified His-tag cleaved spastin and **(x)** 6XHis-tagged mCherry. **(B)** 6XHis-tag cleaved eGFP and eGFP-tagged proteins.

We measured Abl2 binding affinity for tubulin dimers using biolayer interferometry. 6XHis-tagged Abl2 constructs tested in this assay are shown in **Figure 2.2, A**, while purified His-tagged Abl2, porcine brain tubulin, and untagged Abl2 fragments are shown in **Figure 2.6 I, viii, ii-vi**, respectively. Tubulin bound biosensor-immobilized His-Abl2 with a $K_D = 42 \pm 13 \text{ nM}$ (**Figure 2.7**).

His-557-C was sufficient to bind tubulin with high affinity ($K_D = 17 \pm 8$ nM), while the N-terminal half, His-N-557, did not bind tubulin (**Figure 2.7**). Abl2 Δ 688-790 also did not bind tubulin dimers (**Figure 2.7**). We discovered two distinct Abl2 fragments within the C-terminal half, comprised of amino acids 688-924 (site I) and 1024-1090 (site II), that bound independently to tubulin dimers, but with significantly reduced affinity ($K_{D, \text{His-688-924}} = 118 \pm 39$ nM; $K_{D, \text{His-1024-1090}} = 252 \pm 123$ nM; **Figure 2.7**) relative to His-Abl2 or His-557-C.

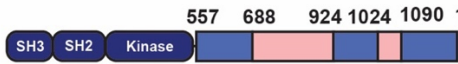





Construct	K_D (nM)	k_{on} ($\times 10^6 \text{ M}^{-1} \text{ min}^{-1}$)	k_{off} (min^{-1})
Abl2 	42 ± 13	3.6 ± 1.1	0.14 ± 0.02
N-557 	N.B.	N.B.	N.B.
557-C 	17 ± 8	8.6 ± 2.1	0.15 ± 0.08
Abl2 Δ 688-790 	N.B.	N.B.	N.B.
688-924 	118 ± 39	5.4 ± 2.6	0.58 ± 0.15
1024-1090 	252 ± 123	8.3 ± 0.83	1.5 ± 0.10

Figure 2.7. Binding affinities for tubulin dimers. Biolayer interferometry (BLI) assays were conducted to determine disassociation constants (K_D) of Abl2 and tubulin dimers. K_D , k_{on} , k_{off} measurements are shown as means \pm S.D., for each BLI assay condition, $n = 3$. N.B.: Not Binding, binding signals were either not observable or significantly low that cannot be fit.

These two binding sites are not homologous to tubulin-binding TOG and CAP-Gly domains (Akhmanova & Steinmetz, 2008), but are enriched in positively charged residues, with calculated pIs of site I = 9.05 (**Figure 2.2, B**) and site II = 10.53 (**Figure 2.2, C**).

To measure MT binding affinities, fixed concentrations of Abl2 proteins were mixed with increasing concentrations of taxol-stabilized MTs and the bound fraction at each concentration was measured after MT co-sedimentation (Hu et al., 2019).

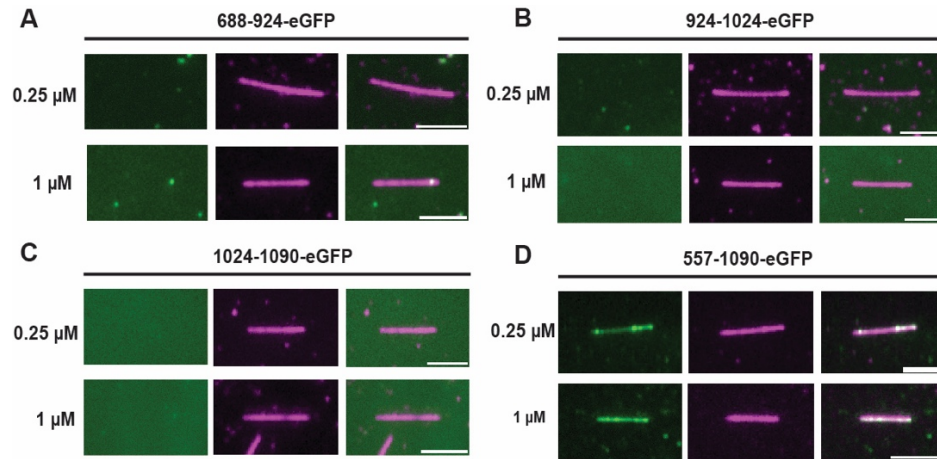


Figure 2.8. TIRF microscopy still images of 0.25 μM and 1 μM of tubulin-binding site I 688-924-eGFP (**A**), Abl2-924-1024-eGFP (**B**), tubulin-binding site II 1024-1090-eGFP (**C**), both tubulin-binding sites I and II in Abl2-557-1090-eGFP (**D**) in the presence of stabilized GMPCPP-MTs. Scale bar, 5 μm.

Strikingly, Abl2 Δ 688-790, which lacks part of the higher-affinity site I, bound MTs with a similar affinity as Abl2-eGFP ($K_{D, Abl2-eGFP} = 0.32 \pm 0.06 \mu M$, $K_{D, Abl2\Delta 688-790} = 0.40 \pm 0.20 \mu M$; **Figure 2.9**), even though it did not bind tubulin. In contrast, neither tubulin binding fragment 688-924-eGFP or 1024-1090-eGFP, nor the region between sites I and II (924-1024-eGFP) bound detectably to MTs (**Figure 2.8, A-C; 2.9**), indicating that the MT- and tubulin-binding regions of Abl2 do not overlap completely. Using 0.5 μM tubulin which is well under the critical concentration, Abl2-eGFP also colocalized prominently with Alexa647-tubulin (Pearson coefficient = 0.93 ± 0.05) on rhodamine GMPCPP-MTs (**Figure 2.10**).

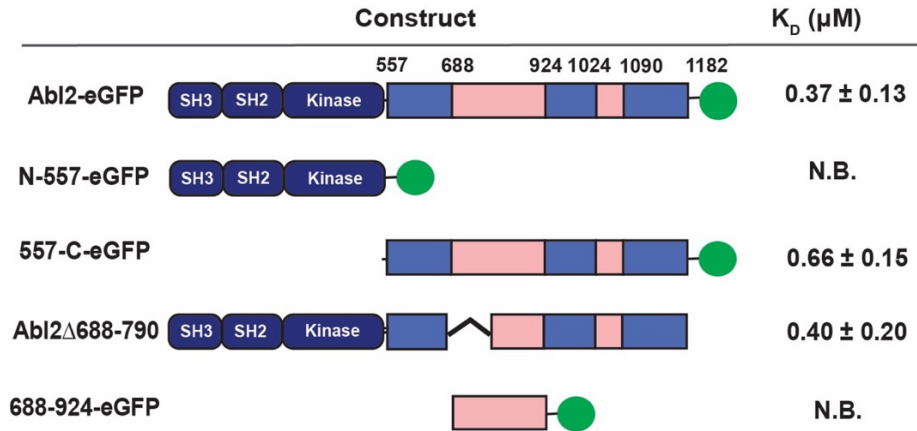


Figure 2.9. Binding affinities for taxol-stabilized MTs. Co-sedimentation assays were conducted to determine disassociation constants (K_D) of Abl2 and taxol-MTs. K_D measurements are shown as means \pm S.D., for each assay condition, $n > 3$. NB: Not Binding.

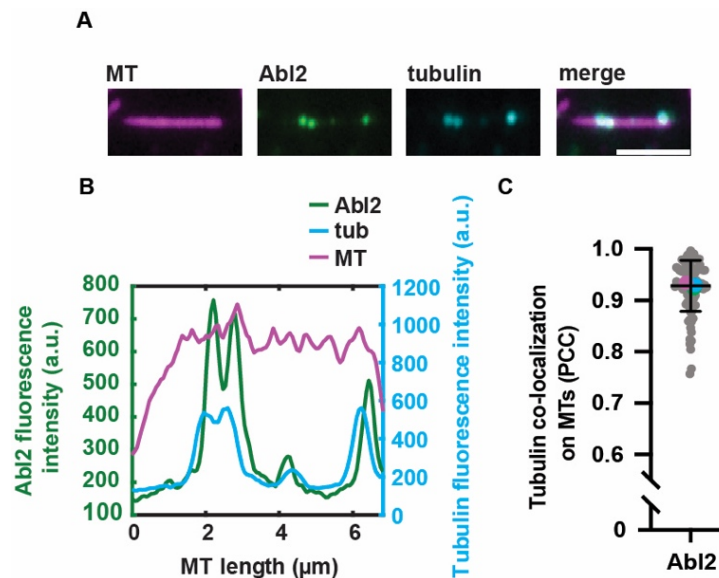


Figure 2.10. Abl2 co-localizes with tubulin dimers on GMPCPP-MTs. (A) Representative Abl2- and tubulin-bound MT. (B) Quantification of fluorescence intensities of Abl2-eGFP and Alexa647-tubulin on the rhodamine-labeled GMPCPP-MT shown in (A). (C) Pearson-correlation coefficient (PCC) analysis reveals that Abl2 and tubulin co-localize on a MT. Magenta, cyan, and green points indicate the mean PCC for each technical replicate. $n = 94$ filaments across 3 technical replicates.

2.2. Abl2 undergoes LLPS and co-condense with tubulin *in vitro*

A growing list of MT-binding proteins regulate MT dynamics through LLPS, which is associated with regions of disorder (Hernández-Vega et al., 2017; King & Petry, 2020; Lin et al., 2017; Maan et al., 2022; Meier et al., 2022; Song et al., 2022; Tan et al., 2019). PONDR-FIT and Diso-Pred3 software predicted the Abl2 C-terminal half to be disordered (Figure 2.11, A). Indeed, deconvolution of

circular dichroism (CD) spectra of 557-C indicated 10-30% disordered secondary structure content (Figure 2.11, B).

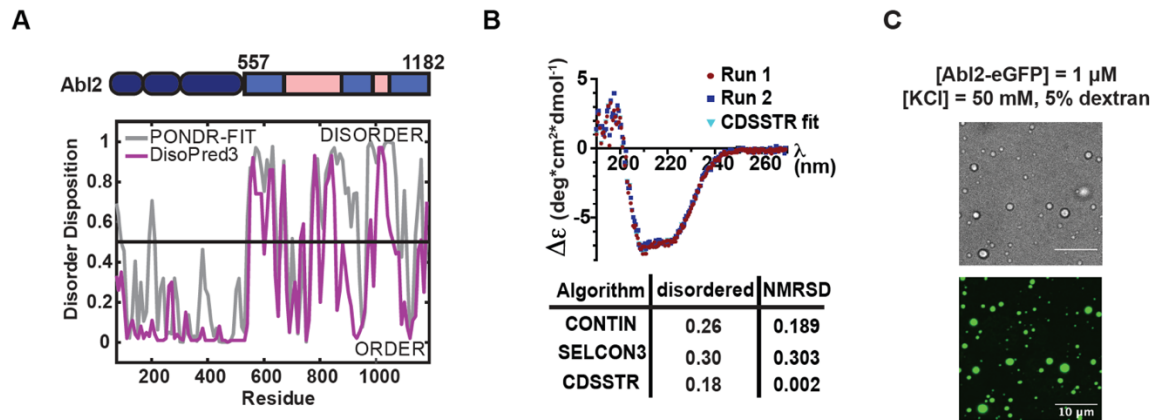


Figure 2.11. Abl2 undergoes phase separation and co-condenses with tubulin. (A) Disorder prediction from primary sequence of murine Abl2 using PONDR-FIT and DisoPred3 algorithms. Disorder disposition of 0.5 was used as the threshold. (B) Buffer-subtracted CD spectra of 6XHis-tag free 557-C collected at 4°C. CD spectra deconvolution algorithms CONTIN, SELCON3, CDSSTR analyses reveal the disordered content of the 557-C. $n = 2$. (C) 1 μM Abl2-eGFP forms condensates in 5% dextran, 50 mM KCl, and BRB80. Condensates were imaged under brightfield (top) and fluorescence (bottom). Scale bar, 10 μm .

To investigate whether Abl2 could undergo LLPS, we observed solutions containing Abl2-eGFP and 5% dextran, a non-physiological agent that mimics intracellular molecular crowding (Speer et al., 2022; Wang et al., 2018). Abl2-eGFP puncta appeared spherical in both brightfield and fluorescence imaging (Figure 2.11, C). We used a partition coefficient (PC), a ratio of the mean condensate intensity relative to background, ≥ 4 as a cutoff for LLPS (King & Petry, 2020). LLPS increased with Abl2-eGFP concentration, but was attenuated by increasing salt concentration, a known disruptor of phase separation (Alberti et al., 2019; Feng et al., 2019; Wang et al., 2018) (Figure 2.12, A). PC analysis revealed that 557-C-eGFP also phase separates (Figure 2.12, B), consistent with its propensity to disorder. We utilized a sedimentation assay to measure the fraction of Abl2-eGFP entering the dense and dilute phases as a function of concentration.

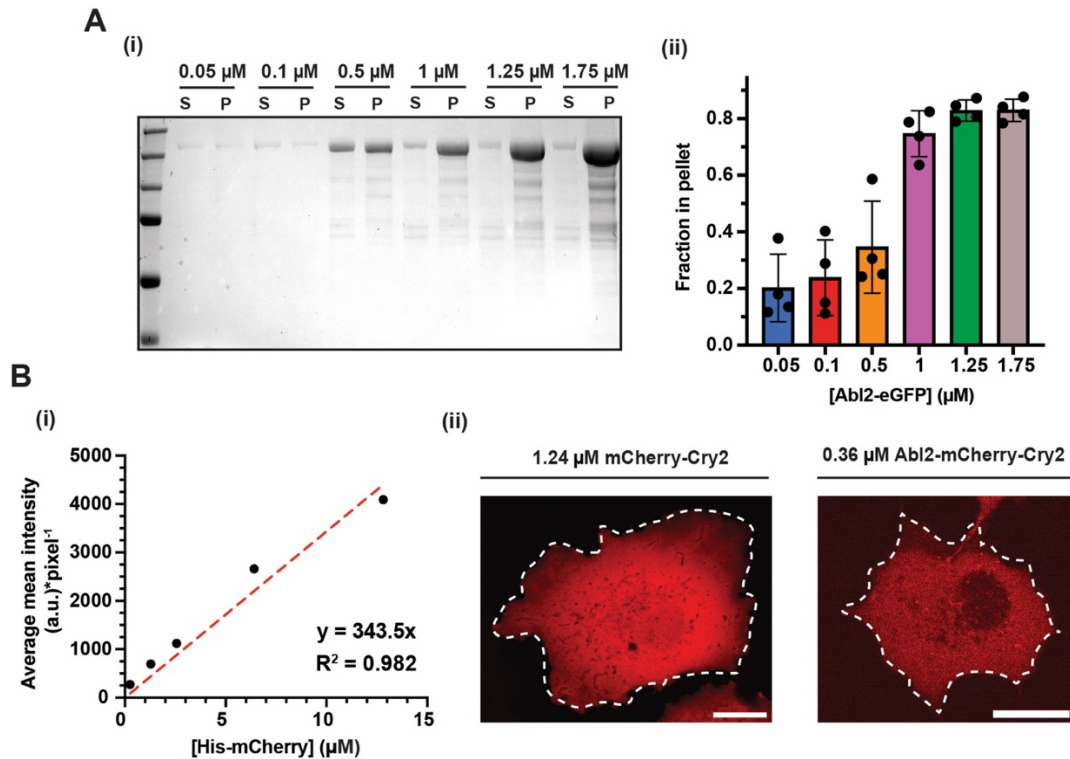


Figure 2.12. The saturation concentration, c_{sat} , of Abl2 is under its physiological concentration in COS-7 cells. (A) Increasing concentrations of purified His-cleaved Abl2-eGFP were incubated in 1X BRB80 buffer supplemented with 50 mM KCl and 5% dextran. After incubating for 20 min at RT, the reactions were spun down in a tabletop centrifuge at 15K rpm for 10 min. S and P fractions were harvested and boiled in Laemmli Sample Buffer at 100°C for 10 min. The supernatant (S) and pellet (P) fractions were determined by fractionation on 10% SDS PAGE and stained with Coomassie Blue (i). Amounts of Abl2-eGFP in S and P fractions were measured as densitometries of proteins bands at ~160 kDa in the pellet fractions (quantified using Fiji) and plotted in (ii). Means \pm SD shown as bars and black lines, respectively. $n = 4$ technical replicates per condition. (B) Estimation of intracellular concentrations of mCherry-Cry2WT and Abl2-mCherry-Cry2 in transfected COS-7 cells. (i) Standard curve generated from measuring the mean intensity per pixel values for a dilution series of recombinant 6XHis-mCherry. Linear regression fit shown in red dotted line. (ii) Measurements of estimated intracellular concentrations of mCherry-Cry2 and Abl2-mCherry-Cry2 in transfected COS-7 cells based on standard curve shown in (i). Same cells are shown in Figure 2O-P. ROIs shown as white dotted outlines. Scale bar, 20 μm .

The proportion of Abl2-eGFP in the dense phase increased strikingly when the Abl2-eGFP concentration was raised from 0.5 to 1 μM in 50 mM KCl (Figure 2.12, A), consistent with the phase transition observed in epifluorescence. This phase transition occurs below the concentration of 1.4 μM Abl2 previously measured in COS-7 cells (Hu et al., 2019). Fluorescence recovery after photobleaching (FRAP) of a confocal plane within Abl2-eGFP condensates revealed a recovery half time ($t_{1/2}$) \approx 1.7 min (Figure 2.12, C).

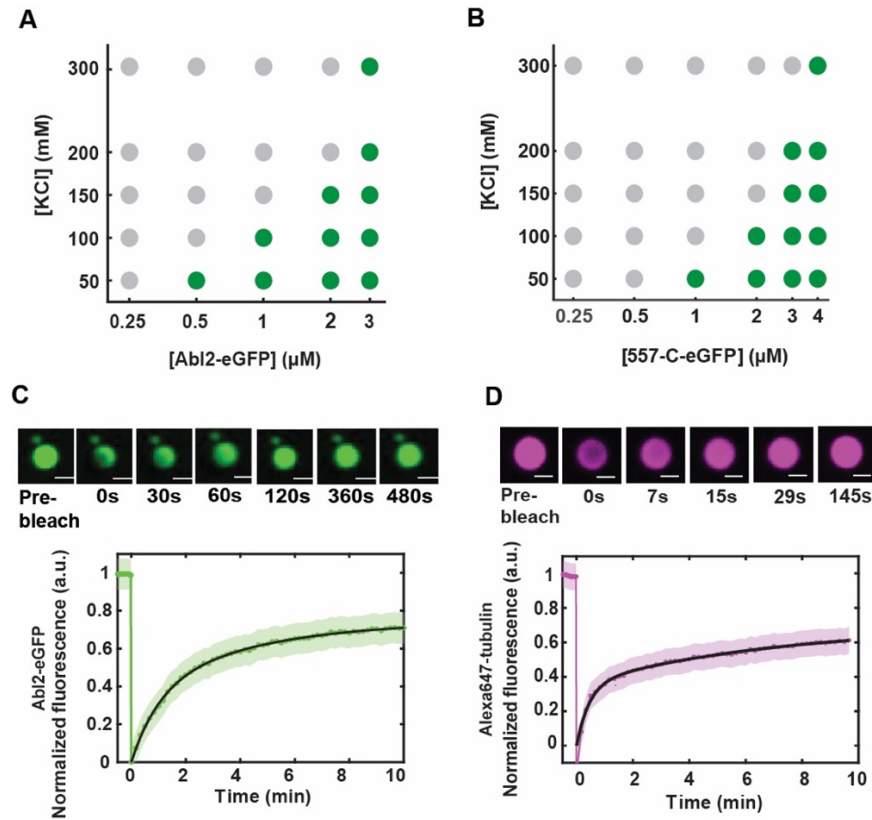


Figure 2.13. Phase separation diagrams of the [Abl2-eGFP] vs. [KCl] (**A**) and [557-C-eGFP] vs. [KCl] (**B**) relationships. Partition coefficient (PC) ≥ 4 was the threshold for phase separation, shown as green dots, PC < 4 is defined as not phase separated, shown as gray dots. X-axis shown on log₁₀ scale. 17-230 condensates were analyzed per condition. (**C**, **D**) FRAP recovery of Abl2-eGFP in condensates (**C**) and tubulin in Abl2-eGFP:Alexa647-tubulin co-condensates (**D**) in solution. Double-exponential fits shown in solid black with SEM shown as green. $n \geq 11$ condensates. Scale bar, 2 μm in (**C**); 1 μm in (**D**).

We next tested whether Abl2-eGFP formed coacervates (charge-driven assembly of liquid condensates (Uversky et al., 2015)) with tubulin. When incubated under conditions that promote Abl2-eGFP LLPS, Alexa647-tubulin dimers partitioned into Abl2-eGFP condensates (**Figure 2.14, A-B**). FRAP analysis revealed that tubulin dimers diffused into an internally bleached region within Abl2:tubulin coacervates (**Figure 2.13, D**). The Abl2 C-terminal half was necessary and sufficient for coacervation with tubulin, as 557-C-eGFP both underwent phase separation and recruited tubulin dimers into the condensate, while N-557-eGFP and the tubulin binding site I, 688-924-eGFP, did not undergo phase separation (**Figure 2.14, A-B**). While it underwent LLPS, tubulin-binding defective Abl2 Δ 688-790-eGFP condensates had significantly reduced ability to partition tubulin into the condensates (**Figure 2.14, B**). Abl2-eGFP condensates recruited tubulin to reach partition

coefficients over 3, while Abl2 Δ 688-790-eGFP condensates only reached tubulin partition coefficients just over the background of 1.

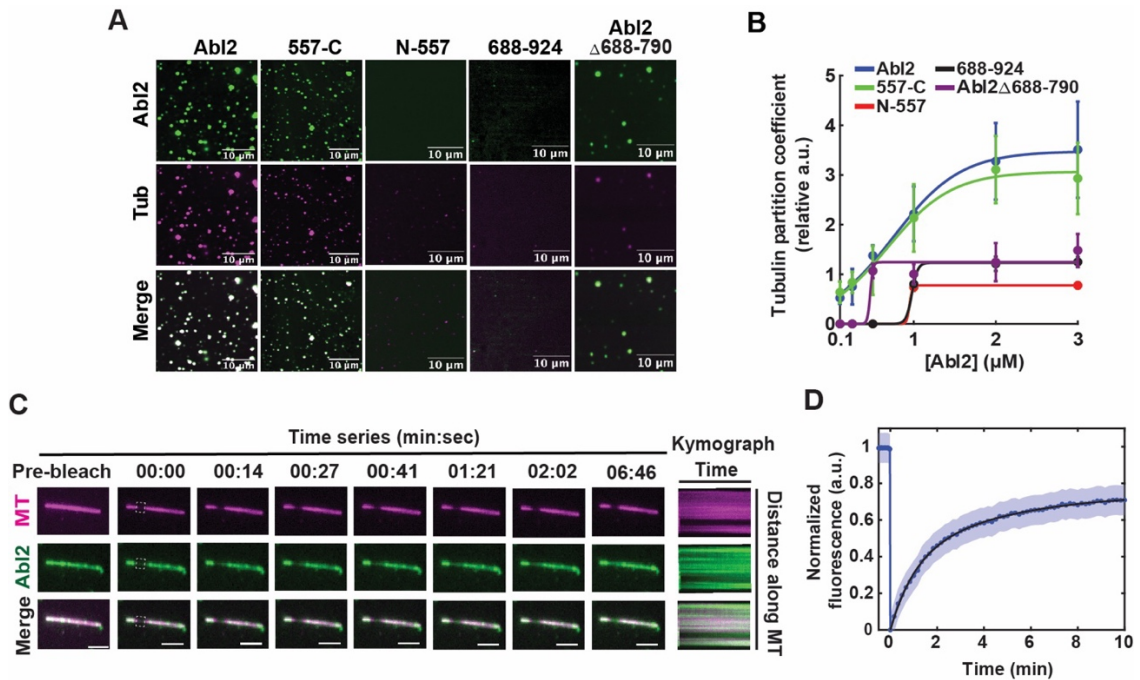


Figure 2.14. Abl2 co-condenses with tubulin in solution and undergoes dynamic exchange with other Abl2 molecules on MTs. (A) 1 μ M Abl2, 557-C, N-557, 688-924, and Abl2 Δ 688-790 were incubated with equimolar concentrations of Alexa647-tubulin in BRB80, 5% dextran, 50 mM KCl to test for co-condensation. (B) PC analysis of co-condensed tubulin in Abl2 condensates at increasing equimolar concentrations of Abl2-eGFP and tubulin at 50 mM KCl. At least 90 tubulin co-condensates were scored for Abl2, 557-C, and Abl2 Δ 688-790. N557: $n_{2\mu\text{M}} = 37$; $n_{3\mu\text{M}} = 89$; 688-924: $n_{2\mu\text{M}} = 53$; $n_{3\mu\text{M}} = 147$. Sigmoidal fits shown in solid lines. Data are mean \pm SD. (C, D) Representative time series of FRAP on Abl2 puncta on GMPCPP-stabilized MTs (C). Bleached ROI shown in dashed white line. Scale bar, 3 μ m. FRAP recovery curve reveals that Abl2 condensates are undergoing dynamic exchange with other molecules on the MT and/or from solution (D). Double-exponential fit in solid black with SEM shown as blue. $n = 15$ filaments.

We also examined how Abl2-eGFP interacted with MTs, either by itself or if soluble tubulin was included. FRAP analysis revealed that 1 μ M Abl2-eGFP bound to GMPCPP-stabilized MTs could undergo slow exchange with Abl2-eGFP molecules in solution, in absence of dextran or free tubulin (Figure 2.14, C-D). Under these same conditions, Abl2-eGFP coacervates were also observed to form, move, and undergo fusion (Figure 2.15, A), with a relative increase in fluorescence intensity proportional to the mean intensities of pre-fusion condensates (Figure 2.15, C). This suggests MTs may serve as a platform to recruit Abl2 and enhance LLPS. We also found that at equimolar 0.5

μM concentrations, Abl2:tubulin co-condensates diffused along GMPCPP-MT templates and could undergo fusion throughout time (**Figure 2.15, B**).

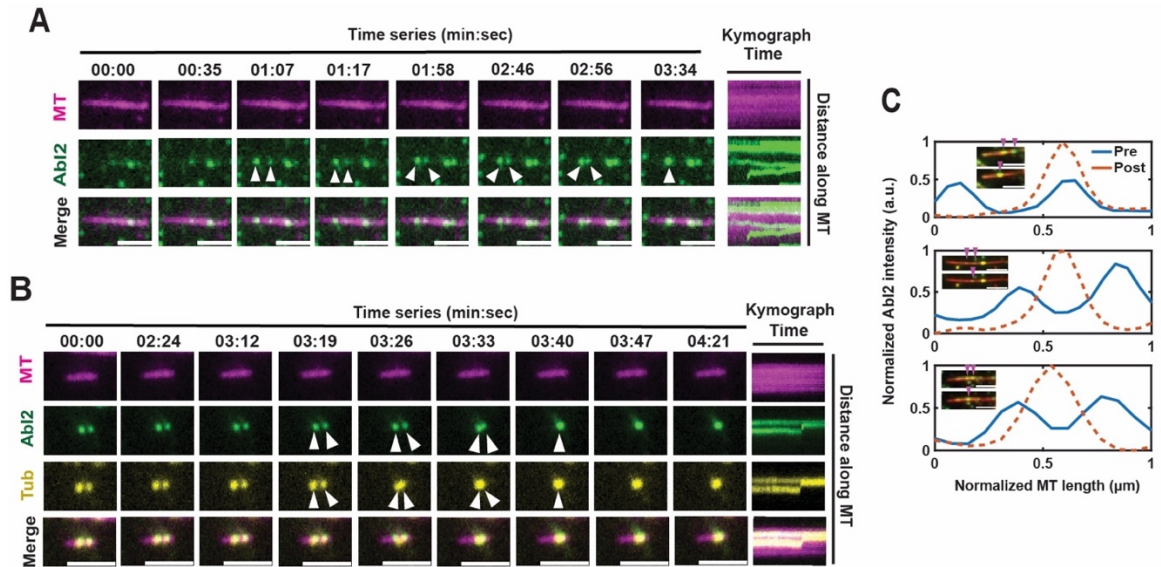


Figure 2.15. Abl2 undergoes fusion on MTs and recruits tubulin into condensates. (A) Representative time series of fusion of Abl2 condensates (**A**, scale bar = $3 \mu\text{m}$) or Abl2-tubulin co-condensates (**B**, scale bar = $5 \mu\text{m}$) on a rhodamine GMPCPP-MT (pseudo-colored magenta). Kymographs are shown on right. **(C)** Fluorescence intensity analysis of fusion events of Abl2-eGFP puncta on stabilized MTs, as shown in **(A)**. Post-fusion condensates yield higher mean fluorescence intensities (dashed orange line) relative to their pre-fusion condensates of various sizes (solid blue lines).

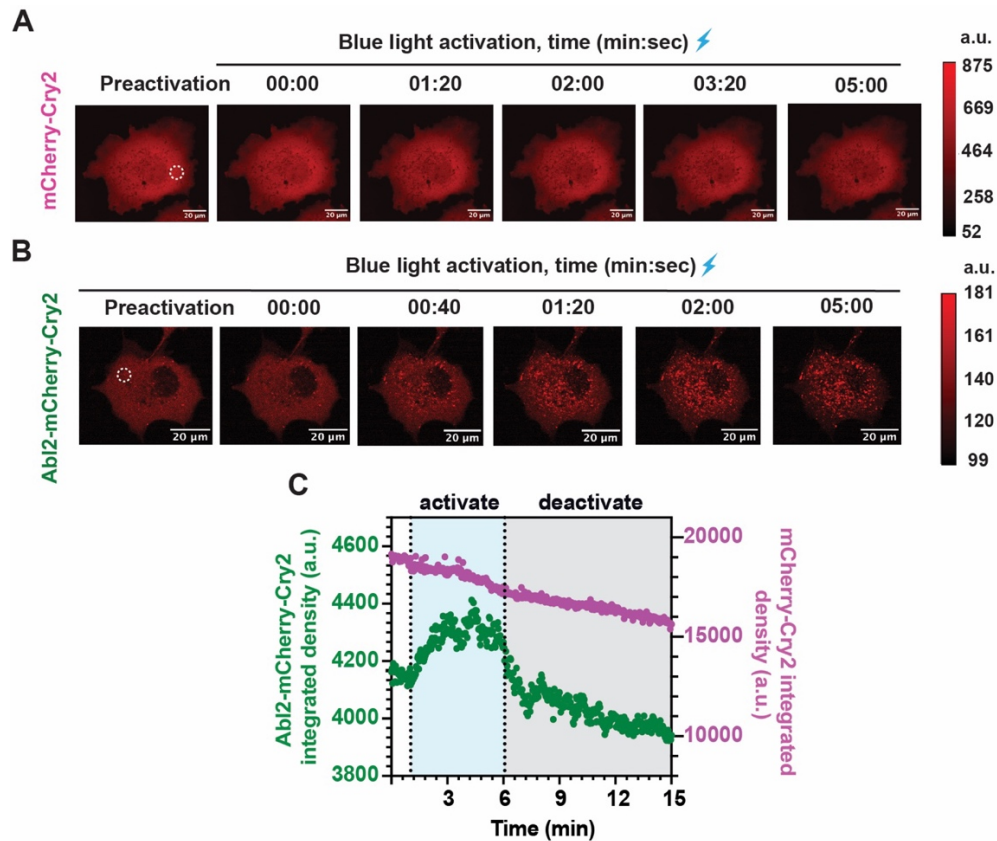


Figure 2.16. Abl2 undergoes phase separation in cells. Representative time series of mCherry-Cry2 (**A**) and Abl2-mCherry-Cry2 (**B**) in transfected COS-7 cells, shown pre- and post-blue light activation ($\lambda = 488$ nm). Raw fluorescence intensity color bars shown on right. (**C**) Quantification of mCherry intensity (integrated densities, a.u.) within the ROIs shown in (A, magenta) and (B, green) indicated by dashed white circles. Blue shaded region depicts 5 min blue light activation period. Gray shaded region depicts 10 min following blue light exposure.

To determine whether Abl2 exhibits self-association in cells, we sought to using *Arabidopsis* cryptochrome 2 (Cry2) as a tool, a photoreceptor that can undergo homo-oligomerization upon blue light-dependent activation (Che et al., 2015). We expressed Abl2-mCherry-Cry2 or control mCherry-Cry2 in COS-7 cells (Shin et al., 2017). We used purified 6XHis-mCherry (**Figure 2.6, A, x**) to generate a standard curve relating concentration to mean fluorescence intensity to cellular concentration (**Figure 2.12, B, i**). Using the initial pre-activation images, we estimated intracellular concentrations of ~ 0.5 - 1.2 μ M mCherry-Cry2 and ~ 0.4 - 0.6 μ M Abl2-mCherry-Cry2, respectively (**Figure 2.12, B, ii; 2.17**). While Abl2-mCherry-Cry2 and mCherry-Cry2 were diffuse within the cytoplasm under pre-activation conditions, blue light induced rapid cytoplasmic clustering of Abl2-mCherry-Cry2 (**Figure 2.16, A, C**), but not mCherry-Cry2 (**Figure 2.16, B, C**). Our data reveal that

Abl2-mCherry-Cry2 forms puncta upon blue light exposure at concentrations at or below the endogenous concentrations of Abl2 – which is 1.4 μM in COS-7 cells (**Figure 2.18, A**; and 500 nM in HeLa cells, **Figure 2.18, B**) – while mCherry-Cry2 does not (**Figure 2.17**).

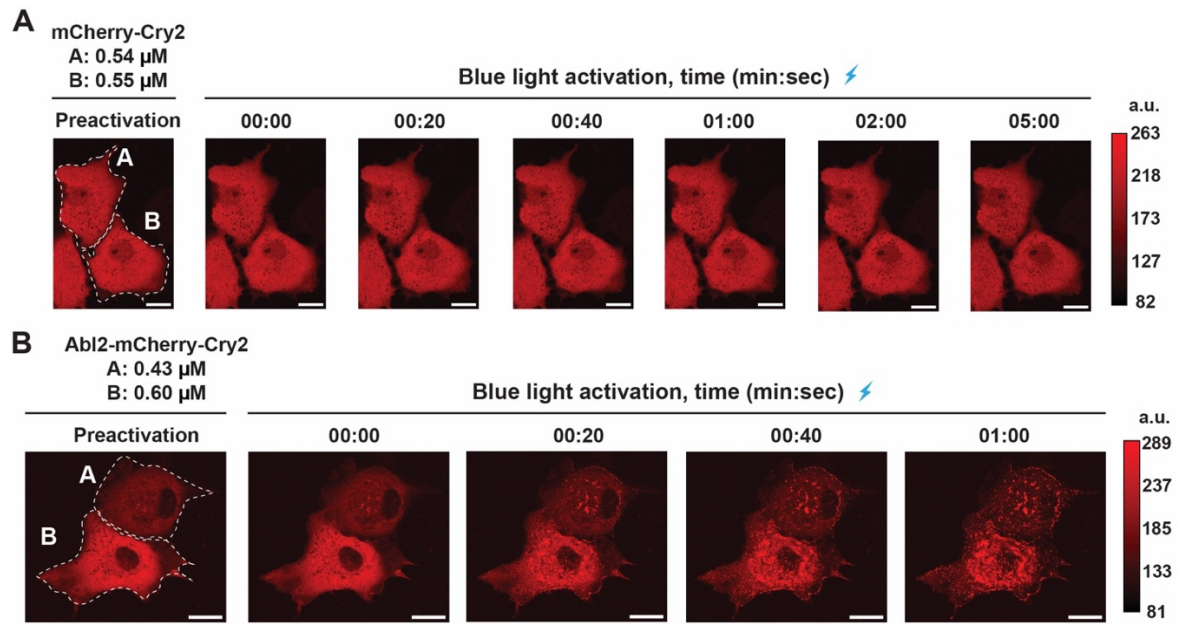


Figure 2.17. Representative time-series of mCherry-Cry2 and Abl2-mCherry-Cry2 expressing COS-7 cells. (A) Still images of mCherry-Cry2 expressing COS-7 cells before (pre-activation), and during blue light activation. Cells shown (labelled A, B) have approximate intracellular concentrations of 0.54 and 0.55 μM mCherry-Cry2, respectively. **(B)** Representative still images of Abl2-mCherry-Cry2 expressing COS-7 cells before (pre-activation), and during blue light activation. Cell A was estimated to have an approximate concentration of 0.43 μM Abl2-mCherry-Cry2, while Cell B has 0.60 μM .

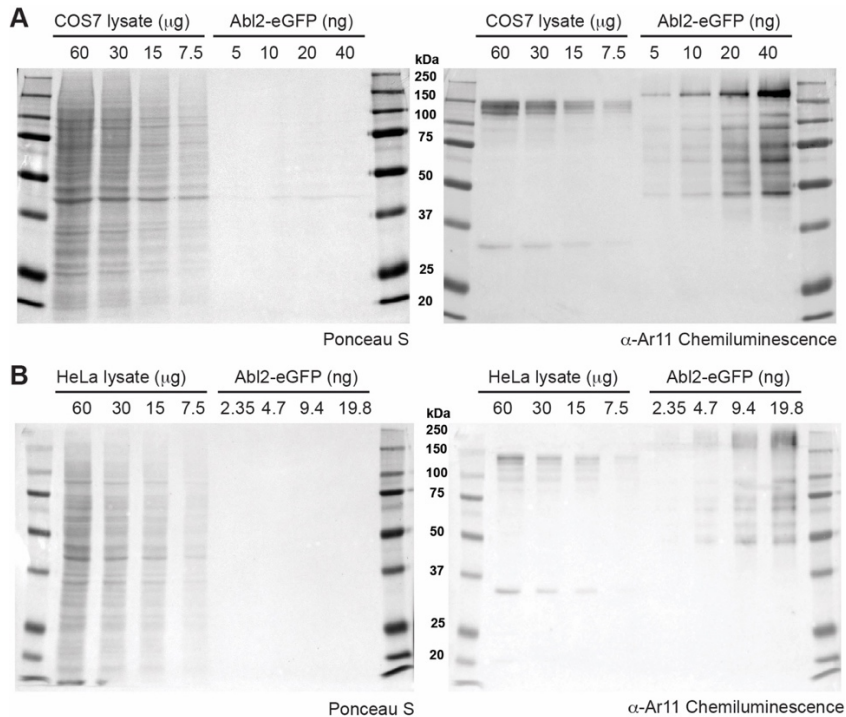


Figure 2.18. Ponceau S stain and chemiluminescence to quantify endogenous levels of Abl2 in COS-7 and HeLa cells. (A) COS-7 cells endogenously express 1.4 μM Abl2. **(B)** HeLa cells endogenously express 140 nM Abl2. Quantifications were obtained given the MW of Abl2 is ~ 130 kDa and assuming a cytosolic protein concentration of $100 \text{ mg} \cdot \text{ml}^{-1}$ (Albe et al., 1990; Finka & Goloubinoff, 2013).

2.3. Abl2 promotes nucleation and rescue *in vitro*

The finding that Abl2 binds both the MT lattice and tubulin dimers led us to investigate whether Abl2 impacts MT nucleation. We measured changes in turbidity (OD_{350}) over time, which increases upon MT polymerization, in the absence or presence of Abl2 (**Figure 2.19, A**). We previously showed that 0-2 μM MBP-tagged 557-C increases MT assembly in a concentration-dependent manner (Hu et al., 2019). Addition of 1 μM Abl2 to 18 μM tubulin increased the plateau of turbidity from $\Delta\text{OD}_{350, \text{tub}} = 0.093 \pm 0.000$ to $\Delta\text{OD}_{350, \text{tub} + \text{Abl2}} = 0.210 \pm 0.173$ (mean \pm SD), a 2.3-fold increase over tubulin alone, **Figure 2.19, A-B**). The increased turbidity reflected greater MT polymerization, as revealed by sedimenting polymerized MTs and analyzing them by SDS-PAGE (**Figure 2.21, A**). The tubulin critical concentration decreased 11-fold from $5.5 \pm 1.1 \mu\text{M}$ in the absence of Abl2 to $0.5 \pm 1.8 \mu\text{M}$ in the presence of Abl2, respectively (**Figure 2.19, C**). Addition of 1 μM Abl2 also lowered

nucleation lag time, when turbidity reaches one-tenth of its maximum⁷¹⁻⁷³, 1.8-fold from 16 ± 2 min to 9 ± 3 min (Figure 2.19, C).

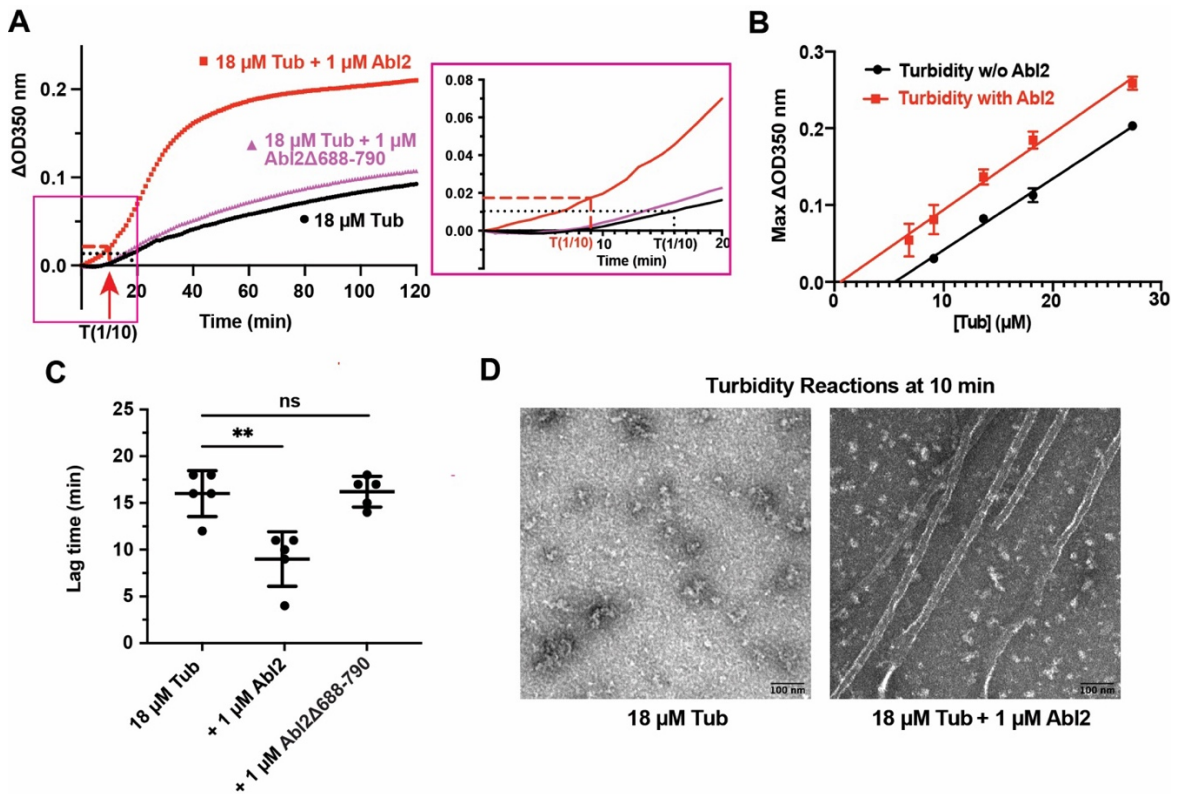


Figure 2.19. Abl2 promotes MT nucleation via interactions with tubulin and MTs. (A) MT assembly was monitored by measuring the increase in turbidity (ΔOD_{350}). 18 μM tubulin and 2 mM GTP were incubated alone (black) or with 1 μM Abl2 (red) or Abl2 Δ 688-790 (magenta). Representative time series of OD_{350} measurements are shown. Curves in the blue dotted window were expanded in the right panel. Lag time of reactions with (red) and without Abl2 (black) are indicated with the dotted line. (B) Turbidity assays with different tubulin concentrations were performed and the maximal ΔOD_{350} was plotted against initial tubulin concentration to determine the critical concentration of tubulin polymerization. $n = 3$ replicates at each concentration for each of these experiments. (C) The lag time until ΔOD_{350} reaches 1/10 of the maximal ΔOD_{350} was measured. The inclusion of Abl2 significantly decreased the lag time for MT nucleation. Mann-Whitney test. $n = 5$. **, $p < 0.001$. (D) Representative samples taken 10 min after turbidity reactions were initiated were visualized under negative-stain EM. More polymerized MT segments were observed in the presence of Abl2. Turbidity conducted by Wanqing Lyu.

The ability of Abl2 to promote MT nucleation was also affirmed by visualizing reaction products at the initial phase of the reaction via negative-stain electron microscopy (EM), which revealed significantly more MTs when Abl2 was included (Figure 2.19, D). Abl2 Δ 688-790 – which does not bind tubulin – had no effect on critical concentration or lag time (Figure 2.19, C). To test if co-condensation of Abl2 and tubulin facilitates MT nucleation, we measured non-templated MT

nucleation using low concentrations (8 μM) of Alexa647-tubulin, 1 μM Abl2-eGFP and 3% dextran (**Figure 2.20, A**). Abl2:tubulin formed co-condensates from which numerous MTs grew. Control eGFP did not form condensates or promote MT formation under these conditions (**Figure 2.20, C**). In the absence of 3% dextran, Abl2-eGFP remained diffuse in solution and few MTs were observed after a 1 hr reaction (**Figure 2.20, B**).

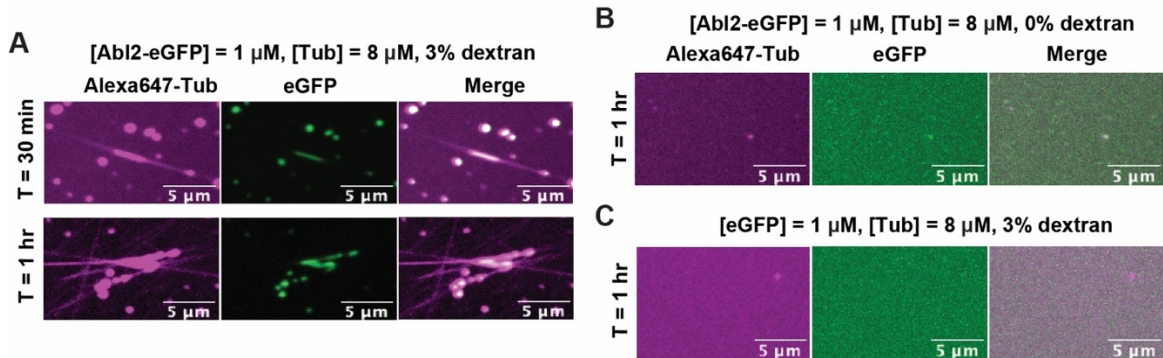


Figure 2.20. Abl2 promotes spontaneous MT nucleation. (A) Representative confocal images of the MT nucleation from the Abl2-eGFP:Alexa647-tubulin co-condensates under 3% dextran. (B-C) Control reactions containing Abl2-eGFP and Alexa647-tubulin without dextran (B), or mixing eGFP and Alexa647-tubulin with 3% dextran (C) did not show observable MTs growing after 1 hr. Spontaneous nucleation experiment by Wanqing Lyu.

We then examined how Abl2 impacts MT reassembly following nocodazole treatment in WT and Abl2 KO COS-7 cells (**Figures 2.21, 2.25**). Cells were treated with 10 μM nocodazole for 1 hr and MT recovery was measured 5 minutes after washout. MT recovery from centrosomes was significantly higher (2.6-fold) in WT COS-7 cells relative to Abl2 KO COS-7 cells ($\text{MTR}_{\text{WT}} = 4.52 \pm 4.23 \text{ a.u.} \cdot \mu\text{m}^{-2} \cdot 10^{-4}$, $\text{MTR}_{\text{KO}} = 1.72 \pm 1.74 \text{ a.u.} \cdot \mu\text{m}^{-2} \cdot 10^{-4}$, $p < 0.0001$, **Figures 2.26, 2.28**).

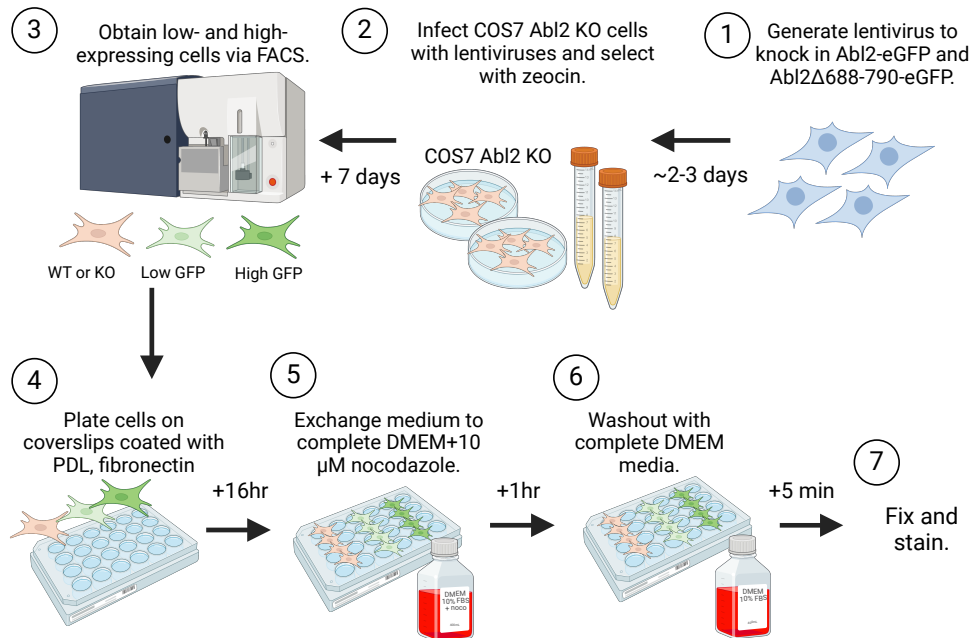


Figure 2.21. Methodology to quantify MT reassembly following nocodazole treatment and washout. Lentiviruses for Abl2-eGFP and Abl2 Δ 688-790-eGFP were generated. Lentiviruses were harvested and used to infect Abl2 CRISPR KO COS-7 cells. After a week, cells that survived zeocin antibiotic selection were FACS sorted for low- and high-expression levels of GFP fluorescence. The cells were plated on poly-d-lysine and human fibronectin coated 10 mm #1.5 glass coverslips in 24-well plates. Cells were allowed treated with DMEM medium supplemented with 10 μ M nocodazole for 1h at 37°C. Nocodazole was washed out and cells were fixed 5 min post-washout. Cells were fixed for immunofluorescence.

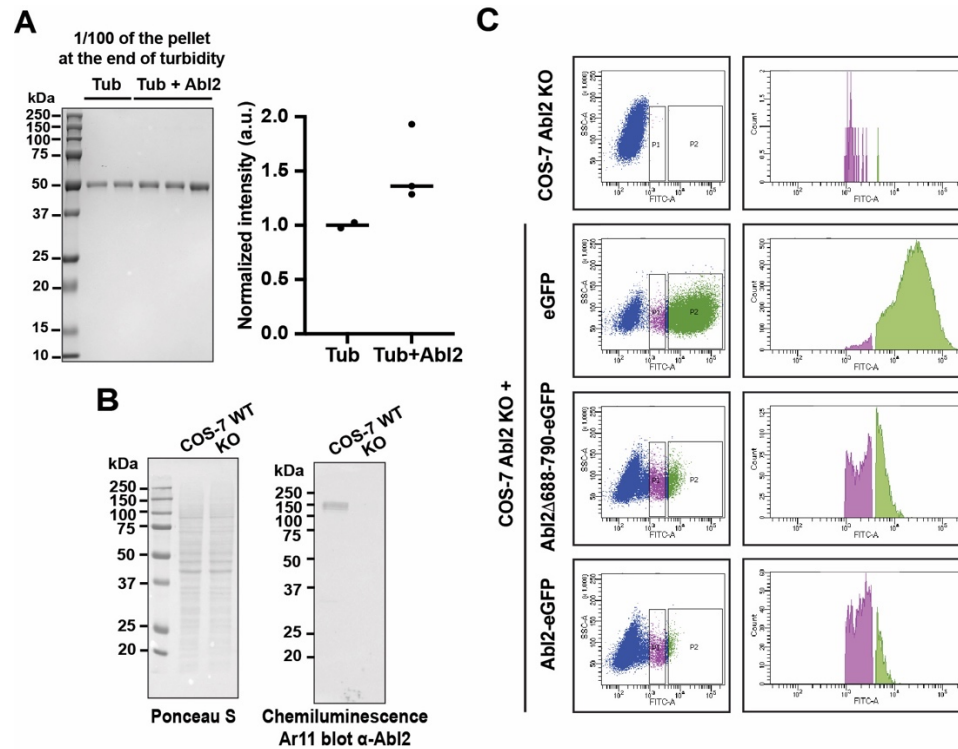


Figure 2.22. Validation of *in vitro* turbidity reactions and FACS sorting of COS-7 cell lines for cellular MT reassembly assays. (A) At the termination of turbidity assays shown in **Figure 2.19, A**, reactions were subjected to ultracentrifugation. 1/100 of the resuspended volume was retrieved from the reactions to visualize the amount of pelleted MTs in reactions alone or with Abl2. Intensities of bands corresponding to tubulin was quantified, shown on right. **(B)** WT and Abl2 KO COS-7 cells were lysed and 30 μ g of the lysates were loaded for SDS-PAGE and Western blot analysis. Ponceau S staining showing the total protein loaded in each lane (left). Immunoblot for Abl2 using the monoclonal antibody Ar11 (right). **(C)** Fluorescence-activated cell sorting (FACS) of COS-7 Abl2 KO and Abl2 KO cells stably expressing eGFP, Abl2 Δ 688-790-eGFP, and Abl2-eGFP. Gating was conducted by assigning the dim population (P1 shown in purple, lower end gate) using negative control Abl2 KO cells, and the bright population (P2 shown in green, higher end gate) using positive control eGFP-expressing Abl2 KO cells. FACS was used to isolate COS-7 cells that stably express eGFP at high levels (P2), and those that express Abl2 Δ 688-790-eGFP and Abl2-eGFP at both low and high levels (P1 and P2, respectively).

To assess whether Abl2 rescued this MT recovery deficit, we generated Abl2 KO cells stably expressing low or high Abl2-eGFP or Abl2 Δ 688-790-eGFP levels (**Figure 2.23**). Cells selected with Zeocin for lentiviral infection yielded consistently higher MT recovery rates over parental cells and thus we used eGFP-expressing Abl2 KO cells as a control group (**Figures 2.23, 2.25**).

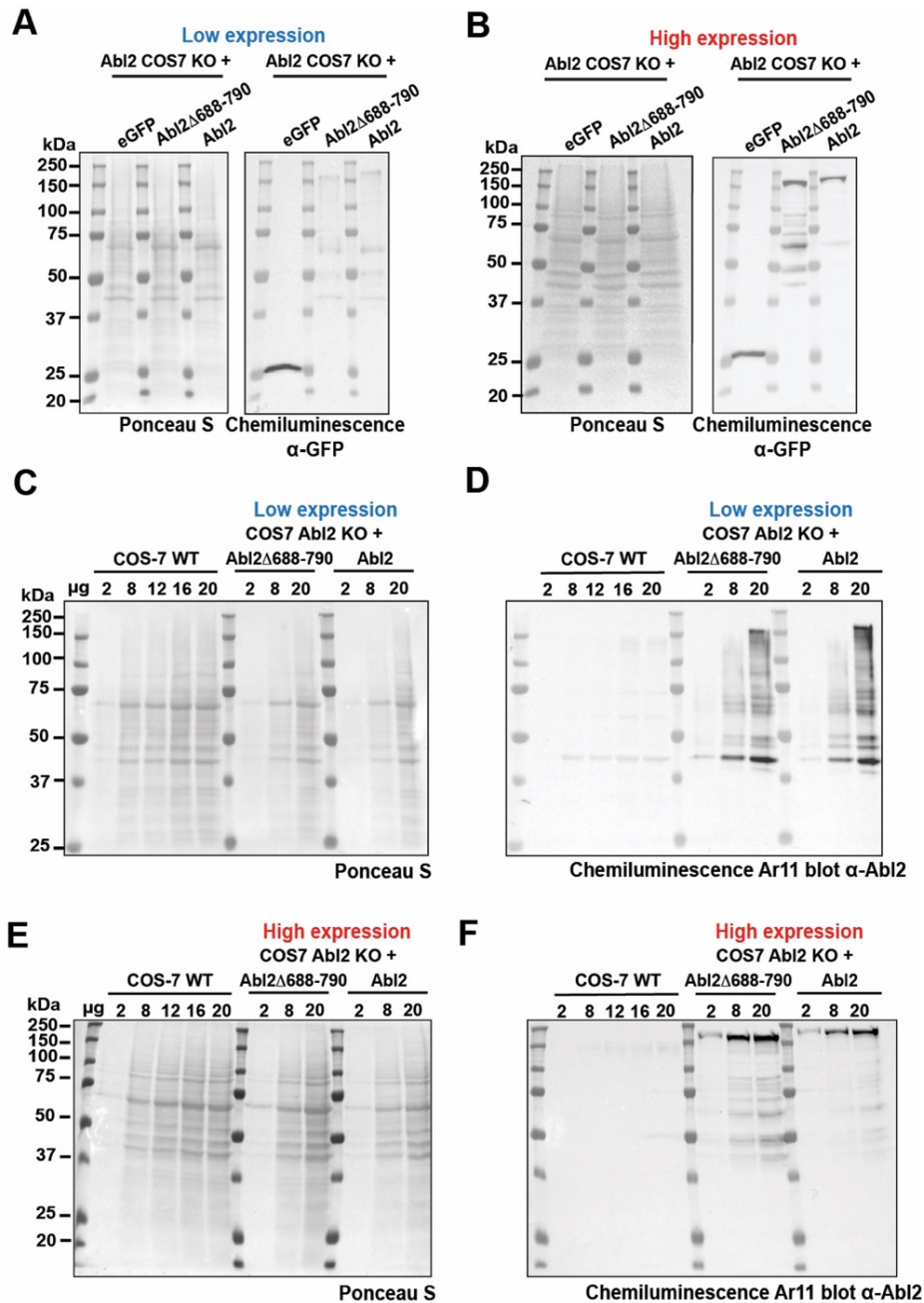


Figure 2.23. Verification and quantification of protein levels in low- and high-expressing Abl2Δ688-790-eGFP and Abl2 COS-7 stable cell lines. (A) 20 μg of Abl2 KO cell lysates that stably expressed eGFP, and low levels (P1, purple) of Abl2Δ688-790-eGFP and Abl2-eGFP were loaded for Western blot analysis. Ponceau S staining showing total protein loaded in each lane (left). Immunoblot for GFP using monoclonal GFP antibody (right). (B) Same as A, except with P2 (green) populations that strongly expressed Abl2Δ688-790-eGFP and Abl2-eGFP in Abl2 KO cells. (C) 2-20 μg of WT and Abl2 KO cell lysates that stably expressed low levels (P1, purple) of Abl2Δ688-790-eGFP and Abl2-eGFP were loaded for Western blot analysis. Ponceau S staining showing total protein loaded in each lane. Immunoblot for Abl2 using Ar11 (D). (E) Same as C-D, except with P2 (green) populations that strongly expressed Abl2Δ688-790-eGFP and Abl2-eGFP in Abl2 KO cells. Immunoblot for Abl2 using Ar11 (F).

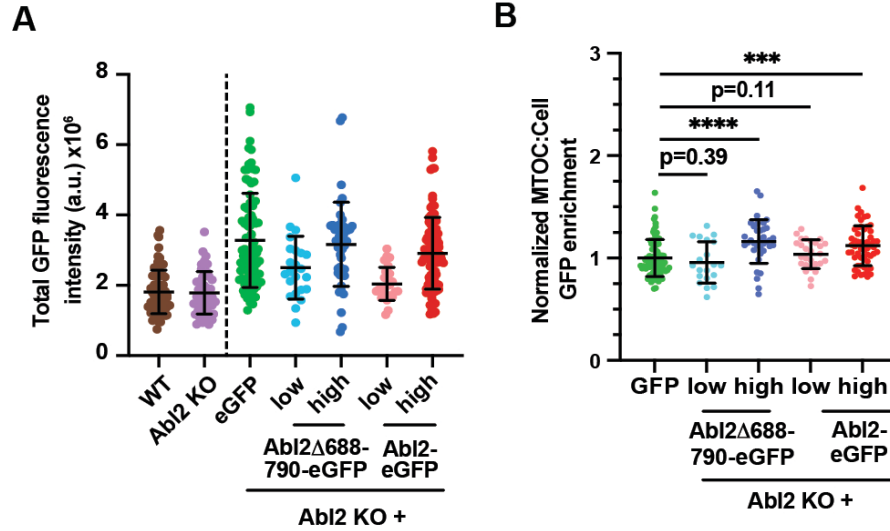


Figure 2.24. Quantification of GFP expression levels in Abl2- and Abl2 Δ 688-790-eGFP re-expressing cell lines. Total (A) and normalized relative MTOC:cell (B) GFP fluorescence intensities of cells analyzed shown in Figure X. Fluorescence values were recorded using “Sum Slices” projection type in FIJI. ***, $p < 0.001$; ****, $p < 0.0001$.

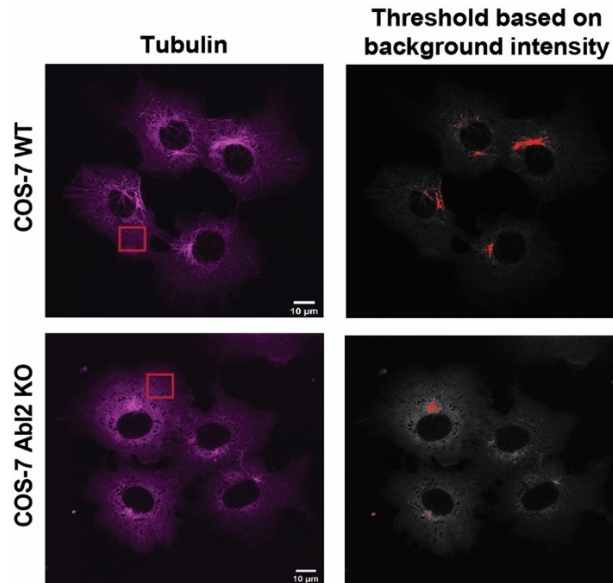


Figure 2.25. Methodology for quantification of MT reassembly. Representative images of FIJI analysis of MT recovery in cells are shown. A region of interest (ROI) was chosen in the cell body where no MT segments were observed, as shown by the red box (left). Images were thresholded using 3X the background ROI intensity to pick up the saturated intensity that reflects recovered MTs, as shown by the red pixels (right). The area of the red pixels was measured for each cell.

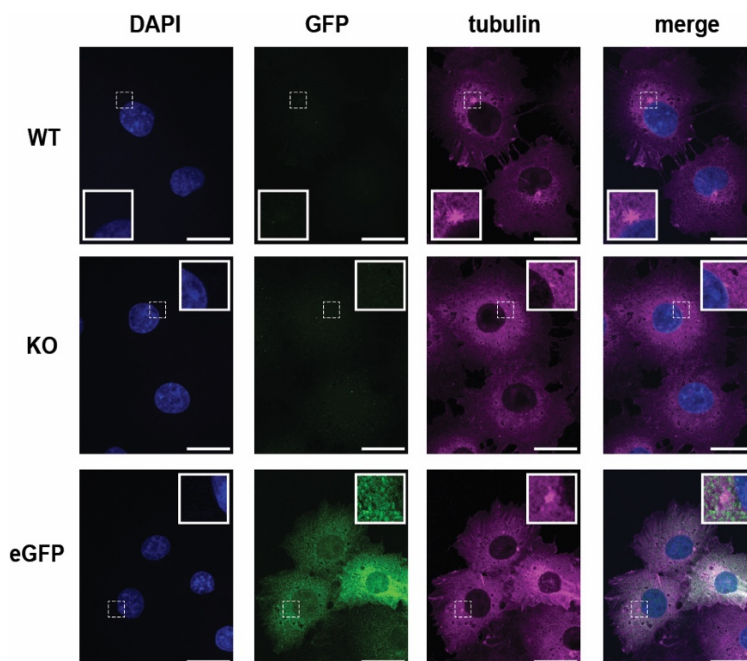


Figure 2.26. WT COS-7, Abl2 KO COS-7, and eGFP-expressing Abl2 KO cells were treated with 10 μM nocodazole for 1 hr, at which time nocodazole was removed and replaced with complete medium. Immunofluorescence images of cells upon 5 min after washout for quantification of MT reassembly from the microtubule organizing center (white dashed inlets with expanded views in solid white borders) shown. Scale bar, 25 μm .

Expression of Abl2-eGFP at low and high levels significantly increased MT recovery by 1.7- and 1.9-fold respectively ($\text{MTR}_{\text{low Abl2-eGFP}} = 6.72 \pm 4.98 \text{ a.u.} \cdot \mu\text{m}^{-2} \cdot 10^{-4}$; $\text{MTR}_{\text{high Abl2-eGFP}} = 7.51 \pm 6.50 \text{ a.u.} \cdot \mu\text{m}^{-2} \cdot 10^{-4}$, $p < 0.05$, $p < 0.0001$ respectively; **Figure 2.28**) over controls ($\text{MTR}_{\text{eGFP}} = 4.02 \pm 4.37 \text{ a.u.} \cdot \mu\text{m}^{-2} \cdot 10^{-4}$). In contrast, even though Abl2 Δ 688-790-eGFP and Abl2-eGFP were both similarly enriched at MTOCs in both low- and high-expressing cells (**Figure 2.24, B**), tubulin binding-deficient Abl2 Δ 688-790-eGFP did not promote increased MT recovery at either expression level ($\text{MTR}_{\text{low Abl2}\Delta$ 688-790-eGFP} = $3.71 \pm 3.40 \text{ a.u.} \cdot \mu\text{m}^{-2} \cdot 10^{-4}$; $\text{MTR}_{\text{high Abl2}\Delta$ 688-790-eGFP} = $3.12 \pm 2.98 \text{ a.u.} \cdot \mu\text{m}^{-2} \cdot 10^{-4}$; **Figure 2.24, A; 2.28**). Together, these data suggest that Abl2 promotes nucleation by binding and recruiting cytoplasmic tubulin and that this correlates with faster MT recovery in cells.

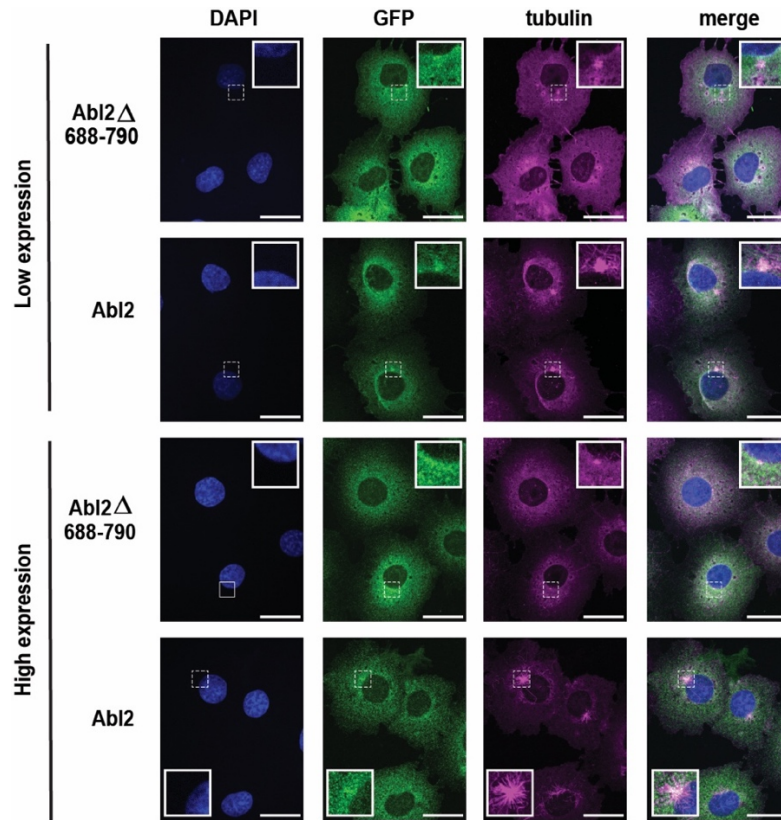


Figure 2.27. Re-expression of Abl2-eGFP, not Abl2 Δ 688-790-eGFP, promotes MT reassembly. High Abl2 Δ 688-790- and Abl2-eGFP-re-expressing Abl2 KO cells were treated with 10 μ M nocodazole for 1 hr, at which time nocodazole was removed and replaced with complete medium. Immunofluorescence images of cells upon 5 min after washout for quantification of MT reassembly from the microtubule organizing center (white dashed inlets with expanded views in solid white borders) shown. Scale bar, 25 μ m.

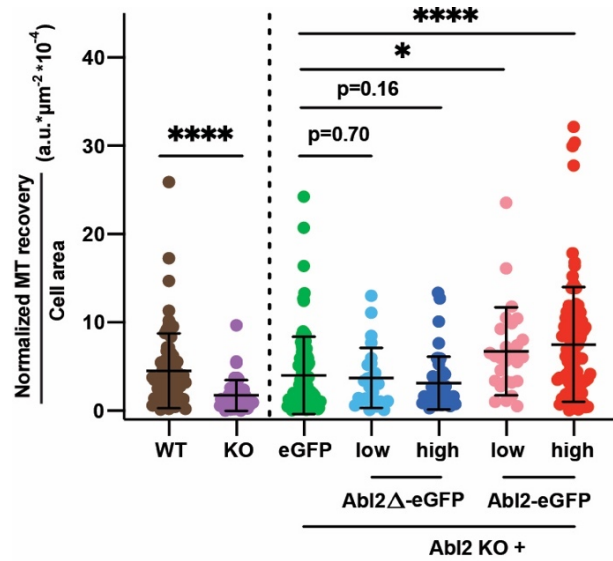


Figure 2.28. Quantification of MT-reassembly upon nocodazole washout. The integrated fluorescence intensity of recovered MTs was measured and normalized to the total cell area. MT recovery values for each condition was normalized to the average MT recovery of WT cells per experimental replicate. Welch's t-test. $n \geq 25$ cells analyzed across 2-3 experimental replicates. Data are mean \pm SD. *, $p < 0.05$; ****, $p < 0.0001$.

2.4. Abl2 preferentially binds expanded over compacted MT lattices.

MBPs bind distinct MT lattices conformational states with different affinities (Manka & Moores, 2018; Siahaan et al., 2019; Siahaan et al., 2022; Tan et al., 2019). Cryo-EM studies show that the GMPCPP-MT lattice is relatively expanded compared to the GDP-MT lattice (Alushin et al., 2014; Estévez-Gallego et al., 2020). Given that Abl2 promotes nucleation which generates tubulin oligomers or immature MT tubes, we measured the nucleotide state preference (NSP) of Abl2-eGFP and control proteins using MTs of GDP-polymerized tubulin, capped with GTP-like GMPCPP-containing segments to prevent catastrophe. The +TIP tracker EB1-eGFP bound GMPCPP-rich regions preferentially with $NSP_{EB1} = 0.38 \pm 0.37$, where $NSP = \log_{10}(\text{fluorescence intensity on GMPCPP versus GDP segments})$ (Figure 2.29, A) (Zanic et al., 2009), while tau-2N4R-eGFP preferentially bound GDP-rich regions ($NSP_{\text{tau}} = -0.67 \pm 0.26$; Figure 2.29, B, purified EB1-eGFP and tau-eGFP are shown in Figure 2.6, B, viii-ix), as expected (Tan et al., 2019). Abl2-eGFP and its cytoskeletal-binding half 557-C-eGFP strongly preferred GMPCPP-MT segments over GDP-MT segments ($NSP_{\text{Abl2}} = 0.35 \pm 0.33$, $p < 0.0001$ relative to NSP_{tau} ; $NSP_{557-C} = 0.41 \pm 0.28$, $p < 0.0001$ relative to NSP_{tau} , Figure 2.29, B).

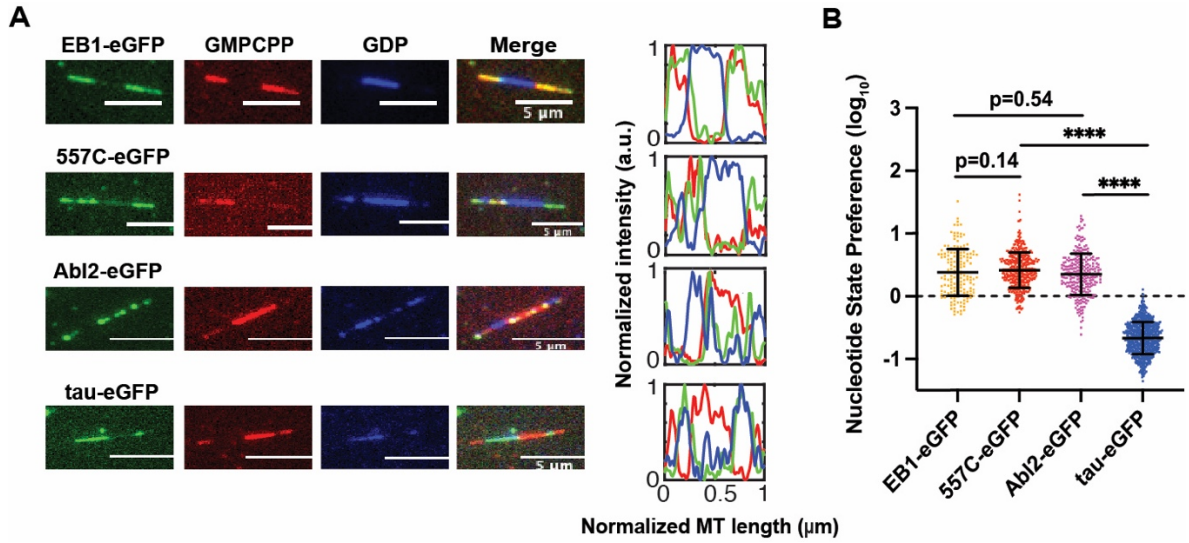


Figure 2.29. Abl2 preferentially localizes onto extended MT lattices. (A) Representative images of 0.8 μM EB1-eGFP, 0.5 μM 557-C-eGFP, 0.5 μM Abl2-eGFP, and 25 nM tau 2N4R-eGFP on segmented end-stabilized MTs. eGFP-tagged MBP shown in green; GMPCPP segments in red; GDP segments in blue. 3 pixel-wide line scans were drawn lengthwise across the microtubule. Normalized lengths and corresponding fluorescence intensities shown on right. **(B)** Nucleotide-state preference (NSP) of EB1-eGFP, tau-eGFP, 557-C-eGFP, and Abl2-eGFP shown in \log_{10} scale. Data are mean \pm SD. Mann-Whitney test. ****, $p < 0.0001$.

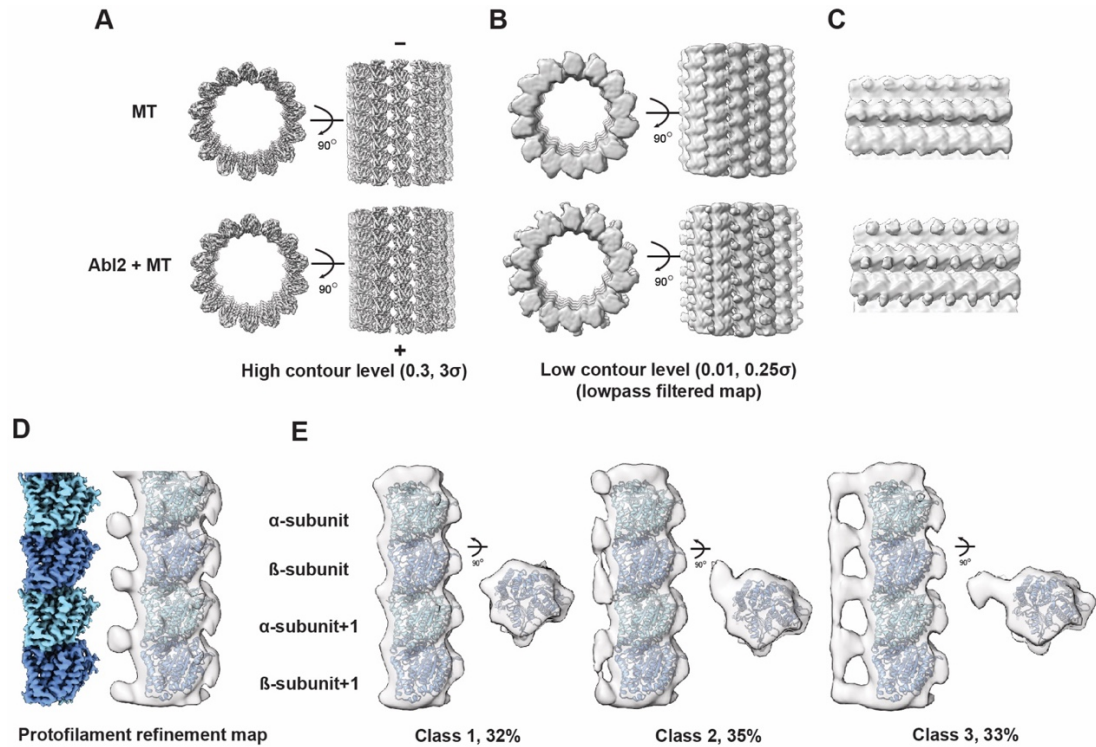


Figure 2.30. AbI2 binds expanded MT lattices through various binding modes. (A, B) Cryo-EM reconstructions of GMPCPP MT lattice alone (top) or with 6XHis-tagged AbI2-557-1090 (bottom) visualized at high (left) and low (right) contour levels. For better comparison of cryo-EM maps at low contour levels, maps were filtered via convolution with a Gaussian filter (one standard deviation of 3 Å). (C) Zoomed-in view of maps shown in (B). (D) Protofilament refinement of the AbI2-MT cryo-EM dataset improves the map resolution and quality. The map after filtering (in transparency) contains extra density around tubulin C-terminal tails. (E) 3D classification reveals that AbI2 bridges multiple tubulins within a protofilament. Class 1 does not show clear extra density near tubulin C-terminal tails. Classes 2 and 3 show clear densities near tubulin C-terminal tails. The densities in class 2 show inter-dimer connectivity while the densities in class 3 show both inter- and intra-dimer connectivity.

We performed cryo-EM analysis of MTs alone or incubated with 6XHis-tagged AbI2 C-terminal fragment (His-AbI2-557-1090) to understand the structural basis for AbI2 interactions with the MT lattice (Figure 2.31, A; Table 1). AbI2-557-1090-eGFP binding to MTs was documented via TIRF microscopy (Figure 2.8, D). Only a portion of the tubulin C-terminal tail was observed via low-pass filtering the cryo-EM map and by setting it at low contour levels, likely due to its high flexibility (Debs et al., 2020; Zhang et al., 2015) (Figure 2.30, B, C). We observed extra density near the tubulin C-terminal tail on the MT lattice decorated with AbI2-557-1090 (Figure 2.30, C, D).

Description	MT only MT reconstruction	AbI2+MT MT reconstruction	AbI2+MT Protofilament reconstruction	AbI2+MT Protofilament reconstruction Class 1	AbI2+MT Protofilament reconstruction Class 2	AbI2+MT Protofilament reconstruction Class 3
EMDB	EMD-41167	EMD-41169	EMD-41170	EMD-41173	EMD-41176	EMD-41177
Microscope	Glacios	Glacios	Glacios	Glacios	Glacios	Glacios
Voltage (kV)	200	200	200	200	200	200
Camera	K2	K2	K2	K2	K2	K2
Magnification	36,000	36,000	36,000	36,000	36,000	36,000
Pixel Size (Å)	1.149	1.149	1.149	1.149	1.149	1.149
Final Pixel Size (Å)	1.628	1.628	1.628	1.628	1.628	1.628
Total Electron Exposure (e-/Å ²)	40	40	40	40	40	40
Defocus Range (µm)	1.5-2.7	1.5-2.7	1.5-2.7	1.5-2.7	1.5-2.7	1.5-2.7
Symmetry Imposed	C1	C1	C1	C1	C1	C1
Final Particles	24 485	84 826	1 187 564	376 640	417 865	393 059
Map pixel size	1.62	1.62	1.62	1.62	1.62	1.62
Map Resolution (FSC 0.143)	4.1	3.9	3.6	3.6	3.6	3.6

Table 1. Cryo-EM data collection, refinement, and validation statistics.

AbI2 binds MTs via both electrostatic interactions with the tubulin acidic C-terminal tails and via additional interfaces (Hu et al., 2019) (**Figure 2.32**). To identify all possible interfaces and capture stable complexes for atomic model building, we used a protofilament refinement method (Debs et al., 2020) to merge different protofilaments into one single protofilament volume, greatly improving EM map resolution and quality (**Figure 2.30, D**). Due to tubulin tail flexibility and non-uniform AbI2-557-1090 decoration, no additional density was observed at high contour levels (**Figure 2.30, B**). However, we created a mask covering four tubulin monomers and their surfaces and performed a focused 3D classification (**Figure 2.31, B**).

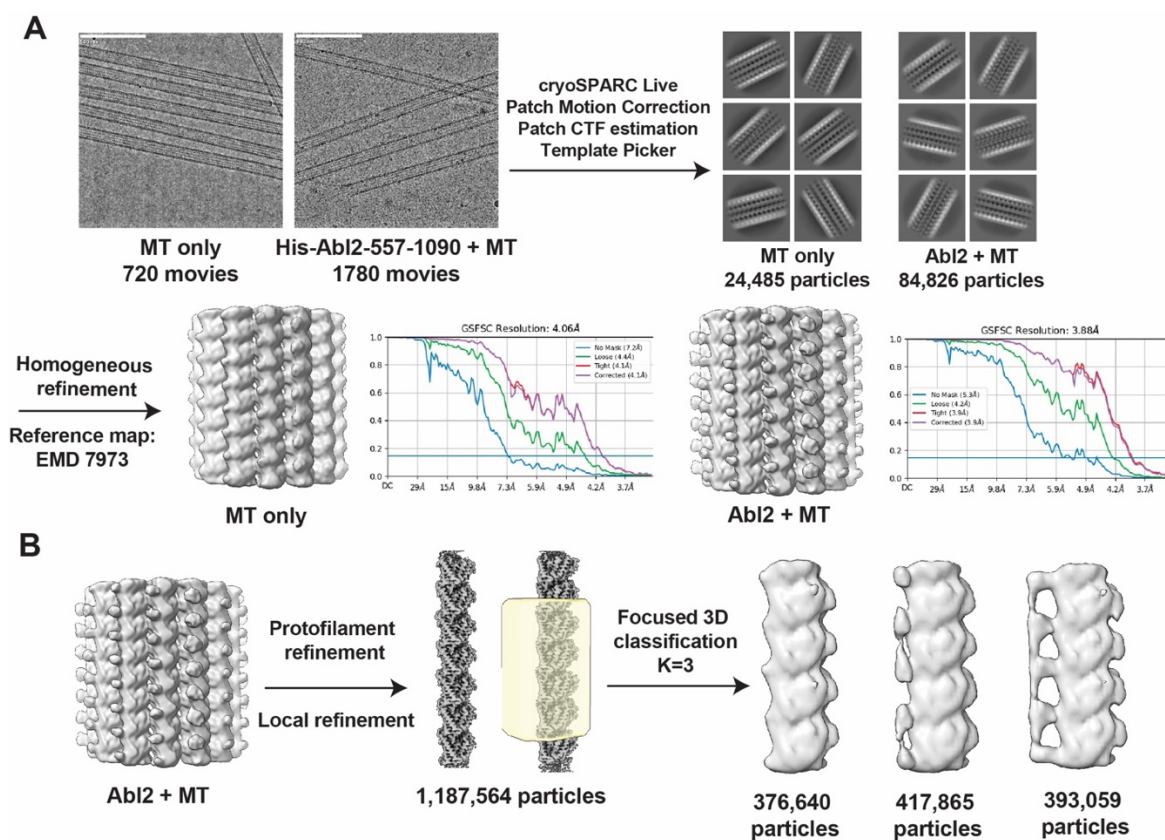


Figure 2.31. Cryo-EM data processing. Flowchart of image processing of MTs alone or with 6XHis-tagged Abl2-557-1090. **(B)** Protofilament refinement and focused 3D classification results of Abl2-MT dataset.

Even after extensive 3D classification, complexes between the Abl2-557-1090 and the protofilament stable enough to enable high-resolution reconstructions were not observed, suggesting that Abl2-557-1090 interacts with the MT lattice in a flexible manner. We did observe, however, three classes with different binding patterns of Abl2-557-1090 (**Figure 2.30, E**). The first class (32%) did not have extra density around tubulin C-terminal tails, suggesting no Abl2-557-1090 binding in this class. In the second class (35%), a connection of extra density was observed between the tubulin β -subunit and the tubulin α -subunit+1 of the adjacent tubulin dimer in the protofilament. In the third class (33%), the extra density was further connected along protofilaments. Together, the cryo-EM analysis suggests that Abl2-557-1090 flexibly and non-uniformly decorates the MT lattice to bridge multiple dimers within a protofilament.

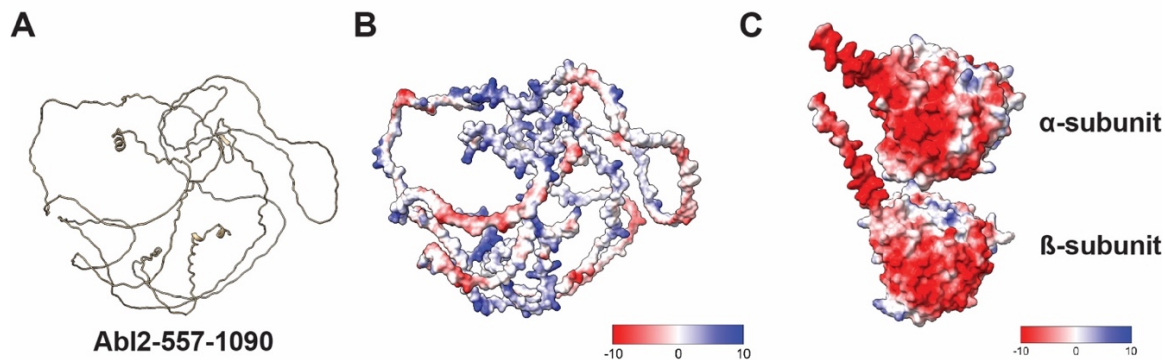


Figure 2.32. Predicted structure of Abl2-557-1090. (A) Alphafold2 prediction of Abl2-557-1090 fragment shows the structure is highly disordered. (B-C) The electrostatic potential surfaces of the predicted structure of Abl2-557-1090 (B) and of tubulin subunits (C). Note that Abl2-557-1090 contains positively or negatively charged fragments while tubulin C-terminal tails are negatively charged.

Future directions include using solid-state NMR (ssNMR) to resolve Abl2:MT structures, and/or cryo-EM if a MT-binding protein that interacts with Abl2 is also discovered. As the C-terminal half of Abl2 is highly disordered and likely floppy in solution, it is worth testing whether binding to a bona-fide MBP at the C-terminal half stabilizes a conformation of a MT-bound complex, making cryo-EM a more feasible experimental technique (see Chapter 5 for the Abl2 interactome). Recent studies have also shown that while X-ray crystallography and cryo-EM have provided detailed information on MBP:MT interactions, very little is known regarding dynamic interactions between the intrinsically disordered regions of MAPs and the MT surface. Luo *et al.* demonstrated that ssNMR is a powerful tool for providing structural insights into dynamic systems at the atomic resolution, specifically dynamics of intact MTs in absence and presence of MBPs. These authors show the C-terminus of the CAMSAP2 CKK domain adopts conformational variability on MTs and dynamically interacts with both C-terminal tubulin tails, while the N-terminus of CKK domain quickly interacts with the C-terminus of β -tubulin (Luo *et al.*, 2020). They also used ssNMR to reveal that for another MBP, MAP7, binding on MTs reduces tail dynamics, contrasting with the fast dynamics observed in the case for CAMSAP-CKK. Previous work by members of the Koleske Lab show that Abl2 has reduced affinity for MTs upon subtilisin treatment, suggesting that the C-terminal tails are essential for Abl2 binding on MTs. A more recent study by Guo and others revealed that using magic-angle spinning NMR, the minimally active domain of TPX2 (TPX2 ^{α 5- α 7}), a key factor in cell

division that stimulates branching MT nucleation, is disordered in solution but adopts a folded structure on the MT (Guo et al., 2023). TPX2 ^{α 5- α 7} can also form a co-condensate with soluble tubulin dimers on MTs, and this binding interaction stabilizes MTs at the intersection of four tubulin heterodimers (analogous to the binding mode of EB proteins). It will be interesting to also determine whether particular aromatic and polar residues within the C-terminal half of Abl2 also promote the formation of a dense core that explains the underlying MT:tubulin co-condensation behavior. As Guo and others conclude that TPX2 likely interacts with MTs under the “stickers and spacers” model, it is likely Abl2:MT binding also follows the same model, which states that aromatic residues serve as ‘stickers’ for phase separation and governs the disordered ‘spacing’ all along the polymer.

2.5. Abl2 mediates repair in damaged MT lattices

Given that Abl2:tubulin coacervates interact with the expanded MT lattice, we next asked if Abl2 impacts damaged MT lattice repair. MT lattice defects were induced by incubating rhodamine-labeled MTs overnight with taxol at 23°C and 37°C (Reid et al., 2017), and visualized as regions of reduced rhodamine intensity along the MT (**Figure 2.34, A**). Visualization by negative stain EM confirmed that taxol-stabilized MTs stored at 23°C overnight had more defects (**Figure 2.33, A**) than those stored at 37°C (**Figure 2.33, B**).

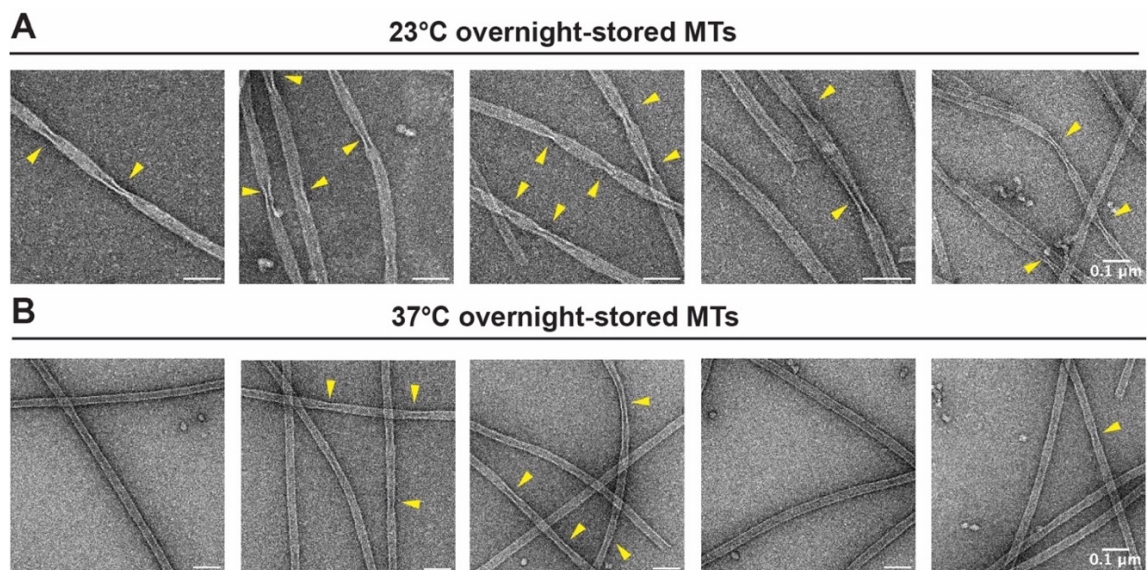


Figure 2.33. Microtubules stored at room temperature overnight harbor more structural defects. Representative negative stain EM images of 23°C overnight-stored (A) or 37°C overnight-stored taxol-stabilized MTs (B). Yellow arrows denote segments along the lattice that are structurally compromised. Majority of lattices stored at 37°C have higher structural integrity than those stored at 23°C overnight (O/N).

We monitored repair via the incorporation of new Alexa647-tubulin at damaged sites, tracking both the number of incorporation events and the fraction of total MT length labeled with new Alexa647-tubulin, termed the reporter fraction (RF). In agreement with previous reports of greater damage to the MTs stored at 23°C versus 37°C (Reid et al., 2017; Reid et al., 2019), we observed a higher RF in MT shafts stored at 23°C overnight relative to those stored at 37°C overnight ($RF_{23^{\circ}\text{C},\text{tub}} = 0.17 \pm 0.13$; $RF_{37^{\circ}\text{C},\text{tub}} = 0.12 \pm 0.10$; **Figure 2.35, B**). Though Abl2-eGFP binds uniformly on fresh taxol-stabilized MTs (**Figure 2.37, C**), Abl2-eGFP bound at 1.3-fold higher density to the more damaged 23°C-stored MTs than 37°C-stored MTs, with mean normalized fluorescence intensities of $1.02 \pm 0.03 \text{ a.u.} \cdot \mu\text{m}^{-1}$ and $0.82 \pm 0.03 \text{ a.u.} \cdot \mu\text{m}^{-1}$, respectively (**Figure 2.37, B**).

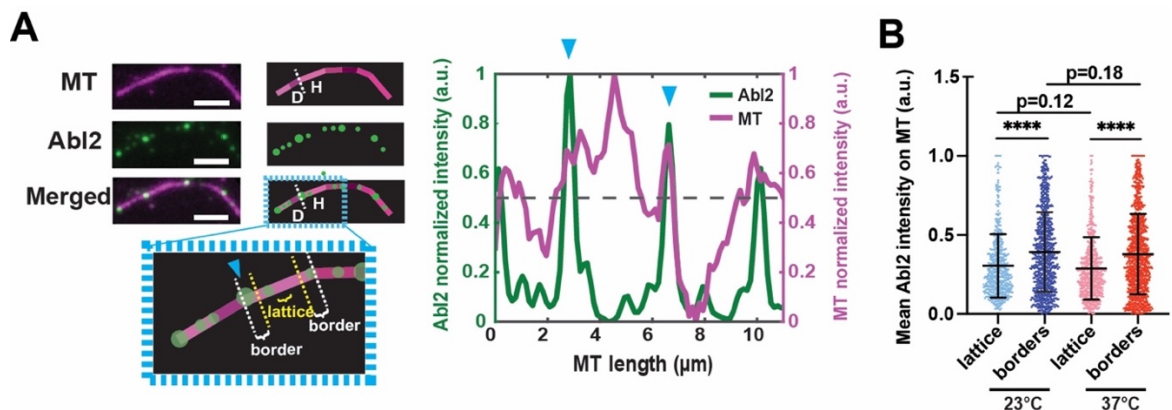


Figure 2.34. Abl2 binds adjacent to sites of MT lattice damage. (A) Left: Representative Abl2-eGFP localization on a 37°C-overnight stored taxol-stabilized MT. Borders were defined as boundaries on ‘healthy’ (“H”) structurally intact MT segments adjacent to ‘damaged’ (“D”) segments, demarcated with a blue arrow. Lattices were stretches that are $\geq 1/5$ of the total MT segment length away from either terminus. Scale bar, 3 μm . Right: Quantification of MT and Abl2-eGFP intensities along the taxol-stabilized MT shown on left. Dotted black line denotes the mean normalized MT fluorescence intensity, which was used as the threshold for scoring a segment as “H” or “D”. Normalized fluorescence intensity scale bar shown on left. (B) Mean intensities of 1 μM Abl2-eGFP at borders and lattices of healthy MT segments along filaments stored at 23°C and 37°C overnight. Means shown as solid horizontal black lines, 25-75% quartiles shown as box plots. $n \geq 600$ healthy segments analyzed per condition. Wilcoxon rank sum test. ****, $p < 0.0001$.

Abl2-eGFP did not uniformly decorate the damaged MTs. To measure whether Abl2 has preference for healthy versus damaged regions, we made line scans of MTs and defined segments of mean normalized fluorescence intensities equal to or above 0.5 as 'healthy' and those below as 'damaged'. This threshold was used across experimental replicates as it best differentiated higher versus lower fluorescent intensities throughout a given MT. 'Borders' were defined as segments directly adjacent to damaged ones, with lengths one-fifth of the total healthy segment length away from damaged sites and 'lattices' defined as the remaining three-fifths middle portion of the healthy segment (Figure 2.34, A). Abl2-eGFP bound preferentially to borders, with mean intensities of 0.39 ± 0.01 a.u. and 0.38 ± 0.01 a.u. on 23°C- and 37°C-stored MT damaged borders, respectively; and mean intensities of 0.31 ± 0.01 a.u. and 0.28 ± 0.01 a.u. on 23°C- and 37°C-stored MT lattices, respectively (mean \pm SEM, Figure 2.34, B).

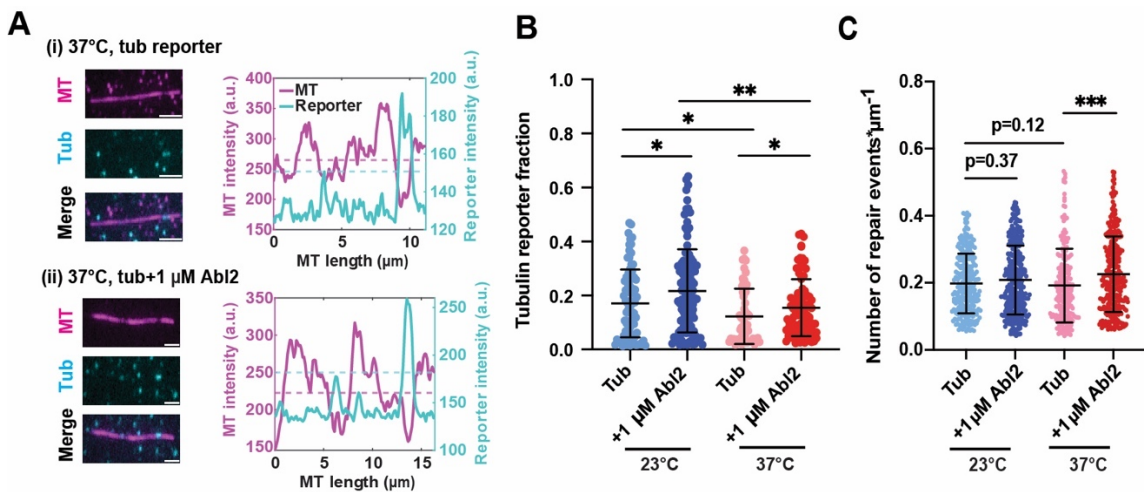


Figure 2.35. Abl2 promotes incorporation of fresh tubulin dimers into damaged lattices. (A) Representative taxol-stabilized rhodamine-MTs stored at 37°C overnight (magenta) and repaired tubulin reporter (cyan). MT mixture was supplemented with 2 μM Alexa647-tubulin (cyan), 10 mM GTP, and 10 μM taxol were allowed to incorporate at damaged sites for 3 hr at 37°C alone (i) or with (ii) 1 μM Abl2-eGFP. Fluorescence intensities of MT and 647-tubulin were plotted. Dashed magenta line denotes the MT intensity threshold (mean normalized fluorescence intensity) to distinguish healthy from damaged segments. Dashed cyan line denotes the reporter intensity threshold to score whether 647-tubulin reporter is present or not. Scale bar, 3 μm . **(B)** Total tubulin reporter fraction per MT was quantified per storage condition in the presence or absence of 1 μM Abl2-eGFP. Data are mean \pm SEM. $n \geq 50$ filaments analyzed per condition. Wilcoxon rank sum test. *, $p < 0.05$. **(C)** Total number of repair/incorporation events per MT was quantified per storage condition in the presence or absence of 1 μM Abl2-eGFP. $n \geq 200$ incorporation events analyzed per condition. Data are mean \pm SEM. Wilcoxon rank sum test performed. *, $p < 0.05$; n.s., no

To measure if Abl2-eGFP impacted tubulin incorporation at damage sites, we incubated 23°C- and 37°C-stored damaged MTs with and without 1 μM Abl2-eGFP (**Figure 2.35, A-C**; representative EM micrographs for tubulin bound 23°C-stored MTs in **Figure 2.36**). Including Abl2-eGFP increased the fraction of total MTs containing Alexa647-tubulin 1.27- and 1.26-fold to $\text{RF}_{23^\circ\text{C}, +\text{Abl2}} = 0.22 \pm 0.15$ and $\text{RF}_{37^\circ\text{C}, +\text{Abl2}} = 0.15 \pm 0.11$, respectively (**Figure 2.35, B**). Abl2-eGFP also increased the frequency of new tubulin incorporation segments into existing shafts in the 37°C storage condition 1.21-fold, from $f_{\text{incorp, tub, } 37^\circ\text{C}} = 0.19 \pm 0.11 \text{ events} \cdot \mu\text{m}^{-1}$ of MT length to $f_{\text{incorp, +Abl2, } 37^\circ\text{C}} = 0.23 \pm 0.11 \text{ events} \cdot \mu\text{m}^{-1}$ in ($p < 0.001$; **Figures 2.35, C; 2.38, A**).

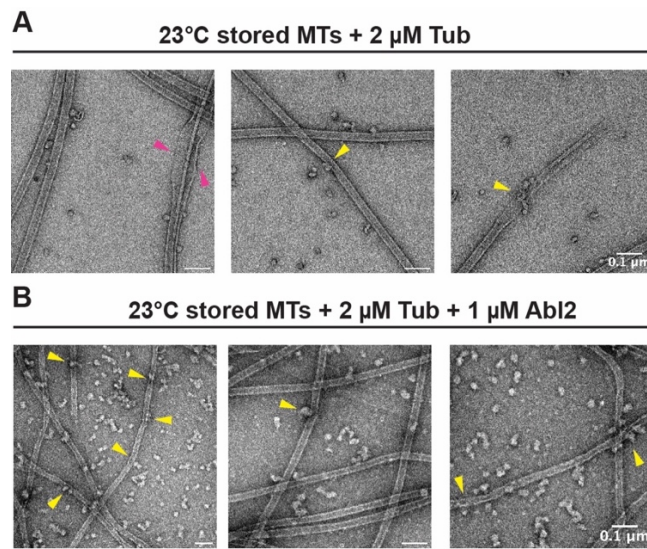


Figure 2.36. Representative negative stain EM images of 23°C-O/N stored MTs in presence of 2 μM tubulin (**A**) and in presence of 2 μM tubulin and 1 μM Abl2 (**B**) after a 3 hr incubation at 37°C. Yellow arrows denote segments along the lattices bound with tubulin dimers and/or tubulin dimers in complex with Abl2. Magenta arrows denote damaged lattice segments that do not have tubulin

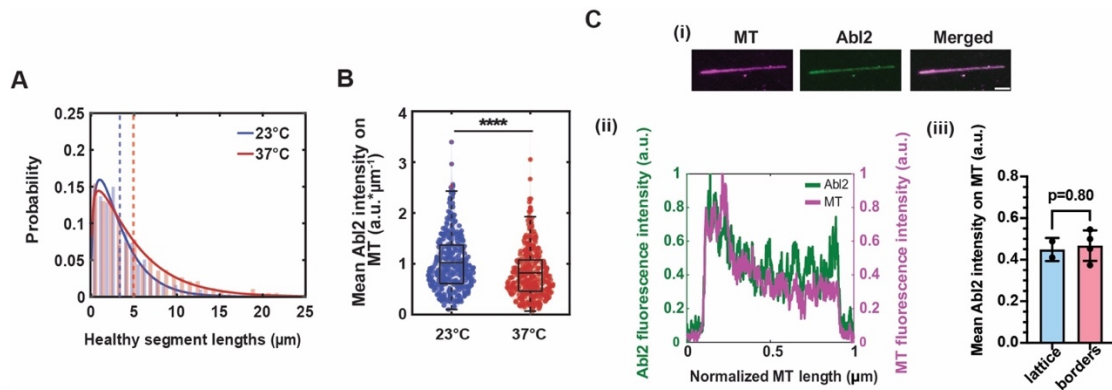


Figure 2.37. Abl2 preferentially localizes to more damaged lattices. (A) Distribution of healthy segment lengths of MTs stored at 23°C and 37°C O/N. Consistent with previous studies, structurally intact segments of longer lengths were observed from MTs stored at 37°C O/N. 37°C storage allows for residual tubulin to repair MT shafts whereas 23°C inhibits. Means of fitted gamma distributions shown as dashed lines (mean lengths of 3.34 μm for 23°C- and 4.92 μm for 37°C-O/N stored MTs). $n \geq 350$ segments per condition. **(B)** Mean global Abl2 fluorescence intensities (normalized intensities relative to MT lengths) on 23°C- and 37°C-stored MTs. Means shown as solid black horizontal lines. 25-75% quartiles shown as box plots. $n \geq 90$ filaments analyzed per condition. **(C) (i)** 0.5 μm Abl2-eGFP on a taxol-stabilized MT that has not undergone O/N treatment. Scale bar, 10 μm . **(ii)** Normalized fluorescence intensities for Abl2-eGFP and taxol-stabilized rhodamine-MT shown in green and magenta, respectively. **(iii)** Quantification of Abl2 localization on lattice versus borders on undamaged taxol-stabilized MT shown in (i).

Although the number of tubulin incorporation events did not change significantly for MTs stored at 23°C upon inclusion of 1 μM Abl2-eGFP ($f_{\text{incorp, tub, 23}^\circ\text{C}} = 0.20 \pm 0.09$ events $\cdot\mu\text{m}^{-1}$ of MT length to $f_{\text{incorp, +Abl2, 23}^\circ\text{C}} = 0.21 \pm 0.10$ events $\cdot\mu\text{m}^{-1}$), the relative length of newly incorporated tubulin (RL) per MT increased 1.34-fold in the presence of Abl2 ($\text{RL}_{\text{tub alone, 23}^\circ\text{C}} = 2.40 \pm 2.04$ μm ; $\text{RL}_{\text{tub+Abl2, 23}^\circ\text{C}} = 3.24 \pm 2.72$ μm) (**Figure 2.38, B**). Together, these data indicate that Abl2-eGFP can promote repair of MT lattice damage.

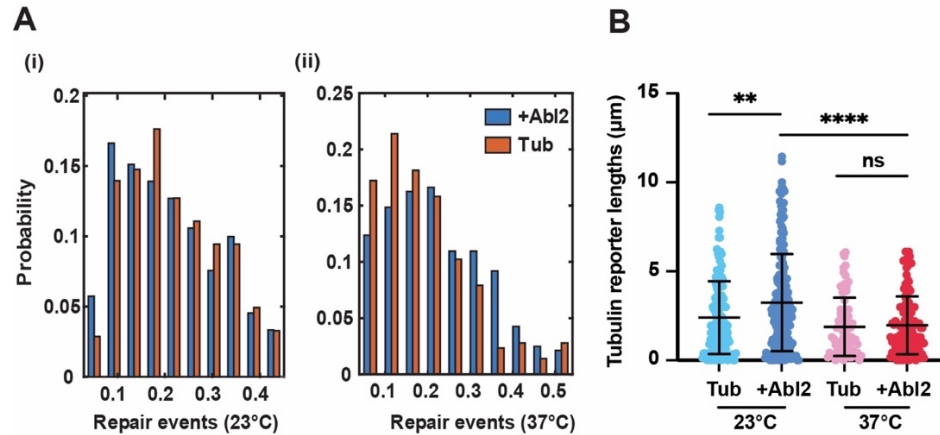


Figure 2.38. AbI2 promotes more complete incorporation of tubulin dimers at stretches of tubulin vacancies. (A) Distributions of incorporation events per μm of 23°C- (i) and 37°C-O/N stored MTs (ii) in the absence and presence of 1 μM AbI2-eGFP. $n \geq 200$ repair events analyzed per condition. **(B)** Tubulin reporter (repair) lengths of 23°C- and 37°C-stored MTs in the absence and presence of 10.5 μM AbI2-eGFP. $n \geq 80$ filaments analyzed per condition.

2.6. AbI2 increases rescue frequency to prolong MT lifetimes

Repair of MT damage leads to the formation of GTP-tubulin enriched islands within MT segments (Dimitrov et al., 2008; Tropini et al., 2012), which promotes rescue (Aumeier et al., 2016; de Forges et al., 2016; Gazzola et al., 2023; Schaedel et al., 2015; Schaedel et al., 2019). We tested how AbI2-eGFP impacts rescue frequency (f_{res}) of MTs elongated from GMPCPP-MT seeds. Consistent with previous work (Hu et al., 2019), AbI2 decreased the MT depolymerization rate 0.6-fold, from $13.49 \mu\text{m} \cdot \text{min}^{-1}$ to $8.49 \mu\text{m} \cdot \text{min}^{-1}$ (Figure 2.39, A). Inclusion of AbI2-eGFP increased rescue frequency in a concentration-dependent manner (Figure 2.39, B), such that inclusion of 0.5 μM AbI2-eGFP induced a 2.4-fold increase in rescue frequency, from $f_{\text{res, tub}} = 0.080 \pm 0.006 \text{ events} \cdot \mu\text{m}^{-1}$ to $f_{\text{res, 0.5 } \mu\text{M AbI2}} = 0.194 \pm 0.014 \text{ events} \cdot \mu\text{m}^{-1}$ (mean \pm SEM). However, 0.5 μM of tubulin-binding 688-924-eGFP fragment decreased rescue frequency relative to control ($f_{\text{res, 0.5 } \mu\text{M 688-924}} = 0.043 \pm 0.001 \text{ events} \cdot \mu\text{m}^{-1}$, $p < 0.0001$), whereas 0.5 μM of MT-binding AbI2 Δ 688-790 did not impact rescue ($f_{\text{res, 0.5 } \mu\text{M AbI2}\Delta$ 688-790} = $0.071 \pm 0.007 \text{ events} \cdot \mu\text{m}^{-1}$; mean \pm SEM).

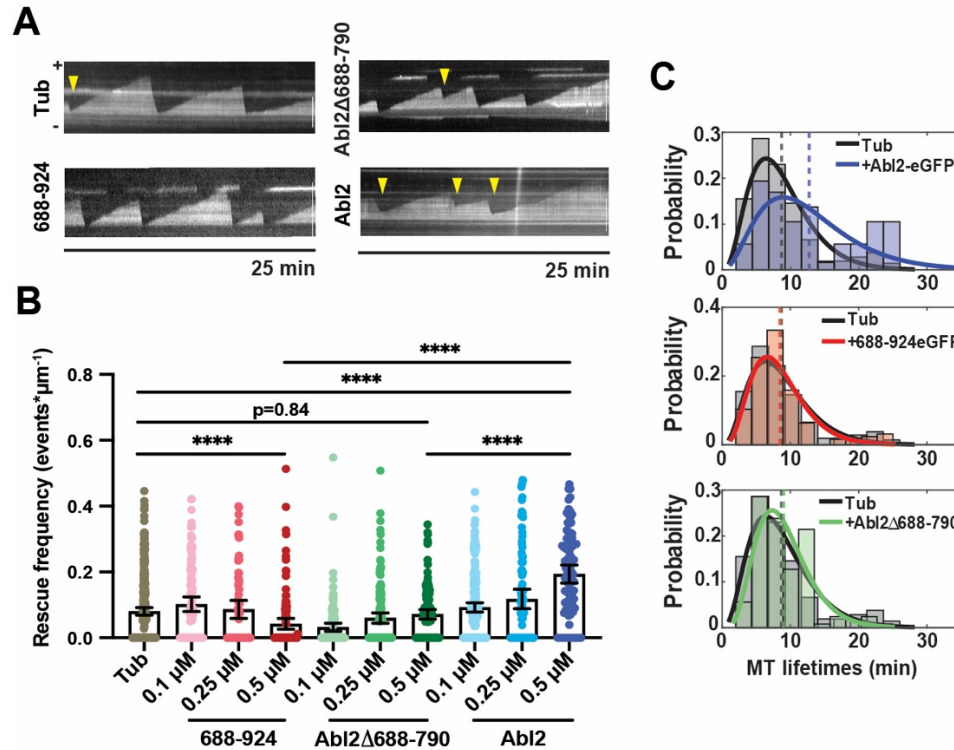


Figure 2.39. Abl2 promotes rescue frequency and increases MT lifetime. (A) Representative kymographs of dynamic MT filaments in presence of 10.5 μM rhodamine tubulin alone, or with 0.5 μM 688-924-eGFP, Abi2 Δ 688-790, or Abi2-eGFP. Scale bar, 8 μm . **(B)** Rescue frequencies (f_{res}) were quantified for 10.5 μM rhodamine tubulin alone, or supplemented with 0.1, 0.25, and 0.5 μM 688-924-eGFP, 0.5 μM Abi2 Δ 688-790, or 0.5 μM Abi2-eGFP. Data are means with 95% CI as black lines. Wilcoxon rank sum test. ****, $p < 0.0001$. **(C)** MT lifetime distributions of filaments grown in presence of 0.5 μM Abi2-eGFP (blue), 0.5 μM 688-924-eGFP (red), and 0.5 μM Abi2 Δ 688-790 (green) relative to tubulin alone (black). Gamma distributions were fit to MT lifetime histograms, shown in solid blue, red, and green curves respectively, relative to tubulin control (solid black). Mean MT lifetimes are denoted as dashed lines.

We speculate that without the ability to bind MT lattices (Abi2-688-924) or tubulin dimers (Abi2 Δ 688-790), Abl2 cannot recruit tubulin dimers to the MT lattice. CLASPs and CSPP1 induce pauses prior to MT rescue (van den Berg et al., 2023), but Abl2 did not impact the pausing frequency prior to growth and shrinkage phases, nor the time spent pausing until either phase (**Figure 2.40, C-E**).

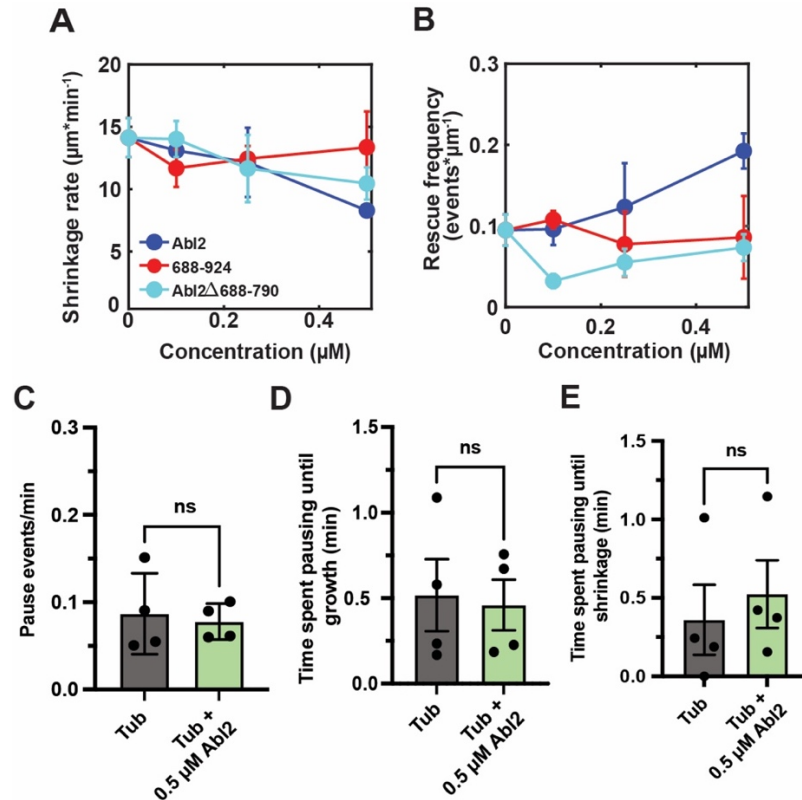


Figure 2.40. Abl2 decreases the shrinkage frequency and promotes rescue frequency without pausing in between events of MT growth and shrinkage. (A) Shrinkage frequency (μm of shrinkage length per min) and (B) rescue frequency (events per μm of shrinkage length) represented as line plots. Consistent with previous findings, Abl2 decreased depolymerization rate of MTs grown from $10.5 \mu\text{M}$ rhodamine tubulin relative to control ($p < 0.0001$, Wilcoxon rank sum test). Whereas the tubulin-binding fragment 688-924-eGFP decreased and tubulin-binding deficient Abl2 Δ 688-790 did not impact rescue frequency relative to tubulin alone ($p < 0.0001$; n.s., respectively), tubulin- and MT-binding Abl2-eGFP increases rescue frequency by 2-fold relative to tubulin alone ($p < 0.0001$). From left to right: $n = 91$ -315 MTs per sample. Means \pm SEM shown as circular markers and error bars, respectively. Frequency of pause events (events/min) prior to a period of growth or shrinkage phase (C), time spent pausing until growth phase (D), and time spent pausing until shrinkage phase (E) of MTs observed under TIRF microscopy in absence or presence of $0.5 \mu\text{M}$ Abl2. $n = 4$ independent experiments per condition ($n \geq 100$ MTs analyzed per condition).

We also measured the net effects of Abl2 and Abl2 fragments on MT lifetime distribution (MTLD). The addition of $0.5 \mu\text{M}$ Abl2 significantly extended the MTLD 1.5-fold to 12.7 ± 7.0 mins from 8.7 ± 4.5 mins for MTs alone. Neither $0.5 \mu\text{M}$ of Abl2-688-924 nor Abl2 Δ 688-790 altered MTLD relative to control (MTLD_{Abl2-688-924} = 8.4 ± 4.0 min; MTLD_{Abl2 Δ 688-790} = 9.0 ± 3.9 min; **Figure 2.39, C**).

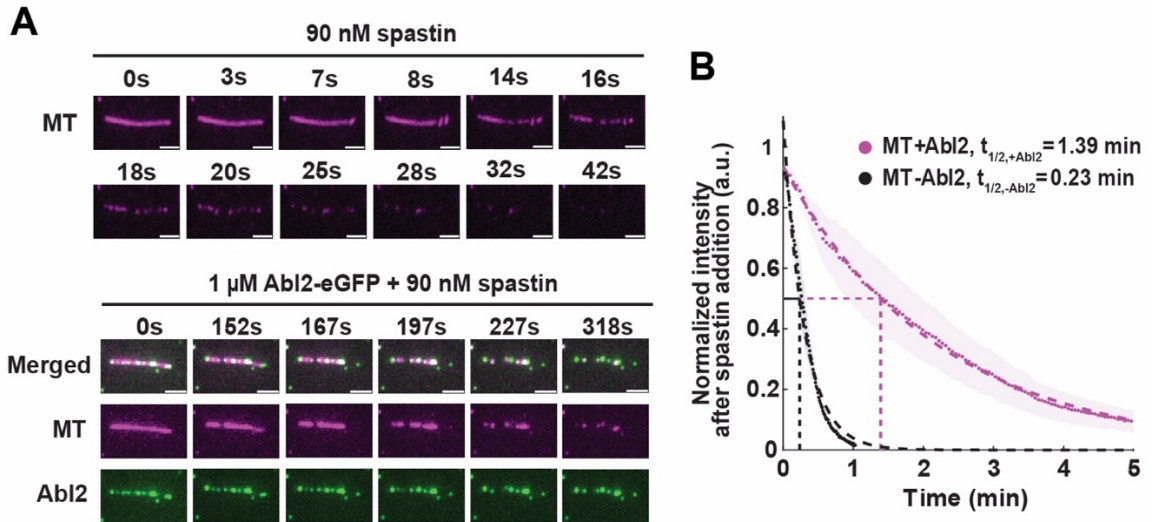


Figure 2.41. Abl2 protects MTs from spastin-mediated severing. (A) Severing assays performed in TIRF chambers containing biotinylated, rhodamine GMPCPP-stabilized MTs (pseudo-colored magenta) with or without 1 μ M Abl2-eGFP supplemented with 90 mM spastin and 2 mM ATP. Representative time series of MTs are shown. Intensity decay curves of severed MTs quantified in (B). Scale bar, 3 μ m. **(B)** Mean intensity decays of MTs in absence (black) and presence of 1 μ M Abl2-eGFP (magenta) shown in scatter dots, and SEMs shown as wider shadowing, respectively. Single exponential decay curves were fit to the data, shown as dashed lines. $n \geq 200$ filaments analyzed per condition.

Considering its ability to maintain MT lattice integrity, we asked whether Abl2 could protect against MT lattice damage mediated by the ATP-dependent MT severing enzyme spastin (**Figure 2.41, A**). Spastin promoted rapid disassembly of MTs with $t_{1/2} = 0.23$ min, while pre-incubation of MTs with 1 μ M Abl2-eGFP greatly slowed the spastin-mediated disassembly rate 6-fold to $t_{1/2, Abl2} = 1.39$ min (**Figure 2.41, B**), suggesting that it protects MT lattices from active damage.

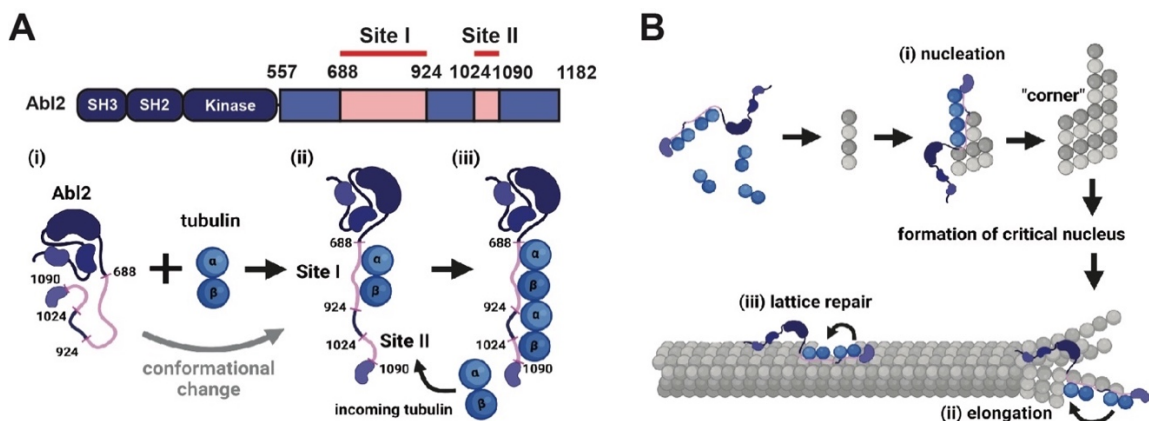


Figure 2.42. Model for Abl2 in regulating MT dynamics. (A) Schematic of full length Abl2 regulating MT growth, nucleation, and lattice repair. **(i)** Abl2 forms a conformational change when it binds a tubulin dimer. **(ii)** Abl2 directly interacts with tubulin dimers using its solvent-exposed 688-924 (site I). The 1024-1090 region (site II) is less accessible in the native conformation. **(iii)** Binding to a single tubulin dimer via site I may induce a conformational change within 557-C, leading to solvent exposure of site II, which can further recruit an additional dimer. **(B)** Abl2 can dock onto: **(i)** tubulin oligomers to facilitate the incorporation of new tubulin dimers for nucleation; **(ii)** on growing MT ends to promote elongation; and **(iii)** on regions along MTs that harbor lattice defects to promote rescue and repair.

Currently, it remains a question how Abl2, with a higher affinity for tubulin dimers, could mediate repair as it needs to localize onto MT lattices. It is likely that through condensation, Abl2 self-associates via oligomerization interfaces (see Section 4.2). As the tubulin binding region resides within aa. 688-924 and the MT-binding region is mapped to aa. 557-1090, it is likely that Abl2 forms coacervates in solution, where some interfaces bind to another Abl2 molecule in trans, or to a tubulin dimer (**Steps 2a, 3, Figure 2.43**). Following coacervation to locally concentrate tubulin dimers, solvent exposed Abl2 may recognize expanded regions within the lattice, *i.e.* sites of structural defects and GTP-tubulin that has not fully incorporated at growing ends, and unload bound tubulin to stabilize inter- and intra- protofilament interactions (**Step 3, Figure 2.43**).

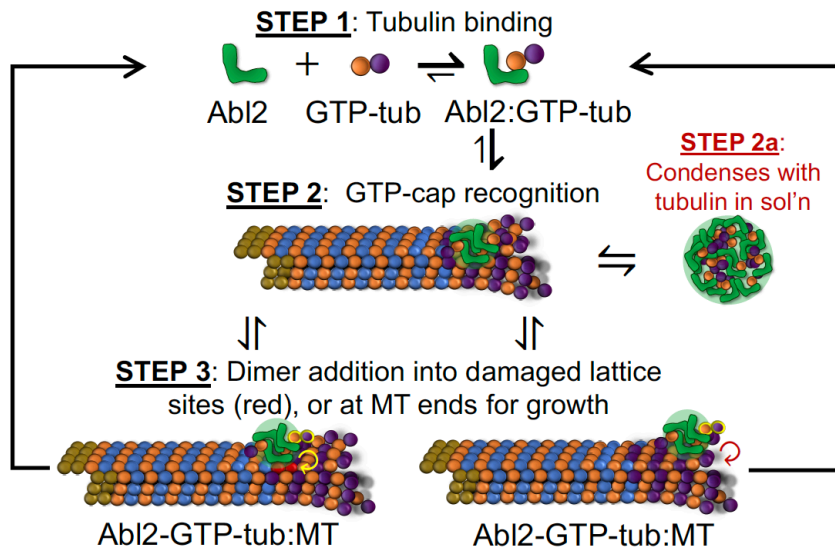


Figure 2.43. Abl2 phase separation model for regulation of lattice repair. Given current findings, it is postulated that Abl2 first recognizes soluble GTP-bound tubulin dimers (**Step 1**). Upon recognition of a specific MT structure within the cell during a specific cellular process (*i.e.* in mitosis for MT assembly at the centrosome or mediating lamellipodial dynamics during cell spreading at the cell periphery), Abl2 localizes at growing ends and/or along sites within the MT lattice that are similarly expanded (*i.e.* sites with tubulin vacancies/structural defects, **Step 2**). It is possible that prior to docking on the MT lattice, Abl2 oligomerizes in the cytosol (**Step 2a**), or self-associates on the MT platform. Lastly, GTP-tubulin bound Abl2 coacervates may incorporate dimers into these sites of lattice damage and/or at growing ends (**Step 3**). It still remains elusive as to how Abl2 phase separated molecules under dissolution. Future studies include identifying whether other interactors compete for tubulin or whether PTMs impact the propensity for Abl2 to oligomerize (*e.g.* perhaps a phosphatase may recognize Abl2 to reduce phosphorylation that otherwise maintains Abl2 in its phase-separated state).

2.7. Materials and Methods

REAGENT or RESOURCE	SOURCE	IDENTIFIER
Antibodies		
Mouse monoclonal anti-Tubulin (clone DM1A)	Sigma-Aldrich	Cat#T9026; RRID: AB_477593
Chicken polyclonal anti-GFP	Novus Biologicals	Cat# NB100-1614-0.02ml
Mouse monoclonal anti-Abl2 (Ar11)	Hybridoma from Dr. Peter Davies, Albert Einstein Medical College, Bronx, NY	N/A
Goat anti-Chicken IgY (H+L) Cross-Adsorbed Secondary Antibody, Alexa Fluor™ Plus 488	Invitrogen	Cat#A32931
Goat anti-Mouse IgG (H+L), Superclonal™ Recombinant Secondary Antibody, Alexa Fluor™ 647	Invitrogen	Cat#A28181
Bacterial and virus strains		
One Shot TOP10 Chemically Competent <i>E. coli</i>	Invitrogen	Cat#C404010
BL21 Competent Cells	Agilent	Cat#200133
DH10Bac Competent Cells	Invitrogen	Cat#10361012
3 rd generation lentivirus produced in 293T cells to express eGFP, Abl2-eGFP, or Abl2 Δ 688-790-eGFP in COS-7 cells	This paper	N/A
Chemicals, peptides, and recombinant proteins		
Paclitaxel	Sigma-Aldrich	Cat#T7191
Guanosine-5'-[(α , β)-methylene]triphosphate, Sodium (GMPCPP)	Jena Bioscience	Cat#NU-405L
Nocodazole	Sigma-Aldrich	Cat#M1404-2mg; CAS: 31430-18-9
Dextran from <i>Leuconostoc spp.</i> Mr ~70,000	Sigma-Aldrich	Cat#31390-25G
Zeocin Selection Reagent	Gibco	Cat#R25005

Deposited data		
cryoEM-map of microtubule only reconstruction	This paper	EMDB: EMD-41167
cryoEM-map of microtubule-Abl2 reconstruction	This paper	EMDB: EMD-41169
cryoEM-map of protofilament reconstruction of Abl2+MT	This paper	EMDB: EMD-41170
cryoEM-map of protofilament reconstruction of Abl2+MT class 1	This paper	EMDB: EMD-41173
cryoEM-map of protofilament reconstruction of Abl2+MT class 2	This paper	EMDB: EMD-41176
cryoEM-map of protofilament reconstruction of Abl2+MT class 3	This paper	EMDB: EMD-41177
Experimental models: Cell lines		
Sf9 insect cells	ATCC	CRL-1711
Hi Five insect cells	Thermo Fisher	B85502
293T cells	ATCC	CRL-3216
COS-7 cells	ATCC	CRL-1651
Abl2 KO COS-7 cells	Hu et al. (Hu et al., 2019)	N/A
Abl2 KO COS-7 cells separately stably expressing eGFP, Abl2-eGFP, and Abl2 Δ 688-790-eGFP	This paper	N/A
Recombinant DNA		
FUGW for lentivirus generation	Lois et al. (Lois et al., 2002)	Addgene#14883; RRID: Addgene_14883
FUGW derived vector to stably express eGFP, Abl2-eGFP, or Abl2 Δ 688-790-eGFP	This paper	N/A
Abl2, Abl2-eGFP, Abl2 fragments, or Abl2 fragments-eGFP cloned into pFastBac1	This paper	N/A
pGEX-6p1-GST-eGFP	This paper	N/A
pRK793 TEV S219V	The laboratory of Dr. Titus Boggon	N/A
pGEX-PP-Spastin(87-616) Δ Exon4	Han et al. (Han et al., 2020)	Addgene#128794; RRID: Addgene_128794
EB1-eGFP	The laboratory of Dr. Jonathon Howard	N/A
FUW-tau 2N4R	The laboratory of Dr. Elizabeth Rhoades	N/A
pHR-HNRNPA1C-mCh-Cry2WT	Shin et al. (Shin et al., 2017)	Addgene #101226; RRID: Addgene_101226
Software and algorithms		
ImageJ/Fiji	Schneider et al.(Schindelin et al., 2012)	https://imagej.nih.gov/ij/
EMBOSS	Madeira et al.(Madeira et al., 2022)	https://www.bioinformatics.nl/cgi-bin/emboss/
PONDR-FIT	Xue et al.(Xue et al., 2010)	https://www.disprot.org/

Diso-Pred3	Jones and Cozzetto et al. (Jones & Cozzetto, 2014)	http://bioinf.cs.ucl.ac.uk/psipred/
Circular Dichroism algorithms (CONTIN, VARSLC, CDSSTR)	Provencher and Glöckner (Provencher & Glöckner, 1981); Compton and Johnson (Compton & Johnson Jr, 1986); Sreerama and Woody (Sreerama & Woody, 2000)	http://dichroweb.cryst.bbk.ac.uk/html/links.shtml
AlphaFold2	Jumper et al. (Jumper et al., 2021)	https://www.deepmind.com/
ChimeraX v1.4	Goddard et al. (Goddard et al., 2018)	https://www.rbvi.ucsf.edu/chimera/
Coot v0.9.5	Brown et al. (Brown et al., 2015)	https://www2.mrc-lmb.cam.ac.uk/personal/pemsley/cool/
cryoSPARC v3.3.2	Punjani et al. (Punjani et al., 2017)	https://cryosparc.com/
Protofilament refinement package	Debs et al. (Debs et al., 2020)	https://gitlab.com/gedeb371/protofilament-refinement/-/tree/smooth_stable
SerialEM v.3.8.5	Schorb et al. (Schorb et al., 2019)	https://bio3d.colorado.edu/SerialEM/
RSEM v1.3.3	Li and Dewey (Li & Dewey, 2011)	https://deweylab.github.io/RSEM/
STAR 2.7.11a	Dobin et al. (Dobin et al., 2013)	https://github.com/alexdobin/STAR
Matlab	The Mathworks, Inc.	https://nl.mathworks.com/products/matlab.html
Nikon Elements Software	Nikon	https://www.microscope.healthcare.nikon.com/products/software/nis-elements
Other		
Superdex 75 Increase 10/300 GL	Cytiva	Cat#29148721
Superdex 200 Increase 10/300 GL	Cytiva	Cat#28990944
Octet® NTA Biosensors	Sartorius	Cat#18-5101
BLItz	ForteBio	https://intellicyt.com/products/fortebio/
Carbon support Film 5-6nm on Square 400 mesh Cu grids	Electron Microscopy Sciences	Cat#CF400-Cu
R2/1, 300 mesh gold, QUANTIFOIL grids	Electron Microscopy Sciences	Cat#258376

Nikon ECLIPSE Ti Series inverted microscope equipped with CFI Apo 100X TIRF 1.49 NA oil objective and Andor Zyla 4.2 sCMOS camera	Nikon, Andor Technology	https://www.microscope.healthcare.nikon.com/products/inverted-microscopes/eclipse-ti-series ; https://www.microscope.healthcare.nikon.com/products/optics/cfi-apochromat-tirf-series
Nikon CSU-W1 SoRa spinning disk confocal microscope	Nikon	https://www.microscope.healthcare.nikon.com/products/confocal-microscopes/csu-series/csu-w1-sora

Table 2.1. Key resources and reagents used for this study.

Cell culture and stable cell line establishment

Mycoplasma-free COS-7 cell lines (ATCC) and the derived stable cell lines were grown in DMEM supplemented with 10% FBS, 100 units*ml⁻¹ penicillin, 100 µg*ml⁻¹ streptomycin, and 2 mM L-glutamine. Abl2 KO COS-7 cells were generated using CRISPR/Cas9, as described previously (Zhang et al., 2018). Resistant Abl2-eGFP, Abl2 Δ 688-790-eGFP, and eGFP were cloned into FUGW vector (Addgene #14883) and then transfected together with pLP1, pLP2, and pLP/VSFG into HEK293T cells to generate lentivirus. Abl2 KO COS-7 cells were infected with the lentivirus and selected with 400 µg*ml⁻¹ Zeocin (Thermo Fisher Scientific) for 7 days.

Abl2-eGFP, Abl2 Δ 688-790-eGFP, and eGFP expressing cells were obtained by fluorescence-activated cell sorting using Abl2 KO COS-7 cells as a negative reference. Cell lysates were collected to determine the expression levels of Abl2 or Abl2 variants via immunoblotting. Cells were lysed with 1x LSB buffer (8% SDS, 20% glycerol, 100 mM Tris pH 6.8, 8% 2-mercaptoethanol) at 100°C. Lysates were run on SDS-PAGE and transferred to 0.45 µm nitrocellulose, blocked using 5% milk and immunoblotted with anti-GFP antibody (Novus Biologicals) or with Ar11 antibody, which specifically recognizes the Abl2 C-terminal half (residues 766-1182; gift from Peter Davies, Albert Einstein Medical College, Bronx, NY).

Tubulin purification and labeling

Porcine brain tubulin was prepared as previously described in Castoldi & Popov (2003) (Castoldi & Popov, 2003). 2 ml 14 mg*ml⁻¹ porcine brain tubulin was labeled with TAMRA as described in Peloquin et al. (2005) (Peloquin et al., 2005). Biotinylated tubulin was obtained from Cytoskeleton.

Molecular cloning and Abl2 purification

Murine Abl2 (residues 74-1182), Abl2-eGFP, N terminal half (N-557), N-557-eGFP, C terminal half (557-C), 557-C-eGFP, and fragments contain amino acids 688-790, 688-924, 688-924-eGFP, 1024-1090 were cloned with an N-terminal 6XHis tag into the pFastBac1 vector (Invitrogen) for insect cell expression. Abl2 Δ 688-790 was generated using PCR-based mutagenesis and confirmed by DNA sequencing. Abl2 and Abl2 Δ 688-790 were cloned into pN1-EGFP expression vector for mammalian cell expression. Recombinant baculoviruses expressing Abl2 or Abl2 fragments in pFastBac were generated using the Bac-to-Bac expression system in Sf9 insect cells according to the manufacturer's instructions (ThermoFisher, Waltham, MA). After 36-48 hr infection with baculoviruses, High Five cells were collected and centrifuged for 3,000 rpm for 5 min at 4°C. Cells were lysed using buffer containing 20 mM HEPES pH 7.25, 5% glycerol, 500 mM KCl, 20 mM imidazole, 1 mM DTT, 1 mM PMSF, 1X protease inhibitor cocktail, 1% Triton-X100 and left to incubate at 4°C on a rotisserie stand for 5-10 min. Lysates were ultracentrifuged using Ti70.1 rotor for 45 min, 40K rpm at 4°C. After collecting and 0.45 μ m filtering the supernatant, proteins were passed through disposable columns with Ni-NTA resin beads via gravity flow three times. Resin was washed in order with the following buffers: wash A (20 mM HEPES pH 7.25, 5% glycerol, 500 mM KCl, 20 mM imidazole, 1 mM DTT, 1 mM PMSF, 1X protease inhibitor cocktail); B (20 mM HEPES pH 7.25, 5% glycerol, 1 M KCl, 20 mM imidazole, 1 mM DTT, 1 mM PMSF, 1X protease inhibitor cocktail), A, and C (20 mM HEPES pH 7.25, 5% glycerol, 300 mM KCl, 20 mM imidazole, 1 mM DTT, 1 mM PMSF, 1X protease inhibitor cocktail). Bound proteins were step eluted off the Ni-NTA resin (Invitrogen) using wash C buffer containing 300 mM imidazole in 5X1 ml fractions. 6XHis-Abl2 and 6XHis-Abl2 fragments for biolayer interferometry assays were exchanged into storage buffer containing 20 mM HEPES pH7.25, 5% glycerol, 100 mM KCl, 1 mM DTT using either Superdex 75 increase 10/300 GL column for proteins with MW < 75kDa, or Superdex 200 increase 10/300 GL column for proteins with MW \geq 75 kDa. His tags were removed by adding TEV protease into purified Abl2 constructs, and were incubated on a rotisserie stand at 4°C for 2.5-4 hrs. His-tag cleaved proteins were exchanged into the storage buffer containing 20 mM HEPES, 5% glycerol,

300 mM KCl, and 1 mM DTT using either Superdex 75 increase 10/300 GL column or Superdex 200 increase 10/300 GL column. Peak fractions were collected, snap frozen, and stored at -80°C until use.

Tau 2N4R-eGFP purification

FUGW-tau 2N4R plasmid was a kind gift from the Liz Rhoades Lab. Human full-length tau 2N4R was cloned into pFastBac1 vector (Invitrogen) with an N-terminal 6XHis tag for insect cell expression. Baculovirus generation and Hi5 insect cell expression and purification follow that of His-cleaved Abl2 constructs, as described above. 6XHis-cleaved tau 2N4R-eGFP was buffer exchanged into 20 mM HEPES, 5% glycerol, 300 mM KCl, 1mM DTT using Superdex 200 increase 10/300 GL column. Each peak fraction was snap frozen and stored at -80°C until use.

EB1-eGFP purification

pETM-11-EB1-eGFP plasmid was a kind gift from the Joe Howard Lab. pETM-11-EB1-eGFP was transformed and expressed into *E. coli* BL21 cells. 4 l expression cultures were grown in 2XYT at 37°C, 200 rpm until A_{600} reached 0.6, followed by induction with 1 mM IPTG at 18°C for 24 hrs. Cells were harvested by centrifugation at 4K rpm in SLC6000 rotor 15 min at 4°C. Cell pellets were resuspended in lysis buffer (20 mM HEPES, 500 mM KCl, 5% glycerol, 1 mM DTT, 0.1% Triton X-100, 1X protease inhibitor cocktail) and lysed with the QSonica Q55 Compact Sonicator for 5 minutes on ice at amplitude 30 (on-off 10s pulses on the thumb switch setting). Cell lysates were ultracentrifuged using Ti70.1 rotor for 45 min, 40K rpm at 4°C. Purification of 6XHis-EB1-eGFP to generate 6XHis-cleaved EB1-eGFP follows that of His-cleaved Abl2 constructs as described above. 6XHis-cleaved EB1-eGFP was buffer exchanged into 20 mM HEPES, 5% glycerol, 300 mM KCl, 1mM DTT using Superdex 75 increase 10/300 GL column. Each peak fraction was snap frozen with the addition of 1X protease inhibitor cocktail and stored at -80°C until use.

Spastin purification

pGEX-PP-Spastin(87-616)DeltaExon4 was purchased from Addgene (item ID #128794). Spastin was transformed and expressed into *E. coli* BL21 cells. 4l expression cultures were grown in 2XYT media at 37°C, 200 rpm until A_{600} reached 0.6, which was then followed by induction with 0.5 mM IPTG. Cultures were grown 16°C for 16 hrs. Cells were harvested by centrifugation at 4K rpm in SLC6000 rotor 15 min at 4°C. Cell pellets were resuspended in lysis buffer (50 mM Tris-HCl pH 8.0, 5% glycerol, 0.1% Triton X-100, 5 mM MgCl₂, 1 mM DTT, 1X PMSF, 1X protease inhibitor cocktail) and lysed with the QSonica Q55 Compact Sonicator for 5 minutes on ice at amplitude 30 (on-off 10s pulses on the thumb switch setting). Lysates were clarified for 20 min in SA600 rotor at 15K rpm at 4°C, and 0.45 µm filtered. 2 ml of glutathione agarose resin was equilibrated using lysis buffer without added detergent and pipetted into a disposable gravity flow column. Lysates were passed through column 3X. Resin was washed with buffers in the following order: A (50 mM Tris-HCl pH 8.0, 300 mM KCl, 5 mM MgCl₂; 5% glycerol, 1X DTT, 1X PMSF); B (50 mM Tris-HCl pH 8.0, 1 M KCl, 5 mM MgCl₂; 5% glycerol, 1X DTT, 1X PMSF); A; and C (50 mM Tris-HCl pH 8.0, 150 mM KCl, 5 mM MgCl₂; 5% glycerol, 1X DTT, 1X PMSF). 5 ml of Wash C supplemented with 1 mg PreScission protease was added into the resin and left to incubate on the column overnight at 4°C. After ~16 hrs, GST-cleaved spastin was removed from PreScission protease by passing through Superdex 200 increase 10/300 GL column and stored in 20 mM HEPES, 5% glycerol, 300 mM KCl, 5 mM MgCl₂, 1 mM DTT. The first three peak fractions were concentrated using 0.5 ml centrifugal filter units (EMD Millipore #UFC501096) that were pre-equilibrated with storage buffer and stored at -80°C until use.

eGFP purification

eGFP from pN1-eGFP plasmid was cloned C-terminus of GST into the pGEX-6p1-GST vector. pGEX-6p1-GST-eGFP was transformed into *E. coli* BL21 cells. 2l expression cultures were grown in 2XYT media at 37°C, 200 rpm until A_{600} reached 0.6, which was then followed by induction with 0.5 mM IPTG. Cultures were grown 16°C for 16 hr. Cells were harvested by centrifugation at 4K rpm in SLC6000 rotor 15 min at 4°C. Cell pellets were resuspended in lysis buffer (20 mM HEPES pH 7.25, 500 mM KCl, 5% glycerol, 0.1% Triton X-100, 1 mM EDTA, 1 mM EGTA, 1 mM DTT, 1

mM PMSF, 1X protease inhibitor cocktail). Lysates were clarified for 20 min in SA600 rotor at 15K rpm at 4°C, and 0.45 µm filtered. 2 ml of glutathione agarose resin was equilibrated using lysis buffer without added detergent and pipetted into a disposable gravity flow column. Lysates were passed through column 3X. Resin was washed with buffers in the following order: A (20 mM HEPES pH 7.25, 500 mM KCl, 5% glycerol, 1 mM EDTA, 1mM EGTA, 1 mM DTT, 1 mM PMSF); B (20 mM HEPES pH 7.25, 1M KCl, 5% glycerol, 1 mM EDTA, 1mM EGTA, 1 mM DTT, 1 mM PMSF); A; and C (20 mM HEPES pH 7.25, 300 mM KCl, 5% glycerol, 1 mM EDTA, 1mM EGTA, 1 mM DTT, 1 mM PMSF). 5 ml of Wash C supplemented with 1 mg PreScission protease was added into the resin and left to incubate on the column overnight at 4°C. After ~16 hr, GST-cleaved eGFP was removed from PreScission protease by passing through Superdex 75 increase 10/300 GL column and stored in 20 mM HEPES, 5% glycerol, 300 mM KCl, 1 mM DTT, 1X protease inhibitor cocktail. Peak fractions were stored in -80°C until use.

mCherry purification

mCherry from pN1-mCherry-Cry2 was cloned in frame with the N-terminal 6XHis tag into pET28b via 5' NheI and 3' BamHI sites. The plasmid was transformed into BL21(DE3) cells and grown to $OD_{600} \approx 0.6$ at 37°C in 2l of 2XYT, then induced with 0.5 mM IPTG at 16°C for 14 hrs. Cells were pelleted and resuspended in lysis buffer containing 20 mM HEPES pH 7.25, 5% glycerol, 500 mM KCl, 20 mM imidazole, 5 mM β-mercaptoethanol, 1 mM PMSF, 1X protease inhibitor cocktail, and lysed by sonication at 60% power for 10 minutes in repeated cycles of 30 s on, 30 s off. 1% Triton-X100 was added and left to incubate at 4°C for 5-10 min. Lysates were clarified in a SA600 rotor for 20 min at 15K rpm at 4°C in. Supernatants were further clarified by 0.45 µm filtration and passed through disposable columns with Ni-NTA resin (Invitrogen) beads via gravity flow three times. Resin was washed in order with the following buffers: wash A (20 mM HEPES pH 7.25, 5% glycerol, 500 mM KCl, 20 mM imidazole, 1 mM DTT, 1 mM PMSF, 1X protease inhibitor cocktail); B (20 mM HEPES pH 7.25, 5% glycerol, 1 M KCl, 20 mM imidazole, 1 mM DTT, 1 mM PMSF, 1X protease inhibitor cocktail). Bound proteins were step eluted off the Ni-NTA resin using wash C buffer containing 100 mM imidazole in 10X1 ml fractions.

TEV protease purification

The plasmid pRK793 TEV S219V was obtained as a gift from the Boggon Lab and transformed into BL21 *E. coli* for purification. The protein was expressed in 2 l of BL21 *E. coli* culture followed by 0.2 mM isopropyl β -D-thiogalactopyranoside (IPTG) induction at 37°C for 3 hrs. Cells were sonicated in buffer containing 20 mM Tris pH 8.0, 5 mM β ME, 500 mM NaCl, 4 mM imidazole, 1 mM DTT, 1 mM PMSF, 1X protease inhibitor cocktail. Lysates were ultracentrifuged using Ti70.1 rotor for 45 min, 40K rpm at 4°C. After collecting and 0.45 μ m filtering the supernatant, proteins were passed through disposable columns with Ni-NTA resin beads via gravity flow 3X. Resin was washed with the following buffers in the following order: wash A (20 mM Tris pH 8.0, 5 mM β ME, 500 mM NaCl, 4 mM imidazole, 1 mM DTT, 1 mM PMSF), B (20 mM Tris pH 8.0, 5 mM β ME, 250 mM NaCl, 40 mM imidazole, 1 mM DTT, 1 mM PMSF), and C (20 mM Tris pH 8.0, 5 mM β ME, 40 mM Imidazole, 100 mM NaCl, 1 mM DTT, 1 mM PMSF). Bound proteins were eluted off the Ni-NTA resin using elution buffer (20 mM Tris pH 8.0, 5 mM β ME, 400 mM Imidazole, 100 mM NaCl, 1 mM DTT, 1 mM PMSF, and 1X protease inhibitor cocktail). The eluted fractions were then applied to a mono S cation exchange column for clean up using buffer A (20 mM HEPES pH 7.25, 5% glycerol, 1 mM DTT) and buffer B (20 mM HEPES pH 7.25, 5% glycerol, 1 M KCl, 1 mM DTT). The eluted fractions containing TEV were pooled, flash-frozen in liquid nitrogen, and stored at -80°C.

Microtubule co-sedimentation assays and quantification

Co-sedimentation assays were performed as previously described (Campbell & Slep, 2011; Miller et al., 2004). Double-cycled GMPCPP (Jena Bioscience, Thuringia, Germany) stabilized MTs were grown as described (Spector et al., 2020). Taxol-MTs were polymerized at a final concentration of 60 μ M at 37°C in polymerization buffer [80 mM PIPES, pH 6.8, 1 mM MgCl₂, 1 mM EGTA, 1 mM GTP, and 15 nM paclitaxel (taxol)]. The taxol-stabilized MTs and GMPCPP-stabilized MTs were set aside for co-sedimentation. For MT co-sedimentation assays, 0.2 μ M Abl2 or Abl2 fragments were mixed with increasing concentration of MTs (0 to 6 μ M) at 37°C for 20 minutes in binding buffer [80 mM PIPES, pH 6.8, 70 mM KCl, 1 mM GTP, 5 nM taxol (100 μ L reaction volume)]. Mixtures were

pelleted by high-speed centrifugation at 120,000 rpm for 20 minutes at 37°C. Pellet and supernatant fractions were recovered and separated by SDS-PAGE, stained with Coomassie Blue G-250 (Bio-Rad Laboratories, Hercules, CA) then destained in water. The SDS-PAGE gels were then scanned with Bio-Rad ChemiDoc™ Touch Imaging System and quantified by densitometry using ImageJ software. Binding affinity was quantified either as the percentage of Abl2/Abl2 fragments bound to MTs over total amount of Abl2/Abl2 fragments in the reaction for each concentration or as the amount of Abl2 bound to MTs for each concentration of Abl2. Experiments were repeated at least 4 times for each experimental condition ($n \geq 4$). Equation $y = B_{max} * \frac{x}{K_D + x}$ (**Equation 1**) was used to fit the curve (Pollard, 2010), where y is specific binding, x is the ligand concentration, B_{max} is the maximal binding (same units as y), and K_D is the binding affinity (same units as x). Binding curves, affinities (K_D), and R^2 values for curve fitting were calculated using GraphPad Prism 9 GraphPad.

Tubulin binding analysis with size-exclusion chromatography

Size-exclusion chromatography used a Superdex 200 increase 10/300 GL column equilibrated in 20 mM HEPES pH 7.25, 5% glycerol, 100 mM KCl, 1 mM DTT. The column was calibrated with standard proteins of known Stokes radii (Sigma-Aldrich, St. Louis, MO). Abl2 or 557-C and tubulin were mixed with tubulin at a ratio of 1:4 and incubated for 30 min on ice, and then injected onto the column. Control experiments were performed with each protein alone. The collected fractions were analyzed by SDS-PAGE, stained with Coomassie brilliant blue G250 (Sigma-Aldrich, St. Louis, MO), and scanned.

Tubulin binding affinity measurements using biolayer interferometry

The biolayer interferometry technique using the BLItz system (ForteBio) was used to measure binding kinetics for the tubulin interaction with 6XHis-Abl2 and 6XHis-Abl2 fragments. His tag-binding Ni-NTA biosensors were hydrated in binding buffer (20 mM HEPES pH 7.25, 5% glycerol, 100 mM KCl, 1 mM DTT, supplemented with 0.02% Tween to reduce noise) for 10 min. For each tubulin concentration (ranging from 7 nM to 2000 nM), the following procedure was performed. An initial baseline was collected by immersing the biosensor in binding buffer for 1 min, and then 4 μ l

of fixed concentrations of 6XHis-Abl2 or 6XHis-Abl2 fragments (0.3 μM or 1 μM) were loaded to the biosensor for 5 min. The Abl2-loaded biosensor was returned to binding buffer for collection of a second baseline for 1 min and then placed in 4 μl of tubulin for a 5-min association step. For each data point, the background binding was also measured. For each tubulin concentration, the difference in the signal (in nm) just prior to the association step and that at the end of the association step was subtracted from the difference in signal for background binding. The binding curves were plotted fit to the one-phase exponential curves assuming a shared k_{off} using the “association kinetics (two or more ligand concentrations)” model with GraphPad Prism to obtain a dissociation constant.

Turbidity assay and preparation of Abl2-MT sample grids for EM imaging

18 μM porcine brain tubulin in BRB80 was incubated with the MT polymerization buffer (2 mM of GTP, 1 mM DTT, 15% glycerol) alone or in the presence of Abl2 and Abl2 fragments at 37°C. Tubulin assembly was monitored by measuring turbidity at 350 nm (A_{350}) for 2 hrs using SpectraMax M6 Multi-Mode Microplate Reader recording spectrophotometer. Control experiments were done by monitoring A_{350} for buffer alone with 0.5 μM Abl2 and Abl2 fragments without tubulin. 4 μl reactions at 10 min were taken out and visualized using electron microscopy (EM) of negatively stained samples. A 400-mesh copper grid (Ted Pella, Redding, CA) overlaid with a very thin continuous carbon layer was gently glow discharged and 4 μl of the diluted protein was applied to the grid. After a 30s adsorption, the reactions were blotted away from the grid with filter paper (Whatman No.1) leaving a thin layer of solution on the grid. 4 μl of 2% uranyl-acetate solution were applied to the grid for 30s before blotting twice. After blotting, the grid was left to dry for 2 min. The negative stain sample of Abl2 was imaged using a Tecnai12 transmission electron microscope (TEM) and images recorded on a Gatan CCD camera at \sim -2-3 μm defocus.

Construction and preparation of flow chambers for TIRF imaging

Glass microfluidic chambers were constructed as described in (Johnson-Chavarria et al., 2011). Briefly, inlet and outlet ports were generated into polydimethylsiloxane (PDMS) molds using a blunt

tip needle. Holes were drilled into a glass cover slide with a diamond tip bit. Plasma cleaning was used to bond PDMS molds onto the cover slides where PDMS ports and holes meet.

Coverslips were cleaned with the following solutions, all incubated in a sonicator for 15 min (unless otherwise stated) and washed with ddH₂O in between steps: 2% Hellmanex, ddH₂O, 90% ethanol, 1M HCl (1 hr to overnight). To extensively rinse off HCl, coverslips were washed with ddH₂O 3X for 15 min per step. Coverslips were then cleaned with 0.22 μm filtered 1M KOH for 30 min, followed by ddH₂O, and 100% ethanol for 60 min to overnight. Coverslips were dried in a 55°C incubator and silanized with 300 ml dichlorodimethyl silane in 300 ml hexane solution for 35-45 min. They were subsequently sonicated in hexanes for 15 min. Coverslips were air dried and stored in sterile 50 ml Falcon tubes at -20°C until use. Immediately before use, TIRF chambers were assembled using parafilm, with rectangular cutouts to allow for flow between inlet and outlet ports; and was sealed between clean coverslips and the PDMS chamber with heat (via pressing the chamber with coverslip-side down onto surface of a 100°C heat block for ~5-10 s).

Flow chambers were prepared by washing in BRB80 and incubating 1 mg*ml⁻¹ biotin-BSA (0.22 μm filtered in BRB80) for 5-10 min. Chambers were blocked with 2% Pluronic F-127 and allowed to incubate at RT for 30-45 min, followed by washing with BRB80 and functionalizing with 50 mg*ml⁻¹ neutravidin (0.22 μm filtered in BRB80). After 5 min incubation, flow chambers were washed with BRB80 and perfused with biotin GMPCPP-MT seeds. Density of seeds were checked under the scope. Chambers were washed with BRB80 to flow out unattached seeds.

Microtubule dynamics assay

Microtubule seeds were prepared by mixing 10% biotin, 1% rhodamine-labelled 10 μM tubulin in BRB80 buffer, supplemented with 1 mM GMPCPP. The seed mixture was incubated in a 37°C water bath for 30-45 min, followed by centrifugation in a TLA100 rotor at 80K rpm for 5 min at 37°C. Single-cycled seeds were resuspended in warm BRB80 buffer and ready for use. Imaging buffer consisted of 10.5 μM 10% rhodamine-labelled tubulin, 1 mM GTP, 0.02% methylcellulose, 1X anti-blink cocktail (1% β-ME, 40 mM glucose, 250 nM glucose oxidase, 64.5 nM catalase, 1 mM Trolox, BRB80), and BRB80. All proteins were centrifuged in TLA100 rotor for 5 min at 80K rpm, 4°C prior

to use to remove aggregates. In conditions with Abl2-eGFP, Abl2 Δ 688-790, or Abl2-688-924-eGFP, salt concentration was adjusted such that the final [KCl] in the imaging buffer was 50 mM. Reaction mixture was pipetted up and down 3X prior to perfusing into flow chamber.

Dynamic MTs were allowed to grow, equilibrating in the chamber for 5 min prior to image acquisition. The objective was maintained at 37°C with an objective heater. Images were acquired at 1 fps for 25min, 2x2 binning with 300 ms integration times per channel, using the Nikon Elements software; and a Nikon ECLIPSE Ti Series Inverted Microscope equipped with a 100X TIRF 1.49NA oil objective and Andor Zyla 4.2 sCMOS camera. Dynamic instability parameters were analyzed from kymographs generated from Multi Kymograph using 'read velocities from tsp' plug-in (tsp050706.txt macro written by J. Rietdorf and A. Seitz, EMBL). Events were scored as pausing if the pause duration lasted at least 10s. At least 3 technical replicates (at least one different TIRF chamber per independent experiment) were conducted for each condition. MT lifetime distributions were fitted to a gamma distribution.

Microtubule segmentation assay and analysis

10% biotinylated rhodamine GMPCPP-MT seeds were prepared as described above. Seeds were flowed into the chamber and allowed to incubate for a minute prior to BRB80 wash out. 11 μ M 10% labelled Alexa647 tubulin in 1X anti-blink cocktail supplemented with 1 mM GTP and 0.02% methylcellulose was perfused into the flow chamber to generate GDP segments. Dynamic MTs were allowed to grow for 10 minutes at 37°C. To generate GMPCPP-caps without inducing catastrophe of existing MTs, 10% rhodamine-labelled 11 μ M tubulin was perfused into the flow chamber in 1X anti-blink cocktail supplemented with 2 mM GMPCPP and 0.02% methylcellulose. GMPCPP-caps were allowed to grow for at least 5 minutes prior to 3X BRB80 washout to remove excess soluble tubulin in the flow chamber. 0.5 μ M Abl2-eGFP, 0.5 μ M 557-C-eGFP, 0.5 μ M EB1-eGFP, or 25 nM tau-eGFP was mixed in 1X anti-blink cocktail supplemented with 0.02% methylcellulose and 50 mM KCl and perfused in flow chamber. Binding was allowed to equilibrate in the flow chamber for 5 minutes prior to 1X BRB80 washout. Images were acquired at 2x2 binning

with 300 ms integration times per channel using the Nikon TIRF 1.49NA oil objective and Andor Zyla 4.2 sCMOS camera.

Nucleotide state preference (NSP) was quantified by first making 3 pixel-wide line scans across a single filament. Fluorescence intensity per unit of length was linearly normalized per channel. Occupancies of EB1, tau 2N4R, 557-C, and Abl2 were determined by taking the fraction of the fluorescence intensity of the 488 nm channel over that of the 561 nm (red, GMPCPP) or 647 nm (pseudo-colored blue, GDP). NSP of the MBP on either GMPCPP- or GDP-segments for that single filament was recorded as the mean ratio of GMPCPP occupancy divided by the mean ratio of GDP occupancy. NSP measurements are shown on \log_{10} scale. Values above 0 indicate preference for GMPCPP; values below 0 indicate preference for GDP.

Preparation of damaged MTs and lattice repair assay

100 μ l mixture of 2% biotinylated, 10% rhodamine-labeled 20 μ M tubulin was thawed on ice and incubated with 1 mM GTP in BRB80 buffer. The mixture was allowed to polymerize in 37°C water bath for 30-45 min. MTs were centrifuged in a TLA100 rotor at 80K rpm for 5 min at 37°C and resuspended in warm BRB80 buffer supplemented with 10 μ M paclitaxel (taxol). Taxol-stabilized MTs were separated into 2 mixtures: 1) one 50 μ l stored at RT (23°C) overnight; 2) the remaining 50 μ l stored in 37°C.

The following day, the MTs were centrifuged for 5 min at 80K rpm, 37°C; and resuspended in warm BRB80 supplemented with 10 μ M taxol. The 2 mixtures were separated into 2 25 μ l Eppendorf tubes. Alexa647-tubulin and Abl2-eGFP were clarified for 5 min at 80K rpm, 4°C. 2 μ M Alexa647-tubulin and 10 mM GTP were added into each 25 μ l mixture of MTs. 1 μ M Abl2-eGFP was added into one of 23°C and 37°C-stored MT reactions. Reactions were left to incubate in a 37°C water bath for 3 hrs prior to imaging. For damaged boundary analysis assays where 0.5 μ M of Abl2-eGFP was added in absence of Alexa647-tubulin, reactions were left to incubate in flow chambers for 10 min prior to imaging. To assess the extent of lattice damage visually, a parallel set of non-fluorescent taxol-stabilized MTs were stored overnight at 23°C and 37°C and supplemented

with 10 μM taxol the following morning for negative stain EM. Reactions were diluted 3-fold in warm 1X BRB80 buffer. 4 μl per reaction were applied onto glow-discharged grids.

After 45s adsorption, the reactions were blotted away from the grid with filter paper (Whatman No.1) leaving a thin layer of solution on the grid. 4 μl of 2% uranyl-acetate solution were applied to the grid for 30 s before blotting twice. After blotting, the grid was left to dry. Negative stain samples of damaged MTs were imaged using a Tecnai12 TEM scope and images recorded on a Gatan CCD camera at \sim -0.8-1.5 μm defocus. The same qualitative assessment using negative-stain EM for recruitment of 1 μM non-fluorescent Abl2 to damaged lattice sites in the presence of 2 μM non-fluorescent tubulin dimers was conducted.

TIRF chambers were functionalized as described above. 25 μl of each reaction (control and +Abl2 conditions) containing MTs stored at either 23°C or 37°C were perfused into the chamber. Warm BRB80 buffer was flowed into the chamber to wash out unattached taxol-MTs. Still images for the green (Abl2), red (MT; pseudo-colored magenta), and far red (tubulin reporter; pseudo-colored cyan) channels were acquired using single-band emission filter sets for 488, 561, and 638 nm, with 2x2 binning 300 ms acquisition times on the Nikon ECLIPSE Ti Series Inverted microscope.

To score for damaged MTs at either temperature, 3-pixel wide line scans across the entire length of rhodamine-MTs and tubulin reporter were recorded. User-defined MT and tubulin reporter intensity thresholds were used as parameters in custom-written MATLAB script to determine borders of MT segments that are structurally damaged, and whether tubulin reporter was present or not. MT segments of mean fluorescence intensity lower than user-defined MT-intensity threshold were scored as 'damaged'. If the mean intensity of tubulin reporter of the equivalent damaged MT length is at least the user-defined reporter intensity threshold, the reporter length, reporter fraction, and frequency of reporter incorporation for that one MT were recorded.

For Abl2 localization and border analysis, MT segments of mean fluorescence intensity at least the user-defined MT threshold value were determined as 'healthy'. Along these 'healthy' segments, borders are defined as edges of healthy segments that border damaged segments (of mean intensity values less than user-defined threshold). Border length was quantified as being 1/5

of the total healthy MT segment away from either terminus, with the lattice length quantified as the middle 3/5 of the MT segment. Localization of 0.5 μM Abl2-eGFP was quantified by taking the mean fluorescence intensity of the green channel along sub-sections of the healthy MT segment that were either borders or lattices.

Microtubule severing assay

10% biotinylated, 10% rhodamine labelled GMPCPP-stabilized MTs were flowed into TIRF chambers, followed by flow-in and incubation of 1 μM Abl2-eGFP in imaging buffer (1X anti-blink cocktail, 0.02% MC, 50 mM KCl, and BRB80) for 5 min to allow for condensate formation. Flow chamber was washed with BRB80 buffer to remove non-bound Abl2. 90 nM spastin in imaging buffer supplemented with 2 mM ATP was introduced into the chamber and image acquisition at 0.34 fps for 15 min immediately followed. 3 pixel-wide line scans of MTs were recorded for MTs at the beginning of each image acquisition and fluorescence intensity decay traces were plotted and fit to a single exponential decay: $y(t) = C_1 e^{-(C_2(t)+C_3)}$ (**Equation 2**).

Phase separation assay

Abl2-eGFP, 557-C-eGFP, and N-557-eGFP were thawed on ice and concentrated to final concentration of 10 μM or higher using 0.5 ml centrifugal filter units (EMD Millipore #UFC501096) equilibrated with Abl2 storage buffer (20 mM HEPES, 300 mM KCl, 5% glycerol, 1 mM DTT).

Concentrated proteins were centrifuged to remove aggregates in a TLA100 rotor at 80K rpm, 4°C for 5 min. Individual wells in Cellvis #1.5 glass-bottom 96-well plates were washed with BRB80 and blocked with 2% Pluronic F-127 for 30-45 min. 20 μl of imaging buffer (0.2% methylcellulose, 1X anti-blink cocktail, BRB80, 0.1-3 μM Abl2-eGFP, 557-C-eGFP or N-557-eGFP) was mixed on ice. 6.25 μl 16% Dextran-70 was added into the imaging buffer reaction to achieve final concentration of 5% dextran. The mixture was pipetted up and down 3X at RT and added into the well. Condensates were left to age for 10 min at RT prior to image acquisition. Epifluorescent imaging was performed using the Nikon ECLIPSE Ti Series Inverted microscope adapted to a mercury lamp source and a 50:50 beam splitter to toggle between TIRF and Epi modalities. Focus

was set just above the coverslip at the bottom of the well (z-height \approx 3795-3850nm) where condensates have sedimented and settled.

To calculate partition coefficients and score for phase-separated condensation, we thresholded still images of sedimented Abl2 coacervates by filtering out particles for sizes $1-\infty$ and those with circularity values of 0.1-100. We then analyzed particles using Otsu, black and white thresholding, followed by color inversion. Circular ROIs were generated to quantify background values. Mean intensities of detected particles and background were calculated for each condition. If $\text{mean}(\text{particles}) \geq \text{mean}(\text{background})$, *i.e.* $\text{PC} \geq 4$, the particle was scored to be phase-separated condensate under the particular Abl2 concentration and salt concentration condition. For Abl2-tubulin co-condensation analysis, all partitioning experiments were maintained at 50 mM KCl, 5% dextran. Tubulin PCs were fitted to a sigmoidal equation, $y = \frac{C_1}{C_2 + e^{-C_3(x-C_4)}}$ (**Equation 3**).

Live-cell imaging of COS-7 cells transfected with mCherry-Cry2 constructs

Abl2 was cloned in frame upstream of mCherry-Cry2 in pHR-HNRNPA1C-mCh-Cry2WT and the entire Abl2-mCherry-Cry2 or mCherry-Cry2 were cloned into the pN1-eGFP vector, replacing the eGFP. COS-7 cells were plated at 0.5×10^6 cells in 6 cm dishes and transfected with 6 μg of pN1-mCherry-Cry2 or pN1-Abl2-mCherry-Cry2 using a calcium phosphate transfection, as per Pear et al (Pear et al., 1993). 12 hrs after transfection, transfected COS-7 cells were plated on 60 mm #1.5 glass dishes with 30 mm bottom wells (Cellvis, Mountainview, CA) that had been acid washed at 55°C overnight and coated with 50 $\mu\text{g} \cdot \text{ml}^{-1}$ poly-d-lysine for 20 min at room temperature and 10 $\mu\text{g} \cdot \text{ml}^{-1}$ fibronectin in phosphate-buffered saline (PBS) for 1 hr at 37°C. Prior to imaging, medium was exchanged into HBSS supplemented with 2% FBS. All live-cell imaging was conducted in a heated stage maintained at 37°C with CO₂. Pre blue light activation recording was done for 1 min.

Activation period recording was done for 5 min, with blue light being turned 'on' and 'off' every other frame interchanging with the 561 nm filter. Recording was continued for 10 min after blue light exposure. Videos for each period were all taken at 2 fps and acquired using a Nikon CSU-W1 SoRa spinning disk confocal, with 35% laser power (LP) for 561 (mCherry), and 50% LP for 488 (blue light activation) nm channels, at 200 ms exposure time each.

Estimation of intracellular levels of mCherry-Cry2 constructs

Recombinant 6XHis-mCherry was used to estimate intracellular concentrations of mCherry-Cry2 constructs expressed in transfected COS-7 cells. 35 mm #1.5 glass bottom dishes (MatTek, Ashland, MA) were coated with $35 \mu\text{g}\cdot\text{ml}^{-1}$ poly-d-lysine in 10 mM HEPES, 1X PBS for 30 min at RT. Dishes were then washed twice with PBS and coated in 250 μL each of 0.01, 0.05, 0.1, 0.25, and $0.5 \text{ mg}\cdot\text{ml}^{-1}$ 6XHis-mCherry diluted in PBS. Images were acquired using the same imaging conditions as done for live-cell imaging of COS-7 cells transfected with mCherry-Cry2 constructs (35% LP for 561 nm, 200 ms exposure with PFS setting on). Average mean intensity per pixel ($\text{a.u.}\cdot\text{pixel}^{-1}$) values were plotted against increasing concentrations of 6XHis-mCherry to acquire a line of best fit. ROIs that outlined the cells were generated and mean intensity $\cdot\text{pixel}^{-1}$ values were collected to extrapolate the intracellular concentrations based on the standard curve, knowing that $MW_{6\text{XHis-mCherry}} \approx 26.6 \text{ kDa}$.

Circular dichroism of Abl2 557-C

Purified His-tag free Abl2 557-C was purified into storage buffer containing 20 mM HEPES pH 7.25, 300 mM KCl, 5% glycerol, 1 mM DTT. CD spectra were collected at a constant temperature of 4°C using a Chirascan CD spectrometer (Applied Photophysics) at 0.5 nm wavelength step size and 0.5 s per wavelength point. CD spectra of the gel filtration buffer were collected to background subtract from the sample spectra. Averages of 2 spectra from 280 to 190 nm were calculated per replicate for duplicate technical replicates.

FRAP of Abl2 and tubulin in solution

Images were acquired using a Cellvis #1.5 glass-bottom 96-well plate. Condensates were prepared and aged as described above, maintained at 50 mM KCl. Prior to photobleaching, images were acquired every second for 30 seconds to obtain an average pre-bleach fluorescence intensity value. Photobleaching was carried out using 20% power of the 405 nm laser line, with 20 μs dwell time at a single focal plane near top of the condensate. An ROI was chosen as a circular region

within the condensate. Intensity of each ROI was recorded every 10s (~0.14 fps) over a 10-15 min acquisition period. Recovery in photobleached ROIs was normalized to changes in background intensity to account for global bleaching. Images were acquired using Nikon CSU-W1 SoRa spinning disk confocal microscope equipped 100X oil objective. Triplicate technical replicates of Abl2 and duplicate replicates of tubulin FRAP curves were fitted to double exponential decay:

$$y(t) = C_1 \left(1 - e^{-\frac{t}{c_2}}\right) + C_3 \left(1 - e^{-\frac{t}{c_4}}\right) \text{ (Equation 4).}$$

FRAP of Abl2 on MTs

Preparation of biotinylated MT seeds and functionalization of TIRF chambers were described as above. 10% biotinylated 10% rhodamine-labelled GMPCPP-stabilized seeds were flowed into the chamber and unattached seeds were washed out with BRB80. Imaging buffer (1 μ M Abl2-eGFP, 1X anti-blink cocktail, 50 mM KCl, 0.02% methylcellulose, and BRB80) was perfused into the flow chamber and left to incubate at RT for 5 min to allow condensates to form on MTs. Prior to photobleaching, images were acquired at 1 fps for 15 seconds for both 488 and 561 nm channels. Photobleaching was carried out using 20% laser power of the 405 nm laser line, with 20 μ s dwell time. Intensity of each ROIs were recorded at ~0.37 fps over a 10 min acquisition period. Images were acquired using Nikon Elements software; and a Nikon Ti2-E inverted microscope equipped with a 100X 1.49NA TIRF objective, stage top Piezo for 405 nm FRAP laser, and a Photometrics Prime 95B CMOS camera. FRAP curves of MTs from 4 TIRF chambers were fitted to **Eqn. 4**.

Microtubule nucleation observation using confocal microscopy

8 μ M 10% Alexa Fluor 647-labeled porcine brain tubulin in BRB80 was incubated with the MT polymerization buffer (2 mM of GTP, 1 mM DTT, 10% glycerol), 1 μ M Abl2-eGFP, 3% dextran at 37°C. Reactions were added to a 384-well glass-bottom plate (Corning, Corning, NY), which was acid-washed and coated with 2% F-127 for 30 min. Tubulin nucleation was monitored using Nikon CSU-W1 SoRa spinning disk confocal 30 min and 1 hr after the start of the reactions.

Fixed-cell sample preparation

Cells were plated on 12 mm #1.5 coverslips (Warner Instruments, Hamden, CT) in 3 cm TC-treated dishes (Corning, Corning, NY) the night prior, such that they were 80-90% confluent the morning of the experiment. Coverslips were acid washed at 55°C overnight and coated with 50 $\mu\text{g}\cdot\text{ml}^{-1}$ poly-d-lysine for 20 min at room temperature and 10 $\mu\text{g}\cdot\text{ml}^{-1}$ fibronectin in PBS for 1 hr at 37°C. Cells were treated with 10 μM nocodazole for 60 min, and the coverslips were taken out at 5 min after washout with complete medium.

Cells were fixed with 4% paraformaldehyde in cytoskeleton buffer (10 mM MES pH 6.1, 138 mM KCl, 3 mM MgCl_2 , 2 mM EGTA, 0.32 M sucrose) for 20 min at room temperature and then permeabilized with permeabilization buffer (0.5% Triton X-100 in PBS) for 20 min. The fixed cells were blocked in blocking buffer (2% BSA, 0.1% Triton X-100 in PBS) for 1 hr at RT, followed by primary and antibody incubation. Primary α -tubulin (DM1a) and α -GFP antibodies were used at 1:500 dilution and cells were left to stain overnight at 4°C. Cells were washed 3x with 0.05% Tween-20 in PBS on a shaker at RT. DAPI was used at 1:1000 to label nuclei (5 $\text{mg}\cdot\text{ml}^{-1}$ stock); Alexa488 goat anti-chicken secondary Ab (Invitrogen) was used at 1:500 to label GFP; and Alexa647 goat anti-mouse secondary Ab (Invitrogen) was used at 1:500 to label α -tubulin. All antibodies were diluted in blocking buffer, and cells were left to stain at RT for ~1 hr. Cells were washed 3x with 0.05% Tween-20 in PBS on a shaker at RT prior to mounting.

MT recovery analysis

Cell areas and MT recoveries were imaged using Nikon CSU-W1 SoRa spinning disk confocal, with 5% LP for 405 (nuclei), 488 (eGFP), and 647 (tubulin) nm channels, at 200 ms exposure time each. Samples were blinded prior to imaging. Images were Z-projected with "Max Intensity". Only mononucleated cells were chosen for analysis. Cell boundaries were defined using polygonal selection to measure cell areas. A background region within the selected cells with no MTs was measured, with mean background intensity recorded as I_{bg} . $I_{bg} * 3$ was used as the threshold to quantify for MTs recovered upon post-nocodazole treatment. Regions throughout the cell of fluorescence intensity above the threshold near the MTOC were measured to determine the

amount of MTs recovered. At least 25 cells from 2-3 experimental replicates were quantified for each assay condition ($n \geq 25$) by a reviewer blinded to sample identity.

SEC-MALS and Stokes radius analyses

To measure the particle size of purified Abl2 and 557-C in solution, we used an experimental setup including an upstream size exclusion chromatography (SEC, Superdex 200 increase 10/300 GL) coupled with a downstream multi-angle light scattering (MALS), which includes a multiple light scattering detector (DAWN HeleosII, Wyatt Technology Corporation) and a refractive index detector (Optilab T-rEX, Wyatt Technology). Each sample injection consisted of 0.5 to 2 mg of purified protein sample in buffer containing 20 mM HEPES pH 7.25, 5% glycerol, 100 mM KCl, 1 mM DTT. The flow rate was set at $0.4 \text{ ml} \cdot \text{min}^{-1}$. Data were recorded at 1 second intervals and processed using ASTRA software (Wyatt Technology). Stokes radius analyses were performed as described previously (La Verde et al., 2017).

Cryo-EM grid preparation and data collection

On-grid incubation method was used to prepare cryo-EM samples of MT decorated with 6XHis-tagged Abl2-557-1090. In brief, glow-discharged cryo-EM grids (Quantifoil Au 2/1, 300 mesh) were loaded into a Vitrobot Mark IV (ThermoFisher Scientific). The chamber was set at 15°C and 95% humidity. $2 \mu\text{L}$ $6 \mu\text{M}$ GMPCPP-stabilized MT was applied onto the grid and incubated for 30 seconds. After that, $2 \mu\text{L}$ $20 \mu\text{M}$ 6XHis-Abl2-557-1090 was added and incubated for 60 seconds. The grid was then blotted for 3-6 seconds and plunged into liquid ethane.

MTs with or without 557-1090 data were collected at the Yale Science Hill CryoEM facility using a Glacios microscope (Thermo Fisher Scientific) operated at 200 keV. The images were collected with a K2 direct electron detector (Gatan) operating in super-resolution mode, at a magnification of 36,000 corresponding to a pixel size of 1.143 \AA . Data collection was automated by SerialEM software with a defocus range $-1.5 \mu\text{m}$ to $-2.7 \mu\text{m}$. In total, 720 movies for MT only and 1780 movies for Abl2-MT were collected and each movie was dose-fractionated to 40 frames with a total dose of $40 \text{ e}^-/\text{\AA}^2$.

Cryo-EM image processing

Cryo-EM data processing workflows are outlined in **Figure 2.31**. Recorded movies were pre-processed using cryoSPARC Live including patch motion correction and patch CTF estimation. CryoSPARC template picker was used to pick MT segments and rounds of 2D classification were used to remove junk particles. For MT 3D reconstruction, a published 14-protofilament MT map (EMD-7973) was used, and low-pass filtered to 6 Å for homogenous refinement. The reconstructed maps were used for the comparison of MT with (84, 826 particles) or without (24, 485 particles) Abl2.

To improve the resolution and map quality of Abl2-MT reconstruction, protofilament refinement protocol (Debs et al., 2020) was applied to the dataset. After this, 1,187,564 protofilament particles were subjected to local 3D refinement and focused 3D classification. Map statistics can be found in **Table 1**. All cryo-EM maps were convoluted with a Gaussian function which has a standard deviation of 3 Å before comparison. ChimeraX was used for the Gaussian filtering and figure preparation.

Quantification and Statistical Analysis

Fiji was used for all image processing and analysis. MATLAB and GraphPad Prism 9 were used for quantification analysis. At least triplicate technical replicates were performed for each experiment unless otherwise stated. Details on the statistical test are presented in the figure legends. Graphs show mean \pm SD, unless otherwise stated in legends. P-values < 0.05 are considered as statistically significant.

Chapter 3: Evolutionary differences between Abl2 and Abl2 Δ 688-791

Tubulin-binding Abl2 and tubulin-binding deficient Abl2 Δ 688-790 exhibit significant differences in regulating MT dynamics. Knowing where these transcripts are expressed in the mouse brain will shed light on how microtubule dynamics are regulated in different cell types to support neuronal function and activity. From previous studies, it is known that loss of Abl2 impairs dendritic development. Thus, determining how spine density and morphology are impacted in cultured neurons overexpressing Abl2 or Abl2 Δ 688-790 will provide an initial glimpse into their differential regulation on cytoskeletal dynamics to modulate neuronal function.

Single-cell and bulk RNA-seq omics data were published in (Duan et al., 2023). Bioinformatic analyses were performed by Shaojie (Jay) Ma from Nenad Sestan's lab. Conceptualization for calculating splice site maximum entropy score analysis was by Tony Koleske, who sought help from Morgan Shrine of the Neugebauer Lab who conducted the analysis using MaxEntScan model (Yeo & Burge, 2004).

3.1. Single-cell and bulk RNA-seq transcriptomics reveal differential Abl2 transcript levels between mice and humans

Murine Abl2, used in this study, is 95% identical to human Abl2, with near identical sequence of the alternatively spliced exon encoding amino acids 688-791, which sits entirely within a larger final coding exon in Abl2 and thus forms part of its IDR. Analysis of the expression of murine and human Abl2 across tissues indicated that the relative abundance of transcripts containing this alternatively spliced exon differed between species (**Figures 3.1, 3.2**; abbreviations found in **Tables 3.1, 3.2**, respectively). Namely, transcripts including the amino acids 688-791 (containing 3 terminal amino acids +MSS in this fragment, denoted in **Figure 3.2**) predominate over those lacking it across human tissues, while the Δ 688-790 isoform is predominant in mouse tissues (**Figures 3.1, 3.2**) (Tasic et al., 2018). Genomic engineering of mice that preferentially express Abl2 isoforms including amino acids 688-791 should reveal how this exon impacts microtubule dynamics and organismal development *in vivo*. It will be interesting to explore in future studies studying the behavioral and

brain anatomical differences between WT mice and mice that predominantly express the Abl2 isoform containing aa. 688-791.

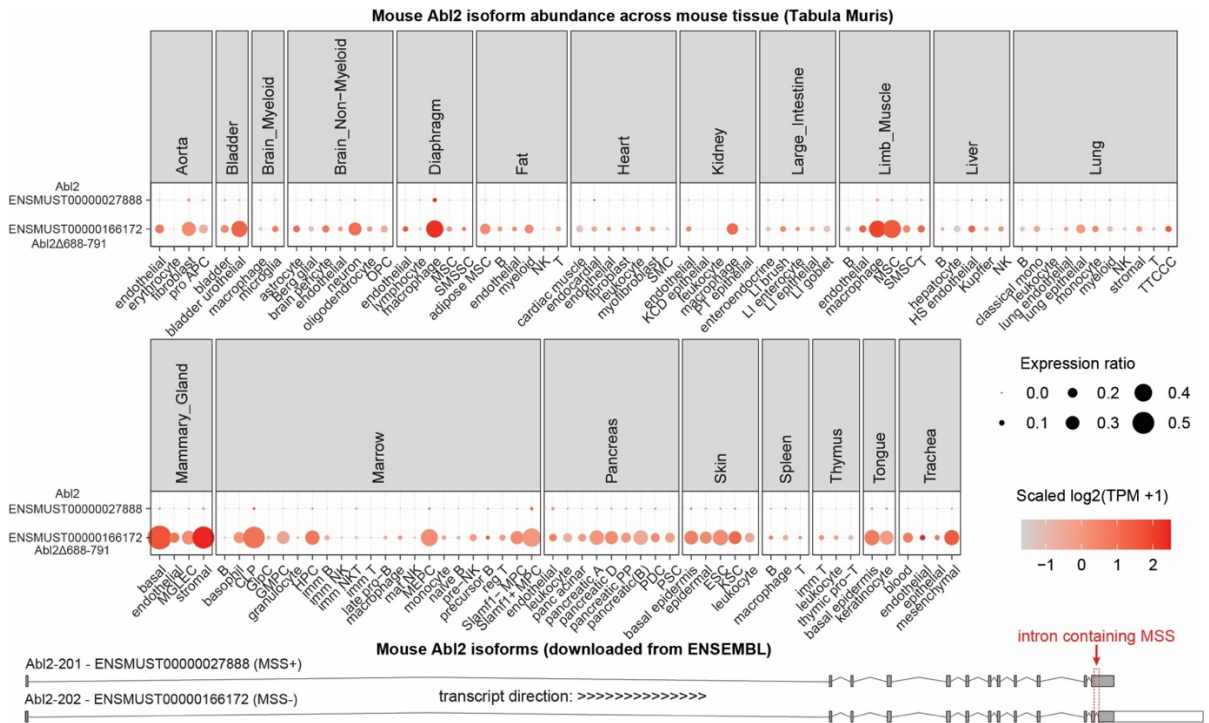


Figure 3.1. Cell- and tissue-specific levels of ABL2/Abl2 isoform expression in *Mus musculus*. (Top) Dot plots illustrating the isoform abundance for the selected *Abl2* transcripts in a single-cell transcriptomic dataset spanning 20 adult mouse organs (Schaum et al., 2018). The two selected *Abl2* transcripts correspond to the full length Abl2 protein and the alternatively spliced Abl2 Δ 688-791, respectively. The size of each dot represents the ratio of cells in the given cell type expressing the transcript and the color gradients denote the scaled gene expression. The full names of the cell types are detailed in Table X. TPM: transcript per million. (Bottom) The exon and intron structures of the two *Abl2* isoforms, with the highlighted intronic region denoting the protein sequence differences between Abl2 and Abl2 Δ 688-791.

ORIGINAL NAME	Abbreviation
epidermal cell	epidermal
endothelial cell	endothelial
basal cell	basal
bladder cell	bladder
leukocyte	leukocyte
microglial cell	microglia
immature T cell	imm T
B cell	B
macrophage	macrophage
mesenchymal stem cell of adipose	adipose MSC
fibroblast	fibroblast

myofibroblast cell	myofibroblast
endocardial cell	endocardial
skeletal muscle satellite stem cell	SMSSC
bladder urothelial cell	bladder urothelial
skeletal muscle satellite cell	SMSC
basal cell of epidermis	basal epidermis
astrocyte	astrocyte
keratinocyte	keratinocyte
granulocyte	granulocyte
basophil	basophil
keratinocyte stem cell	KSC
mesenchymal cell	mesenchymal
natural killer cell	NK
stromal cell	stromal
lung endothelial cell	lung endothelial
oligodendrocyte	oligodendrocyte
Slamf1-positive multipotent progenitor cell	Slamf1+ MPC
megakaryocyte-erythroid progenitor cell	MEPC
epithelial cell of large intestine	LI epithelial
immature B cell	imm B
Slamf1-negative multipotent progenitor cell	Slamf1- MPC
large intestine goblet cell	LI goblet
pancreatic A cell	pancreatic A
stem cell of epidermis	ESC
neuron	neuron
monocyte	monocyte
Brush cell of epithelium proper of large intestine	LI brush
late pro-B cell	late pro-B
naive B cell	naive B
granulocyte monocyte progenitor cell	GMPC
cardiac muscle cell	cardiac muscle
hepatocyte	hepatocyte
myeloid cell	myeloid
T cell	T
granulocytopoietic cell	GlpC
oligodendrocyte precursor cell	OPC
common lymphoid progenitor	CLP
type B pancreatic cell	pancreatic(B)
endothelial cell of hepatic sinusoid	HS endothelial
luminal epithelial cell of mammary gland	MGLEC
hematopoietic precursor cell	HPC
kidney collecting duct epithelial cell	KCD epithelial

pre-natural killer cell	pre-NK
Bergmann glial cell	Berg glial
precursor B cell	precursor B
Kupffer cell	Kupffer
pancreatic acinar cell	panc acinar
blood cell	blood
epithelial cell of proximal tubule	PT epithelial
enterocyte of epithelium of large intestine	LI enterocyte
pancreatic PP cell	pancreatic PP
brain pericyte	brain pericyte
mature natural killer cell	mat NK
epithelial cell	epithelial
pancreatic ductal cell	PDC
professional antigen presenting cell	pro APC
erythrocyte	erythrocyte
immature natural killer cell	imm NK
pancreatic D cell	pancreatic D
classical monocyte	classical mono
enteroendocrine cell	enteroendocrine
DN1 thymic pro-T cell	thymic pro-T
epithelial cell of lung	lung epithelial
pancreatic stellate cell	PSC
ciliated columnar cell of tracheobronchial tree	TTCCC
smooth muscle cell	SMC
regulatory T cell	reg T
mesenchymal stem cell	MSC
immature NK T cell	imm NKT
lymphocyte	lymphocyte

Table 3.1. Abbreviation of mouse cell types.

Minor Salivary Gland	MSG
Cortex	Cortex
Adrenal Gland	Adrenal Gland
Thyroid	Thyroid
Lung	Lung
Spleen	Spleen
Pancreas	Pancreas
Muscularis	Muscularis
Mucosa	Mucosa
Gastroesophageal Junction	GoJ
Stomach	Stomach
Sigmoid	Sigmoid
Terminal Ileum	Terminal Ileum
Transverse	Transverse
Prostate	Prostate
Testis	Testis
Sun Exposed (Lower leg)	Skin (SE)
Left Ventricle	Left Ventricle
Cerebellum	Cerebellum
Cultured fibroblasts	Cult fibroblasts
Whole Blood	Blood
Aorta	Aorta
EBV-transformed lymphocytes	EBVt lymph
Pituitary	Pituitary
Frontal Cortex (BA9)	Frontal
Caudate (basal ganglia)	Caudate
Nucleus accumbens (basal ganglia)	Accumbens
Putamen (basal ganglia)	Putamen
Hypothalamus	Hypothalamus
Spinal cord (cervical c-1)	Spinal cord
Hippocampus	Hippocampus
Anterior cingulate cortex (BA24)	ACC
Ovary	Ovary
Cerebellar Hemisphere	Cerebellar
Liver	Liver
Substantia nigra	Subs nigra
Amygdala	Amygdala
Ectocervix	Ectocervix
Fallopian Tube	Fallopian Tube
Endocervix	Endocervix
Bladder	Bladder
Medulla	Medulla

Table 3.2. Abbreviation of human tissue types.

3.2 Ongoing work to generate a CRISPR mouse model

To begin exploring whether and how the inclusion of aa. 688-791 impacts neuronal development, I investigated how the tubulin-binding region contributes to regulating dendritic spine morphogenesis and density. Dendritic spines are the major sites of excitatory synaptic transmission. Not only do spine size, stability, and density impact neuronal circuitry, dendritic arborization is also critical for supporting proper neuronal function – a readout for coverage of the receptive field that dictates size and shape of dendrites (Jan & Jan, 2010; Koleske, 2013). Dysregulation of processes supporting spines and arbor stability resulting in their loss contributes to pathology due to altered synaptic connectivity. Thus, to begin understanding how the inclusion of the exon encoding amino acids 688-791 contribute to spine density and arborization, I dissociated and cultured hippocampal neurons from P0-P0.5 C57BL/6 mice. At DIV7, these cultured neurons were co-transfected with a pLL-RFP fill and Abl2-eGFP or Abl2 Δ 688-790-eGFP, overexpressed in a wildtype background. At DIV17, neurons were fixed, imaged, and analyzed based on spine density and arborization in basal dendrites (**Figure 3.3, A**). The number of spines in secondary dendritic branches in the Abl2 Δ 688-790-eGFP overexpression condition is higher than in neurons overexpressing Abl2-eGFP ($n_{\text{spines, Abl2}\Delta}=0.79\pm 0.02$ spines $\cdot\mu\text{m}^{-1}$; $n_{\text{spines, Abl2}}=0.71\pm 0.03$ spines $\cdot\mu\text{m}^{-1}$; mean \pm SEM, $p<0.05$, **Figure 3.3, B**). Preliminary data may suggest neurons overexpressing Abl2 Δ 688-790-eGFP exhibit more dendritic arbor complexity relative to those in the Abl2-eGFP overexpression background ($n_{\text{branch tip, Abl2}\Delta}=21.9\pm 2.2$ tips; $n_{\text{branch tip, Abl2}}=18.5\pm 1.6$ tips; mean \pm SEM, **Figure 3.3, C**), though the results are not statistically significant due to low sample size. These data suggest that in mice, which predominantly express transcripts of the isoform lacking the tubulin-binding region, Abl2 Δ 688-790-eGFP may contribute to both dendritic spine density and supporting dendritic arborization.

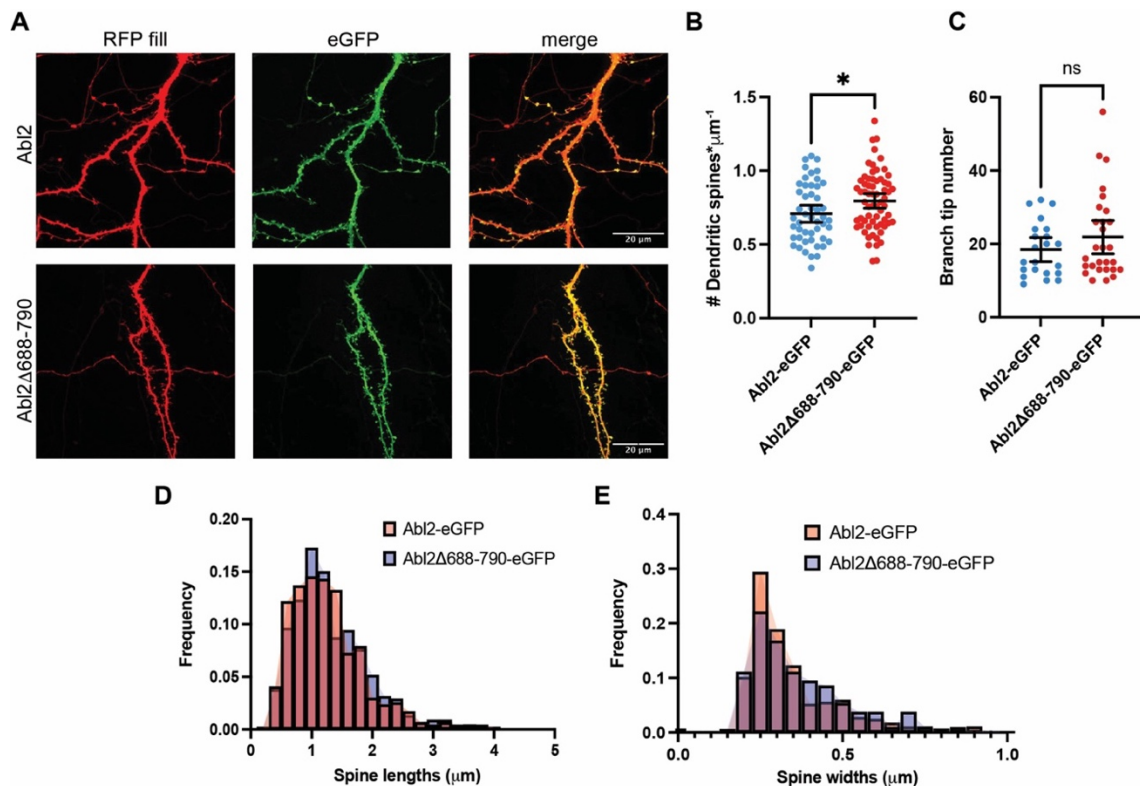


Figure 3.3. Overexpression of Abi2-eGFP or Abi2 Δ 688-790-eGFP in DIV17 cultured hippocampal neurons increases the density of dendritic spines. (A) Representative confocal images of secondary dendritic branches overexpressing Abi2-eGFP or Abi2 Δ 688-790-eGFP. (B) Dendritic spine density quantified by number per μm of secondary branch length. $p < 0.05$, Mann-Whitney test. (C) Quantification of arborization (branch tip number) in secondary dendritic branches overexpressing Abi2-eGFP or Abi2 Δ 688-790-eGFP. Mann-Whitney test reveals no statistical significance. (D-E) Histogram analyses of spine length and width (μm) distributions. Komogorov-Smirnov tests performed. No statistical significance between Abi2 and Abi2 Δ 688-790-eGFP distributions for either parameter. $n_{\text{Abi2}}=12$ neurons, $n_{\text{Abi2}\Delta 688-790}=10$ neurons from 1 culture each.

Additionally, morphology of dendritic spines is diverse, and it is known that dendritic morphology has an impact on synaptic function (Fifková & Anderson, 1981; Tamada et al., 2020). In fact, literature suggests spine head volume is proportional to the synaptic strength, as changes in the morphology of spine head has been linked to different forms of activity. Analyzing spine head dimensions will provide hints as to how changes in size and density of spines contribute to effects in synaptic transmission. Thus far, given the current sample size, analysis of spine head dimensions in either background reveals no significant differences in spine widths nor lengths between backgrounds ($\text{width}_{\text{Abi2}\Delta}=0.37 \pm 0.38 \mu\text{m}$, $\text{width}_{\text{Abi2}}=0.35 \pm 0.01 \mu\text{m}$; $\text{length}_{\text{Abi2}\Delta}=1.26 \pm 0.03 \mu\text{m}$, $\text{length}_{\text{Abi2}}=1.29 \pm 0.03 \mu\text{m}$; $\text{mean} \pm \text{SEM}$, **Figure 3.3, D-E**). Five additional cultures over-expressing

RFP alone or with Abl2-eGFP or Abl2 Δ 688-790-eGFP were fixed and imaged. Immediate follow-up steps include completing the analysis of blinded images and determining if there is statistical significance in Abl2 Δ 688-790-eGFP promoting dendritic arborization; and comparing the spine densities and spine morphological features in these neurons relative to those in neurons over-expressing RFP alone as proper control. Future experiments include knocking down endogenous Abl2 isoforms and re-expressing Abl2-eGFP, Abl2 Δ 688-791-eGFP, and oligomerization-defective Abl2-eGFP (see section 4.1).

As Abl2 transcripts are alternatively spliced, we wondered if we could generate a mouse line that strongly suppresses the exclusion of the exon encoding aa. 688-791. Calculation of splice site maximum entropy scores reveals that the 5' and 3' splice sites flanking the exon are highly favorable for splicing (bolded in row 1, **Table 3.3**). However, there are site-directed mutations that could be made to strongly disfavor splicing (mutations whose max entropy score < 0). A plasmid carrying Abl2-eGFP harboring point mutations at the +2 position of 5' splice site sequence (max entropy score of -2.33) and at the +1, +2 positions of the 3' splice site sequence (max entropy score of -14.33) was cloned and transfected into murine N2A cells. Proof-of-principle PCR analyses reveal that these transfected N2A lysates contain Abl2 transcripts with more inclusion of the exon relative to non-transfected N2A cell extracts. An immediate future direction is developing a mouse line that expresses the full Abl2 transcript using CRISPR/Cas9 technology to mutate two sites within the 5' (U→A) and 3' (CA→GT) splice site sequences within Abl2 (Hall et al., 2018). Downstream experiments include determining whether there are behavioral differences and anatomical differences (brain mass, size, dimensions of cortical layers, etc) between these mice and wildtypes, and how inclusion of aa. 688-791 impacts MT dynamics via live-cell imaging and synaptic transmission via electrophysiology.

5' splice site variants		3' splice site variants	
MaxEnt inputs	Max entropy score	MaxEnt inputs	Max entropy score
cgggtaact GUAACU	5.86	tacatcttccatgtcctcagggc CAG	9.58
cgggaaact GAAACU	-2.33	tacatcttccatgtcctctgggc CUG	1.21
cgggcaact GCAACU	-1.90	tacatcttccatgtcctccgggc CCG	1.54

cgggtaatt G <u>UAAUU</u>	6.79	tacatcttccatgtcctcggggc CGG	1.62
cgggaaatt G <u>AAAUU</u>	-1.40	tacatcttccatgtcctgtgggc GTG	-14.33
cgggcaatt G <u>CAAUU</u>	-0.97	tacatcttccatgtcctagcggc AGC	-9.02
cggggaatt G <u>GAAUU</u>	-0.86		

Table 3.3. Splice site maximum entropy scores. Cells bolded are original splice sites (5' site: cgggtaact at nt 2060-2068; 3' site: tacatcttccatgtcctcagggc at nt 2355-2377). Scores were calculated using MaxEntScan model (Yeo & Burge, 2004).

3.3. Materials and Methods

Isoform abundance profiling for ABL2/Abl2 across adult human and mouse organs

We downloaded the SMART-seq2-based single cell transcriptomic data profiling 20 adult mouse organs from Tabula Muris (Schaum et al., 2018) and conducted RSEM analysis (Li & Dewey, 2011) to measure the abundance of *Abl2* isoforms (**Figure 3.1, Table 3.1**). Specifically, we first built the genome reference by running *rsem-prepare-reference* on the mouse GRCm39 genome assembly and the GENCODE vM32 gene annotation. The built reference was then piped into *rsem-calculate-expression* function together with the STAR algorithm for alignment and isoform abundance quantification. We extracted the TPM values from the RSEM outputs and log-transformed the values for visualization using R ggplot2 package.

In measuring the ABL2 isoform abundance in the GTEx human bulk-tissue RNA-seq data across 30 organs, we directly utilized the processed expression data from the GTEx Portal (Lonsdale et al., 2013) followed by visualization using R ggplot2 package (**Figure 3.2, Table 3.2**). The GTEx also applied RSEM in the isoform abundance quantification, which enabled direct comparisons of the transcript expression patterns between human and mouse.

Neuronal cell culture

Hippocampal cultures were prepared from P0-P0.5 WT C57BL/6 mice. Hippocampi were dissected in ice-cold HBSS supplemented with 10 mM HEPES, 1X pyruvate, 100 units*ml⁻¹ penicillin, 100 µg*ml⁻¹ streptomycin (HBSS+). Tissue was digested with 0.2U*ml⁻¹ papain supplemented with 0.2 mg*ml⁻¹ L-cystine at 37°C for 10 min. Digested tissue was washed twice in HBSS+ medium and triturated in Neurobasal Plus medium supplemented with 10% FBS and B-27 (Thermo Fisher

Scientific). $\sim 0.3 \times 10^6$ cells were plated onto poly-d-lysine coated #1.5 10 mm acid-washed glass coverslips in a 24-well plate. Medium was switched to Neurobasal Plus medium supplemented with B-27 after 3 hours. On day 3, cultures were treated with 1 μ M Ara-C to inhibit glia growth. Half of medium was exchanged at day 6 with fresh Neurobasal Plus medium supplemented with B-27 to deplete Ara-C.

Neuronal cell transfection, fixation, and image acquisition

DIV7 hippocampal neurons were transfected with pN1-Abl2-eGFP or with pN1-Abl2 Δ 688-790-eGFP via calcium-phosphate transfection. In brief, medium was exchanged with pre-warmed DMEM medium. Conditioned medium was filtered with 0.22 μ m syringe filter and kept in 37C water bath. DNA/CaCl₂ mix was prepared with 3 μ g of pN1-Abl2-eGFP or pN1-Abl2 Δ 688-790-eGFP with 0.5 μ g of pLL-RFP as fill, and 350 mM CaCl₂. DNA/CaCl₂ was mixed with equal volume of 2X HeBS at 1/10 of volume at a time via vortexing for 3s per addition. Mixture was allowed to incubate for 20 min at RT prior to adding to neurons/well. Transfection medium was allowed to incubate for \sim 3h. Conditioned medium was supplemented with 100 units*ml⁻¹ penicillin, 100 μ g*ml⁻¹ streptomycin up to original volume (fresh Neurobasal/B27 was added to desired volume if needed). Neurons were washed with 3 changes of HBS0/2, pH 6.7. Conditioned medium was added back into the well.

DIV17 neurons were fixed with 4% PFA supplemented with 4% sucrose for 15 min. Fixed neurons were washed 3X with PBS followed with 20 min permeabilization period with 0.1% Triton X-100 in PBS, and a quick wash in PBS after. Cells were blocked with 10% donkey serum for 1h at RT. α -RFP and α -eGFP primary antibodies were diluted at 1500 ratio in 1:1 donkey serum: PBS solution (AbDil). Neurons were stained overnight at 4C. Coverslips were washed 3X with PBS solution supplemented with 0.05% Tween-20 at RT on a shaker. Secondary antibody AbDil solution was prepared at 1:500 ratio for RFP and eGFP. Coverslips were quickly washed in dH₂O prior to mounting on #1.5 glass cover slides with ProLong Diamond Antifade mountant. Images were acquired using a Nikon CSU-W1 SoRa spinning disk confocal, with 5% laser power (LP) for 561,

and 5% LP for 488 nm channels, at 200 ms exposure time each. All samples were blinded during image acquisition and analysis.

Chapter 4: Regulation of Abl2 on the tubulin code

My work shown here reveals that Abl2 binds tubulin dimers and tubulin-binding is required for Abl2 to promote MT nucleation (see Chapter 2). Identifying the interfaces on Abl2 and tubulin dimer that mediates the binding interaction will provide rich structural insight as to how Abl2 stabilizes inter- and intra-dimer interactions, as revealed from cryo-EM data (**Figure 2.30**). For example, HDX analysis from an early mass-spectrometry revealed that Taxol binding applies pressure on the H10 helix of the β -subunit at the intradimer interface likely to maintain the dimer in a straight lattice-competent conformation (Xiao et al., 2006). A follow-up study demonstrated that Taxol increases the flexibility of the β -tubulin and contacts the adjacent α -monomer of the next dimer along the protofilament to maintain longitudinal contacts (Mitra & Sept, 2008). It will be interesting to determine whether Abl2 stabilizes inter- and intra-dimeric interactions along the lattice through similar binding modes.

Additionally, both α - and β -tubulin acidic tails carry post-translational modifications that vary in levels of polyglutamylation, polyglycylation, acetylation, tyrosination, deytrosination, to name a few. MTs are also polymerized from a combinatorial code of multiple α - and β -tubulin isotypes. The combination of different PTMs and isotypes makes up the 'tubulin code', which generates a diversity of microtubule lattices. Multiple biochemical studies have demonstrated that the tubulin code differentially recruits MBPs onto MTs in various signaling cascades. Determining whether Abl2 has a tubulin code readout mechanism and whether Abl2 functionally interacts with a particular tubulin isotype(s) in a developing mouse brain may shed light on how Abl2 may regulate MT dynamics for dendritic development and synapse stability.

Data from this chapter have not been published. Cross-linking mass spectrometry was done in collaboration with Mike Trnka from the UCSF Mass Spectrometry Facility. All animal behavior assessments were performed by Noële Certain.

4.1. Crosslinking mass spectrometry to identify the Abl2:tubulin binding interface

Crosslinking mass spectrometry (CLMS) is a powerful tool that provides structural information on the folds of proteins (*i.e.* intramolecular interactions), and binding interfaces between binding

partners. As CLMS detects interactions between individual residues, it is a technology that provides information on protein complex topology. CLMS has been used, for example, to elucidate the structural arrangement of autoinhibited kinesin-1, which will shed light on how kinesin-1 inhibits motility for transporting cellular cargo (Tan et al., 2023). Tan and others discovered that kinesin-1 undergo four intramolecular interactions: 1) crosslinks within the motor domain; 2) motor-to-tail crosslinks that involve residues at the C-terminus of its fourth coiled-coiled CC4 domain; 3) motor-to-CC2 crosslinks; 4) and crosslinks within CC2, CC3, and CC4. These results disproved the original notion that kinesin-1 folded back through the proposed hinge between CC2 and CC3 domains. Rather, their CLMS results rigorously prove the folding of the stalk domain is mediated by a small region within CC3 that serves as a hinge to allow CC3b and CC4 to interact with CC2 and CC3a. In an earlier study, CLMS was also shown to provide structural information on the heteromeric complex between tau and tubulin dimers (Kadavath et al., 2015). BS³ crosslinking revealed that tau binds at the interface between α - β -tubulin heterodimers, specifically at the N-terminal end of helix H10 of α -tubulin. Gaining a detailed view on where tau binds to tubulin heterodimers provided authors a greater understanding of how tau remodels longitudinal dimer contacts for MT assembly and stability.

To further elucidate how Abl2 stabilizes protofilaments to mediate MT nucleation, I was determined to identify the binding interfaces between Abl2 and α - β -tubulin. As with tau and other MBPs that promote nucleation such as doublecortin (Fourniol et al., 2013), I hypothesized that Abl2 may bind at the heterodimeric interface, acting as a molecular stapler to stabilize inter- and intra- protofilament interactions. To test this hypothesis, I conducted BS³ crosslinking between 6XHis-Abl2 and porcine tubulin by preincubating the protein mixture with freshly prepared crosslinker (3.3 mM BS³) on ice for 30 min, which was followed by visualization via Coomassie-stained SDS/PAGE. Gel bands of complexes that migrated at ~235 kDa were excised and sent to Mike Trnka (UCSF Mass Spectrometry Facility) for mass-spectrometry analysis. Immunoblot analysis reveals that the sample includes both Abl2:tubulin crosslinked and Abl2 self-associating oligomers in the final reaction (**Figure 4.1**).

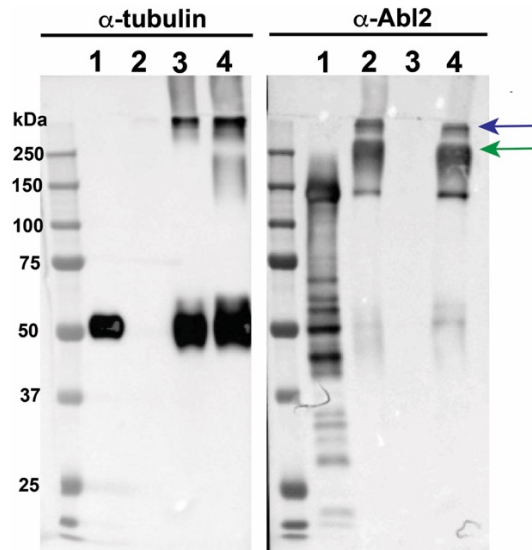


Figure 4.1. Immunoblots confirm that while there is a subpopulation of Abl2:tubulin crosslinked complexes, high molecular weight Abl2 oligomers predominate. Chemiluminescence using α -DM1a antibody shown on left, α -Ar11 (Abl2 C-terminal half epitope) shown on right. Blue arrow denotes the top band that contains the Abl2:tubulin crosslink (map of crosslinks shown in Figure 4.1). Green arrow denotes the bottom band that contains only Abl2 self crosslinks. 1: Abl2 and tubulin, no crosslinking. 2: Abl2 crosslinked. 3: tubulin crosslinked. 4: Abl2 and tubulin, crosslinked.

Crosslinked peptides with an SVM score > 0.5 were mapped using xiVIEW (Graham et al., 2019). CLMS reveals that Abl2 K811 crosslinks to aa. 163 of α -tubulin, localizing to the linker region between helix H4 and β -strand S5; and aa. 58 of β -tubulin, which localizes in a linker region between helix H1 and β -strand S2 (**Figure 4.2**). Since the same peptide containing K811 in Abl2 contacts both subunits, it is likely that two Abl2 molecules interfaces with a single tubulin dimer. This may be sterically possible given that the tubulin binding region, Site I encompassing aa. 688-924, is predicted to be unstructured. However, given our biochemical data that suggest Abl2 contains two tubulin-binding sites (the other localized to Site II, aa. 924-1024), it is curious that there is not an heteromeric crosslink that maps between Site II and tubulin detected in CLMS results. There exist several experimental differences, one of them being CLMS set-up requires higher amounts of purified 6XHis-Abl2 at concentrations that promote self-association. This is in stark contrast to BLItz which requires immobilized Abl2 ligand to be used at nanomolar concentrations. Thus, it is probable that Abl2 oligomerizes via Site II (to be discussed below), thereby competing off tubulin dimers from accessing the site.

Unsurprisingly, both residues within the tubulin subunits are localized at interfaces that are oriented along the outer MT surface. It was shown before through co-sedimentation assays that Abl2 binds to the acidic C-terminal tails of tubulin dimers, as subtilisin cleavage of taxol-stabilized MTs substantially reduced Abl2 affinity (Hu et al., 2019). However, these electrostatic interactions are not detected, likely because BS³ is not capable of capturing these weaker, more transient interactions and instead targets stably interacting residue pairs within a distance of ~20Å (Merkley et al., 2014).

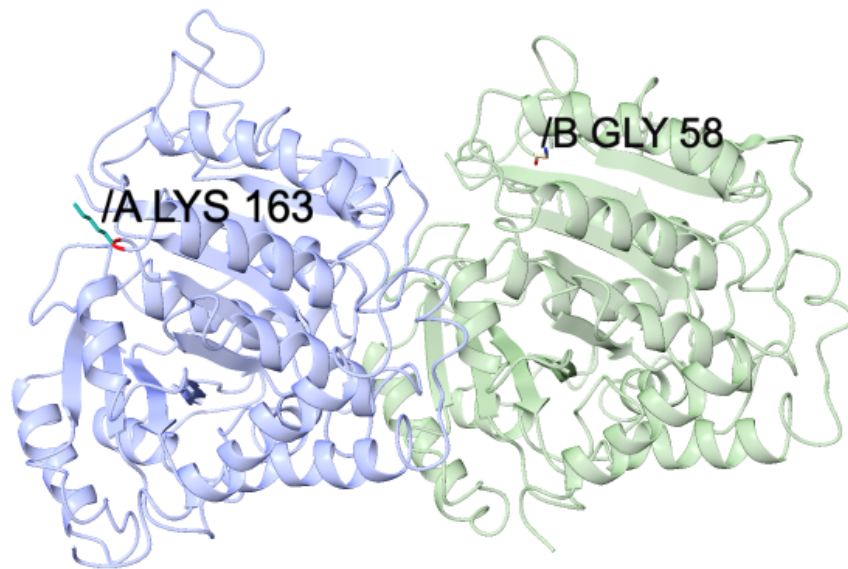


Figure 4.2. Structure of *Sus scrofa* tubulin heterodimer. α -subunit shown in blue-purple. β -subunit shown in green. Sticks are residues (K163 in chain A; G58 in chain B) that are crosslinked with Abl2 K811. PDB: 1TUB.

Due to poor database annotation, we were only able to match the peptides to the following isotypes: crosslinked peptide belonging to TUBA1A, TUBA1B, TUBA4A, TUBA3, and TUBA3C; and the crosslinked peptide within the β -subunit uniquely matched back to TUBB2B (**Figure 4.3**). Identification of tubulin isotypes that may be recognized and targeted by Abl2 in cells and neurons will shed light on the tubulin code, which is a molecular pattern generated by combinations of both isotypes and post-translational modifications (PTMs, more discussion in Section 4.3). MTs assembled from different isotype incorporation has been shown to impact dynamics and mechanical properties (Janke & Magiera, 2020; Roll-Mecak, 2020; Vemu et al., 2016). Thus, future studies include purifying tubulin heterodimers with β 2B and β III subunits (e.g. α 1A/ β III) from insect

cells for *in vitro* binding assays and functional MT dynamics assays (Ti et al., 2020). Doing so will provide greater resolution into Abl2 specificity for tubulin dimers in the cells for regulating MT assembly.

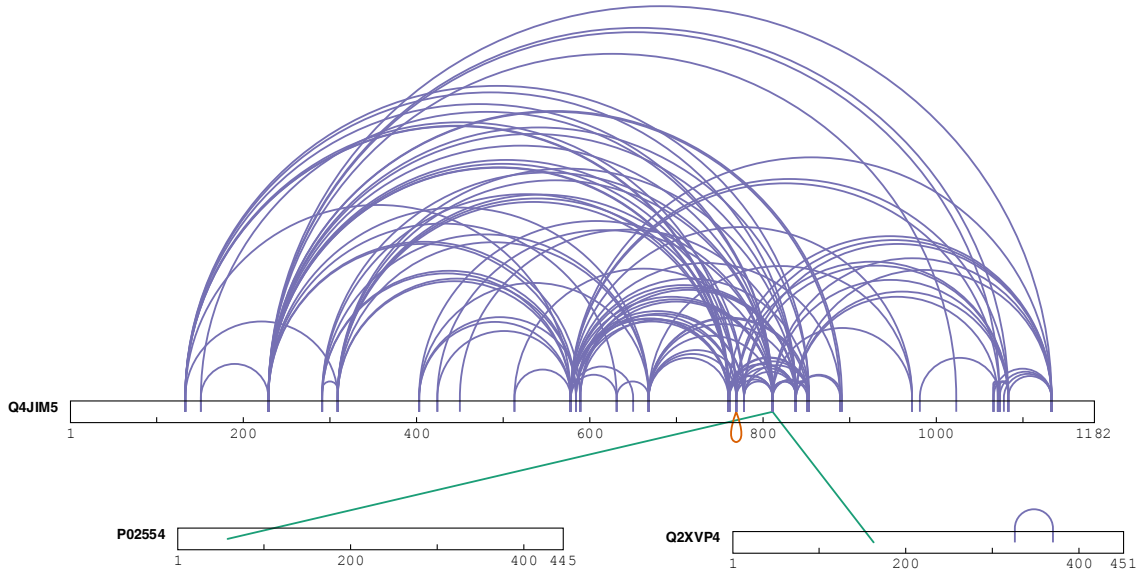


Figure 4.3. Circular map of intra- and inter-molecular interactions between Abl2, tubulin α - and β -subunits. Only interactions whose SVM scores were higher than 0.5 are shown. 1: Abl2 and tubulin, no crosslinking. 2: Abl2 crosslinked. 3: tubulin crosslinked. 4: Abl2 and tubulin, crosslinked. Links shown in red are homo-multimeric (overlapping peptides). Links shown in purple are self interactions. Links in green are heteromeric. Schematic was generated using xiVIEW (Graham et al., 2019). Q4JIM5: *Mus musculus* Abl2. Q2XVP4: *Sus scrofa* tubulin alpha-1B chain. P02554: *Sus scrofa* tubulin beta chain.

Of the 132 unique self-crosslinks within Abl2, 79 (59.8%) of them are within the C-terminal half (557-1182); 49 (37.1%) are interactions between the N- and C-terminal half; with 4 (3%) of them residing only within the N-terminal half (aa. 74-556, **Figure 4.3**). Interestingly, 24% of the crosslinked peptides mapped to the N-terminal half (aa. 74-556), 21.8% of self-crosslinked peptides mapped back to aa. 557-687, 14% mapped to aa. 925-1182 (F-actin binding domain), with the rest (40%) mapping back to aa. 688-924. The majority of the self-interacting interfaces reside within the tubulin-binding region. Of note, a portion of the tubulin binding region site I, aa. 688-791, is the one of the most structured regions within the C-terminal half (**Figure 4.4, A**), despite the larger aa. 688-924 region being enriched in amino acids (prolines, glycines, serines) that increase the propensity of phase separation (**Figure 4.4, B**). Site II, aa. 924-1024, has the highest proportionate content of prolines, which is a hallmark property of many intrinsically disordered proteins (IDPs, **Figure 4.4,**

B) (Theillet et al., 2013). Though prolines are disorder-promoting, it is possible that the abundance of this amino acid in the C-terminal half of Abl2 helps rigidify its backbone conformation to spatially separate itself as a functionally important protein region. Further discussion of proline content can be found in Section 5.1. Additional information on oligomerization and implications of phase-separated Abl2 molecules can be found in Section 6.2.

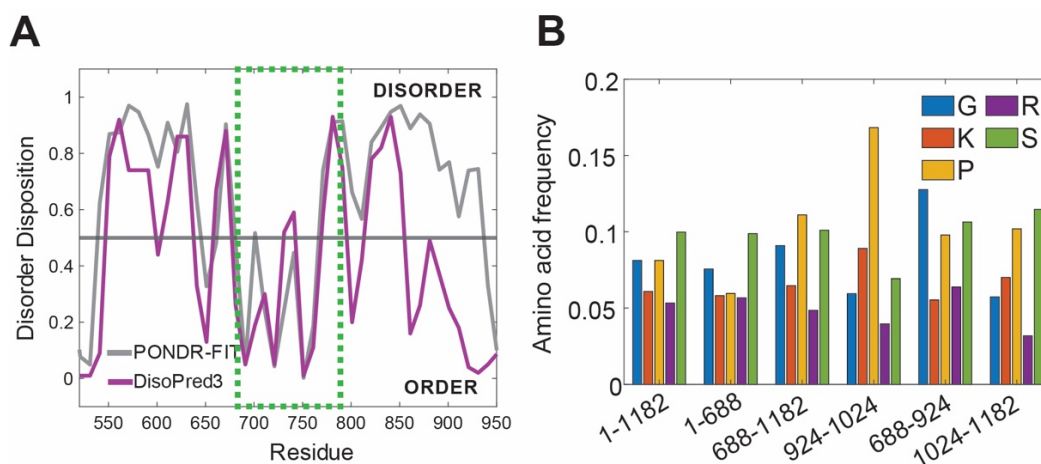


Figure 4.4. Disorder content prediction for tubulin-binding region, aa. 688-924 (Site I). (A) Disorder prediction from primary sequence of murine Abl2 aa. 557-924 using POND-R-FIT and DisoPred3 algorithms. Disorder disposition of 0.5 was used as the threshold, shown in gray line. Green dashed box highlights portion of the identified tubulin binding region, aa. 688-791. (B) Amino acid frequency of glycines (G), lysines (K), arginines (R), serines (S), and prolines (P) in each fragment within Abl2.

4.2. Structure of Abl2:tubulin complex

Knowing that Abl2 binds to tubulin dimers and promotes MT nucleation, I was determined to know whether Abl2 binds at the intradimer interface. I hypothesized that analogous to kinesin-5 which promotes MT nucleation, one way Abl2 reduces the lag time for MT assembly by stabilizing a conformation of the dimer to make it lattice-competent, *i.e.* bent to straight (Chen et al., 2019). To do this, Abl2 would likely bind at the intradimeric site. To test whether Abl2 promotes a structural change in tubulin dimers, I conducted a simple fluorescence-based assay to quantify colchicine-binding kinetics. Colchicine is an intradimeric wedge inhibitor and locks the dimer at the kinked conformation. Upon binding to tubulin dimers, colchicine-tubulin complex naturally excites at $\lambda=366$ nm (Bhattacharyya & Wolff, 1974). Incubation of 1 μ M Abl2 with 5 μ M tubulin followed by addition of 50 μ M colchicine will reveal whether Abl2 sterically competes for the colchicine binding site at

the intradimeric interface (**Figure 4.4**). Fitting the fluorescence signal to a biexponential (Equation 4.1) will yield fitted values to two rate constants indicative of two phases: 1) k_1 which reflects the initial encounter or binding event (fast phase); and 2) k_2 which reflects conformational change (slow phase).

$$y = C_1 e^{-k_1 x} + C_2 e^{-k_2 x} \text{ (Equation 4.1)}$$

If Abl2 binds at the intradimeric site, this will sterically inhibit colchicine from binding, thereby altering the k_1 parameter. If Abl2 stabilizes the straight dimer conformation rather than the bent, this would also prevent colchicine from binding, thereby affecting the k_2 rate constant due to differences in tubulin conformation. Upon fitting the fluorescence curves of reactions with and without Abl2 to **Equation 4.1**, I found that the rate parameters, k_1 nor k_2 , do not significantly change in the presence of Abl2 which suggests that Abl2 does not bind at the intradimeric interface nor does it change the intrinsic kinked/curved conformation of soluble tubulin ($k_{1,\text{tub alone}} = 0.0063 \text{ s}^{-1}$, $k_{2,\text{tub alone}} = 5.7\text{e-}5 \text{ s}^{-1}$; $k_{1,+Abl2} = 0.0058 \text{ s}^{-1}$; $k_{2,+Abl2} = 6.8\text{e-}5 \text{ s}^{-1}$).

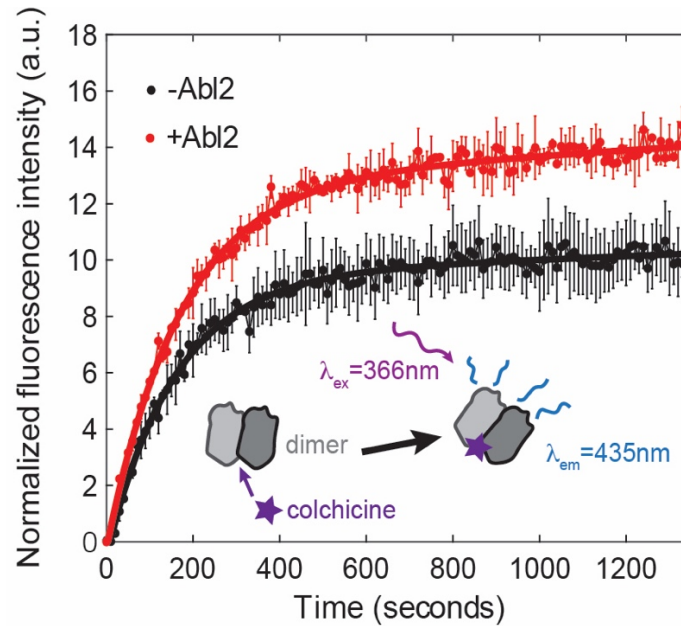


Figure 4.4. Abl2:tubulin:colchicine binding kinetics reveal that Abl2 does not bind at the wedge inhibitor site nor induce a bent-to-straight conformational transition. 5 μM tubulin incubated with 50 μM colchicine yielded an amplitude of 10 a.u., $k_{1,\text{tub alone}} = 0.0063 \text{ s}^{-1}$, $k_{2,\text{tub alone}} = 5.7\text{e-}5 \text{ s}^{-1}$. Presence of 1 μM Abl2 yielded an amplitude of 14 a.u., $k_{1,+\text{Abl2}} = 0.0058 \text{ s}^{-1}$; $k_{2,+\text{Abl2}} = 6.8\text{e-}5 \text{ s}^{-1}$. Scatter plots denote the mean of normalized fluorescence intensities upon excitation at $\lambda=366 \text{ nm}$. Measurements recorded at $\lambda=435 \text{ nm}$ for 1350s. Fluorescence curves (solid lines) were fitted to a biexponential $y = C_1 e^{-k_1 x} + C_2 e^{-k_2 x}$, where k_1 is the rate parameter for the initial tubulin binding or association event (fast phase); k_2 is the rate parameter for tubulin conformation change (slow phase). $n = 2$ technical replicates.

To gain a higher resolution of the Abl2:tubulin structure, I pursued negative-stain EM to resolve 2D class averages of the complex. Initial attempts revealed that Abl2:tubulin complexes were too heterogeneous. Thus, I pursued glutaraldehyde gradient fixation (GraFix) to stabilize the Abl2:tubulin complex on grids (Stark, 2010). A glutaraldehyde gradient was formed for 18h and fractions were harvested manually. Silver stain revealed unbound and bound proteins at various molecular weights (**Figure 4.5, A**). Fractions 7 and 8 yielded Abl2:tubulin structures of the expected size ($\sim 235 \text{ kDa}$, **Figure 4.5, A**). However, despite troubleshooting various percentages of glutaraldehyde and glycerol cushion to weakly crosslink and stabilize the Abl2:tubulin complex, I still observed heterogeneity amongst the particles in the fractions (**Figure 4.5, B**).

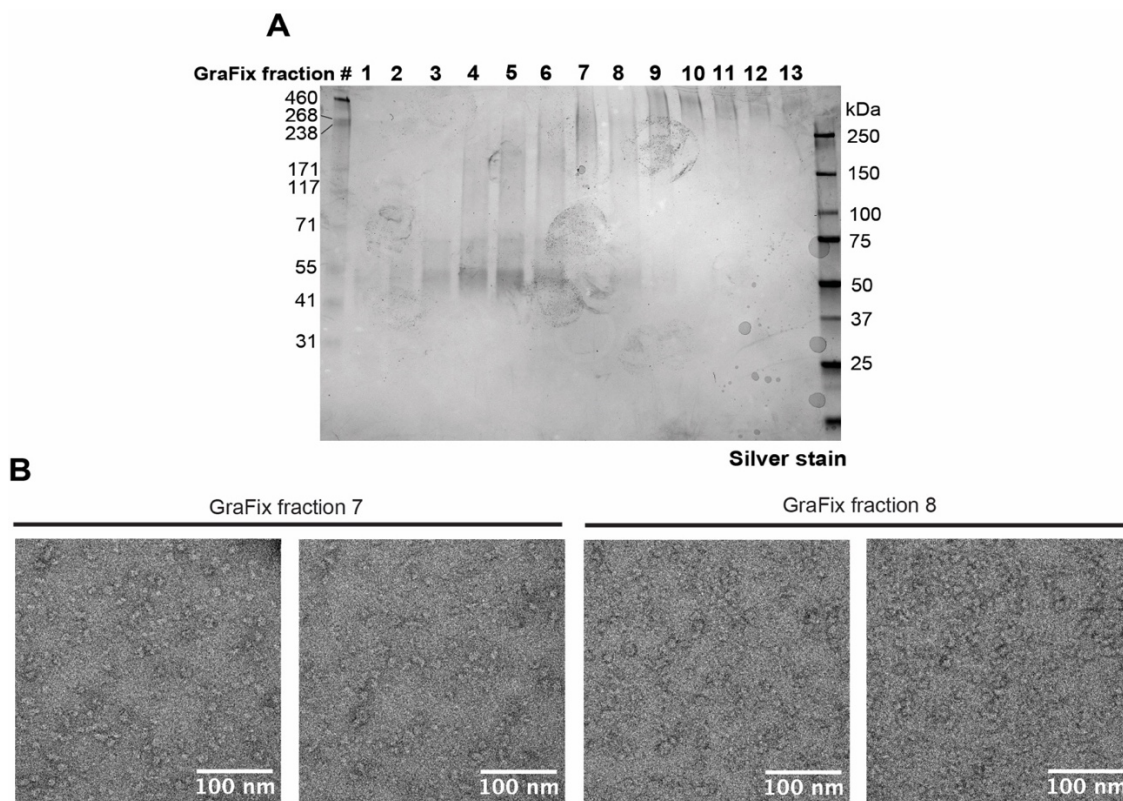


Figure 4.5. Negative stain EM reveals that GraFix fractions contain heterogeneous structures of Abl2:tubulin complexes. (A) Representative silver stain image of a GraFix experiment using $0.5 \text{ mg}\cdot\text{ml}^{-1}$ 6XHis-Abl2 and $0.35 \text{ mg}\cdot\text{ml}^{-1}$ tubulin dimers. Fractions 7 and 8 yielded complexes of predicted complex size of $\sim 235 \text{ kDa}$ for a 1:1 stoichiometry. **(B)** Negative stain EM micrographs of fractions from the same GraFix run shown in (A). 2D class averaging reveals high heterogeneity in structures (not shown).

It is likely that a binding partner at the C-terminus or N-terminus to mediate long-range conformational changes in Abl2 is required to stabilize the non-tubulin/MT-binding region to achieve 2D class averages for negative stain EM and single-particle cryo-EM. It is unlikely that the N-terminal half solely contributes to Abl2 binding on MTs (**Figure 4.6**). Imatinib is a type II inhibitor thereby occupying the ATP-binding pocket to stabilize the closed, inactive conformation. Purifying Abl2-eGFP from STI571-treated (imatinib-treated) insect cells reveals that Abl2-eGFP maintains the molecule in an unphosphorylated, inactive state (**Figure 4.6, A**).

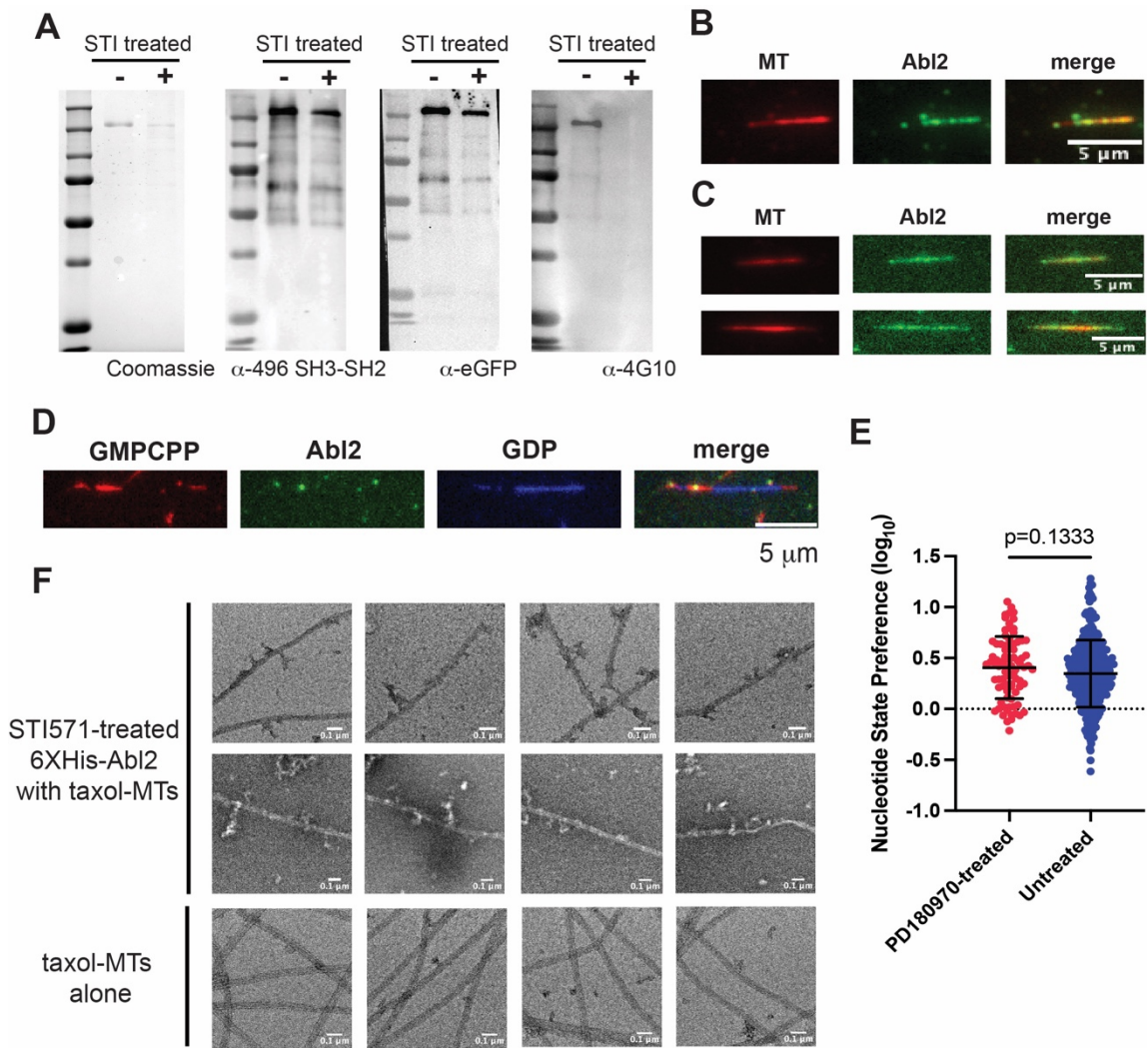


Figure 4.6. Imatinib-treated Abl2 display similar MT-binding characteristics as phosphorylated Abl2. (A) 10 ng of protein loaded for each immunoblot shown. (B) 0.5 μ M STI571-untreated Abl2 on GMPCPP-MTs. (C) 0.5 μ M STI571-treated Abl2 on GMPCPP-MTs. (D) PD180970-treated 6XHis-cleaved Abl2-eGFP on a segmented MT. (E) Quantification of PD180970-treated Abl2-eGFP occupancies on GMPCPP (GTP-like) and GDP-polymerized MT segments. $n_{\text{PD180970-treated}} = 82$ segmented MTs; $n_{\text{non-treated}} = 288$ segmented MTs across 2 technical replicates. Unpaired t-test with Welch's correction performed. (F) Representative negative-stain EM micrographs of imatinib-treated 6XHis-Abl2 on taxol-stabilized MTs. Kinase-inactive closed conformation of Abl2 does not improve its decoration pattern on MTs.

Upon visualizing the binding behavior of Abl2 on MTs under TIRF microscopy, though at first glance imatinib-treated Abl2-eGFP adopts a more uniform decoration on MTs relative to its phosphorylated kinase-active form (Figure 4.6, B-C), negative stain EM reveals, at much greater resolution, that kinase-inactive Abl2 forms aggregated-like oligomers on taxol-stabilized MTs (Figure 4.6, F) which is analogous to untreated Abl2 (Hu et al., 2019). Interestingly, however, compared to its

phosphorylated form (shown in **Figure 2.26**), Abl2 treated with ATP-competitive inhibitor PD180970, which targets both Abl1 and Abl2, retains its preferential localization on expanded MTs (**Figure 4.6, D-E**). The pursuit of resolving the structure of the Abl2:tubulin complex and obtaining particles with a more uniform decoration of Abl2 on MTs is likely hindered from identifying a binding partner that may otherwise stabilize the floppy, unstructured C-terminal half. Future directions include identifying and validating binding partners of Abl2 from BioID-mass spectrometry screen via *in vitro* binding assays and Abl2 co-immunoprecipitation from cell lysates.

4.3. Post-translational modifications of tubulin in whole brain lysates

Tubulin subunits assemble into MT polymers whose dynamics are tightly coupled to nucleotide hydrolysis. The dynamics are further tuned in the cell by post-translational modifications (PTMs), which predominantly influence the recruitment of various MBPs including MAPs and molecular motors (Janke & Magiera, 2020; Roll-Mecak, 2020). These PTMs include tyrosination, detyrosination, polyglutamylation, polyglycylation, $\Delta 2$ -detyrosination, and acetylation, among others. PTMs on tubulin have been shown to be linked to lattice integrity and MT dynamics. For example, acetylation of tubulin in the lattice has been shown to be resistant against mechanical forces as acetyltransferase TAT1 can enter into the lumen, locally acetylate tubulin dimers to increase lattice plasticity, such that the polymers become more labile and resistant against breakage (Portran et al., 2017; Xu et al., 2017). Interestingly, acetylation of the α -subunit at K40 residue has been shown to directly impact the local MT structural architecture by promoting stability via weakening both lateral tubulin-tubulin contacts and inter-protofilament interactions (Eshun-Wilson et al., 2019; Portran et al., 2017).

Polyglutamylation of tubulin C-terminal tails regulates kinesin-3 KIF1A mobility and induces pausing (Lessard et al., 2019). MAP7 was also shown through cell-based assays to promote axonal branch maturation by stabilizing microtubules at junctions, preferring to bind acetylated polymerized tubulin and not tyrosinated (Tymanskyj & Ma, 2019). Additionally, glycylation and glutamylation are PTMs that have antagonistic effects on katanin activity: glutamylation of the α -tubulin subunit tail by tubulin tyrosine ligase-like (TTLL) TTLL6 enhances MT binding and severing;

whereas glycylation by TLL3 and TLL10 in cilia decreases katanin binding and severing (Szczesna et al., 2022). The number of glycines has been shown to be proportional to inhibition. Importantly, they show that glutamylation on the β -tail by TLL7, whose expression is essential for nerve growth factor-stimulated MAP2-positive neurite growth (Ikegami et al., 2006), regulates katanin severing. Tyrosination of α -tubulin is critical for dynein-dynactin-BicD2 (DDB) motility and p150 binding (McKenney et al., 2016), whereas plus-end directed kinesin-2 prefers detyrosinated MTs for robust motility (Barisic et al., 2015; Sirajuddin et al., 2014). It is postulated that these PTMs could bias direction of cargo transport in cells and neurons.

The detyrosination/tyrosination cycle of α -tubulin along with other PTMs encodes information on MTs to properly regulate coordinated intracellular processes. Disruption of this information encoding on tubulins can lead to cancer, cardiac diseases, and neurodevelopmental disorders. Tubulin detyrosination accumulates at early stages of muscle cell differentiation, with acetylation levels gradually increasing throughout (Kerr et al., 2015). Proper regulation of detyrosinated tubulin levels ensures load-bearing of buckling MTs during cardiomyocyte contraction. Upregulation of detyrosinated tubulin correlated with impaired function in animal models of heart disease, and has been found in patients with hypertrophic cardiomyopathies (Robison et al., 2016). Additionally, decreased tubulin acetylation has been found to be linked to various neurodegenerative disorders including Huntington's Disease, Amyotrophic lateral sclerosis, and Parkinson's disease due to dysregulation of axonal transport (Magiera et al., 2018). Neurons from patient-derived pluripotent stem cells reveal that chemical inhibition of deacetylating enzyme HDAC6 was sufficient to restore normal tubulin acetylation levels and normal axonal transport. Another study reveals that MT acetylation is directly linked to mechano-sensation, as *Atat1^{ckO}* mice (α -tubulin acetyltransferase) display loss of mechanical sensitivity to touch and painful stimuli (Morley et al., 2016). It remains elusive as to how acetylation at residue K40 of α -tubulin within the lumen of a MT impacts axonal transport. However, tubulin PTM levels are carefully regulated in physiology, and upon getting slightly tuned, give rise to disease and pathology.

In addition PTMs, there exists 8-10 isotypes of α -tubulin and 7-9 isotypes of β -tubulin in humans, making the tubulin code combinatorial and expansive (Wethekam & Moore, 2023). One

of the isotypes is the β -tubulin neuronal isoform, *Tubb3*. Latremoliere *et al.* show that *Tubb3* gene is not required for normal development of the nervous system, as there was compensation by other β -tubulin isoforms (Latremoliere *et al.*, 2018). However, depletion of *Tubb3* decreased MT dynamics in growth cones and delayed functional recovery following peripheral nerve injury. Additionally, MTs in *Tubb3*^{-/-} brains exhibit higher levels of polyglutamylation and acetylation, suggesting that MTs are more stable than those in WT brains. PTM quantification suggested that MTs in *Tubb3*^{-/-} mice were more stable, exhibiting a reduction in MT dynamics. *Tubb3*^{-/-} growth cones exhibit decreased MT growth velocities and a significant reduction in total displacement relative to WT growth cones. These data suggest that *Tubb3* is necessary for MT dynamics to regulate growth cone function.

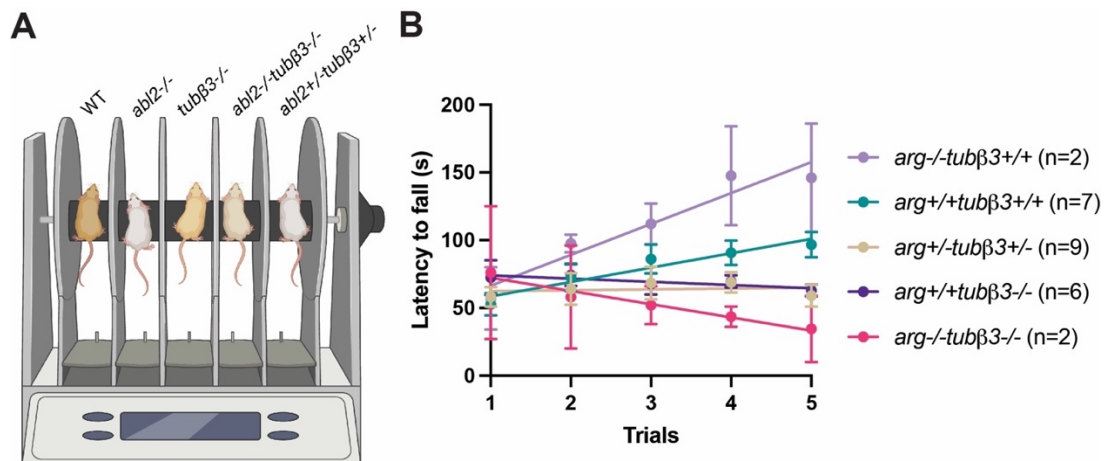


Figure 4.7. Rotarod performance test reveals an *abl2* and *tubβ3* gene-dosage effect on motor coordination. (A) Rotarod performance test assesses locomotion and balance and detects motor deficits in mice. (B) Loss of *tubβ3* impairs motor coordination. Loss of *abl2* on top of *tubβ3* deletion severely compromises motor coordination in mice.

Given that Abl2 binds to tubulin dimers and regulates MT dynamics *in vitro* and in cells, I hypothesized that Abl2 may interact with tubulin $\beta3$, the predominant neuron-specific isotype, to support growth cone behavior, particularly in growth cone repellent guidance. To test this, new mouse lines harboring different number of *abl2* and *tubb3* gene copies (particularly *abl2*^{-/-}*tubβ3*^{-/-} and *abl2*^{+/-}*tubβ3*^{+/-}) were generated by crossing *abl2*^{+/-} and *tubb3*^{+/-} mouse lines. To first assess whether there was a gene-dosage effect on motor coordination, postdoctoral fellow Dr. Noële Certain of the Koleske Lab conducted rotarod performance tests to measure locomotion balance (Figure 4.7, A). Preliminary results show that while mice with a reduced gene dosage of both *abl2*

and *tubβ3* (latency to fall by 5th trial = 59 s, **Figure 4.7, B**) and mice with complete loss of *tubβ3* (latency to fall by 5th trial = 62.83 s, **Figure 4.7, B**) exhibit similar coordination, loss of both *abl2* and *tubβ3* substantially reduces the ability of mice to balance on the rotarod (latency to fall by 5th trial = 34.50 s). The mice not only exhibited motor deficits but failed to learn the test despite multiple trials (**Figure 4.7, B**). More biological replicates are required to draw conclusions, in addition to conducting behavioral tests on *abl2*^{+/-}*tubb3*^{+/+} and *abl2*^{+/-}*tubb3*^{+/-} (single heterozygotes). Nonetheless, these data exhibit a trend towards clear behavioral differences between mice with varying gene dosages of *abl2* and *tubβ3*. This suggests that Abl2 and tubulin β3 may be functionally interacting at the molecular level to regulate processes underlying motor skill learning. If there are statistically significant phenotypic differences in double heterozygotes versus single heterozygotes, this will be the true indication for a functional interaction.

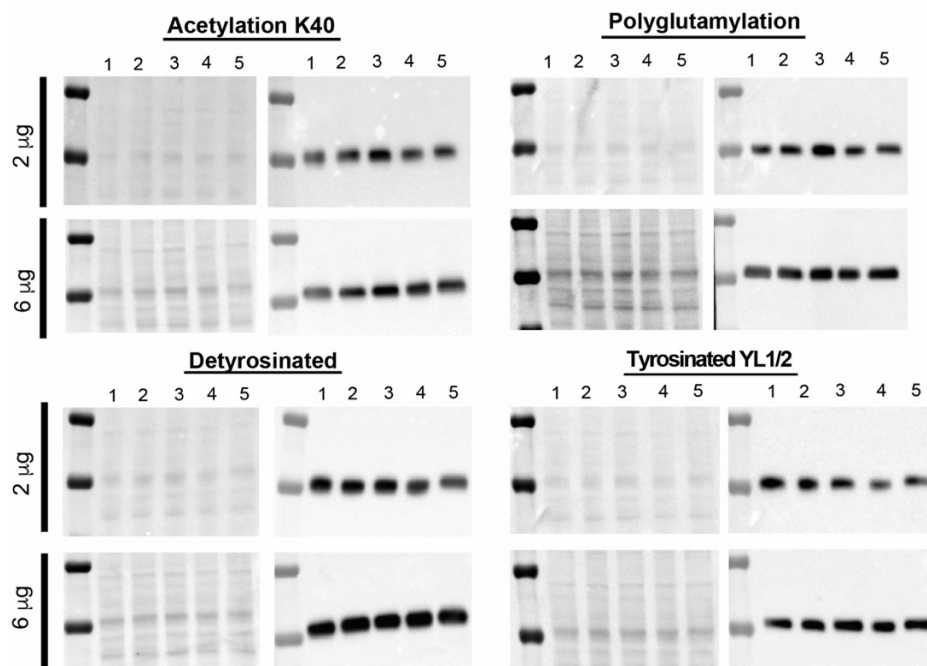


Figure 4.8. Representative immunoblots for acetylation, polyglutamylation, detyrosinated, and tyrosinated tubulin. 2 (top) and 6 μg (bottom) of total protein were loaded per genotype. Lane assignments are as follows: 1: WT, 2: *abl2*^{-/-}, 3: *tubβ3*^{-/-}, 4: *abl2*^{-/-}*tubβ3*^{-/-}, 5: *abl2*^{+/-}*tubβ3*^{+/-}. Ponceau stain for total protein levels on left; immunoblot on right.

Considering recent studies that demonstrate the importance of tubulin PTMs in regulating MT dynamics, I investigated whether PTM levels are altered in animals harboring partial or

complete loss of *abl2* and/or *tubβ3* genes. Brains were harvested from P42 mice and lysed to detect for changes in acetylated, polyglutamylated, detyrosinated and tyrosinated tubulin (**Figure 4.8**). Upon quantification of PTMs normalized to total protein levels from Ponceau staining, I observed that MTs from *tubβ3*^{-/-} mice exhibited higher levels of acetylation and polyglutamylation relative to those of WT (acetyl_{*tubβ3*^{-/-}}=1.09; polyglut_{*tubβ3*^{-/-}}=1.18; **Figure 4.9**), which aligns with literature (Latremoliere et al., 2018). Interestingly, *abl2*^{-/-} brains contains lower levels of acetylated tubulin, and lower levels of detyrosinated tubulin which corroborates with the higher levels of tyrosinated tubulin (acetyl_{*abl2*^{-/-}} = 0.98; detyrs_{*abl2*^{-/-}} = 0.93; tyrs_{*abl2*^{-/-}} = 1.078, **Figure 4.9**). These preliminary data suggest that Abl2 stabilizes MTs, which aligns with biochemical findings presented here that Abl2 promotes and MT reassembly by stabilizing inter- and intra-protofilament contacts. Mice harboring half a gene copy of *abl2* and *tubβ3* exhibit a substantial reduction in tyrosinated tubulin levels (tyrs_{*abl2*^{+/-}*-tubβ3*^{+/-}} = 0.79, **Figure 4.9**).

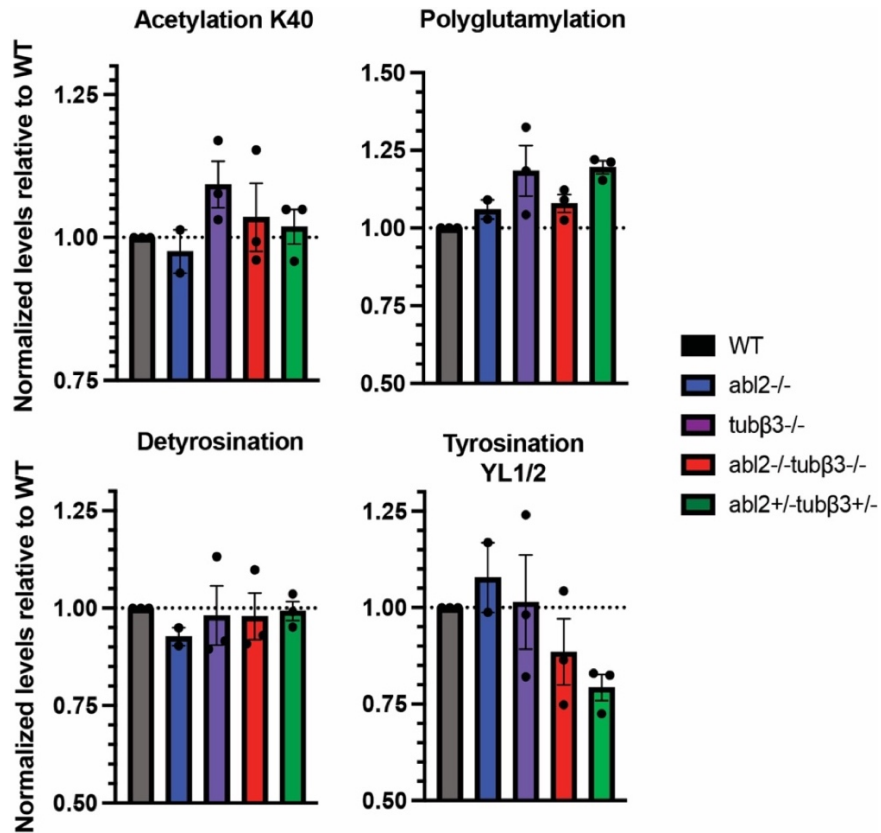


Figure 4.8. Quantification of PTM levels from 2 µg of whole brain lysates. Western blots shown in Figure 4.5. n=3 biological replicates for WT, *tubβ3*^{-/-}, *abl2*^{-/-}*tubβ3*^{-/-}, and *abl2*^{+/-}*tubβ3*^{+/-}. n=2 biological replicates for *abl2*^{-/-}.

Complete KO of *abl2* and *tubβ3* in mice likewise display a significant reduction in tyrosinated tubulin relative to those in WT mice ($\text{tyrs}_{\text{abl2}^{-/-}\text{tub}\beta 3^{-/-}} = 0.89$, **Figure 4.9**). Interestingly, though preliminary data suggest Abl2 has a role in stabilizing MTs while tubulin β3 does not significantly impact dynamics (minute changes in detyrosinated and tyrosinated tubulin levels), partial to complete reduction of both genes severely reduce MT dynamics. More biological replicates are required to draw conclusions, but preliminary data thus far show that live-cell imaging of neurons dissociated from these brains is needed to quantify how MT dynamics are affected in both axons and dendrites. It will be interesting to determine how Abl2 and tubulin β3 synergize to promote MT dynamics at different neuronal compartments (*i.e.* transfection of MACF43 into neurons and quantifying comet lifetimes, velocities, and lengths in axonal and dendritic sub-compartments).

4.4. Materials and Methods

REAGENT or RESOURCE	SOURCE	IDENTIFIER
Antibodies		
Rat monoclonal anti-tyrosinated tubulin, clone YL1/2	abcam	Cat# ab6160
Rabbit monoclonal Acetylated tubulin (K40)	Cell Signaling	Cat# 5335T
Mouse monoclonal anti-polyglutamylated tubulin, clone GT335	ApidoGen Life Sciences	Cat# AG-20B-0020-C100
Rabbit polyclonal anti-detyrosinated tubulin	Sigma	Cat# AB3201
Goat anti-rat IgG (H/L) HRP	Biorad	Cat# 5204-2504
BS3 (bis(sulfosuccinimidyl)suberate)	ThermoFisher	Cat# 21580

Brain tissue preparation for PTM quantification

Whole brain tissue from P21 wildtype, *abl2*^{-/-}, *tubβ3*^{-/-}, *abl2*^{-/-}*tubβ3*^{-/-}, and *abl2*^{+/-}*tubβ3*^{+/-} mice from C57BL/6 background were collected and kept frozen in -80°C until ready for lysis. Brains were homogenized in lysis buffer (50 mM Tris-HCl, 150 mM NaCl, 1 mM EDTA, 1% NP-40, 1% SDS pH 6.8), supplemented in 1X cOmplete protease inhibitor cocktail and 1X PhosSTOP phosphatase inhibitor cocktail. Whole brains were homogenized using pestle tissue grinders in 200 μL volume. Additional lysis buffer was added once large chunks were dissolved and transferred into a 5 ml Eppendorf tube. Tubes were kept on ice and sonicated at amplitude 30 (on-off 15s pulses on the thumb switch setting). Samples were centrifuged at 80K RPM for 5 min at 4°C using TLA120.2 rotor. Supernatant were collected and placed in new 5 ml tubes and diluted to 5 ml with lysis buffer. 200-300 μL aliquots of supernatant were snap frozen in liquid nitrogen and stored in -80°C until ready for Western blot. Upon thawing out, total protein levels were quantified using BCA assay for 2 μg and 6 μg of total cell lysate load. PTM level measurements were measured via quantitative Western blotting using anti-tyrosinated, -acetylated (K40), -polyglutamylated, and -detyrosinated tubulin antibodies. Blots were incubated overnight at 4°C with primary antibodies at 1:3000 dilution and exposed after 1hr RT incubation with secondary antibodies at 1:1000 dilution.

Accelerating rotarod

The rotarod is used to assess motor coordination and motor learning in rodents (Jones & Roberts, 2011). Mice were habituated to a quiet, moderately lit (100 lux) room separate from housing for 30 minutes prior to experimentation. A five-lane rotarod treadmill (Harvard Apparatus) was used for accelerating analyses. Mice were acclimated to the rotating rod at 4 RPM for 10 s, a day before the test. Then, the rod accelerated from 4 to 40 RPM over the course of 5 minutes before leveling off at 40 RPM for 2.5 minutes. Five trials were performed per mouse with a rest time of at least 10 minutes between trials. The latency to fall was recorded per trial.

BS³ crosslinking

1.25 μM of 6XHis-Abl2 was incubated with 0.4 μM tubulin dimers at RT in 20 mM HEPES, 5% glycerol, 50 mM KCl, pH 7.25. The mixture was pipetted up and down several times to allow for binding. After 30 RT incubation, a final concentration of 3.3 mM BS3 crosslinker dissolved in 20 mM HEPES was added into the mix. The mixture was run in a 10% SDS-PAGE gel and bands were cut off with new sterile razor blades. Excised gel bands were acetone precipitated to isolate the crosslinked fraction and processed for mass spectrometry at UCSF Mass Spectrometry Facility.

Glutaraldehyde gradient fixation of Abl2:tubulin for negative stain EM

Gradient buffers A (20 mM HEPES pH 7.25, 50 mM KCl, 10% glycerol) and B (20 mM HEPES pH 7.25, 50 mM KCl, 30% glycerol, 0.1% glutaraldehyde) were first prepared and stored at 4°C to cool. Interphase was marked on tubes with a marker, and Buffer A was added into the tube up to the mark. Buffer A was overlaid with Buffer B via a syringe and metal needle. Mixing was carefully avoided to maintain clean interphase. Gradients were mixed using the GradientMaster (Biocomp). Mixtures containing 0.5 $\text{mg}\cdot\text{ml}^{-1}$ 6XHis-Abl2 and 0.35 $\text{mg}\cdot\text{ml}^{-1}$ tubulin dimers, and 0.35 $\text{mg}\cdot\text{ml}^{-1}$ tubulin dimers alone were mixed on ice and carefully laid on top of each gradient tube. Gradients were left to settle for 10 min on ice. Gradient tubes were placed in SW41 rotor for an 18h spin at 35K rpm, 4°C, with deceleration rate set to "SLOW". 500 μL fractions were harvested manually from top of gradients. 20 μL from each fraction was immediately run on an SDS-PAGE gel for silver staining to determine which fractions to use for negative-stain EM.

400-mesh copper grids (Ted Pella, Redding, CA) overlaid with a very thin continuous carbon layer were gently glow discharged and 4 μ l of the protein mixture (Abl2:tubulin or tubulin alone) was applied to the grid. After a 30s adsorption, the reactions were blotted away from the grid with filter paper (Whatman No.1) leaving a thin layer of solution on the grid. 4 μ l of 2% uranyl-acetate solution were applied to the grid for 45s before blotting twice. After blotting, the grid was left to dry for 2 min. The negative stain sample of Abl2:tubulin was imaged using a Tecnai12 transmission electron microscope (TEM) and images recorded on a Gatan CCD camera at \sim -0.8-1.5 μ m defocus.

Chapter 5: The Abl2 interactome and phosphoproteome in mouse brain tissue

For many cellular processes, MBPs often interact with other upstream and downstream substrates through direct (*i.e.* binding) and indirect (*i.e.* phosphorylation) interactions to exert function on regulating actin and microtubule dynamics. Proteome and phosphoproteome profiling of distinct neuroanatomical regions of the mouse brain can uncover novel pathways in which Abl2 regulates neuronal function and activity.

The following chapter has not been published. Mass spectrometry analyses for co-IP, proteomics, and phosphoproteomics were done by Cindy Manriquez from Sam Myers' lab at La Jolla Institute. Pilot pyrene actin polymerization assays were conducted by Naomi Courtemanche, University of Minnesota. Generation of stably re-expressing Abl2-BioID2-eGFP and Abl2-557-C-BioID2-eGFP in COS-7 Abl2 KO cell lines was done by Matt Vitarelli. Molecular cloning for BioID2 project was done by Tony Koleske.

5.1. Co-immunoprecipitation of Abl2 from mouse brain lysates

Previous work in the Koleske Lab and work presented here reveal that Abl2 directly binds and regulates MT dynamics and nucleation. However, in cells and neurons, Abl2 interacts with various other known cytoskeletal regulators including N-WASp and cortactin to stabilize F-actin filaments to mediate cellular processes, including morphogenesis, migration, and maintenance of dendritic spine morphology. A seminal study by Boyle and others demonstrated through a protein microarray that Abl2 phosphorylates and directly binds to cortactin (Boyle et al., 2007). It remains elusive what other cytoskeletal proteins that Abl2 directly interacts with, particularly those that involve the microtubule cytoskeleton.

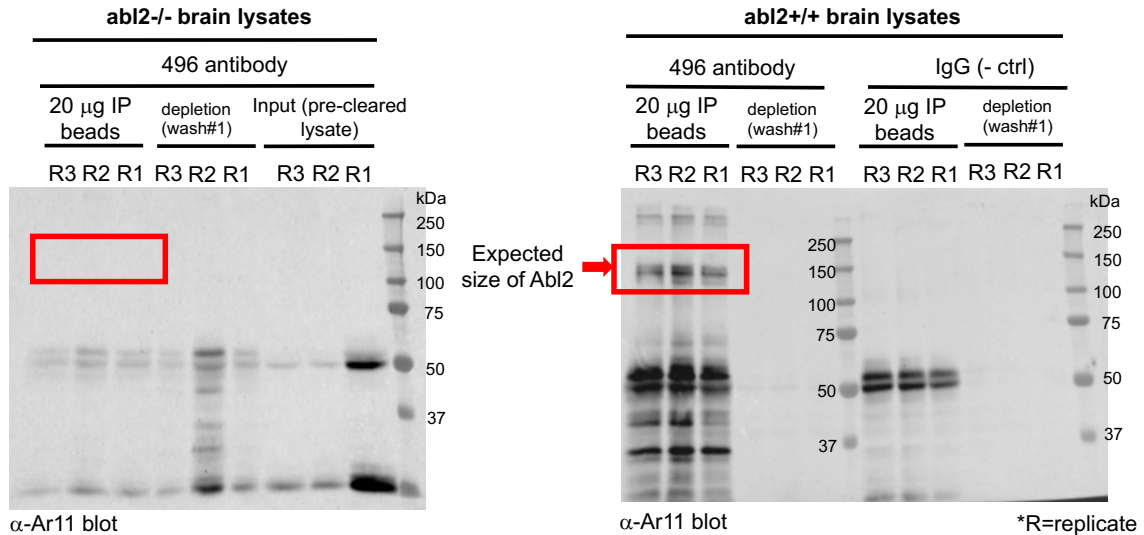


Figure 5.1. Western blots verifying that rabbit 496 antibody (Abl2 C-terminal half epitope) immunoprecipitated endogenous Abl2 from P22 mouse brain lysates. *abl2*^{-/-} brain lysates were used as a control. Multiple bands of various sizes highlighted in red box correlate to the isoforms of Abl2 expressed in the brain. Bands running at 50 and 25 kDa correspond to the heavy and light chains of immunoglobulin, respectively.

To identify novel protein interactors of Abl2, I utilized co-immunoprecipitation (co-IP). Verification of co-IP experiments from three biological replicate sets (3 *abl2*^{+/+} brain lysates, 3 *abl2*^{-/-} brain lysates as IP controls) reveals that Abl2 has been precipitated via Western blot analysis using Ar11 mouse antibody. Beads were frozen and sent to the Myers Lab for mass spectrometry (MS) analysis.

Co-IP MS results reveal 69 statistically significant interactor proteins of Abl2 in the mouse brain (adjusted p-value < 0.1). Pathway and process enrichment analyses using interactors from this list show that Abl2 is highly involved in regulation of nucleotide-excision repair (*i.e.* processes involving DNA damage), glycolysis and gluconeogenesis, metabolism of amino acids and derivatives, regulation of fatty acid metabolic processes, and dendrite development (**Figure 5.2**). Interestingly, some Abl2 interactors have either been implicated to localize at (through high-throughput assays) or have been directly shown to reside in the myelin sheath: Mdh1/2 (also can be found at the centrosome/MTOC), Ckb (also in dendrites), Eno1 (and in the nuclear outer membrane), Tkt (in peroxisomes), Pebp1 (in the axon terminus), and Ppia (**Figure 5.3, C**). In these cellular compartments, these proteins participate in processes involving actin-, glutamate/GABA

receptor-, lipid-, chromatin-, DNA/transcription factor-, and RNA-binding (**Figure 5.3, D**). Of note, peptidyl prolyl isomerase A (Ppia) is a molecular chaperone that enhances the cis/trans-isomerization of proline. A recent study has demonstrated that Ppia concentrates inside condensates formed by two proline-rich IDPs: tau droplets implicated in Alzheimer's disease and RNA coacervates of a proline-arginine dipeptide repeat protein (Babu et al., 2022). Once recruited into the condensates, Ppia dissolves the droplets formed by the IDPs, and in the case of tau, likely remodels the conformational ensemble of tau molecule via proline isomerization. Future studies include determining whether Ppia binds Abl2 and co-partitions into Abl2 condensates. As noted in Section 4.3, Abl2 contains a proline-rich tubulin-binding region, Site II, located at aa. 924-1024. It is possible that Ppia binds and isomerizes Abl2 at these residues as to change its conformation, making aa. 924-1024 amenable for interacting with downstream partners in the cell (perhaps tubulin dimers?). This will be interesting to investigate to explore whether Ppia modulates cellular phase separation behavior of Abl2 (whose C-terminal half is proline-rich, **Figure 4.3, B**) in the myelin sheath where it is predominantly localized.

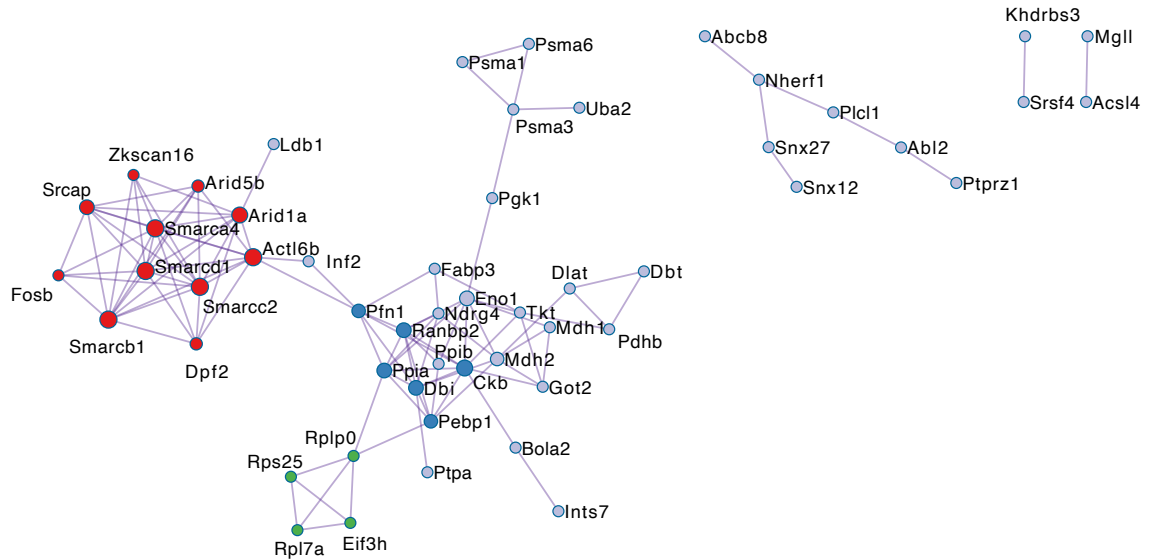


Figure 5.2. Protein-protein interaction network of Abl2 reveals that Abl2 is involved in various biological processes including regulation of nucleotide excision repair, regulation of fatty acid metabolic process, and metabolism of amino acids and derivatives. Nodes in red: regulation of nucleotide-excision repair, regulation of G0 to G1 transition, and ATP-dependent chromatin remodeling; blue: regulation of transferase activity, negative regulation of protein modification, and signaling of RhoGTPases; green: translation, peptide biosynthetic process, cytoplasmic ribosomal proteins. PPI enrichment analysis performed using Molecular Complex Detection (MCODE) algorithm via Metascape. Network generated using Cytoscape.

Mdh1/2 are malate dehydrogenases 1 and 2 that mediate cell glycolysis to promoting glucose intake by converting malate to oxaloacetate during the tricarboxylic acid cycle (Hanse et al., 2017). In mouse models, MDH activity has been shown to increase postnatally in parallel with increased functional malate-aspartate shuttling for promoting neurotransmitter synthesis during brain development (Rothe et al., 1983). These molecular functions correlate to those of other interactors Eno1, Dlat, Tkt, Ckb, Pepb1, Ppia, Dbp1, and Smarcb1, as they are all involved in metabolic and catabolic processes (**Figure 5.3, B**), e.g. acetyl-CoA biosynthesis (Dlat), acetylcholine biosynthesis (Pepb1), amino acid catabolic process (Dbt), and negative regulation of protein lipidation (Dib). Given the diverse roles Abl2 interactors play, future directions include testing whether Abl2 and Eno1 bind, for example, at distinct neuronal compartments and in various cell types. Eno1 (adj. p-value = 0.049; log₂FC = 0.86) is a glycolysis enzyme (“moonlight protein”) that is involved in hypoxia-induced apoptosis signaling pathway in the cytoplasm and serves as a receptor for stimulating the migration and invasion ability of cells. It can also bind directly to DNA and mRNA,

and plays roles in the cytoskeleton by promoting myogenesis via interacting with MTs during embryonic stem cell differentiation, cardiomyocyte contraction with actin filaments, and regulates cell cycle at the centrosome (**Figure 5.3, C**) (Didiasova et al., 2019; Fougousse et al., 2001; Huppertz et al., 2022).

The most statistically significant interactor of Abl2 (whose log₂FC score was also the highest) is protein tyrosine phosphatase receptor type Z (Ptpz1, whose adj. p-value = 0.013; log₂FC = 2.14, **Figure 5.3, A**). Ptpz1 is important for myelination, which is an essential feature of the CNS. Differentiation of oligodendrocytes and myelin formation relies on protein tyrosine phosphorylation, which is carefully controlled by the balance of tyrosine kinases and phosphatases. Interestingly, it was shown that Fyn KO mice exhibit a 50% decrease in myelination (Umemori et al., 1994). As p190RhoGAP is a crucial target for Fyn signaling to mediate oligodendrocyte differentiation and myelination, p190RhoGAP is tyrosine phosphorylated to become activated during oligodendrocyte differentiation (Kuboyama et al., 2012). p190RhoGAP suppresses Rho GTPase activity, thus the phosphorylation and dephosphorylation cycle of p190RhoGAP must be carefully regulated for oligodendrocyte maturation. Kuboyama and others found that Ptpz acts as the counterpart of Fyn by dephosphorylating Fyn substrates including p190RhoGAP. Mice deficient in *Ptpz* exhibit an early onset of myelin basic protein expression, a major component of the myelin sheath which induced early onset of oligodendrocyte differentiation. As Abl2 is a phosphorylation substrate of Fyn, it will be interesting to explore whether Ptpz1 binds and dephosphorylates Abl2 to inactivate its kinase activity. This would not be too surprising as it was shown previously by Boyle and others, dorsal wave formation in fibroblasts is mediated by Abl2 phosphorylation on cortactin, which acts through Src/Yes/Fyn upstream phosphorylation signaling (Boyle et al., 2007). It has not yet been explored whether Abl2 plays a role in myelination, though it has been shown in a recent study that Abl1 phosphorylates transcription factor Olig2, which is essential for proliferation of oligodendrocyte progenitor cell proliferation (Zhang et al., 2022). As the co-IP experiment was conducted using whole brain lysates, resolution is lost at the neuronal compartment (dendrites, axons, soma) and cellular level. Additional studies are required to dissect the mechanisms Abl2 interacts with these co-IP candidates in different cellular pathways (e.g. mitosis, DNA damage, viral

host entry, etc.) and cell types (e.g. HEK293, 3T3 fibroblasts, cultured hippocampal neurons, cortical neurons, oligodendrocytes).

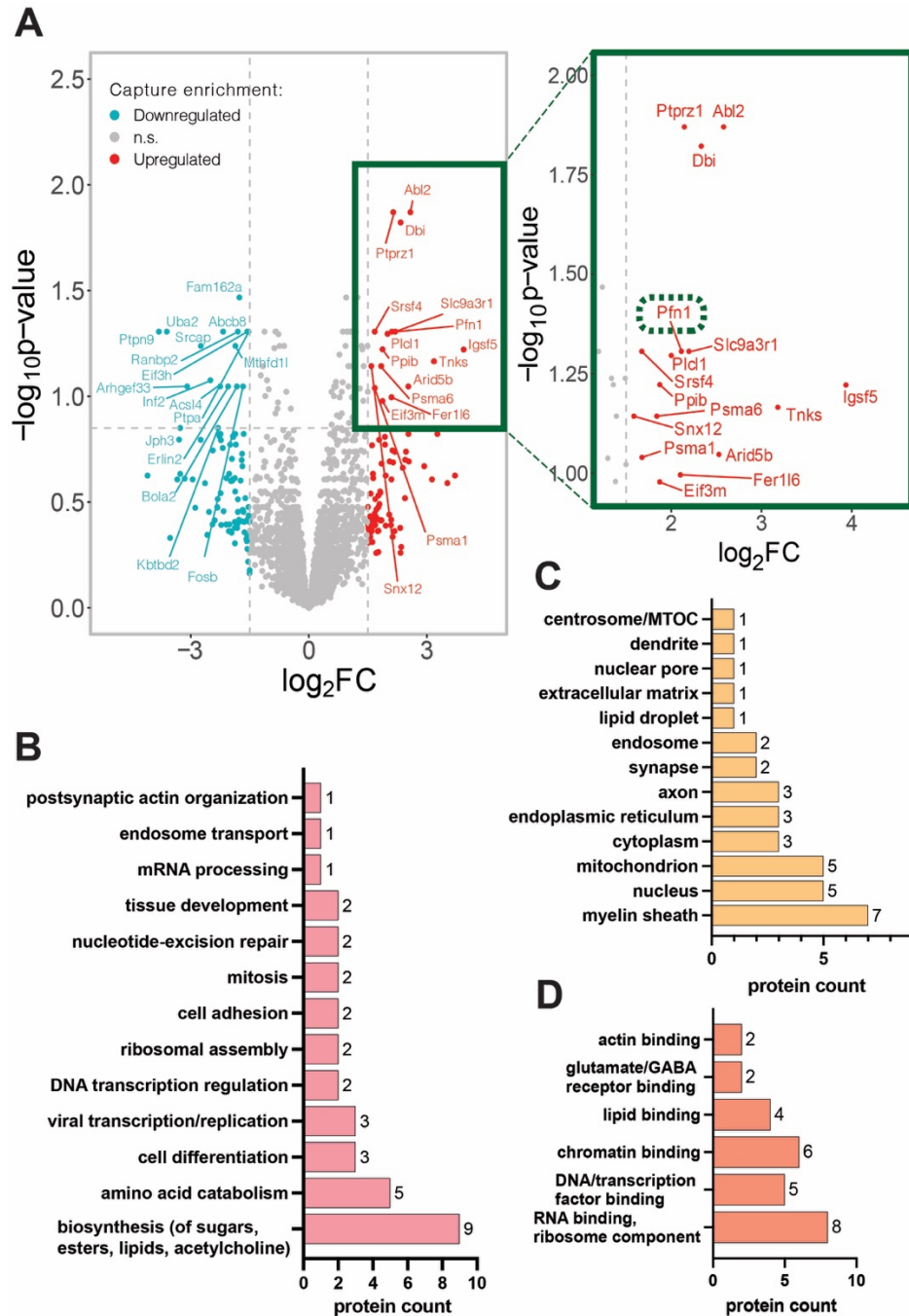


Figure 5.3. Statistically significant Abl2 interactor proteins from co-IP MS are involved in various biological pathways. (A) Volcano plot highlighting statistically significant and enriched proteins that precipitated with Abl2. Only proteins whose adj. p-value ≤ 0.15 and $\log_2FC \geq 1.5$ are labelled ($n=40$). **(B)** 40 interactors have been categorized based on associated biological processes. **(C)** Cellular components the 40 statistically significant interactors belong to. **(D)** Molecular function groups that the 40 statistically significant interactors are involved in. Not all interactors were involved in the specific pathways, components, nor functions listed here.

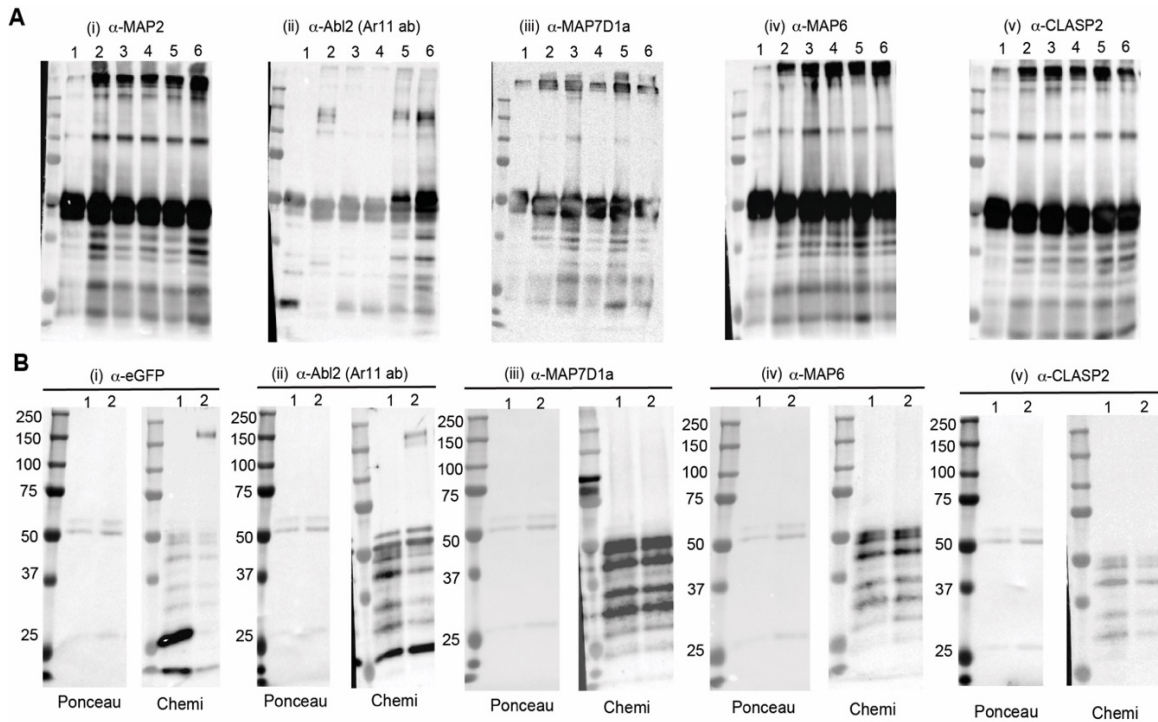


Figure 5.4. Abl2 does not co-IP with other MT cytoskeletal regulators. (A) Abl2 co-IP immunoblots to test whether predicted proteins, MAP2 (i), MAP7D1a (iii), MAP6 (iv), and CLASP2 (v), are pulled down at endogenous levels in HEK293T cells. Abl2 (ii) has been blotted as verification that co-IP was successful. **(i-v)** Lane assignments are the following: (1) HEK lysate with rabbit IgG antibody as control; (2) HEK lysate with C-terminal Abl2 antibody; (3-4) two biological replicates of P22 *abl2*^{-/-} mouse brain lysate with C-term Abl2 antibody; (5-6) two biological replicates of P22 *abl2*^{+/+} mouse brain lysate with C-term Abl2 antibody. **(B)** HEK293T cells over-expressing pN1-eGFP or pN1-Abl2-eGFP. 2 μ g of IP beads were loaded and immunoblotted for respective antibodies labelled on each blot. Ponceau shown on left, Chemiluminescence on right.

Curiously, some of these proteins are involved in viral replication and transcription (Pfn1, Ppib, Smarcb1, **Figure 5.3, B**). This is interesting to point out as Abl kinase activity has been shown to directly promote both HIV-1 and hepatitis C viral entry. In fact, Abl2 has been shown to directly interact with several proteins involved in positive regulation of viral genome replication and transcription: peptidylprolyl isomerase B (Ppib), profilin-1 (Pfn1), and SWI/SNF related, matrix associated, actin dependent regulator of chromatin, subfamily b member 1 (Smarcb1). Abl kinase and the Wave2 signaling complex are required for HIV-1 Env-mediated fusion (not on VSV-G mediated which is pH-dependent) (Harmon et al., 2010). siRNA against Abl and imatinib treatment to cells reveal decreased levels of Env-mediated cell-cell fusion in cellosaurus cells (cell line suitable for HIV infection). The study revealed that Abl phosphorylates the Ras GEF complex to promote Rac GEF Tiam-1 activity, which is required for HIV-1 fusion. The authors postulate a model

where HIV-1 Env binding to CCR5 (chemokine coreceptor for HIV) activates Rac, and activated Rac interacts with IRSp53. IRSp53 promotes Rac activation of the Wave2 complex. Downstream of Rac, Abl phosphorylates and activates Wave2 to mediate interaction with the Arp2/3 complex that is critical for HIV-1 infection, suggesting that Abl kinase coordinates with the Wave2 complex to activate Arp2/3-mediated actin rearrangements for facilitating pore formation, enlargement, and entry of HIV-1. Additionally, Abl kinase has recently been shown to form a phosphorylation-dependent complex with dimeric nonstructural protein 5A (NS5A) that is required for hepatitis C viral particle assembly (Min et al., 2017; Miyamoto et al., 2022). Abl activation via phosphorylation at Y412 by tyrosine-phosphorylated NS5A via homodimerization is responsible for assembly of HCV particle in cellosaurus (Huh-7.5) cells. HCV enters cells via clathrin-mediated endocytosis (CME) and it has been shown that imatinib treatment caused a significant reduction in transferrin uptake, thereby blocking CME. Collectively, these studies strongly suggest that Abl2 interacts with various interactors to mediate different cellular functions in pathways involving cytoskeletal rearrangements.

Perhaps the most interesting interactor upon plotting the $\log_2(\text{fold change})$ ($\log_2\text{FC}$) of WT versus Abl2 KO enrichment and filtering for $-\log_{10}(\text{adj. p-value})$ of 0.85 (adj. p-value of ~ 0.15) is profilin-1. Profilin-1 is also involved in actin-dependent regulation of viral transcription (Burke et al., 2000), and is the only known cytoskeletal regulator within this list that directly modulates postsynaptic actin turnover (**Figure 5.3, A**; no known MBPs were detected from HEK293T cell lysates and mouse brain lysates using co-IP method, **Figure 5.4**). Profilin-1 plays an essential role in actin-based motility as it selectively recognizes barbed ends of both G-actin and F-actin (Pollard & Cooper, 1984). Profilin-actin complexes promote formin-mediated barbed end assembly (Kovar et al., 2003). In cells, profilin-1 is recruited to sites of actin assembly via association with N-WASp (Suetsugu et al., 1998) and Arp2/3 complex at the lamellipodia to promote actin branching (Mullins et al., 1998). In neurons, profilin-1 localizes to dendritic spine heads and axon terminals, specifically at excitatory and inhibitory synapses (Neuhoff et al., 2005). Following treatment with KCl, neurons have been shown to undergo activity-dependent cytoskeletal changes, that include re-localization of profilin-1 to synaptic sites, co-localizing with PSD-95 and synaptophysin. In line with conclusions

from another study by Ackermann & Matus, these data by Neuhoff and others show that profilins can be present at pre- and post-synaptic sites to mediate activity-dependent remodeling of actin-rich synaptic structures (Ackermann & Matus, 2003).

There are two predominant neuronal profilin isoforms. Profilin-1 is ubiquitously expressed and is important for spine formation, whereas profilin-2 is involved in synapse function and spine stabilization (Michaelsen-Preusse et al., 2016). In a study by Michaelsen-Preusse *et al.*, profilin-1-deficient neurons displayed significantly increased actin turnover time relative to that of control neurons. This reveals that the stable actin fraction was significantly increased in shPFN1-expressing cells, which suggests profilin-1 promotes actin polymerization. Profilin-2 is another brain profilin isoform that is required during synaptogenesis and, unlike profilin-1, is indispensable for adult spine plasticity. In profilin 2a-deficient neurons, actin turnover time was significantly decreased – which is in direct opposition to the phenotype observed for profilin 1-deficient neurons. As it is known that profilin competes with actin nucleators for free-actin monomers, it is likely that profilin-2 is the predominant neuronal isoform that prevents Arp2/3-dependent formation of F-actin branches. Increased actin polymerization rate may interfere with profilin-2 mediated spine stabilization. As profilin-1 and profilin-2 isoforms are developmentally regulated and the co-IP was conducted using P22 mouse brains, it will be interesting to explore whether the interactomes of Abl2 in juvenile and aged brains alter to include profilin-2. Earlier work from the Koleske Lab demonstrated that Abl2 promotes Arp2/3 stimulated actin branching *in vitro* (Courtemanche et al., 2015). However, it remains unexplored whether Abl2 modulates profilin-1 activity in Arp2/3 actin branching to ensure proper maturation of dendritic spines.

The study that first hinted at a functional interaction between Abl kinases and profilins was a 1999 study from the Van Vactor Lab. Zachary Wills and others demonstrated there exists a genetic interaction between Abl tyrosine kinase and chickadee (*Drosophila* profilin) at the CNS, as both *chic* and *abl* mutant embryos display similar growth cone arrest phenotypes, and substantial disorganization in the fascicles of FasII-positive axons at either side of the CNS midline (Zachary Wills et al., 1999). Both Abl and profilin are required to foster proper axon outgrowth. However, it

remains unclear whether Abl kinases and profilin directly interact to mediate actin turnover for stabilizing dendritic spines.

To determine if Abl2 interacts with profilin to modulate actin polymerization kinetics, I collaborated with Naomi Courtemanche's lab to conduct pilot bulk actin polymerization assays using pyrene-labelled actin. Inclusion of 100 nM 6XHis-Abl2 (**Figure 5.5, B, C**) did not alter polymerization kinetics in a reaction containing 4 μM actin (20% pyrene-labelled) with 200 nM – 1 μM profilin-1 relative to the reaction kinetics containing profilin-1 alone (**Figure 5.5, A**). Binding interaction needs to be validated with rigorous quantitative binding assay using biolayer interferometry and/or *in vitro* pull down. Additional pilot actin polymerization assays will be conducted using higher concentrations of Abl2 (500 nM – 1 μM) in the presence of profilin-1.

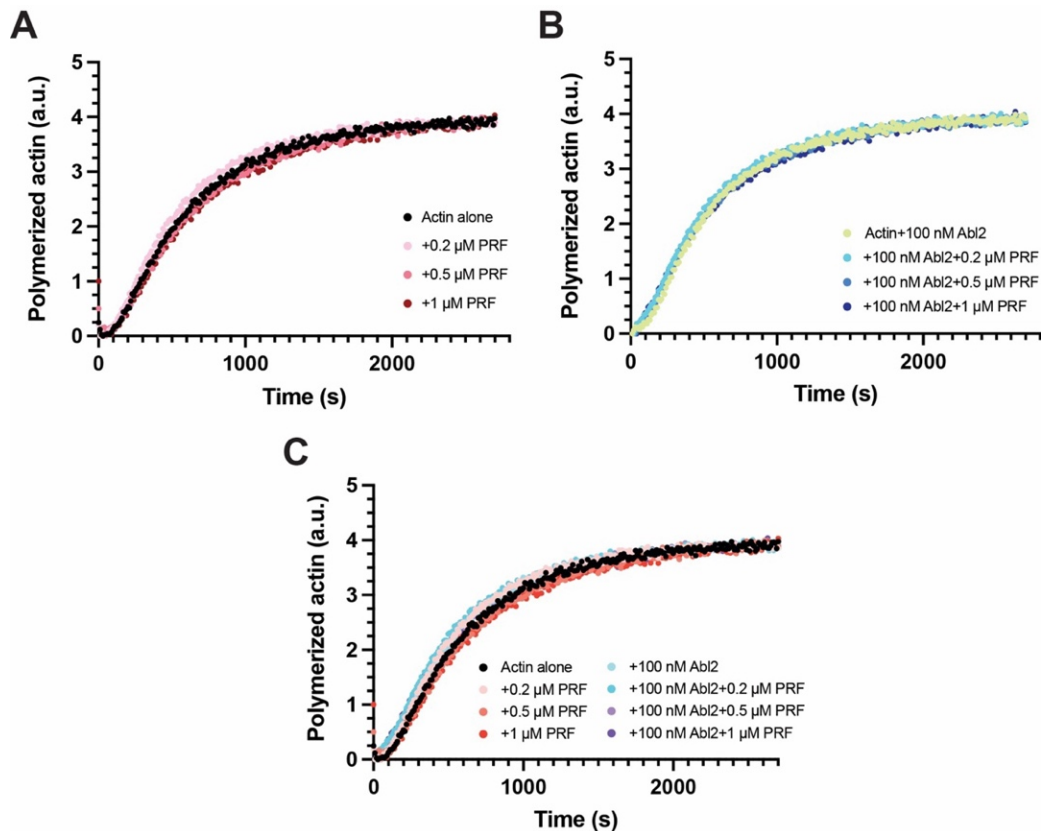


Figure 5.5. Pyrene-actin polymerization assays reveal that inclusion of 6XHis-Abl2 does not impact actin polymerization kinetics. **(A)** 4 μM actin with inclusion of 0.2, 0.5, 1 μM profilin-1. **(B)** 4 μM actin with inclusion of 100 nM 6XHis-Abl2, supplemented with 0.2, 0.5, 1 μM profilin-1. **(C)** Overlay of all the polymerization assays shown in (A) and (B). Pyrene assays conducted by members of Naomi Courtemanche's lab.

Profilin-1 has been shown to directly promote MT growth *in vitro* (Henty-Ridilla et al., 2017). From the same study, profilin-1 expression in N2A cells increases the growth rate of MTs and promotes MT entry into filopodia, a process that is regulated by MT-actin crosstalk (Schaefer et al., 2002). Through dynamic MT TIRF assays, titrating increasing concentrations of monomeric actin into TIRF chambers substantially attenuates the effect of profilin on MT growth rates. These data imply that both actin and MTs share the same binding site on profilin. Thus, it will be interesting to explore whether Abl2 and profilin-1 interact to modulate microtubule dynamics. Both Abl2 and profilin-1 have stronger affinities for F-actin, though they can independently bind to MTs to increase growth rate. Preliminary data from fixed COS-7 cells stably expressing Abl2-eGFP suggest that profilin-1, which also localizes at the nucleus, and Abl2 co-localize at the cell periphery during initial adhesion and cell spreading (**Figure 5.6**). Additional experiments are required to determine when and where within the cell (3T3 fibroblasts, HEK293) Abl2 and profilin may interact to promote lamellipodia formation and (activity-dependent targeted?) dendritic spine stability.

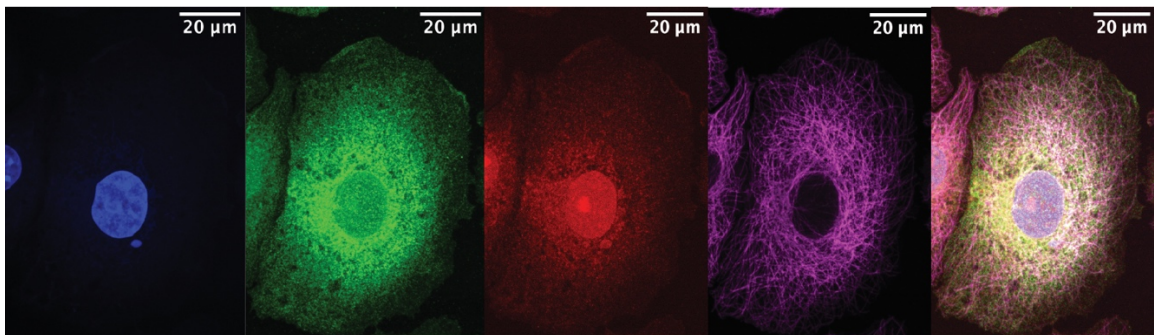


Figure 5.6. Abl2 and profilin co-localize at the cell periphery during the initial phases of cell spreading and adhesion. Abl2 shown in green (488 nm), endogenous profilin-1 shown in red (568 nm), tubulin shown in magenta (647 nm), and nucleus in blue (405 nm). Cells were fixed in 3% paraformaldehyde, 0.1% glutaraldehyde in PHEM buffer.

5.2. Using BioID as a proximity labeling technique to capture Abl2 interactions in cells

A very common technique for detecting and/or validating protein-protein interactions is co-immunoprecipitation (co-IP). Co-IPs are effective in capturing protein-protein interactions in native conditions as it requires an antibody against the protein of interest conjugated to agarose beads that will precipitate not only the protein of interest, but also its interactor proteins. However, as

revealed from my co-IP mass spectrometry results (**Figures 5.1, 5.2**), a lot of known interactors of Abl2 such as cortactin are not pulled down. Many are cytoskeletal regulators, and, as co-IPs are conducted in non-denaturing conditions, cytoskeletal proteins remain insoluble in lysis buffers with weak detergents.

To overcome the limitations of co-IP, a postbaccalaureate junior lab assistant, Matt Vitarelli, generated COS-7 Abl2 KO cells stably re-expressing Abl2-BioID2-eGFP and Abl2-557C-BioID2-eGFP. BioID is one of the newer protein-protein interaction screening techniques, involving the use of the biotin ligase, BirA (Sears et al., 2019). Plasmid containing the biotin-ligase fused to Abl2 is transfected into cells so that upon incubation with excess biotin in the media, BirA will release highly reactive molecules of an AMP intermediate that will lead to biotinylation of proteins within a ~10-20 nm radius of Abl2-eGFP or 557-C-eGFP. This also means that weak, transient protein-protein interactions that normally co-IP – which relies on stable, strong PPIs – can't detect, can be captured using BioID. These captured proteins can then be further purified using streptavidin-coated beads which have a high affinity for biotin. Because BioID takes advantage of the strong noncovalent bond between biotin and streptavidin (which can withstand harsh lysis conditions), this screen enables a lot of cytoskeletal proteins, such as cortactin, to become solubilized and captured.

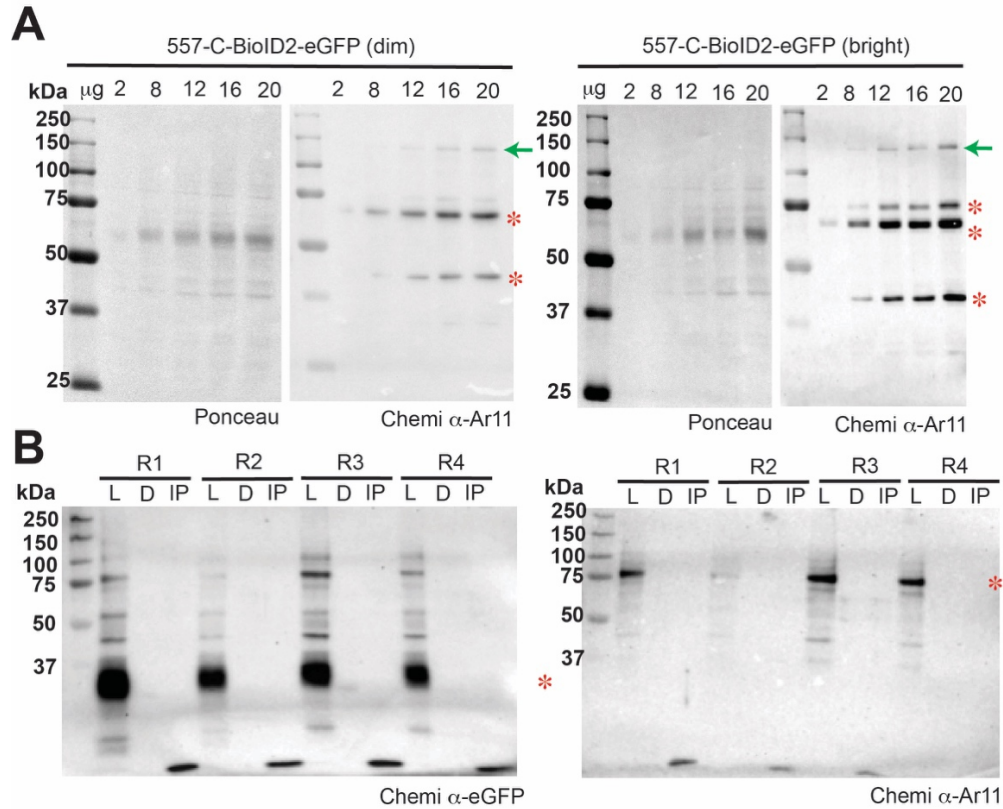


Figure 5.7. COS-7 Abl2 KO cells stably re-expressing Abl2-557C-BioID2-eGFP at dim and bright levels of fluorescence. (A) Validation of cells expressing constructs of correct size using Ar11 antibody (recognizes the C-terminal half of Abl2). Cells were treated with 100 mM biotin for 24 hours. Green arrow denotes band of correct molecular weight (~120 kDa). Red asterisks denote degradation product. **(B)** Four replicates (R1, R2, R3, R4) of pull-down experiments conducted using streptavidin-conjugated agarose reads. Lane assignments are as follows: L = pre-cleared lysate; D = depletion or last wash step; IP = beads after pulldown. Red asterisks denote degradation product.

Upon FACS sorting Abl2-BioID2-eGFP and Abl2-557C-BioID-eGFP cell lines based on fluorescence levels, I validated BioID2 fusion protein expression using an antibody that specifically recognizes Abl2 (Ar11). Cell lines exhibiting bright and dim fluorescence levels of Abl2-557C-BioID2-eGFP were expressing constructs of the right size (**Figure 5.7, A**), albeit exhibiting substantial amounts of degradation. However, Abl2-BioID2-eGFP cell lines did not express detectable amounts of the fusion protein, likely due to the lack of protein stability. An immediate next step is to construct a plasmid with BioID2 at the N-terminus and Abl2 at the C-terminus, flanking the eGFP tag.

Streptavidin pull-down experiments were conducted using the dim population of Abl2-557C-BioID2-eGFP cells. The dim population was used to identify bona-fide interactor proteins that have a higher likelihood of interacting with Abl2 C-terminal half at its endogenous levels. However, upon troubleshooting various experimental conditions (lysis conditions, biotin concentration, biotin incubation time), I saw that across all 4 replicates, blotting using eGFP and Ar11 antibodies revealed products of various sizes in the pre-cleared lysate (**Figure 5.7, B**). I observed a prominent band corresponding to the size of eGFP alone (red asterisk in **Figure 5.7, B, left**), with faint band at ~120 kDa corresponding to 557C-BioID2-eGFP. This corresponds to the Ar11 blot, as I only saw a band corresponding to 557-C alone (red asterisk in **Figure 5.7, B, right**; migration pattern verified also from Coomassie stained gel shown in **Figure 2.6, A, iii**). Since having Abl2 and Abl2-557-C at the N-terminus had adverse effects in the cell (*i.e.* significant protein degradation or cleavage of BioID2-eGFP), the immediate next step is to reconstruct BioID2 plasmids with an N-terminal BioID2 and C-terminal Abl2 or Abl2-557-C with a longer flexible linker (GGGS repeat). The longer flexible linker may help to prevent steric hindrance between the ligase and protein. Identification of novel actin and MT cytoskeletal interactors of Abl2 by BioID will open many doors into uncovering the various biological processes Abl2 is involved in.

5.3. Abl2 whole brain proteomics

The application of proteomics in identifying the interactomes of a protein of interest in anatomically distinct mouse brain regions allows for further understanding of specific functions at the molecular level. While our current understanding of Abl2 lies within its essential role in maintaining dendritic spine stability and morphology via interactions with cortactin, integrin $\alpha 3$, and integrin $\beta 1$ (Kerrisk et al., 2013; Shaw et al., 2021; Warren et al., 2012), there are still many questions that remain as to whether Abl2 phosphorylates or directly binds to other substrates for dendritic spine maintenance, and whether Abl2 is involved in other processes in non-dendritic neuronal compartments. To address this, I collaborated with Matt Vitarelli in the Koleske Lab for whole brain proteomic analysis, comparing the proteomes between P21 *abl2*^{+/+} and *abl2*^{-/-} brains. Matt

dissected each brain region (hippocampus, cortex, cerebellum) from 3 sets of biological replicates (**Figure 5.8, A**). Brain regions were frozen and sent off to Sam Myers' Lab for MS.

gene	molecular function	cellular component(s)	biological process(es)	HIPPOCAMPUS		CORTEX		CEREBELLUM	
				adj. p-value	log ₂ FC	adj. p-value	log ₂ FC	adj. p-value	log ₂ FC
Apoa2	heat shock protein-, cholesterol-, phospholipid-, signaling receptor binding	extracellular space, very-low- and high-density lipoprotein particles	lipoprotein metabolic process, protein oxidation, immune response, cholesterol transport, phagocytosis	0.0043	9.0435	0.0013	8.91625	0.02718	7.5885
Nit1	hydrolase activity	cytoplasm, mitochondrion	amide catabolic processes	0.0852	2.0838	0.3063	1.44492	0.2464	0.7520
Apcs	virion-, metal ion-, carbohydrate-binding	extracellular space	negative regulation by host of viral glycoprotein metabolic process	0.0975	-6.2792	0.3257	-4.5742	0.2709	-3.2945
Mndal	dsDNA binding, transcription factor binding	nucleus, cytoplasm	positive regulation of transcription by RNA PolII, negative regulation of cell growth, defense response to virus, cell response to glucose starvation	0.6154	0.63474	0.9989	0.00065	0.0019	6.5747
Rnf39	ubiquitin protein ligase activity	cytoplasm	protein ubiquitination	0.1296	2.00094	0.7578	0.53975	0.81043	0.2826
Tatdn3	hydrolase and nuclease activities, metal ion-binding	nucleus, mitochondrion	n/a	0.5310	-2.8039	0.7393	-1.2756	0.08744	-2.2888

Table 5.1. Proteins whose absolute expression levels have been statistically significantly altered in the hippocampus, cortex, and cerebellum with absolute log₂FC values ≥ 2. Cells highlighted in green correspond to proteins whose expression levels are statistically significant per brain region.

Upon plotting log₂FC values versus adjusted p-values on log₁₀ scale, only 4 proteins are differentially expressed in the hippocampus (Apcs, Rnf39, Nit1, ApoA2); 3 in the cerebellum (Mndal, Tatdn3, ApoA2), and 1 in the cortex (ApoA2, **Figure 5.7, B-C**). Interestingly, the expression level of apolipoprotein 2, ApoA2, is significantly impacted upon complete KO of Abl2 across all brain regions (log₂FC ≥ 7 in each region). ApoA2 is an abundant high-density lipoprotein that exists in the extracellular space and, in conjunction to its lipoprotein metabolic process, can be found to be regulated in protein oxidation, cholesterol transport, and phagocytosis (**Table 5.1**). Though not much is known about ApoA2, we do know that ApoA1 is one of the most abundant apolipoproteins in the cerebrospinal fluid (Elliott et al., 2010). Decreased levels of ApoA1 has been reported in the brain tissue of patients diagnosed with schizophrenia. The exact functional roles of ApoA1 are not known, however, both ApoA1 and ApoA2 play a major role in peripheral cholesterol transport in the

liver. Thus, it is probable that both ApoA proteins play analogous roles in the CNS. Whole brain proteomics data correlates with co-IP MS significant hits, as most Abl2 interactors have been found to be localized in myelin sheath, where most cholesterol products in the brain that remains unesterified is present within. Interestingly, Abl activation has been linked to Niemann-Pick Type A (NPA) disease, a fatal lysosomal neurodegenerative disorder (Marín et al., 2022). NPA mouse model exhibits progressive lipid storage in reticuloendothelial organs.

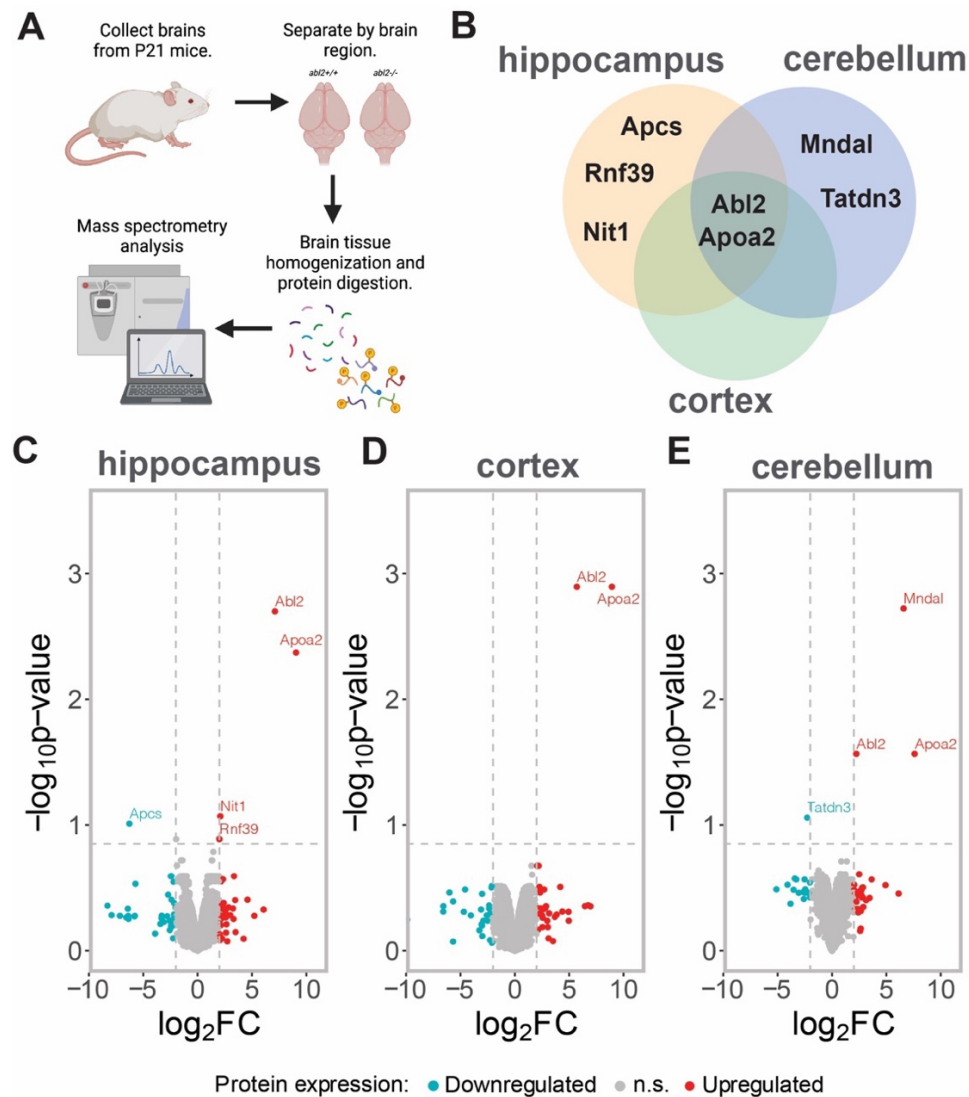


Figure 5.8. There are only few statistically significant Abl2 interactor proteins from whole brain region proteomic analysis. (A) Brains were harvested from P21 *abl2*^{+/+} and *abl2*^{-/-} mice and separated by brain region. Brain regions were sent off for MS. **(B)** Hippocampus, cerebellum, and cortex share one statistically significant protein whose expression levels are altered ($\log_2FC > 2$ as threshold for differential expression). **(C)** Volcano plots displaying the differentially expressed proteins by brain region. Proteins whose absolute \log_2FC values ≥ 2 are labelled. Descriptions for each labelled protein shown in Table 5.1.

It was found that phosphorylated c-Abl levels were significantly increased in NPA primary neurons compared to WT, and imatinib treatment substantially decreased sphingomyelin accumulation in NPA primary neurons. It has been recently shown that apolipoprotein D (ApoD) is overexpressed in the brains of NPA patients, and absence of ApoD leads to Purkinje neuron degeneration (Pascua-Maestro et al., 2020). Addition of ApoD to human NPA fibroblasts improves lysosomal physiology

by stabilizing the pH and reducing lysosomal permeabilization, resulting in significant increase in cell viability. Apolipoproteins share little structural homology; however, there is evidence suggesting that, for example, ApoD and ApoE share complementary and redundant functions in binding to A β plaques. Additionally, in the hippocampus, amyloid P component (Apc) is significantly downregulated and becomes enriched upon complete loss of *abl2* (**Table 5.1; Figure 5.8, C**). Apc is a highly preserved plasma protein that is ubiquitous in amyloid deposits, and has been shown to colocalize with retained ApoA1, ApoB, ApoC2, and ApoE in human atheroma (degeneration of arteries), with deposition correlating most strongly with ApoA1 and ApoE. It has been postulated that Apc marks the presence of aggregated apolipoproteins that display amyloid-like properties. Thus, it is possible that Abl2 and ApoA2 interact in the brain to support myelin lipid metabolism.

Further directions include conducting the same mass-spectrometry experiment of P42 adult mouse brains for an in-depth comparative proteomic analysis. It was shown in earlier studies that *abl2*^{-/-} neurons develop normally up to postnatal day 21, but thereafter, dendrites become destabilized and begin to shrink (Gourley et al., 2012; Moresco et al., 2005; Sfakianos et al., 2007). The number of spines in *abl2*^{-/-} neurons also appear to be normal, but as these neurons age, the numbers substantially drop. The net effect of losing both dendrite arbor and dendritic spines is that the synapse numbers significantly decrease after postnatal day 21. Thus, it is not surprising that there are only several proteins with statistically significant expression changes in the hippocampus, cortex, and cerebellum. It will be interesting to explore how the proteomes are altered as brain develops from adolescence into adulthood, and what pathways Abl2 are involved in to maintain dendritic spine morphology when neurons become more mature.

5.4. Abl2 phospho-proteomics

Major cellular processes, *e.g.* cell proliferation, cell cycle, and apoptosis, are mediated by phosphorylation-mediated signaling cascades. Understanding how protein phosphorylation networks are regulated during these processes sheds light on kinase activity, especially in the context of cancer where constitutively active kinases promiscuously phosphorylate and also bind (independent of kinase activity) multiple downstream substrates to hamper cell death (Bertram,

2000). Mass spectrometry-mediated global phosphoproteomics analysis allows for identification of thousands of phosphopeptides that indirectly contain information on the activities of other kinases (Kinase-Substrate Enrichment Analysis, KSEA (Wiredja et al., 2017)). Knowing that Abl2 binds to various substrates, I was curious to explore what biological processes that Abl2 kinase activity is involved in the P21 adolescent mouse brain.

Using the same dissected P21 *abl2*^{+/+} and *abl2*^{-/-} brain tissue for whole brain proteomics, the Myers Lab performed global phosphoproteomics MS analysis in the cortex, cerebellum, and hippocampus (**Figure 5.9**). Surprisingly, the phosphoproteomes in the cerebellum and cortex were minimally altered, with only one protein in the cortex (formin 2, encoded by *Fmn2*), and 3 proteins (synaptopodin encoded by *Synpo*, AT-hook containing transcription factor 1 *Ahctf1*, ephrin receptor EphB2 by *Ephb2*) in the cerebellum exhibiting significant enrichment (threshold set by adj. p-value < 0.05 and $|\log_2FC| \geq 3$; **Figure 5.9, A**). In stark contrast, Abl2 kinase activity significantly impacts the hippocampal phosphoproteome (**Figure 5.9, B**).

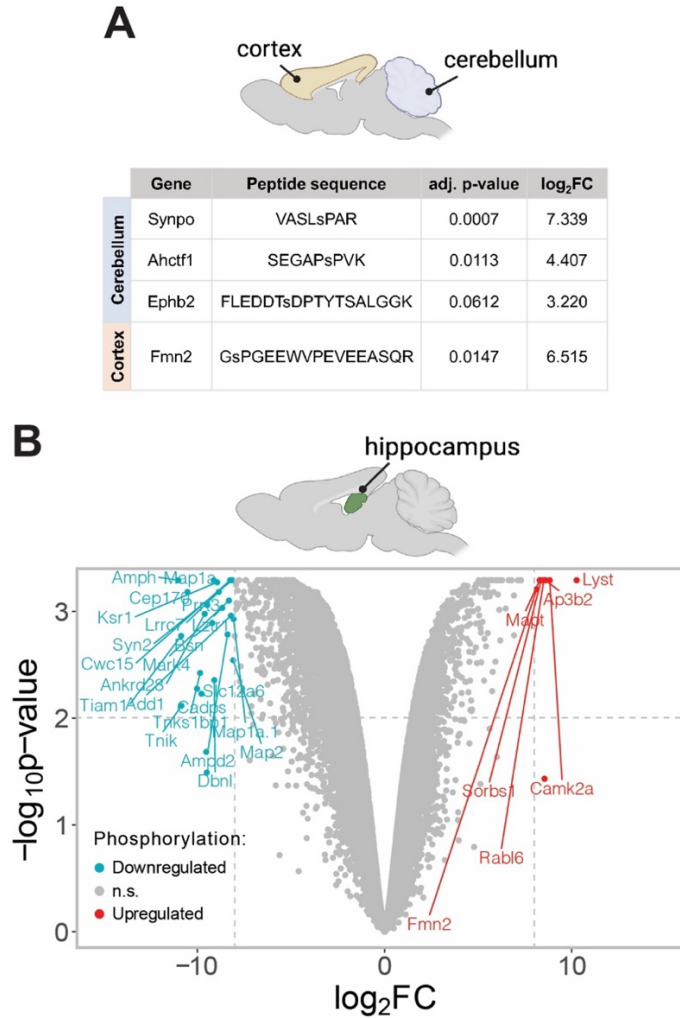


Figure 5.9. Abl2 phosphorylation significantly impacts the phosphoproteome within the hippocampus, having minimal impact in the cortex and cerebellum. (A) Proteins encoded by *Synpo*, *Ahctf1*, and *Ephb2* are affected in the cerebellar phosphoproteome and *Fmn2* in the cortex under the regulation of Abl2 (adj. p-values ≤ 0.1). **(B)** Total of 2,282 proteins whose phosphorylation levels are significantly up- or down-regulated under Abl2 regulation (adj. p-value < 0.05). Proteins labelled have absolute $\log_2FC \geq 10$ and adj. p-values ≤ 0.01 .

Within the hippocampus, of the 11,001 proteins identified from global phosphoproteomic analysis whose false discovery rate (FDR) adjusted p-values are less than 0.05, 2,282 substrates have phosphorylation levels that are significantly up- or down-regulated ($|\log_2FC| \geq 3$). Amongst this list of substrates, 1962 (86%) are phosphorylated on serines; 308 (13.5%) are phosphorylated on threonines; while with the remaining 8 (0.3%) are phosphorylated on tyrosines.

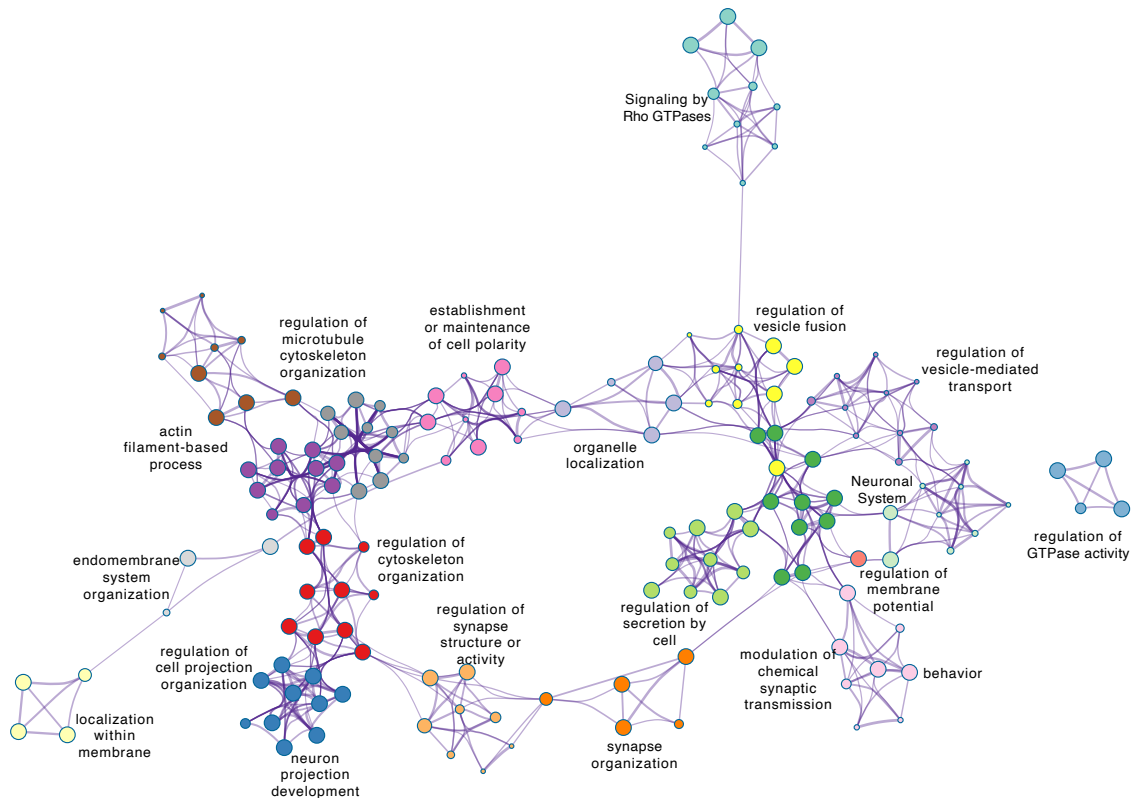


Figure 5.10. Phosphoproteome of Abl2 clustered by biological process reveals that its substrates are involved in pathways highly interconnected by the cytoskeleton. Abl2 phosphorylation mediates a wide variety of pathways. Most, if not all, proteins cluster in overlapping pathways for regulating cell/neuronal projection, synapse structure or activity, and dendrite development; and in regulation of vesicle-mediated transport and modulation of synaptic transmission. Pathway and process enrichment analysis performed via Metascape. Network generated using Cytoscape.

Tyrosine phosphorylation regulates proteins in various ways, but perhaps one of the most important functions of phosphotyrosines is that they serve as docking sites that promote specific interactions with a pY-binding domain-containing (*i.e.* SH2 domain) interactor. These docking interactions are critical for signal transduction at the membrane. Closer analysis of the 8 substrates whose phosphotyrosine residue levels are significantly impacted reveals proteins encoded by genes *Grin2a* and *Grin2b* (NR2B variants), *Map4* (MAP4), *Mapt* (tau), *Ptpn11* (SHP-2), *Rab4a* (member of the Ras superfamily of small GTPases) and *Nefn* (neurofilament heavy chain I). Phosphorylation enrichment of tau by Abl2 is not surprising as a biochemical study has previously shown that tyrosine 394 is phosphorylated and pY-tau is found in Alzheimer's disease brains and Abl2 can directly phosphorylate this site independent of Abl activity (Tremblay et al., 2010). It is

known that tau phosphorylation reduces its affinity and promotes its axonal transport (Rodríguez-Martín et al., 2013). However, the significance of tau phosphorylation by Abl2 outside of the disease context remains unclear. Previous studies in the Koleske Lab demonstrated that dendritic spine density is substantially reduced upon Abl2 knockdown (KD) in cultured hippocampal neurons, which can be rescued by blocking NMDA receptor activity via NR2B inhibition (Lin et al., 2013). These *abl2* KD neurons also exhibit altered synaptic transmission, with lower frequency and higher amplitude of mEPSCs. Given that the NMDA function is tightly regulated by tyrosine phosphorylation of NR2B tail, it is of interest to determine whether Abl2 phosphorylates NR2B directly to regulate synapse stability. Of note, neurofilament heavy chain 1 is phosphorylated at sites S523 and S529, which is located within lysine-serine-proline (KSP) repeats. Phosphorylation within neurofilament heavy chain KSP repeats mediates interaction with neighboring neurofilaments to regulate transport rate from the soma to axons; and is implicated to be associated with molecular motors (Dale & Garcia, 2012). As the heavy chain is heavily phosphorylated upon neurofilament assembly, it remains elusive as to whether and how tyrosine phosphorylation of the heavy chain contributes to axonal transport. Another significant tyrosine-phosphorylated substrate is Rab4a, a member of the family of Rab GTPases which are master regulators of membrane trafficking. When active, Rab GTPases bind to various effector proteins to mediate roles in transport vesicle formation, docking, and motility. There is no study that points to tyrosine phosphorylation of Rab4a, but there is one that provides evidence of Rab4 phosphorylation at S204 by p34^{cdc2} during the cell cycle. However, the functional significance of Rab4 phosphorylation remains to be determined (Bailly et al., 1991). Interestingly, Rab7, a marker for late endosomal trafficking, is phosphorylated at Y183 by Src kinase upon activation by EGF, making it unable to recruit its partner, Rab-interacting lysosomal protein, thereby enhancing Akt signaling as EGF receptor cannot be degraded (Waschbüsch & Khan, 2020). Likewise, Src kinase can phosphorylate Rab34 at Y247 (Sun et al., 2018). Rab34 is localized to membrane ruffles, and phosphorylation stimulates β 3 integrin recycling which is mediated by direct Rab34:integrin β 3 interactions. Additional biochemical studies are needed to elucidate the functional significance of Abl2 phosphorylation at Rab4a Y101. Collectively, these studies point to the importance of tyrosine phosphorylation on Rab

GTPases and other listed substrates in mediating various signaling processes across neuronal compartments.

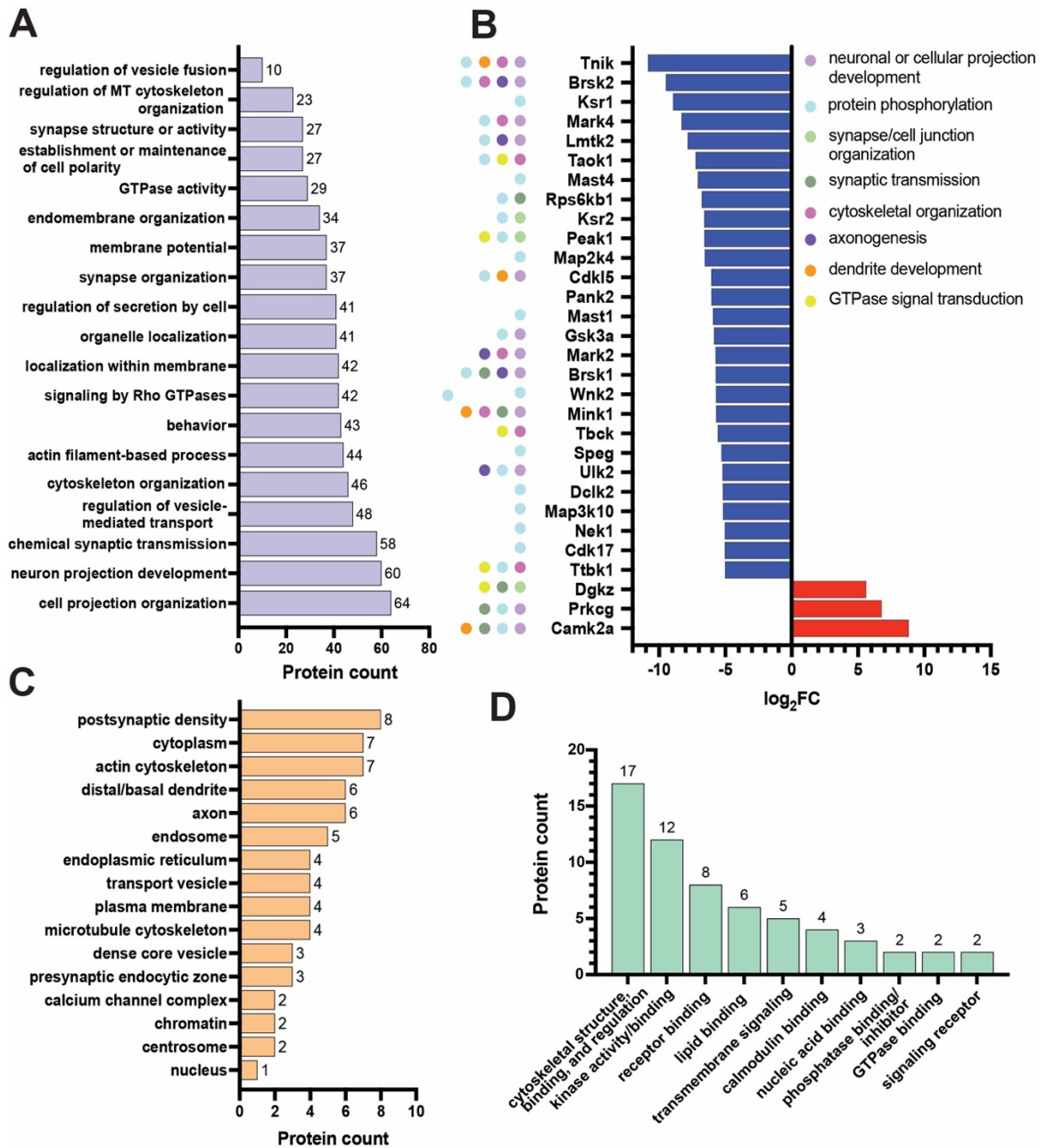


Figure 5.11. Biological pathways, cellular components, and molecular functions of proteins whose phosphorylation levels are statistically significantly affected by the presence of Abl2 in P21 hippocampus. (A) The majority of the proteins (absolute $\log_2FC \geq 3$) undergoing significant changes in phosphorylation levels (adj. p-value $\leq 10^{-4}$) are involved in cell/neuron projection development, synaptic transmission, actin filament-based processes, and membrane/organelle localization, among others. All biological processes have been able to be categorized into the groups shown here. **(B)** Kinase substrates whose phosphorylation levels are impacted under Abl2 regulation in the hippocampus with biological processes shown (n=44). Substrates whose absolute $\log_2FC \geq 5$ and adj. p-values < 0.005 are shown. **(C)** Cellular components for substrates whose $|\log_2FC| \geq 7$ and adj. p-value ≤ 0.05 are shown (n=77). Not all components could be categorized into classes shown here. **(D)** Molecular functions for substrates whose $|\log_2FC| \geq 7$ and adj. p-value ≤ 0.05 are shown (n=77). Not all functions could be categorized into classes shown here.

To further narrow down the list of significantly enriched phosphorylated proteins, I have chosen to focus on proteins whose adj. p-values are $< 10^{-3}$ with $|\log_2FC| \geq 3$ (n=402). Phosphoproteomics reveal that these significant substrates are tightly involved in many clustered, overlapping biological processes, ranging from regulation of the synapse structure, the MT- and F-actin-cytoskeleton, vesicle fusion and transport, and modulation of synaptic transmission (**Figures 5.10, 5.11, A**). Proteins encoded by *Amph*, *Map1a*, *Cwc15*, *Syn2*, *Abi2*, *Dnm1*, *Tbc1d4*, *Luzp1*, and *Ptpn12* are downregulated ($\log_2FC \leq -7$), whereas those encoded by *Lyst*, *Camk2a*, *Ap3b2*, *Rabl6*, *Sorbs1*, *Mapt*, *Ap3b2*, *Mff*, and *Sptbn1* are upregulated ($\log_2FC \geq 7$, **Figure 5.9, B**). In the *abl2*^{-/-} background, phosphorylation of proteins encoded by *Amph*, *Map1a*, *Syn2*, and *Tbc1d4* are significantly upregulated, whereas phosphorylation of proteins encoded by *Lyst*, *Ap3b2*, and *Rabl6* are downregulated. These proteins are involved in shared processes of axonal protein transport, peroxisome and lysosome organization, and synaptic vesicle endocytosis and recycling. Proteins encoded by *Mapt* and *Abi2* are tightly involved with stabilizing the MT/F-actin cytoskeleton or regulating cytoskeletal dynamics. Follow-up experiments are required to determine if Abl2 directly phosphorylates these substrates *in vitro* and in cells (e.g. Western blot analysis comparing WT vs. *abl2*^{-/-} HEK293 and/or COS-7 cells). Functional assays are also needed to determine the relevance of Abl2 phosphorylation on these substrates via live-cell imaging to track axonal transport, for example, in WT and *abl2*^{-/-} neurons; and if functional phenotype can be rescued using the N-terminal half of Abl2 along with kinase-dead Abl2 mutants.

As dendrites undergo extensive growth and remodeling to receive and integrate synaptic input, their development into heterogeneous morphological structures is critical for function. Dysregulation in external cues and/or neuronal activity that contribute to proper dendritic development leads to neurodevelopmental disorders (Frese et al., 2017). Some of the common disorders include Parkinson's disease (PD), which is characterized by progressive degeneration of dopamine producing neurons and results from dysfunction of kinase activities and phosphorylation pathways. One of the major protein kinases associated with PD is leucine-rich repeat kinase 2 (LRRK2). The pathogenic forms of LRRK2 include mutations in its catalytic regions, namely its kinase and GTPase domains. For example, a mutation in the activation loop of the kinase, G2019S, causes neurite shrinkage by inducing mislocalization of tau and MT fragmentation in dopaminergic neurons (Lin et al., 2010). Mechanistically, through extensive biochemical and structural studies, LRRK2 carrying either G2019S or I2020T mutations (located in the active site of kinase domain) extensively decorate MTs (Deniston et al., 2020; Snead et al., 2022; Watanabe et al., 2020). This aberrant MT decoration acts as a significant roadblock for molecular motors undergoing cellular trafficking. Thus, it comes as no surprise that inhibitors targeting the kinase domain are developed to prevent disease progression (Dederer et al., 2023; Sanz Murillo et al., 2023). Thus, I decided to analyze the kinomes impacted under Abl2 phosphoregulation.

Amongst the list of phosphorylation substrates, there are 44 kinases whose phosphorylation levels are significantly impacted under Abl2 regulation. These kinases are localized predominantly at the postsynaptic density, at the distal and basal dendrite, axon, and more structure-specifically, localized along the actin and MT cytoskeleton, endosomes, and transport vesicles (**Figure 5.11, C**). Within these compartments, most of these kinases regulate and bind to cytoskeletal structures; and mediate receptor-, lipid-, transmembrane, calmodulin-, and nucleic acid-binding (**Figure 5.11, D**). The phosphorylation levels of the following proteins are significantly enriched, with $\log_2FC \geq 7$: calcium/calmodulin-dependent protein kinase II α isoform (CaMKII α), protein kinase C γ isoform (PKC γ), and diacylglycerol kinase ζ (DGK ζ , **Figure 5.11, B**). Both CaMKII α and PKC γ are involved in synaptic transmission, downstream substrate phosphorylation in their respective signaling cascades, and neuronal projection development. It is

known that CaMKII α is autophosphorylated at Thr²⁸⁶ (located in the autoinhibitory domain) and Thr^{305/306} (in the CaM-binding domain) for activation. However, depending on its local cellular environment, the CaMKII autophosphorylation response can be modulated depending on its binding partner or upstream kinase that impacts its conformation to confer a different activity (Rostas & Skelding, 2023). Ser²⁷⁹, the site that Abl2 likely phosphorylates, is situated within the same autoinhibitory domain as Thr²⁸⁶. Thus, it is possible that Abl2 phosphorylation can directly or indirectly induce slight allosteric changes in CaMKII, such that it adopts a conformation that substantially favors autophosphorylation for activation. It is also possible that phosphorylation at Ser²⁷⁹ can cause CaMKII to dissociate from proteins in a particular molecular pathway. Likewise, for full activation, PKC γ is an important determinant of Purkinje cell dendritic development (Metzger & Kapfhammer, 2000) and is part of the large PKC family, whose members need full activation via phosphorylation at 3 sites: one at the activation loop, followed by phosphorylation at turn motif T641, with final autophosphorylation at S660 on a hydrophobic motif (Freeley et al., 2011). PKC proteins are involved in a wide variety of neuronal processes, ranging from regulation of MT dynamics via direct phosphorylation of tau to phosphorylating GluA2 subunits of AMPARs to promote long-term depression. Though there is not much literature on non-autoregulatory phosphorylation of PKC, it is likely that phosphorylation of PKC γ under Abl2 kinase activity is compartment- and process-specific, *i.e.* serine phosphorylation may trigger PKC γ relocalization and/or (de)activate activity.

Lastly, DGK ζ is tightly involved in GTPase signal transduction, synaptic transmission, and synapse junction organization. DGK ζ is a member of the diacylglycerol kinase (DGK) family which phosphorylates DG to produce phosphatidic acid, serving as a key enzyme to regulate cellular responses by regulating the balance of these two lipid messengers. DGK ζ is important for dendritic spine maintenance and long-term potentiation in the hippocampus (Topham & Epand, 2009). Phosphorylation within the MARCKS domain is known to modulate DGK ζ localization and activity, *e.g.* phosphorylation by PKC α within the MARCKS domain increased DGK ζ association with RhoA thereby decreasing interaction with Rac1 during cell migration (Ard et al., 2021). However, under Abl2 kinase activity, Ser⁷ is phosphorylated, a site at the very N-terminus. The DGK ζ

phosphorylation status dictates its translocation and subcellular localization, whose functions range from interacting with the cytoskeleton at the plasma membrane to regulating the PtdIns cycle in the nucleus (Barbernitz & Raben, 2023; Topham & Epand, 2009). As Ser⁷ is an uncharacterized site, it will be interesting to explore whether and how this novel serine phosphorylation impacts biological function of DGK ζ in cells. It is important to note that these are global phosphoproteomic analyses analyzed from brain tissue in *abl2*^{+/+} versus *abl2*^{-/-} mice. Thus, these data do not directly indicate that these phosphorylation sites are directly mediated by Abl2 phosphorylation itself, but rather, Abl2 kinase is involved in overlapping signaling cascades that include CaMKII α , PKC γ , and DGK ζ . Nonetheless, these proteins are highly interconnected in regulating various neuronal processes that involve phosphorylation that confer allosteric changes and revealing novel binding sites for downstream interactors.

Interestingly, all four proteins are implicated in programmed cell death. CaMKII α and PKC γ have been proven to be functional for cellular apoptosis. In a study by Konishi and others, COS-7 cells transfected with all PKC isoforms were stimulated with hydrogen peroxide (Konishi et al., 1997). ³²P-tracer experiment with PKC γ revealed that H₂O₂ treatment enhanced phosphorylation of the isoform. Another study revealed that CaMKII can sense redox states, as increased levels of reactive oxygen species can induce oxidative modification of Met^{281/282} within the CaMKII autoregulatory domain to block reassociation with its catalytic domain. To demonstrate that CaMKII activity plays a role in apoptosis, CaMKII KD in cardiomyocytes rescued with CaMKII mutant harboring deletion of Met^{281/282} residues did not undergo programmed cell death. Under Abl2 regulation, PKC γ is phosphorylated at multiple serine residues: Ser³²², Ser³²⁶, and Ser³³³. These amino acids are within the hinge region between the regulatory and kinase domains. There is not much information on PKC γ . However, it can be gleaned from other isoforms, namely PKC δ , that phosphorylation sites within the hinge domain, though not conserved on other PKCs, are important in apoptosis and cell proliferation. It is implicated that the apoptotic stimulus TRAIL induces phosphorylation of PKC δ , which signals for translocation of the kinase to the endoplasmic reticulum for cleavage to the kinase domain. Oxidative stress has also induced phosphorylation at Tyr334 within the hinge domain, and that this is mediated by Src kinases. Likewise, from genetic studies,

DGK ζ been implicated to be involved in the cell death pathway. After multiple excitatory stimuli, DGK ζ re-localizes from the nucleus to the cytoplasm for degradation after phosphorylation by protein kinase C (Topham et al., 1998). More discussion on oxidative stress and programmed cell death can be found in **Section 6.4**.

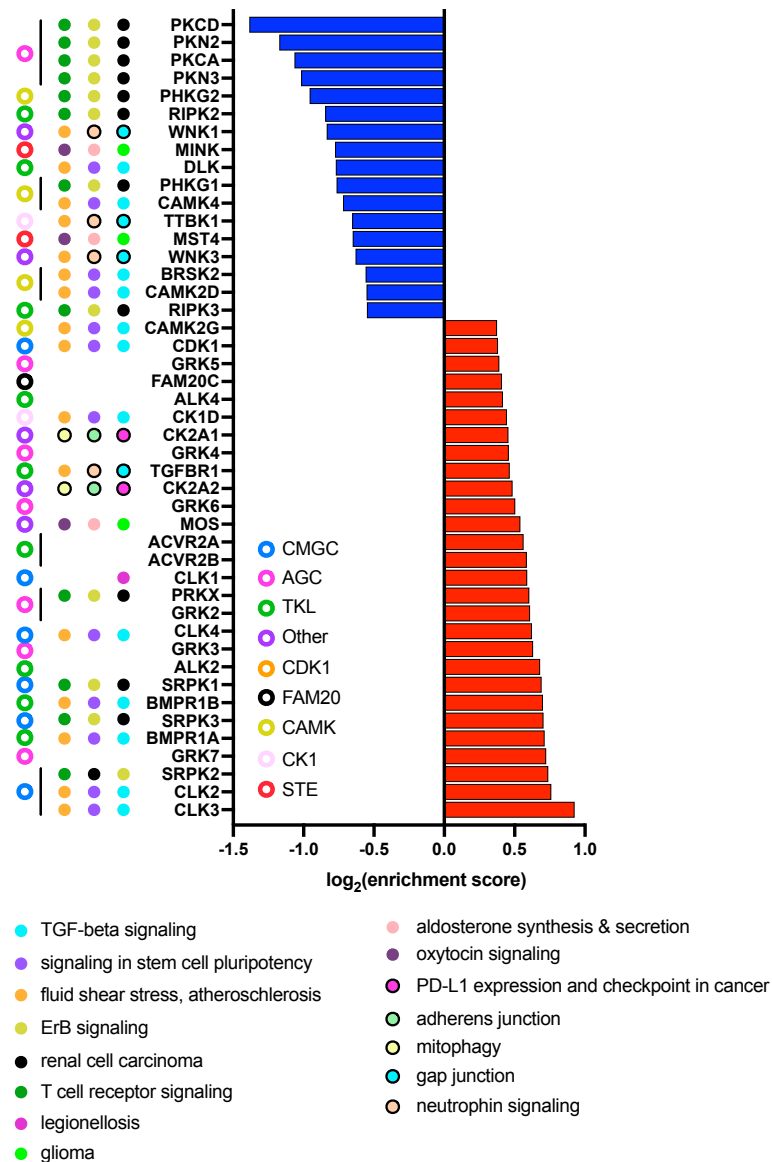


Figure 5.12. KSEA analysis reveals protein kinases involved in multiple biological pathways. Kinases shown have adj. p-values < 0.01 and $\log_2(\text{enrichment score}) \geq 0.35$ (n=45). Kinases are also denoted with their corresponding kinase group, classified based on catalytic domains. AGC: cytoplasmic serine/threonine protein kinase A, G, C families (PKA, PKC, PG); CAMK: Ca^{2+} /calmodulin-dependent protein kinase; CK1: casein kinase 1 family; CMGC: cyclin-dependent kinases (CDKs), mitogen-activated protein kinases (MAP kinases), glycogen synthase kinases (GSK) and CDK-like kinases; FAM20: family with sequence similarity 20; PDHK: pyruvate dehydrogenase kinase; STE: consists of three main kinase families, Ste7 that phosphorylate MAPKs, Ste20 (MAP4K) that act on Ste11 kinases, and Ste11 group which contains MEKK subfamily kinases; TKL: tyrosine kinase-like group that lack the TK-specific motifs of the TK group (e.g. Leucine Rich Repeat Kinases (LRRK), receptor interacting protein kinase, RIPK, that couple TNF receptors to NF- κ B signaling).

Phosphoproteomics MS also allows for the robust interference of kinase activities in proximal pathways. Kinase-substrate enrichment analysis (KSEA) measures global kinase

pathway activation, by taking altogether the phosphorylation sites and motifs to calculate the enrichment of substrate groups relative to phosphoproteomics data set and infers activities of other kinase cascades. Among the significant kinases whose activities are also impacted by Abl2 kinase activity, there is clear clustering of biological processes amongst KSEA proteins that are either up- or down-regulated. Downregulated kinases PKN3, PKCA, PKN2, and PKCD are all involved in renal cell carcinoma, T-cell receptor signaling, and ErbB signaling (**Figure 5.12**). CLK3, CLK2, BMPR1A, BMPR1B and CLK4, whose activities are substantially enriched, are kinases involved in TGF- β signaling, stem cell pluripotency, and fluid shear stress/atherosclerosis (drag force acting on vessel wall that is crucial for normal vascular functioning (Cunningham & Gotlieb, 2005)). 20% of the 105 differentially enriched kinases belong to the AGC group, 19% in CAMK, 14% in TKL, 11% in CMGC, 10% in STE, 6% in CK1, a minority (<2%) belonging to PDHK and FAM20 families, with 14% belonging to unclassified groups (**Figure 5.13, A**). CLK2/3-involved pathways are significantly impacted by Abl2 kinase activity. Murine CLK2/3 are nuclear dual-specificity kinases that colocalize with and redistribute SR proteins in nuclear speckles to regulate alternative splicing in vivo (Duncan et al., 1998). Interestingly, Abl2 co-IPs with serine and arginine rich splicing factor 4, SRSF4 (**Figure 5.3, A**). SRSF4 is directly involved in cisplatin-induced splicing events in cell death. Cisplatin is an agent that covalently binds to DNA to form bulky DNA adducts that interfere with DNA transcription, thus activating DNA damage response pathway for cell death (Gabriel et al., 2015). In another scenario, alternative splicing of exon 6 in Fas pre-mRNA, a type I transmembrane cell surface receptor, induces apoptosis. Interestingly, SRSF4 stimulates exon 6 inclusion to protect against Fas-mediated apoptosis by directly binding to GGGGUG RNA sequence on exon 6 (Jang et al., 2018). It remains unclear whether and how Abl2:SRSF4 binding interactions contribute to programmed cell death, and how Abl2 may coordinate with CLK2/3 to do so. In fact, though some KSEA proteins regulate synaptic transmission, vesicle docking, and dendrite development, the majority are involved in apoptosis and regulating DNA damage, and in oxidative/glucose stress cell response pathways (**Figure 5.13, B**). Future directions include correlating KSEA results with systematic Western blot analyses of these differentially enriched kinases with WT and Abl2 KD N2A cell extracts, in normal versus hyperosmotically stressed conditions.

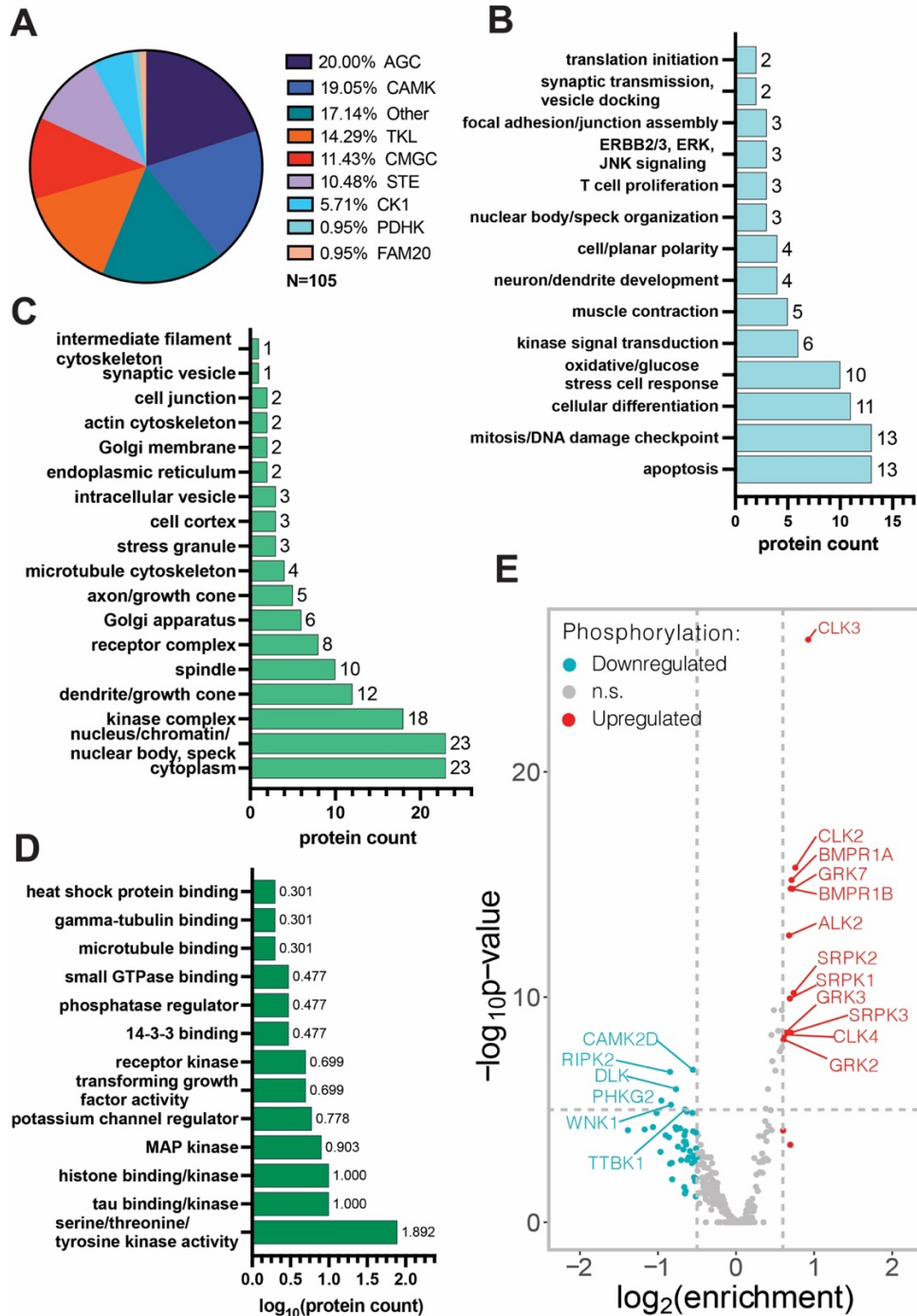


Figure 5.13. KSEA analysis from the Abl2 phosphoproteome reveals proteins enriched in DNA damage and apoptosis pathways. (A) Kinase group classifications based on catalytic domain. Abbreviations of kinase group classifications in Figure 5.11. **(B)** Biological processes that significantly enriched kinases are involved in. **(C)** Majority of KSEA proteins are localized in the cytoplasm, nuclear bodies/specks/chromatin, and mitotic spindles. **(D)** Molecular functions for KSEA proteins. Protein count shown on \log_{10} scale. Note for (B)-(D), not all kinases fell under the classes shown here. **(E)** Labels shown for significant up- or down-regulated proteins with adj. p-value $\leq 10^{-5}$ and $\log_2(\text{enrichment}) \geq 0.6$ or $\log_2(\text{enrichment}) \leq -0.5$.

5.5. Materials and Methods

REAGENT or RESOURCE	SOURCE	IDENTIFIER
Antibodies		
Rabbit polyclonal eGFP antibody	Origene	Cat# TA150032
Rabbit polyclonal profilin-1 antibody	Cell Signaling	Cat# 3237S
Other		
Gelatin Sepharose 4B	Cytiva	Cat# 17095601
Streptavidin Sepharose High Performance affinity resin	Cytiva	Cat# 17511301

Abl2 co-IP from mouse brain lysates

Whole brain tissue from 3 P22 wildtype and 3 P22 *abl2*^{-/-} mice from C57BL/6 background were collected and weighed. For every 100 mg brain tissue, 1 ml of lysis buffer was added. Lysis buffer consisted of 50 mM Tris-HCl pH 7.4, 250 mM KCl, 1 mM EDTA, 0.5% NP-40 supplemented with 1X cOmplete protease inhibitor cocktail and phosphatase inhibitors NaF, NaVO₄, Na₄P₂O₇, and β-Glycerophosphate. Brain tissue was homogenized using pestle tissue grinders in 200 μL volume and transferred to a 5 ml Eppendorf tube. Lysis buffer was added until the target volume (based on brain weight) was reached. Lysates were allowed to incubate and solubilize on a rotator at 4°C overnight.

The following day, samples were centrifuged at 14K RPM for 30min at 4°C. 300-400 μL aliquots of supernatant was transferred into clean 1.5 ml Eppendorf tubes, snap frozen, and kept at -80°C until ready for co-IP. Lysates were thawed and total protein levels were quantified via BCA assay. Brain lysates were diluted in lysis buffer to 1 mg* mL^{-1} concentration (~5 mg total in 5 mL). Lysates were pre-cleared using 50 μL Protein A/G agarose resin for 2h on a rotator at 4°C.

For each sample, 100 μL Pierce Protein A/G agarose slurry was washed 10V 1X PBS 4 times at 500 g for 3 min. For each sample, 50 μg of 496 antibody was added into the A/G agarose slurry. 496 antibody recognizes the C-terminal half of Abl2 (purified by Tony Koleske circa 1997 in the Baltimore Lab, MIT). The antibody and beads were allowed to rotate at RT for 2 hr to allow binding of antibody to beads. 100 mM sodium borate pH 9 and 200 mM ethanolamine pH 8 solutions were prepared fresh and sterile filtered. The binding suspension of antibody and beads was spun down at 500 g for 3 min at RT. Antibody-beads were washed with 10V of 100 mM sodium

borate 2X, spun down each time at 500 g for 3 min at RT. Beads were resuspended after the last wash with 10 bead volumes (BV, ~1 mL) of 100 mM sodium borate, and the crosslinking reaction was initiated by adding in fresh dimethylpimelimidate powder to a final concentration of 20 mM. The crosslinking reaction was allowed to incubate on a rotator at RT for 30 min. 10 BV of 200 mM ethanolamine was added to stop the crosslinking reaction and washed once with an additional 10 BV 200 mM ethanolamine. The crosslinked antibody-beads were allowed to incubate on rotator for 2h at RT. After stopping the crosslinking reaction, antibody-linked beads were washed with 10BV of PBS 10X and spun down each time at 500 g for 3 min. Pre-cleared brain lysates were added to the beads and allowed to incubate on rotator at 4°C overnight. The following day, lysates were spun down at 500 g, 4°C for 5 min. Beads were washed once in wash buffer (50 mM Tris-HCl pH 7.4, 250 mM KCl, 1 mM EDTA). Co-IP was verified via immunoblotting against Abl2 using Ar11 antibody (recognizes C-terminal half epitope).

Abl2 co-IP from HEK293T cell lysates

HEK293T cell lysates were transfected using PEI, at 1:4 DNA:PEI ratio, with pN1-eGFP or pN1-Abl2-eGFP. 4 70% confluent 10 cm plates were transfected 16h prior to harvest. Cells were lysed using the same lysis buffer as described for Abl2 co-IP from mouse brain lysates. Immunoprecipitation experiments were conducted using the same protocol as described above, using rabbit polyclonal α -eGFP antibody (Origene) for bait.

Abl2 BioID2 stable cell line construction and pulldown

BioID2 cell lines were generated by linearizing pN1-BioID2-eGFP or pN1-Abl2-BioID2-eGFP plasmids via restriction digest (ApaI). The linearized plasmids were then randomly incorporated into the genome via calcium phosphate transfection into COS-7 Abl2 KO cells.

BioID2 cell lysis and pulldown protocols were adapted from (Sears et al., 2019). In brief, our 70% confluent 10 cm plates per BioID cell line were plated. Upon fully adhering, the medium was switched to complete DMEM medium supplemented with 50 μ M biotin the night before harvest. Cells were incubated overnight for ~16-18 h. The following morning, cells were washed 3X with 5

ml of PBS each. Cells on each plate were lysed with 1 ml of lysis buffer (8M urea in 50 mM Tris pH 7.4, 1X cOmplete protease inhibitor cocktail, 1mM DTT), and gently scraped using a cell scraper. 0.1 μ L of Pierce Universe Nuclease and Triton X-100 to a final concentration of 1% (v/v) was added to each sample. Cells were then sonicated using QSonica Q55 Compact Sonicator on ice at amplitude 30 (on-off 5 s pulses on the thumb switch setting) for 15 s; and supernatant was harvested after 80K rpm 5 min centrifuge spin at 4°C.

200 μ L gelatin Sepharose beads were equilibrated using 1 ml lysis buffer and centrifuged for 500 rpm for 3 min. This step was repeated twice to fully remove ethanol. Lysates were pre-cleared with the beads for 2h at 4°C. Supernatants were harvested. The same wash steps were performed for 50 μ L streptavidin Sepharose beads. Following the 2 hr pre-clearing step, lysates were incubated with streptavidin beads for 4 hr at 4°C. Lysates with beads were centrifuged at 500 rpm for 3 min at 4°C. Supernatant was discarded and beads were suspended in 1 ml wash buffer (lysis buffer without 1X protease inhibitor cocktail, 1mM DTT). Beads were transferred to a new Eppendorf tube and washed with 1 ml lysis buffer for 8 min on a rotator at RT 3 additional times. After the last wash, beads were resuspended in 50 ml 50 mM ammonium bicarbonate containing 1 mM biotin. Beads were flash frozen in liquid nitrogen and stored in -80°C.

Chapter 6: Ongoing work and future directions

Actin and microtubules contribute to the internal structural organization of the cytoplasm through forces generated from the disassembly-reassembly remodeling cycle. Generating these forces drive cell shape changes and motility. There is increasing evidence that these two cytoskeletal systems work together intimately through functional crosstalk for promoting processes including cell motility and cell polarity. A seminal 2004 study by Miller *et al.* demonstrated that Abl2 co-localizes with both the actin and microtubule cytoskeleton to promote lamellipodial formation in fibroblasts (Miller et al., 2004). Interestingly, the tubulin-binding region, Site I, falls within the (I/L)WEQ domain, which is one of the two F-actin binding regions of Abl2 (Courtemanche et al., 2015). However, it remains elusive what the minimal domain of Abl2 is that can crosslink both F-actin filaments and microtubules; where crosstalk can be observed in cells based on Abl2 localization during initial cell spreading; and whether Abl2 modulates cytoskeletal regulation in non-homeostatic cellular processes such as in a state of hyperosmotic stress. This chapter will present my initial strides taken to address these questions.

Work shown in this section has not been published. Sample preparation and image acquisition for correlative light electron microscopy were done alongside Zhongyuan Zuo, Senior Staff Scientist from Yale School of Medicine Cellular and Molecular Imaging Electron Microscopy Facility. 4pi imaging acquisition was done by Maohan Su, Associate Research Scientist of the Rothman Lab. RNA-sequencing was processed at the Yale Center for Genome Analysis, and preliminary analysis was done by Leonard Schärfer of the Neugebauer Lab.

6.1 Abl2 mediates F-actin-MT crosstalk.

F-actin and MTs engage in crosstalk that is important for regulation of cellular morphogenesis and polarity, cellular migration, cell division, and in neuronal function (Dogterom & Koenderink, 2018). Though the two components of the cytoskeleton have been extensively studied individually, these sub-cytoskeletal systems collectively contribute to the organization of the cytoplasm to drive cell shape and motility. Given previous work that Abl2 binds to F-actin and MTs, I investigated whether Abl2 could crosslink both F-actin and MTs *in vitro*. GMPCPP-stabilized MTs were flowed into TIRF

chambers and anchored onto coverslips via biotin-neutravidin interactions, followed by 0.5 μM Abl2 and stabilized F-actin filaments (**Figure 6.1**).

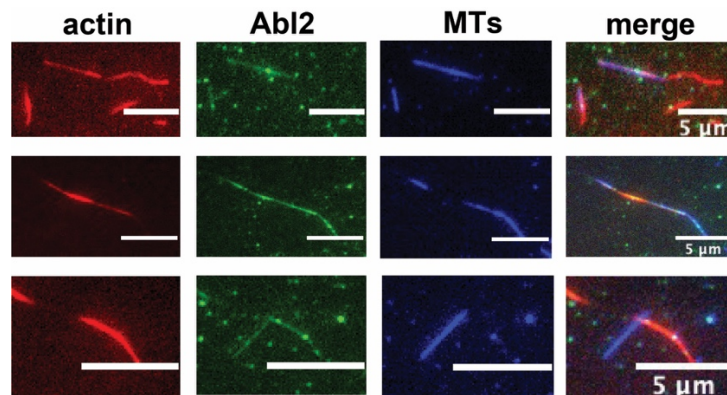


Figure 6.1. Abl2 simultaneously binds F-actin and MTs *in vitro*. Abl2 mediates crosstalk between Alexa647-labelled GMPCPP-stabilized MTs and rhodamine-actin filaments. F-actin filaments can be seen to directly bind to Abl2, aligning in parallel to MTs (first row). Abl2 can also mediate crosstalk between multiple microtubule filaments and F-actin (second row). Multiple Abl2 molecules can also serve as a bridge (likely through self-association) to crosslink a predominantly Abl2-bound MT with a predominant Abl2-bound F-actin filament (third row).

Crosstalk could be mediated by proteins that have distinct binding sites for MTs and actin bundles. There is also evidence that MTs can directly localize F-actin factors to promote local actin assembly, as was seen for the formin mDia1 which associates with MT ends directly with +TIP CLIP-170 to promote rapid polymerization of actin filaments (Henty-Ridilla et al., 2016). Excitingly, I also observed this for Abl2. Inclusion of 0.5 μM Abl2-eGFP in a reaction containing 1 μM rhodamine-actin and 0.1 mM ATP reveals potent actin nucleation from Abl2 puncta localized on coverslip-bound GMPCPP-MTs (**Figure 6.2, A**). This is Abl2-dependent, as neither actin nucleation events nor actin filaments were found to localize onto MTs without a crosslinker (**Figure 6.2, B**). This suggests Abl2 forms phase-separated puncta, and in absence of MTs, potentially activates actin nucleation forming aster-like arrays that stem from Abl2 'hotspots' (**Figure 6.3**).

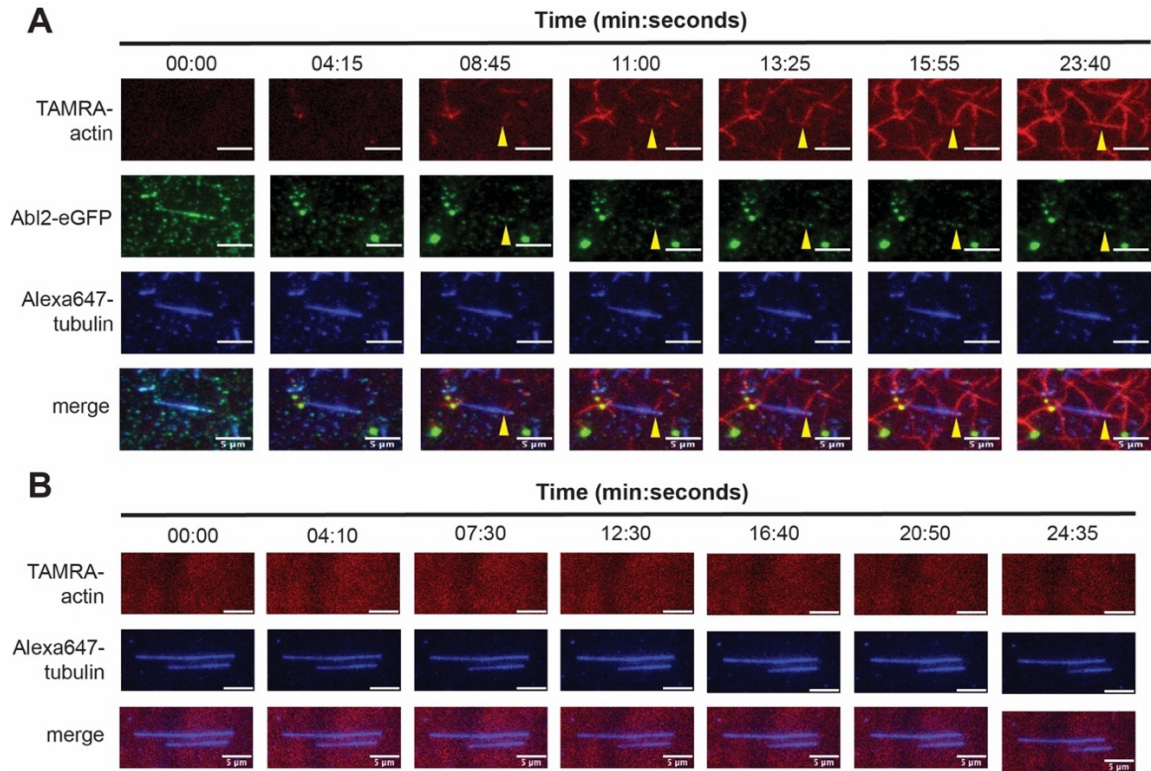


Figure 6.2. Abl2 promotes actin nucleation on MTs. (A) 0.5 μ M Abl2-eGFP, 1 μ M rhodamine-actin, Alexa637-biotinylated GMPCPP-MTs supplemented with 0.1 mM ATP were flowed into a TIRF chamber. Video acquisition started after a 5 min incubation. Non-specific phase-separated Abl2-eGFP were bound onto coverslips, which served as hotspots for actin monomers to co-partition into and began nucleating. (B) Same experimental conditions as in (A) but in absence of Abl2. No actin critical nuclei nor polymerization of existing F-actin oligomers were observed on MTs in absence of Abl2. does not promote localization of actin critical nuclei nor F-actin onto stabilized MTs on coverslips.

This phenomenon is not unique, as this has been observed from other actin-binding proteins that play prominent roles in forming actin networks (e.g. abLIM1 for mediating stable plasma membrane-cortex interactions by maintain a highly interconnected cortical actin network (Yang et al., 2022)). It remains elusive as to whether this Abl2-mediated phenomenon occurs in cells, and if so, when, and where. However, given previous and current work, I propose a model whereby Abl2 stabilizes the MT lattice by replenishing damage sites by binding to soluble GTP-tubulin dimers in non-neuronal cells (**Steps 0-2, Figure 6.4**). MTs will grow until they reach actin structures at near the cell periphery which serve as physical barrier for growth. Abl2 ‘surfs’ or diffuses on MTs until it recognizes F-actin filaments, likely through interactions with nearby actin regulators *i.e.* cortactin and/or N-WASP (**Step 3, Figure 6.4**). Abl2 transiently mediates MT-actin crosstalk (**Step 4, Figure**

6.4), and eventually “hops” onto the actin filament to coordinate actin cytoskeletal changes for lamellipodial dynamics and dorsal ruffling (**Step 5, Figure 6.4**).

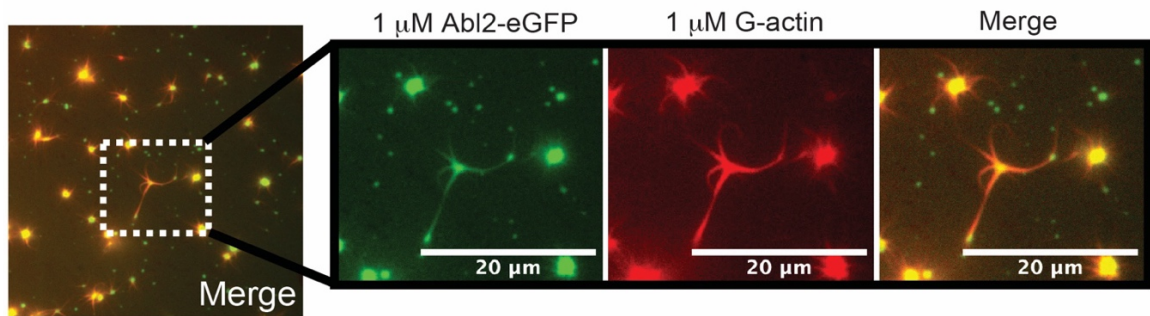


Figure 6.3. Abl2 promotes actin nucleation. Nucleation reactions were visualized under TIRF microscopy. 1 μM Abl2-eGFP, 1 μM rhodamine G-actin, 0.1 mM ATP, 5% dextran-70, and 50 mM KCl were mixed in TicTac buffer (Farina et al., 2016). Reaction was allowed to equilibrate in the TIRF chamber for 5 min at RT prior to video acquisition.

Additionally, it was discovered by Woodring and others that the kinase activity of c-Abl is inhibited upon binding to F-actin *in vitro* and in cells through a regulatory feedback loop (Woodring et al., 2001). Woodring *et al.* predicted that c-Abl may adopt a kinase inactive conformation on actin filaments via long-range structural rearrangement that hinders the c-Abl active site at the N-terminus. Though it has been demonstrated the kinase activity of Abl2 is not required to mediate cell edge protrusions in fibroblasts, it is not known whether or how Abl2 kinase activity is impacted upon F-actin-binding and/or MT-binding, and how this is implicated in a cellular context. Future biochemical studies include co-sedimentation assays to quantify the binding affinities of Abl2 and kinase-dead Abl2 for F-actin and MTs (*i.e.* keeping [Abl2] and [F-actin] or [MT] constant, while titrating in increasing amounts of [MT] or [F-actin], respectively).

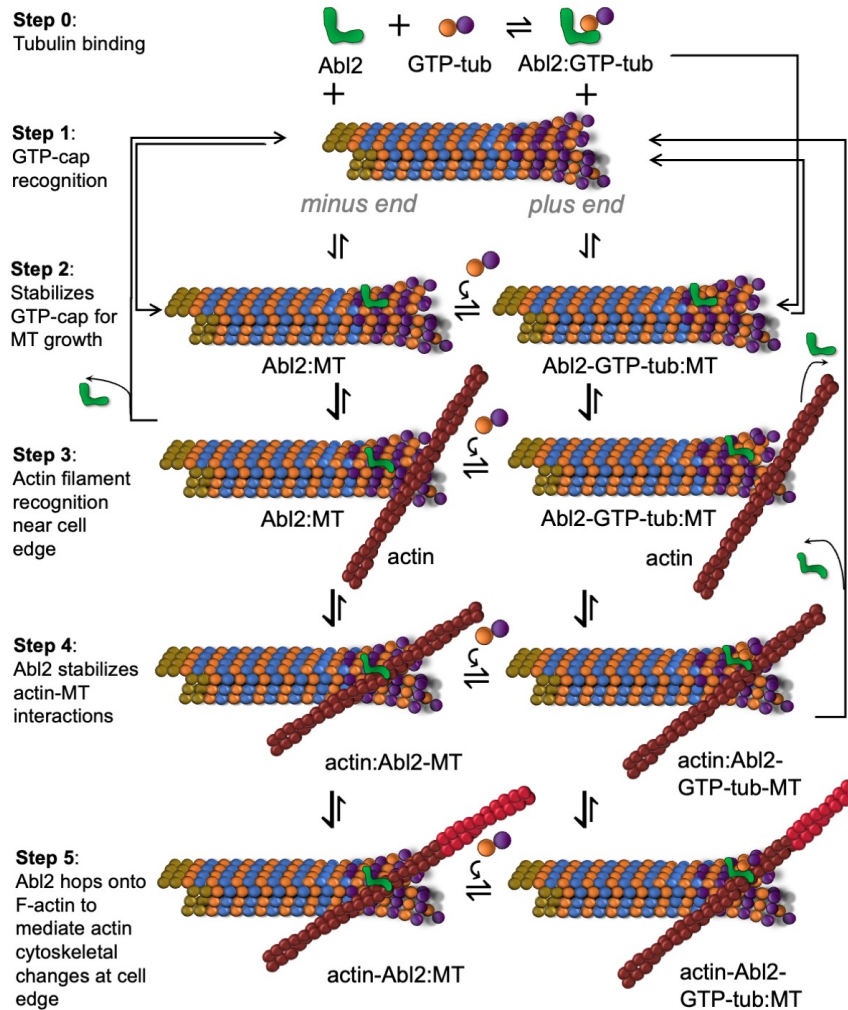


Figure 6.4. Proposed mechanism for Abl2 mediating F-actin:MT crosstalk. Because it is unlikely that a simple reversible binding mechanism solely explains its ability to promote growth and suppress catastrophe, Abl2 is mechanosensitive and can distinguish between nucleotide-bound states of polymerized tubulin. Abl2 likely binds to GTP-tubulin dimers in solution (**Step 0**) before its association with the MT lattice, recruit dimers during its “surf” along the GDP-lattice, or recruit dimers once it reaches the tip. Once Abl2 recognizes the GTP-cap (Bodakuntla et al., 2019; Bowne-Anderson et al., 2013; Caplow & Shanks, 1996; Drechsel & Kirschner, 1994; Vandecandelaere et al., 1999), Abl2 may enhance its affinity for the lattice due to a conformational change (**Step 1**) and load its recruited GTP-tubulin to the growing end (**Step 2**). Note that Abl2 may also do this during its ‘surf’ and incorporate tubulin into damage sites. Once Abl2 reaches the growing MT ends, it may stay on until MTs reach the actin-rich “peripheral domain” of cells (**Step 3**). Abl2 may also associate with F-actin and stabilize crosstalk (**Step 4**). Abl2 has a stronger preference for F-actin, thus it likely switches its localization from the MT to F-actin (**Step 5**). Abl2 stabilizes actin filaments at the cell edge to promote cell morphogenesis, lamellipodia formation, and migration.

6.2 Function of phase separated Abl2 *in cellulo*

Phase separation of cytoskeletal regulators and kinases have been implicated in various cellular processes (covered in **Section 1.3**). It remains a question as to what proteins are recruited, if any,

into Abl2 condensates in COS-7 cells, and how PTMs contribute to the propensity of Abl2 to undergo LLPS. Curiously, treating COS-7 cells overexpressing Abl2-mCherry-Cry2 with 10 μ M PD180970 kinase inhibitor reveals that apparent Abl2 condensates distinctly cluster at the cell periphery (**Figure 6.5**). It is hypothesized that because the kinase activity of Abl2 is not employed, the cytoskeletal regulating C-terminal half of Abl2 plays a more dominant role and potently interacts with the F-actin cytoskeleton. Surface receptors including integrins trigger formation of adhesion structures upon receiving extracellular cues and can directly engage the actin cytoskeleton.

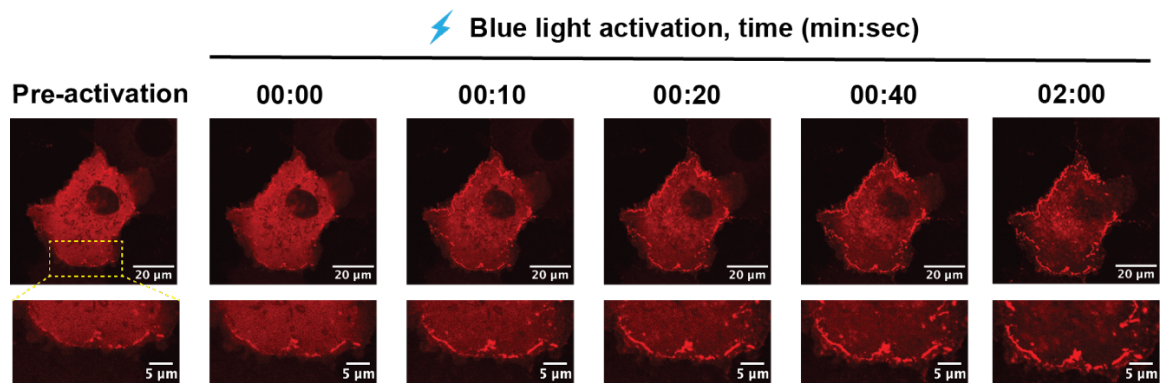


Figure 6.5. PD190870-treated COS-7 WT cells overexpressing Abl2-mCherry-Cry2 reveal distinct clustered islands at the cell periphery.

Actin dynamics can also trigger recruitment of adapter proteins to the cell periphery including Abl2. At the cell periphery, Abl2 can interact with integrin β 1 cytoplasmic tails to achieve full kinase activation via interaction with its SH2 domain (Simpson et al., 2015). Thus, without the ability for Abl2 to phosphorylate its various downstream cytoplasmic substrates (N-WASp, cortactin, p190RhoGAP), it is postulated that Abl2 fails to receive and translate cellular inputs, as it remains in its closed kinase-inactive state. However, these data raise the question of whether other cytoskeletal interactors may be promoting Abl2 localization to the cell periphery. To determine whether Abl2 may partition actin and/or tubulin into these condensates, I utilized immunofluorescence to detect for co-localization of Abl2 with actin/tubulin in blue-light activated COS-7 cells overexpressing Abl2-mCherry-Cry2 (**Figure 6.6**). Unfortunately, a recent study revealed that PFA fixation can both enhance or diminish LLPS behaviors depending on the rate of fixation relative to protein-protein interaction dynamics, thereby introducing biological artifacts

(Irgen-Gioro et al., 2022). In the case of Abl2, PFA seemed to diminish Abl2-mCherry-Cry2 puncta formation, despite a 2 min blue-light activation period using 488 nm laser power of 50%. Thus, I sought to live-cell imaging to address the question, that is whether Abl2 co-partitions tubulin and/or actin monomers into condensates.

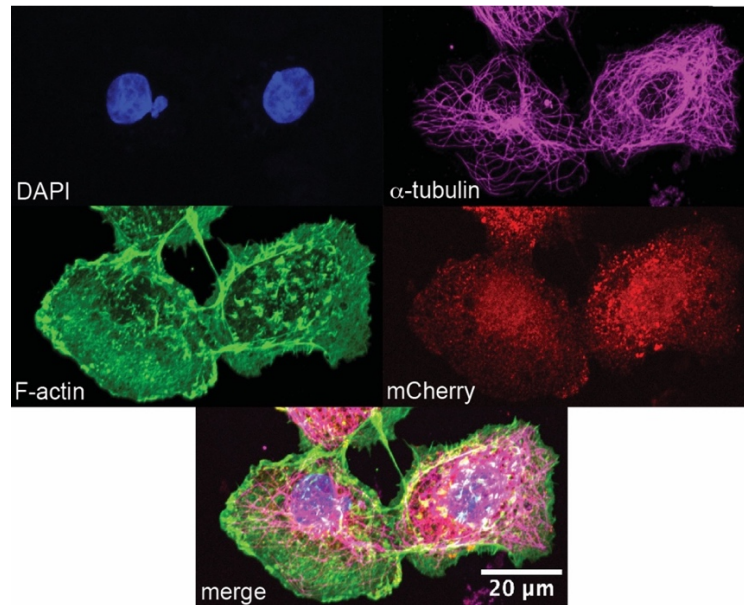


Figure 6.6. PFA fixation of COS-7 cells overexpressing Abl2-mCherry-Cry2 induces condensate artifacts. Maximum z-projection.

I co-transfected COS-7 cells with tubulin-CFP and Abl2-mCherry-Cry2 (**Figure 6.7**). It can be observed that small Abl2-mCherry-Cry2 condensates have begun to form prior to blue light activation likely due to exposure to white light (Hernández-Candia & Tucker, 2020). Nonetheless, Abl2-mCherry-Cry2 puncta appear less diffuse and less uniform throughout the cytoplasm and begin to cluster by the 3 min timepoint relative to the pre-activation state (**Figure 6.7**). Abl2-mCherry-Cry2 condensates and tubulin-CFP do not appear to coalesce. However, upon closer observation, it is evident that Abl2-mCherry-Cry2 condensates appear to be moving along MT tracks in cells, pre- and post-blue light activation (**Figure 6.8**).

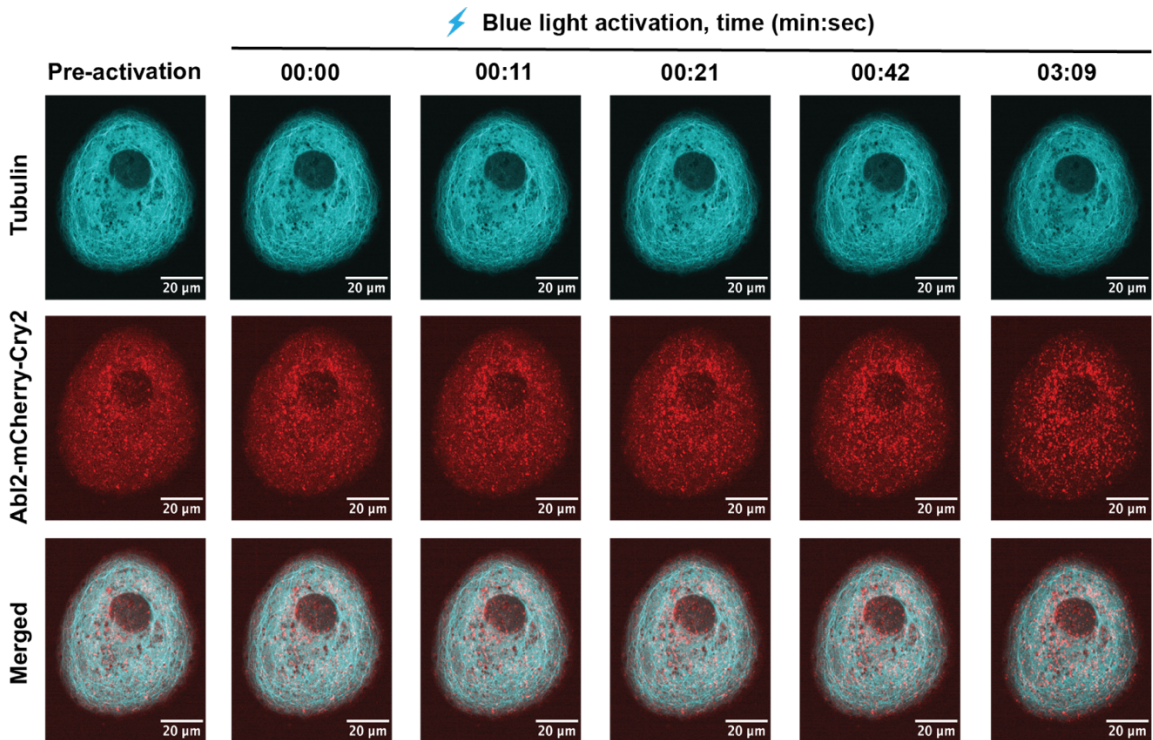


Figure 6.7. COS-7 WT cells overexpressing tubulin-CFP and Abl2-mCherry-Cry2.

Future experiments include live-cell imaging of COS-7 Abl2 KO cells co-transfected with a +TIP tracker (EB1/3 fused to CFP) and Abl2-mCherry-Cry2; LifeAct-BFP/CFP with Abl2-mCherry-Cry2; and pN1-cortactin-CFP with Abl2-mCherry2-Cry2 to determine what other cytoskeletal regulators are recruited into Abl2 phase-separated condensates. It will be interesting to explore whether and how localization of these proteins changes upon treatment with Abl kinase inhibitors (PD180970, STI571).

Additionally, though BS³ cross-linking mass spectrometry results (**Section 4.1**) yielded only one bona-fide interaction between murine Abl2 and porcine tubulin dimer, the experiment yielded a lot more bona-fide intermolecular interactions between two 6XHis-Abl2 molecules. Interestingly, 79% of the unique cross-links with an SVM score above 0.5 mapped back to the C-terminal half of Abl2, with only 4% that resided solely within the kinase domain-containing N-terminal half (**Figure 4.2**). This suggests that the disordered C-terminal half contains amino acids (serine, proline, glycine, arginine, lysine) that dominate the molecular grammar underlying phase separation (Hong et al., 2022; Wang et al., 2018).

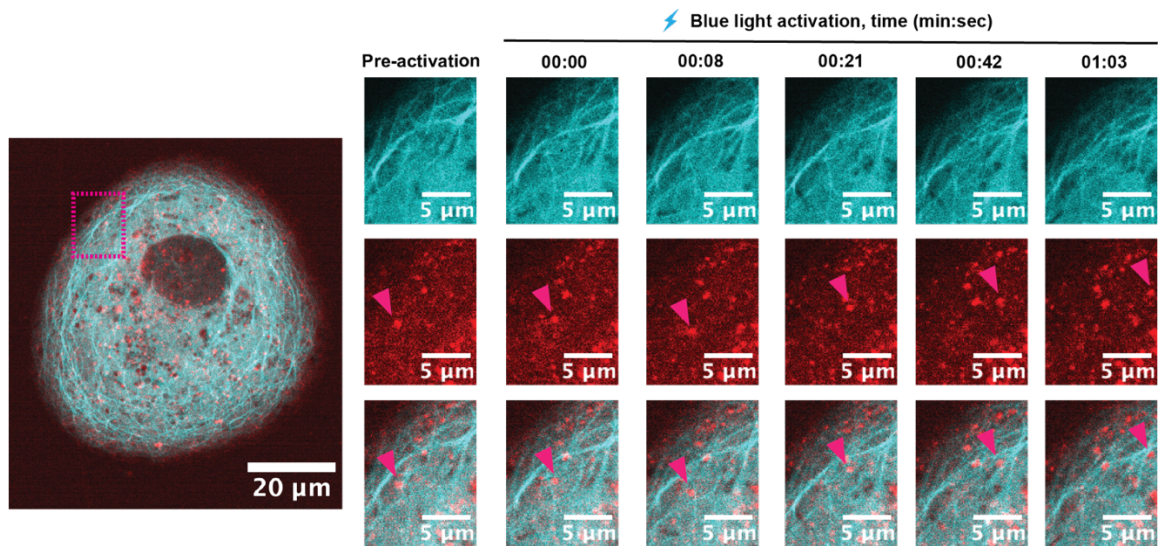


Figure 6.8. Representative mobile Abl2-mCherry-Cry2 condensate ‘swimming’ along MT tracks. Abl2-eGFP and tubulin-CFP were transfected into COS-7 cells for 24 hr. Cells were exposed to 488 nm laser in sequence with video acquisition of the CFP and mCherry channels for 5 min. Magenta arrow points to an Abl2 condensate ‘surfing’ on a MT track near the cell periphery of COS-7 cell.

Future experiments include transfection of Abl2-mCherry-Cry2 oligomerization mutants into COS-7 Abl2 KO cells that harbor K/R→A point mutations in the C-terminal half and quantitatively assess the propensity to phase separate under blue light activating conditions. As per above, it will be interesting to see whether actin and/or MT dynamics change by co-transfecting LifeAct or a +TIP marker.

6.3 Visualizing F-actin and microtubule crosstalk under the regulation of Abl2 *in cellulo*

It is known that there is little to no co-localization of Abl2 with the actin and MT cytoskeleton when cells have fully adhered onto glass coverslips and dishes, *i.e.* completed cell spreading (**Figure 6.9**, 4pi imaging in **Figure 6.10**). Abl2 appears to be punctate-like and diffuse throughout the cytoplasm. However, it can be observed via immunofluorescence that Abl2 does bind appreciably to MTs and F-actin when the cells are undergoing initial stages of cell spreading (**Figure 6.11**).

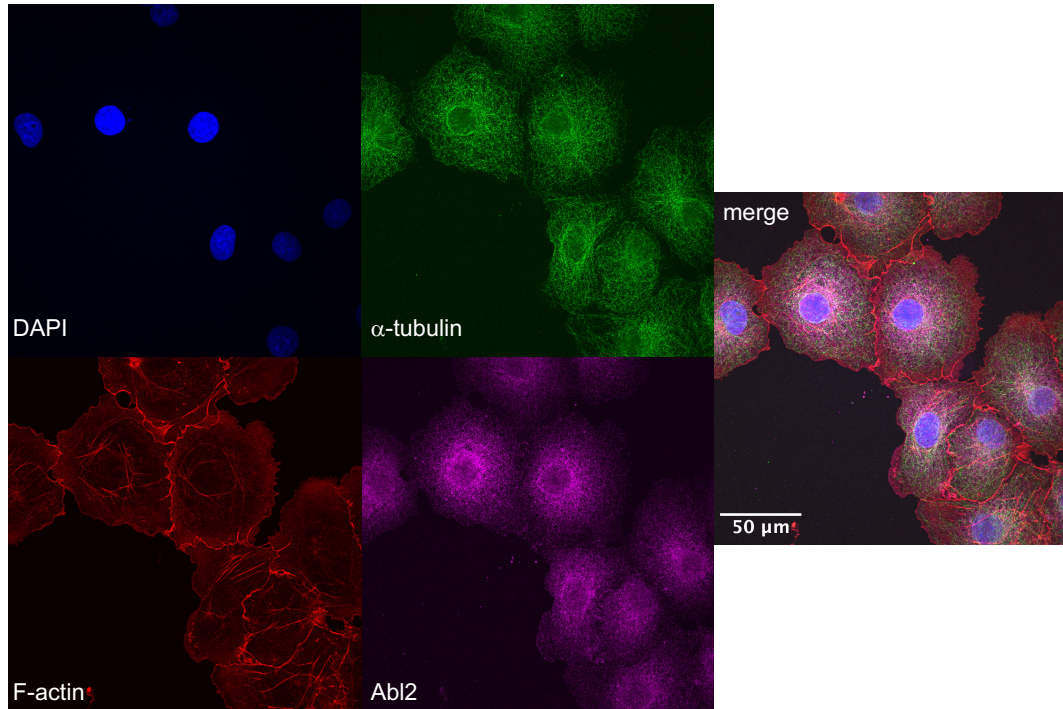


Figure 6.9. Endogenous staining for α -tubulin, F-actin, and Abl2 in COS-7 cells reveals no clear co-localization of Abl2 with the F-actin nor MT cytoskeleton. COS-7 cells were allowed to adhere to the coverslips overnight in 37°C incubator prior to fixation.

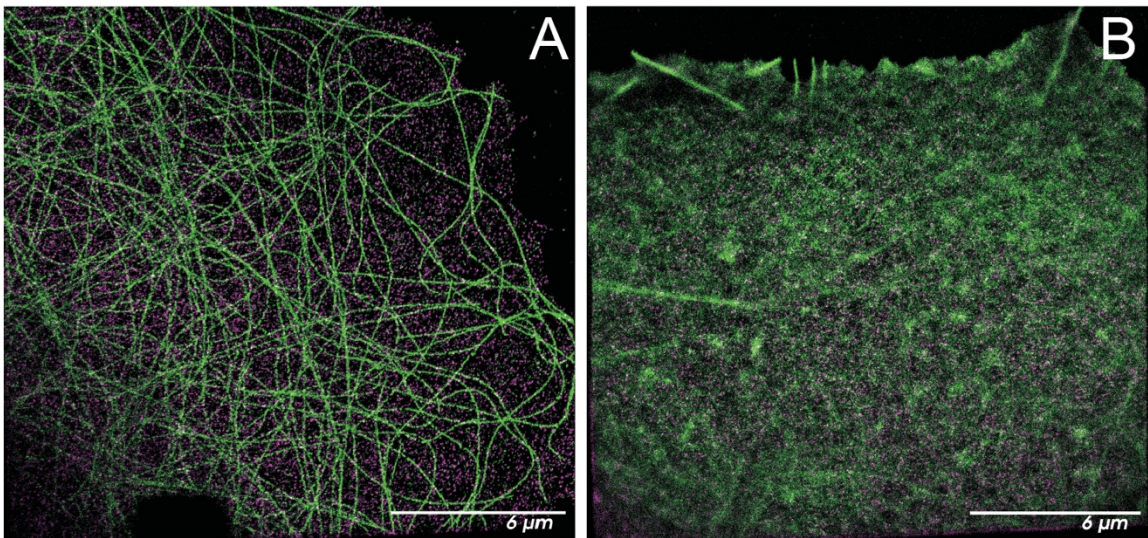


Figure 6.10. Super-resolution 4pi imaging reveals that Abl2 does not co-localize appreciably with α -tubulin nor F-actin in COS-7 Abl2-eGFP stably expressing cells that have fully adhered. (A) Abl2 in magenta (punctate), MTs in green. (B) Abl2 in magenta (punctate), F-actin in green. Images acquired by Dr. Maohan Su, Rothman Lab.

Correlative light electron microscopy (CLEM) reveals, through drastic changes in contrast and density, that there are significant changes in the organization of the F-actin cytoskeleton in *arg*^{-/-}

3T3 fibroblasts re-expressing Abl2-eGFP relative to that of eGFP alone during initial cell spreading (**Figure 6.12**). Confirming earlier work from the Koleske Lab, while *arg*^{-/-} 3T3 fibroblasts over-expressing eGFP do not exhibit formation of dorsal ruffles (**Figure 6.12, A, B**), cells over-expressing Abl2-eGFP do (**Figure 6.12, C, D**). Upon closer look at the cell periphery reveals that only in *arg*^{-/-} cells re-expressing Abl2-eGFP, but not eGFP alone (**Figure 6.12, E**), stimulates the formation of actin-rich structures at these protrusions (**Figure 6.12, F**). Future work includes gaining structural insight during this stage – when cells are sampling their environment – into Abl2:actin:MT crosstalk using super-resolution technique 4pi-imaging to study these protrusive structures in both COS-7 and 3T3 fibroblast cells.

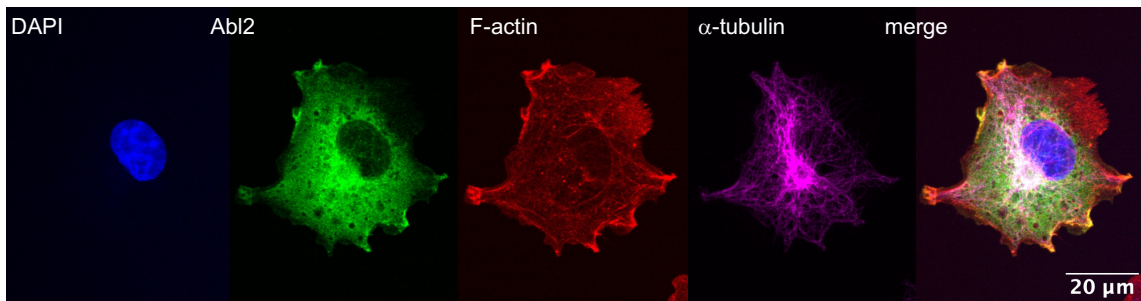


Figure 6.11. COS-7 cells overexpressing Abl2-eGFP and tubulin-CFP were fixed within couple hours of adhering onto glass coverslips. COS-7 cells were transfected with 3 μ g pN1-Abl2-eGFP and 3 μ g tubulin-CFP for 24 hr. Cells were then stained with DAPI, α -eGFP, Phalloidin-Alexa647.

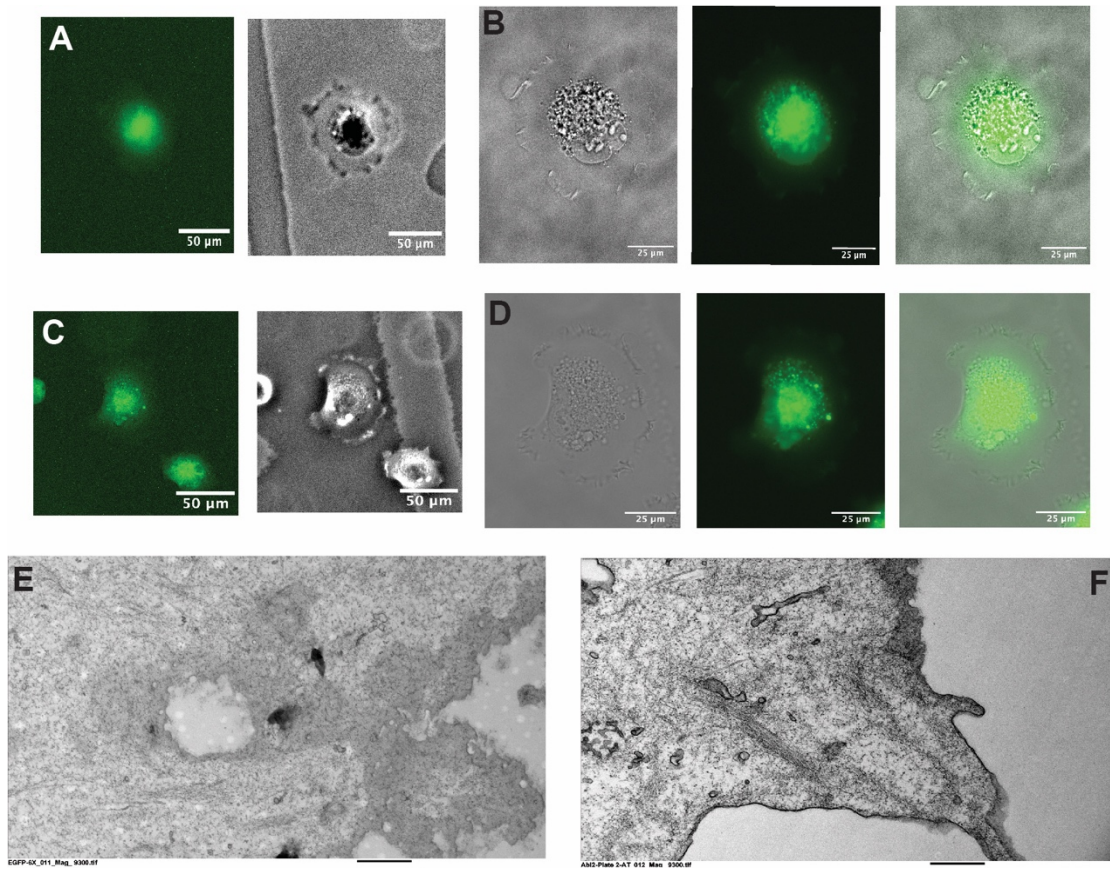


Figure 6.12. Correlative light images (fluorescence, brightfield) for *arg*^{-/-} 3T3 fibroblasts overexpressing (A-B) eGFP and (C-D) Abl2-eGFP. 10X magnification shown in A, C. 40X magnification shown in B, D. Electron micrographs of *arg*^{-/-} 3T3 fibroblasts overexpressing (E) eGFP and (F) Abl2-eGFP in 9300X magnification. Same cells as shown in A-B, and C-D, respectively. Scale bar, 600 nm. CLEM images were acquired alongside Zach Zuo at Yale Center for Cellular and Molecular Imaging Electron Microscopy Core.

6.4. Determining whether, and if so how, Abl2 kinase impacts F-actin and MT cytoskeletal organization under hyperosmotic stress

Whole brain proteomics and phosphoproteomics MS data reveal that Abl2 indirectly and directly interacts with many regulators involved not just in dendritic spine development and processes underlying proper neuronal development, but in programmed cell death pathway (Figures 5.3, 5.10, 5.12). Apoptosis can be induced via prolonged exposure to hyperosmotic stress due to accumulation of DNA damage (Burg et al., 2007). During hyperosmotic stress, the cell volume decreases, resulting in increased intracellular crowding (Kitamura et al., 2023). Within the first few minutes or the initial phase of apoptosis, the microtubule network becomes reorganized in which dynamics are halted. However, actin filaments mediate cell remodeling during this phase and there

is evidence that demonstrates that the actin cytoskeleton during apoptosis is targeted by caspases and undergo N-myristoylation for targeting to mitochondria (Utsumi et al., 2003). Because actin monomers harness energy from ATP hydrolysis, it's been thought that cells coordinate dynamics of the actin cytoskeleton during times of stress by rapidly shifting to a less dynamic ADP-actin-rich structure (Atkinson et al., 2004). This is done to conserve ATP for housekeeping tasks (Gourlay & Ayscough, 2005). Through bulk RNA-sequencing analyses, I sought to determine whether Abl2 kinase activity impacts transcriptional responses and cytoskeletal remodeling under hyperosmotic stress. To test this, I treated COS-7 WT and COS-7 Abl2 KO cells with or without 10 μ M imatinib and underwent 2 h treatment to 500 mM sucrose (**Figure 6.13**).

Relative to untreated COS-7 WT cells, COS-7 cells treated with sucrose express more transcripts that encode *ZFP37*, *ZBTB41*, *PUS7L*, *CCDC82*, *FER*, *TWF1*, *CLGN*, *SRFBP1*, *LOC103229645*, and *YES1* (**Figure 6.14, A**). Zinc finger proteins (Zfps) are known for regulating gene expression, cell proliferation, and apoptosis. Zfp37 encodes a transcription factor that modulates structures of the nucleolus and centromere in neurons in mice. Zfp-37 has been found to localize to heterochromatin and decorates the interior of the nucleolus. As it contains a truncated KRAB-A region, it has been suggested that Zfp-37 is a transcriptional repressor, thus preferring to bind to dsDNA (Payen et al., 1998). Unsurprisingly, transcripts encoding Zinc Finger and BTB Domain Containing 41 (ZBTB41), and pseudouridine synthase 7 like (PUS7L) are also upregulated. The BTB domain is highly conserved and is known to serve crucial roles in transcriptional regulation, chromatin remodeling, and cytoskeletal regulation (Cheng et al., 2021). Likewise, PUS7L binds to various RNAs and affect co-transcriptional pre-mRNA pseudouridylation, a modification to RNA that affects global gene expression in cells.

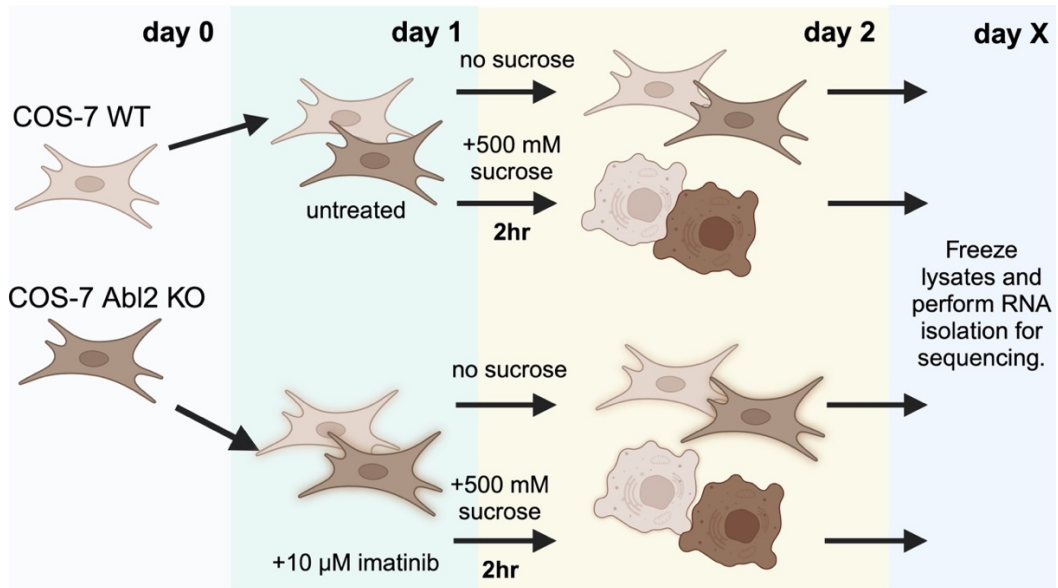


Figure 6.13. Workflow schematic that describes how RNA isolation was prepared for each condition. COS-7 WT and Abl2 KO cells were separated into 4 distinct groups: 1) untreated; 2) imatinib-treated; 3) underwent hyperosmotic stress; 4) imatinib-treated and underwent hyperosmotic stress. 10 mM imatinib was added into complete DMEM medium for 24 h. The following morning, cells within the hyperosmotic stress groups (+/- imatinib) were treated with 500 mM sucrose for 2 h prior to harvest. For each technical replicate per condition, 4 confluent 96 cm plates were harvested. Lysates were snap frozen in liquid nitrogen and placed into -80°C. When ready, lysates were fully thawed prior to RNA isolation.

These results indicate that the DNA damage response has been activated in the presence of high sucrose but it remains a question whether apoptosis has initiated in some cells. An immediate future experiment will be to conduct cell viability assays via cell counting pre- and post-2 h stress treatment. A statistically significant decrease in viable cells (adhered cells) would indicate apoptotic initiation. Hyperosmotic stress leads to changes in oxidative metabolism, thereby generating higher levels of reactive oxygen species (Zhang et al., 2004). In absence of Abl2, COS-7 cells upregulate MAB21L4 under hyperosmotic stress, but downregulate expression of transcripts encoding zinc finger protein ZNF14, activator of ATR kinase ETAA1, and basic leucine zipper nuclear factor BLZF1 (**Figure 6.14, B**). MAB21L4 can be found in the cytoplasm bound to transcriptional regulator Smad3 and transcriptional corepressor c-Ski within the TGFβ pathway (Ogami et al., 2022). c-Ski is known to bind to activated Smad2/3/4/ heteromeric complexes and repress the ability to activate TGFβ target genes. However, MAB21L4-binding to c-Ski has been shown to inhibit c-Ski repression and upregulate target gene expression in the TGFβ pathway (Ogami et al., 2022). Curiously,

activator of the ATR kinase ETAA1 is downregulated, which has been shown to accumulate at DNA damage sites to promote ATR signaling and cell signaling (Haahr et al., 2016). ATM and ATR kinases are master regulators of the DNA damage response pathway that trigger various downstream damage-specific signaling cascades via direct phosphorylation of checkpoint proteins, Chk1 and Chk2. This reveals that in the absence of Abl2, cells undergoing hyperosmotic stress activates TGF β signaling pathway to strongly inhibit cell cycle progression (e.g. downregulation of augmin-like complex subunit 3 HAUS3 which plays a key role in mitosis, log₂FC = -3.5, **Figure 6.14, B**) and transcription of cell cycle regulators. In parallel to log₂FC analysis comparing WT cells treated with sucrose versus those untreated, the transcription of Zfp37 is downregulated in KO cells under stress, which suggests that Abl2 directly impacts the expression of the zinc finger protein to repress transcription (**Figure 6.14, B**). Whether transcriptional repression of target genes is selective or not remains an open question. Interestingly, as revealed from MS proteomics data that Abl2 plays an active role in mediating lipid transport, loss of Abl2 also downregulates transcription of DHHC-type palmitoyltransferase ZDHHC17 which is located in the Golgi membrane and is involved in lipoprotein transport; and basic leucine zipper nuclear factor BLZF1, which regulates ubiquitin protein ligase binding and mediates Golgi to plasma membrane protein transport.

Perhaps the most drastic changes in transcriptional response and most revealing of the positive regulation Abl2 kinase activity has on DNA damage response comes from RNA-seq analysis from cells treated with imatinib. Type II kinase inhibitor imatinib selectively targets Abl1 and Abl2. Though most genes are unidentified, LOC103241347 encodes peptidyl-prolyl cis-trans isomerase A-like protein (PPIA) and is upregulated in imatinib-treated Abl2 KO COS-7 cells (**Figure 6.14, C**). Excitingly, PPIA has also been identified to be a direct partner of Abl2 from co-IP MS (**Figure 5.3, C**), indicating that Abl2 potentially plays a direct role in regulating PPIA for cellular homeostatic processes such as protein folding. Overexpression of *PPIA* is likely induced to compensate for loss of Abl2 and/or its kinase activity. The most downregulated gene is *LYST*, which encodes the lysosomal trafficking regulator, specifically a protein that regulates intracellular transport in endosomes. This aligns with phosphoproteomics MS data, which show that Abl2

phosphorylation substrates are primarily localized at endosomes and transport vesicles for mediating transmembrane and lipid binding properties (Figure 5.10, D).

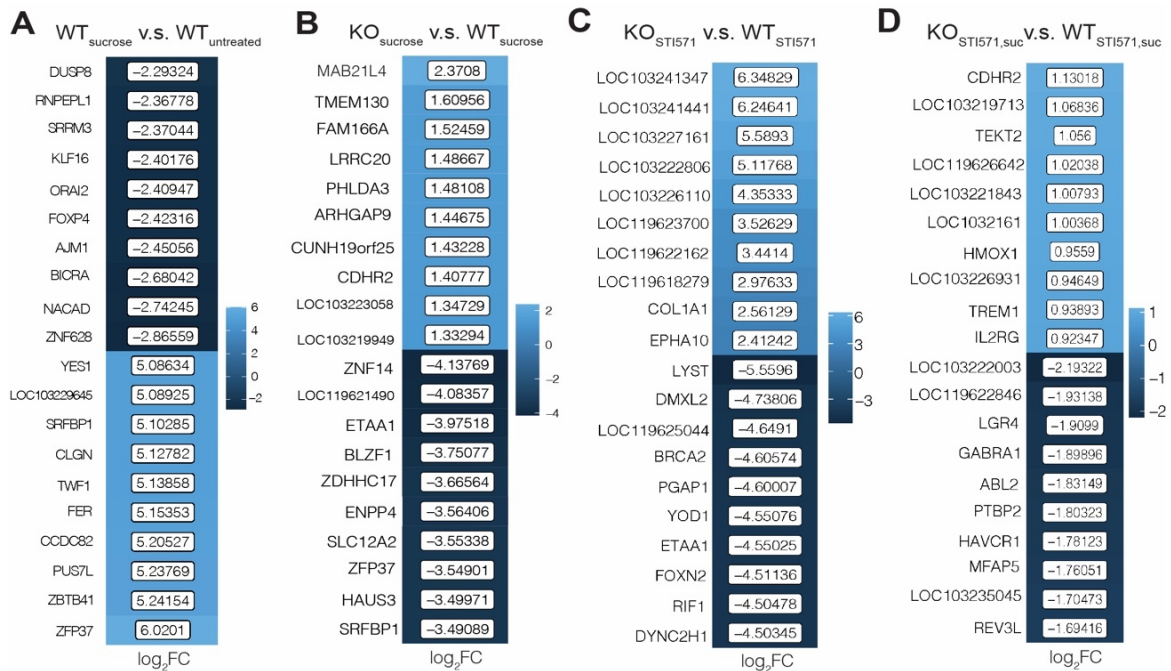


Figure 6.14. Transcripts that are most differentially expressed in various conditions. (A) Transcripts most differentially expressed in COS-7 cells that underwent hyperosmotic stress versus untreated cells. **(B)** Expression levels of transcripts in Abi2 KO COS-7 versus wildtype. **(C)** Expression levels of transcripts in cells with Abi2 KO background versus wildtype upon 10 μ M imatinib O/N treatment. **(D)** Expression levels of transcripts between imatinib-treated Abi2 KO cells versus imatinib-treated COS-7 WT cells in hyperosmotic stress conditions. Lighter blue signifies upregulation. Darker blue signifies downregulation. Values shown on right. Only pairwise comparisons can be performed due to one replicate.

Interestingly, the only transcript whose $|\log_2FC| \geq 2$ (threshold for enrichment) is LOC103222003, which encodes for H2A clustered histone 4, H2AC4. H2AC4 is downregulated in stress- and imatinib-treated Abi2 KO cells versus stressed imatinib-treated WT cells. H2AC4 binds to DNA and is involved in negatively regulating cell proliferation. A study by Falinski and others reveal that BCR-ABL1 kinase facilitates localization of histones 3 and 4 on ds-DNA breaks (Falinski et al., 2012). Thus, Abi2 likely shares a redundant function in DNA damage repair. Two additional technical replicates have been sent out for RNA sequencing and will be included in the analysis. No definitive conclusions can be made from the low sample size (n=1 technical replicate). However, these preliminary results reveal that Abl kinase activity play a crucial role in the transcriptional response to hyperosmotic stress. It remains elusive whether and how Abi2 contributes to actin

cytoskeletal reorganization in classical apoptotic pathways such as ATM-/ATR- or p53-mediated transcriptional regulation and activation cascades.

6.5. Materials and Methods

RNA isolation for bulk RNA-seq analysis

Four 70% confluent 10cm plates per condition (COS-7 WT or Abl2 KO COS-7 +/- STI571 +/- hyperosmotic stress) were either treated or not treated with 10 μ M STI571 overnight. The following morning, cells +/- imatinib treatment underwent hyperosmotic stress for 2h with complete DMEM supplemented with 50 mM sucrose +/- 10 μ M STI571. After 2h treatment, medium from all cells in each condition was removed and washed once with 10 ml PBS. 1 ml Trizol was added to each plate of cells and rocked slowly on shaker at RT for 15 min. Cells were transferred to Eppy tubes, then supplemented with 200 μ l chloroform. Tubes were vigorously shaken for 15-30 s and incubated at RT for 3 min, followed by 15 min centrifugation at 20K rpm, 4°C. The aqueous phase was moved to a new tube, and chloroform extraction was performed once more. The tube was shaken and incubated for 2 min at RT, followed by a 15 min 20K rpm centrifugation at 4°C. The aqueous phase was moved to a 5 ml Eppy tube.

The following instructions were adapted from RNeasy Mini Kit manual. 3.5X volume of RLT buffer was added to the tube and vortexed to mix. 2.5X of the original volume of 100% ethanol was added to the tube and mixed well by pipetting up and down. The sample was transferred 700 μ L at a time to an RNeasy Mini spin column in a collection tube. Eppy tube was centrifuged for 15 s at 18K rpm RT. Flowthrough was discarded. This was performed until the entire sample passed through the column. 350 μ l of RW1 buffer was added to the RNeasy spin column, centrifuged, with flowthrough discarded. 80 μ l of DNase I incubation mix was added to each sample, which was done by combining 10 μ l of DNase I stock solution and 70 μ l RDD buffer. The mixture was incubated for 15 min at RT. 350 μ L of RW1 buffer was added to the spin column, centrifuged, and flowthrough was discarded. 500 μ l of RPE buffer was added to spin column, centrifuged at 18K rpm for 2 min at RT, and flowthrough discarded. This step was repeated once more.

Column was transferred to a new collection tube and spun for 1 min at 18K rpm. Column was transferred once more to a new 1.5 ml tube. 100 µl of RNase-free MilliQ water was added to the column, incubated for 3 min at RT and spun for 1 min at 10,500 rpm. RNA was frozen at -20°C until ready for sequencing.

7. Conclusions and future perspectives

Alongside my close collaborator Wanqing Lyu, I demonstrate here for the first time that Abl2 undergoes phase separation, forms coacervates with tubulin, and promotes MT nucleation. Abl2 also engages an extended and damaged MT lattice, spanning over single MT protofilaments to promote lattice repair and increase rescue and lifetime. Our results are consistent with a model in which Abl2 promotes the recruitment and addition of tubulin to MTs in different functional scenarios.

7.1. Abl2 binds tubulin using two distinct C-terminal regions.

We have identified two tubulin-binding regions in Abl2, contained within amino acids 688-924 (site I) and 1024-1090 (site II), each sufficient to bind tubulin dimers itself, albeit with weaker affinity than Abl2 fragments containing both sites. Curiously, Abl2 Δ 688-790 did not bind detectably to tubulin even though it retains site II (**Figure 2.7**). We propose that Abl2 initially interacts with tubulin via site I (**Figure 2.42, i**), which has a higher affinity to tubulin. Binding of tubulin to site I may be required to expose site II to an additional tubulin dimer and promote their interactions in a head-to-tail fashion (**Figure 2.42, ii-iii**). This model would explain why Abl2 Δ 688-790, which lacks all or part of site I, fails to bind tubulin and promote MT nucleation. The two tubulin-binding sites in Abl2 do not resemble known tubulin-binding domains but are enriched in positively charged residues. Interestingly, Abl2 binds to tubulin with lower affinity than Abl2-557-C, suggesting that in addition to substrate phosphorylation, the N-terminal half sterically hinders tubulin binding. Most soluble Abl2 molecules undergo phase separation and co-condense with tubulin, and we believe this underlies the patchy appearance of Abl2:tubulin co-condensate binding to assembled MTs (**Figure 2.10**).

7.2. Abl2 interacts with MTs and tubulin to promote MT nucleation, growth, and lattice repair.

Abl2 reduces the critical concentration for spontaneous tubulin polymerization and shortens the MT nucleation lag time. Tubulin binding-deficient Abl2 Δ 688-790 did not impact nucleation, indicating that tubulin binding is critical to promote nucleation (**Figure 2.19, A-C**). Classical models for MT nucleation proposed that new MTs form via a nucleation-elongation mechanism. A recent study demonstrated that 'critical nuclei' are first formed as 2D layers of a growing lattice prior to its

maturation into a cylindrical tube (Rice et al., 2021). Enlargement of 2D lattices is energetically favorable but kinetically impeded by the difficulty in adding new protofilament layers. Given our structural data that Abl2 binds to extended lattices and potentially bridges multiple dimers along a single protofilament (**Figures 2.26, 2.27**), we propose that Abl2 may facilitate nucleation by binding a nascent protofilament and recruiting tubulin dimers to promote layer formation. In addition, Abl2 may then bind the lattice and facilitate tubulin addition at corners of 2D lattices, which may be structurally akin to the corners at growing MT ends and damaged holes (**Figure 2.39, i**). While growing MT ends contain a heterogeneous mixture of curled multi-protofilament sheets, and straight, flared, or ragged ends (Höög et al., 2011; McIntosh et al., 2018), damaged sites are also likely to contain a heterogeneous mixture of these structures. We propose that Abl2 recognizes one or more of these structures within the damaged region, recruiting tubulin for incorporation (**Figure 2.39, ii-iii**). It is also possible that Abl2 binding along the protofilament recruits new tubulin dimers for incorporation at protofilament ends. In doing so, Abl2 may stabilize inter-protofilament interactions to promote MT nucleation, growth, and lattice repair. Tools developed here should facilitate future studies to probe how Abl2 promotes MT assembly.

7.3. Abl2 localizes to expanded lattices via multiple binding patterns.

Our cryo-EM analysis reveals that Abl2-557-1090 primarily binds to the tails of polymerized tubulin (**Figure 2.27, C, E**), a binding mode that differs from other conventional MBPs (e.g. tau, MAP7, and EB3), which bind multiple interfaces along a polymerized MT or protofilament (Ferro et al., 2022; Kellogg et al., 2018; Zhang et al., 2015). Abl2-557-1090 did not form a highly stable complex with MTs, as we did not observe extra density surrounding the tails (**Figure 2.27, B**). Our sequence and biophysical analyses (**Figure 2.11, A, B**) and AlphaFold2 (**Figure 2.29, A**) indicate that Abl2-557-1090 is disordered, lacking a well-ordered microtubule-binding domain, which likely underlies the difficulty in obtaining highly ordered structures. Cryo-EM analysis did reveal that Abl2-557-1090 can bridge multiple tubulin dimers, which is supported by our observations of Abl2 diffusion along stabilized MT lattices (**Figure 2.15, A, C**). We propose that Abl2 can dynamically “slide” across the negatively charged lattice surface with its net positively charged tubulin-binding fragment, which

can simultaneously bind and potentially locally concentrate soluble dimers at damage sites. The ability of MT-bound Abl2 to move on a bed of negatively-charged tubulin tails may serve as an economic means to transport along the lattice for damage recognition and repair; or toward ends for recruiting dimers for growth (Bigman & Levy, 2020a, 2020b). A similar mode of diffusion along the MT lattice is employed by tau (Hinrichs et al., 2012; Kellogg et al., 2018).

7.4. Phase separation contributes to Abl2 function in regulating MT nucleation.

A growing number of MT plus-end regulators undergo phase separation (Jijumon et al., 2022; Maan et al., 2022; Meier et al., 2022; Miesch et al., 2023; Song et al., 2022), but less is known about how LLPS contributes to microtubule nucleation. Under conditions of molecular crowding in solution or in the presence of stabilized MT lattices, Abl2 underwent phase separation and recruited tubulin into the dense phase. FRAP recovery times reported for other GFP-fusion protein condensates within highly compartmentalized structures in cells have timescales of seconds (Brangwynne et al., 2009; Chen & Huang, 2001). In contrast, Abl2-eGFP and tubulin FRAP recovery times in condensates extended to minutes, consistent with measurements of other MT regulators in in vitro biomolecular condensates (Kanaan et al., 2020; King & Petry, 2020). Taylor et al. have developed an infinite 2D model that accurately captures the relatively slower kinetics of extracellular molecular condensates which depend critically on factors such as bleach spot size and droplet size. As such, we appropriately implemented their model here to quantify the $t_{1/2}$ values (Taylor et al., 2019).

Protein condensation is often driven by intrinsically disordered regions and multivalent binding regions (Alberti et al., 2019; Boeynaems et al., 2018; Feng et al., 2019; Lin et al., 2017; Wang et al., 2018). Phase separation is a common feature of diverse MT regulators (Hernández-Vega et al., 2017; Tan et al., 2019) (Maan et al., 2022; Meier et al., 2022; Safari et al., 2021; Song et al., 2022). Consistent with this, we found that the Abl2 C-terminal half is significantly disordered and has two distinct sites for tubulin binding (**Figure 2.7; 2.11, A**). We showed that new MTs nucleated from Abl2-eGFP:tubulin co-condensates. Under the same conditions, eGFP alone was not able to phase separate or interact with tubulin to promote MT assembly (**Figure 2.20**). Our data

suggest that the ability of Abl2 to co-condense with tubulin dimers may help concentrate tubulin onto nascent or damaged protofilaments to facilitate nucleation and promote lattice repair.

7.5. The tubulin-binding Abl2 splice isoform is more predominant in human tissues than in mouse tissues.

Despite the high conservation of Abl2 isoform between mice and humans (~95%), transcript expression levels differ substantially across all cell types and tissues between the two organisms (**Figures 3.1, 3.2**). Recent study from the Peifer Lab reveals that the IDR, flanked by the kinase domain and terminal F-actin binding domain of *Drosophila* Abl, is essential for proper development and adult viability (Rogers et al., 2021). Deletion of the IDR induced a strong cuticle phenotype such that the epidermal integrity was severely compromised. Additionally, it affects cell shape change during the process known as dorsal closure. In wildtype, cells at the leading edge make up a contractile actin cable that maintains a straight leading edge that exerts tension along the dorsal cell margin. Loss of Abl induced a hyper-constricted phenotype, likely owing to the failure of the leading edge cable. Expression of wildtype Abl transgene, but not Abl Δ IDR, rescued defects, which suggests that the IDR is critical for actin regulation. Interestingly, though Abl Δ IDR protein is more stable than Abl, as it accumulates to significantly higher levels than GFP-tagged Abl in *Drosophila* embryos, the IDR is required for actin regulation of Ena at the leading edge. Given the work presented here, it would be interesting to explore whether oligomerization of Abl2 (whose self-interacting interfaces lie predominantly in aa. 688-924 – a predominant IDR within its MT-binding region) plays a role in mediating crosstalk between F-actin and MTs to ensure proper *Drosophila* development.

In summary, I have demonstrated that co-condensates of Abl2 and tubulin act as compartmentalized reactors which may contribute to (but are not required for): 1) MT nucleation; and 2) promotion of incorporation of tubulin dimers at damaged lattice sites for repair and rescue. My work shown here provides a mechanistic model to probe how Abl2 regulates MT assembly and repair and provides tools to explore how these mechanisms regulate cell morphogenesis and migration. I have also demonstrated that Abl2 mediates crosstalk between F-actin and MTs *in vitro*.

Many questions still remain as to whether the binding interactions between Abl2:F-actin and Abl2:MT affect one another, and what is the minimal region required for Abl2 to sustain actin-MT crosslinking. Previous work from the Koleske Lab revealed that Abl2 interacts with both cytoskeletal systems to support lamellipodial dynamic and dorsal ruffling, and treatment with either an actin- or MT-dynamics inhibitors, latrunculin A and nocodazole, abolishes Abl2 localization to the cell periphery and lamellipodial dynamics (Miller et al., 2004). However, as Abl2 is predominantly enriched in dendritic spines and is essential for dendritic spine stability, it will be interesting to explore: 1) how Abl2:MT interactions impact spine stability and density throughout development; 2) whether Abl2 mediates crosstalk between F-actin and MTs in neurons; 3) whether cross-talking under Abl2 regulation is kinase-independent, -dependent, or a mixture of both; and 4) whether there exists novel functions of Abl2 in neuron-specific processes, *i.e.* transport of organelles that may utilize its cross-talking mechanism. Many significantly enriched phosphorylation substrates have been identified in the Abl2 phosphoproteome of the P21 mouse hippocampus. Currently, many opportunities exist for determining how Abl2 phosphorylation of downstream substrates impact neuronal development and dissecting the molecular mechanisms that underly its regulation that likely involve changes in the actin and MT cytoskeletal organization.

References

- Abelson, H. T., & Rabstein, L. S. (1970). Lymphosarcoma: Virus-induced Thymic-independent Disease in Mice¹. *Cancer Research*, 30(8), 2213-2222.
- Ackermann, M., & Matus, A. (2003). Activity-induced targeting of profilin and stabilization of dendritic spine morphology. *Nat Neurosci*, 6(11), 1194-1200. <https://doi.org/10.1038/nn1135>
- Aher, A., Kok, M., Sharma, A., Rai, A., Olieric, N., Rodriguez-Garcia, R., Katrukha, E. A., Weinert, T., Olieric, V., Kapitein, L. C., Steinmetz, M. O., Dogterom, M., & Akhmanova, A. (2018). CLASP Suppresses Microtubule Catastrophes through a Single TOG Domain. *Developmental Cell*, 46(1), 40-58.e48. <https://doi.org/10.1016/j.devcel.2018.05.032>
- Aher, A., Rai, D., Schaedel, L., Gaillard, J., John, K., Liu, Q., Altelaar, M., Blanchoin, L., They, M., & Akhmanova, A. (2020). CLASP Mediates Microtubule Repair by Restricting Lattice Damage and Regulating Tubulin Incorporation. *Current Biology*, 30(11). <https://doi.org/10.1016/j.cub.2020.03.070>
- Ahmad, F. J., & Baas, P. W. (1995). Microtubules released from the neuronal centrosome are transported into the axon. *J Cell Sci*, 108 (Pt 8), 2761-2769. <https://doi.org/10.1242/jcs.108.8.2761>
- Akhmanova, A., & Hoogenraad, C. C. (2015). Microtubule Minus-End-Targeting Proteins. *Current Biology*, 25(4), R162-R171. <https://doi.org/10.1016/j.cub.2014.12.027>
- Akhmanova, A., & Steinmetz, M. O. (2008). Tracking the Ends: A Dynamic Protein Network Controls the Fate of Microtubule Tips. *Nature Reviews Molecular Cell Biology*, 9(4), 309-322. <https://doi.org/10.1038/nrm2369>
- Akhmanova, A., & Steinmetz, M. O. (2011). Microtubule End Binding: EBs Sense the Guanine Nucleotide State. *Current Biology*, 21(8), R283-285. <https://doi.org/10.1016/j.cub.2011.03.023>
- Akhmanova, A., & Steinmetz, M. O. (2015). Control of microtubule organization and dynamics: two ends in the limelight. *Nature Reviews Molecular Cell Biology*, 16, 711-726. <https://doi.org/10.1038/nrm4084>
- Akhmanova, A., & Steinmetz, M. O. (2019). Microtubule minus-end regulation at a glance. *Journal of Cell Science*, 132, jcs227850. <https://doi.org/10.1242/jcs.227850>

Al-Bassam, J., Kim, H., Brouhard, G. J., van Oijen, A., Harrison, S. C., & Chang, F. (2010). CLASP Promotes Microtubule Rescue by Recruiting Tubulin Dimers to the Microtubule. *Developmental Cell*, 19(2), 245-258. <https://doi.org/10.1016/j.devcel.2010.07.016>

Al-Bassam, J., Ozer, R. S., Safer, D., Halpain, S., & Milligan, R. A. (2002). MAP2 and tau bind longitudinally along the outer ridges of microtubule protofilaments. *Journal of Cell Biology*, 157(7), 1187-1196. <https://doi.org/10.1083/jcb.200201048>

Albe, K. R., Butler, M. H., & Wright, B. E. (1990). Cellular concentrations of enzymes and their substrates. *Journal of Theoretical Biology*, 143(22), 163-195. [https://doi.org/10.1016/S0022-5193\(05\)80266-8](https://doi.org/10.1016/S0022-5193(05)80266-8)

Alberti, S., Gladfelter, A. S., & Mittag, T. (2019). Considerations and Challenges in Studying Liquid-Liquid Phase Separation and Biomolecular Condensates. *Cell*, 176(3), 419-434. <https://doi.org/10.1016/j.cell.2018.12.035>

Alexandrova, V. V., Anisimov, M. N., Zaitsev, A. V., Mustyatsa, V. V., Popov, V. V., Ataulakhanov, F. I., & Gudimchuk, N. B. (2022). Theory of tip structure-dependent microtubule catastrophes and damage-induced microtubule rescues. *Proceedings of the National Academy of Sciences*, 119(46). <https://doi.org/10.1073/pnas.2208294119>

Alushin, G. M., Lander, G. C., Kellogg, E. H., Zhang, R., Baker, D., & Nogales, E. (2014). High resolution microtubule structures reveal the structural transitions in $\alpha\beta$ -tubulin upon GTP hydrolysis. *Cell*, 157(5), 1117-1129. <https://doi.org/10.1016/j.cell.2014.03.053>

Ambadipudi, S., Biernat, J., Riedel, D., Mandelkow, E., & Zweckstetter, M. (2017). Liquid-liquid phase separation of the microtubule-binding repeats of the Alzheimer-related protein Tau. *Nature Communications*, 8(1), 275. <https://doi.org/10.1038/s41467-017-00480-0>

Andreu-Carbó, M., Fernandes, S., Velluz, M., Kruse, K., & Aumeier, C. (2022). Motor usage imprints microtubule stability along the shaft. *Developmental Cell*, 57, 5-18. <https://doi.org/10.1016/j.devcel.2021.11.019>

Ard, R., Maillet, J. C., Daher, E., Phan, M., Zinoviev, R., Parks, R. J., & Gee, S. H. (2021). PKC α -mediated phosphorylation of the diacylglycerol kinase ζ MARCKS domain switches cell migration

modes by regulating interactions with Rac1 and RhoA. *J Biol Chem*, 296, 100516.

<https://doi.org/10.1016/j.jbc.2021.100516>

Arellano-Santoyo, H., Geyer, E. A., Stokasimov, E., Chen, G.-Y., Su, X., Hancock, W., Rice, L. M., & Pellman, D. (2017). A Tubulin Binding Switch Underlies Kip3/Kinesin-8 Depolymerase Activity.

Developmental Cell, 42(1), 37-51.e38. <https://doi.org/https://doi.org/10.1016/j.devcel.2017.06.011>

Atkinson, S. J., Hosford, M. A., & Molitoris, B. A. (2004). Mechanism of Actin Polymerization in Cellular ATP Depletion*. *Journal of Biological Chemistry*, 279(7), 5194-5199.

<https://doi.org/https://doi.org/10.1074/jbc.M306973200>

Aumeier, C., Schaedel, L., Gaillard, J., John, K., Blanchoin, L., & Théry, M. (2016). Self-repair promotes microtubule rescue. *Nature Cell Biology*, 18, 1054-1064.

<https://doi.org/10.1038/ncb3406>

Ayaz, P., Munyoki, S., Geyer, E. A., Piedra, F.-A., Vu, E. S., Bromberg, R., Otwinowski, Z.,

Grishin, N. V., Brautigam, C. A., & Rice, L. M. (2014). A tethered delivery mechanism explains the catalytic action of a microtubule polymerase. *eLife*, 3, e03069. <https://doi.org/10.7554/eLife.03069>

Azam, M., Latek, R. R., & Daley, G. Q. (2003). Mechanisms of Autoinhibition and STI-571/Imatinib Resistance Revealed by Mutagenesis of *BCR-ABL*. *Cell*, 112(6), 831-843.

[https://doi.org/10.1016/S0092-8674\(03\)00190-9](https://doi.org/10.1016/S0092-8674(03)00190-9)

Baas, P. W., Deitch, J. S., Black, M. M., & Banker, G. A. (1988). Polarity orientation of microtubules in hippocampal neurons: uniformity in the axon and nonuniformity in the dendrite.

Proceedings of the National Academy of Sciences of the United States of America, 85(21), 8335-8339. <https://doi.org/10.1073/pnas.85.21.8335>

Baas, P. W., Rao, A. N., Matamoros, A. J., & Leo, L. (2016). Stability Properties of Neuronal Microtubules. *Cytoskeleton*, 73(9), 442-460. <https://doi.org/10.1002/cm.21286>

Baas, P. W., & Yu, W. (1996). A composite model for establishing the microtubule arrays of the neuron. *Molecular Neurobiology*, 12(2), 145-161. <https://doi.org/10.1007/BF02740651>

Babu, M., Favretto, F., Rankovic, M., & Zweckstetter, M. (2022). Peptidyl Prolyl Isomerase A Modulates the Liquid–Liquid Phase Separation of Proline-Rich IDPs. *Journal of the American Chemical Society*, 144(35), 16157-16163. <https://doi.org/10.1021/jacs.2c07149>

Bailey, M. E., Sackett, D. L., & Ross, J. L. (2015). Katanin Severing and Binding Microtubules Are Inhibited by Tubulin Carboxy Tails. *Biophysical Journal*, *109*, 2546-2561.

<https://doi.org/10.1016/j.bpj.2015.11.011>

Bailly, E., McCaffrey, M., Touchot, N., Zahraoui, A., Goud, B., & Bornens, M. (1991). Phosphorylation of two small GTP-binding proteins of the Rab family by p34cdc2. *Nature*, *350*(6320), 715-718. <https://doi.org/10.1038/350715a0>

Bär, J., Kobler, O., van Bommel, B., & Mikhaylova, M. (2016). Periodic F-actin structures shape the neck of dendritic spines. *Sci Rep*, *6*, 37136. <https://doi.org/10.1038/srep37136>

Barbernitz, X., & Raben, D. M. (2023). Phosphorylation of DGK. *Advances in Biological Regulation*, *88*, 100941. <https://doi.org/https://doi.org/10.1016/j.jbior.2022.100941>

Barisic, M., Silva e Sousa, R., Tripathy, S. K., Magiera, M. M., Zaytsev, A. V., Pereira, A. L., Janke, C., Grishchuk, E. L., & Maiato, H. (2015). Mitosis. Microtubule deetyrosination guides chromosomes during mitosis. *Science*, *348*(6236), 799-803.

<https://doi.org/10.1126/science.aaa5175>

Basnet, N., Nedožralova, H., Crevenna, A. H., Bodakuntla, S., Schlichthaerle, T., Taschner, M., Cardone, G., Janke, C., Jungmann, R., Magiera, M. M., Biertümpfel, C., & Mizuno, N. (2018). Direct induction of microtubule branching by microtubule nucleation factor SSNA1. *Nature Cell Biology*, *20*(10), 1172-1180. <https://doi.org/10.1038/s41556-018-0199-8>

Bechstedt, S., Lu, K., & Brouhard, Gary J. (2014). Doublecortin Recognizes the Longitudinal Curvature of the Microtubule End and Lattice. *Current Biology*, *24*(20), 2366-2375.

<https://doi.org/https://doi.org/10.1016/j.cub.2014.08.039>

Bertram, J. S. (2000). The molecular biology of cancer. *Molecular Aspects of Medicine*, *21*(6), 167-223. [https://doi.org/https://doi.org/10.1016/S0098-2997\(00\)00007-8](https://doi.org/https://doi.org/10.1016/S0098-2997(00)00007-8)

Bhattacharyya, B., & Wolff, J. (1974). Promotion of fluorescence upon binding of colchicine to tubulin. *Proc Natl Acad Sci U S A*, *71*(7), 2627-2631. <https://doi.org/10.1073/pnas.71.7.2627>

Bigman, L. S., & Levy, Y. (2020a). Protein Diffusion on Charged Biopolymers: DNA versus Microtubule. *Biophysical Journal*, *118*(12), 3008-3018. <https://doi.org/10.1016/j.bpj.2020.05.004>

- Bigman, L. S., & Levy, Y. (2020b). Tubulin tails and their modifications regulate protein diffusion on microtubules. *Proceedings of the National Academy of Sciences*, 117(16), 8876-8883.
<https://doi.org/10.1073/pnas.1914772117>
- Bodakuntla, S., Jijumon, A. S., Villablanca, C., Gonzalez-Billault, C., & Janke, C. (2019). Microtubule-Associated Proteins: Structuring the Cytoskeleton. *Trends in Cell Biology*, 29(10), 804-819. <https://doi.org/10.1016/j.tcb.2019.07.004>
- Boeynaems, S., Alberti, S., Fawzi, N. L., Mitag, T., Polymenidou, M., Rousseau, F., Schymkowitz, J., Shorter, J., Wolozin, B., Van Den Bosch, L., Tompa, P., & Fuxreiter, M. (2018). Protein Phase Separation: A New Phase in Cell Biology. *Trends in Cell Biology*, 28(6), 420-435.
<https://doi.org/10.1016/j.tcb.2018.02.004>
- Bowne-Anderson, H., Hibbel, A., & Howard, J. (2015). Regulation of Microtubule Growth and Catastrophe: Unifying Theory and Experiment. *Trends in Cell Biology*, 25(12), 769-779.
<https://doi.org/10.1016/j.tcb.2015.08.009>
- Bowne-Anderson, H., Zanic, M., Kauer, M., & Howard, J. (2013). Microtubule dynamic instability: A new model with coupled GTP hydrolysis and multistep catastrophe. *Bioessays*, 35(5), 452-461.
<https://doi.org/10.1002/bies.201200131>
- Boyle, S. N., Michaud, G. A., Schweitzer, B., Predki, P. F., & Koleske, A. J. (2007). A Critical Role for Cortactin Phosphorylation by Abl-family Kinases in PDGF-induced Dorsal-Wave Formation. *Current Biology*, 17(5), 445-451. <https://doi.org/10.1016/j.cub.2007.01.057>
- Bradley, W. D., Hernández, S. E., Settleman, J., & Koleske, A. J. (2006). Integrin Signaling Through Arg Activates p190RhoGAP by Promoting Its Binding to p120RasGAP and Recruitment to the Membrane. *Molecular Biology of the Cell*, 17(11), 4827-4836.
<https://doi.org/10.1091/mbc.e06-02-0132>
- Bradley, W. D., & Koleske, A. J. (2009). Regulation of cell migration and morphogenesis by Abl-family kinases: emerging mechanisms and physiological contexts. *Journal of Cell Science*, 122, 3441-3454. <https://doi.org/10.1242/jcs.039859>
- Brangwynne, C. P., Eckmann, C. R., Courson, D. S., Rybarska, A., Hoege, C., Gharakhani, J., Jülicher, F., & Hyman, A. A. (2009). Germline P Granules Are Liquid Droplets That Localize by

Controlled Dissolution/Condensation. *Science*, 324(5935), 1729-1732.

<https://doi.org/10.1126/science.1172046>

Brasher, B. B., & Van Etten, R. A. (2000). c-Abl Has High Intrinsic Tyrosine Kinase Activity That Is Stimulated by Mutation of the Src Homology 3 Domain and by Autophosphorylation at Two Distinct Regulatory Tyrosines. *Journal of Biological Chemistry*, 245(45), 35631-35637.

<https://doi.org/10.1074/jbc.M005401200>

Brouhard, G. J., & Rice, L. M. (2018). Microtubule dynamics: an interplay of biochemistry and mechanics. *Nature Reviews Molecular Cell Biology*, 19, 451-463. <https://doi.org/10.1038/s41580-018-0009-y>

Brouhard, G. J., Stear, J. H., Noetzel, T. L., Al-Bassam, J., Kinoshita, K., Harrison, S. C., Howard, J., & Hyman, A. A. (2008). XMAP215 Is a Processive Microtubule Polymerase. *Cell*, 132, 79-88.

<https://doi.org/10.1016/j.cell.2007.11.043>

Brown, A., Long, F., Nicholls, R. A., Toots, J., Emsley, P., & Murshudov, G. (2015). Tools for macromolecular model building and refinement into electron cryo-microscopy reconstructions. *Acta Crystallographica Section D Biological Crystallography*, 71(Pt 1), 136-153.

<https://doi.org/10.1107/S1399004714021683>

Burg, M. B., Ferraris, J. D., & Dmitrieva, N. I. (2007). Cellular response to hyperosmotic stresses. *Physiol Rev*, 87(4), 1441-1474. <https://doi.org/10.1152/physrev.00056.2006>

Burke, E., Mahoney, N. M., Almo, S. C., & Barik, S. (2000). Profilin is required for optimal actin-dependent transcription of respiratory syncytial virus genome RNA. *J Virol*, 74(2), 669-675.

<https://doi.org/10.1128/jvi.74.2.669-675.2000>

Burton, E. A., Oliver, T. N., & Pendergast, A. M. (2005). Abl Kinases Regulate Actin Comet Tail Elongation via an N-WASP-Dependent Pathway. *Molecular and Cellular Biology*, 25(20), 8834-8843. <https://doi.org/10.1128/MCB.25.20.8834-8843.2005>

Cai, D., McEwen, D. P., Martens, J. R., Meyhofer, E., & Verhey, K. J. (2009). Single Molecule Imaging Reveals Differences in Microtubule Track Selection Between Kinesin Motors. *PLOS Biology*, 7(10), e1000216. <https://doi.org/10.1371/journal.pbio.1000216>

Campbell, J. N., & Slep, K. C. (2011). $\alpha\beta$ -Tubulin and Microtubule-Binding Assays. *Methods in Molecular Biology*, 777, 87-97. https://doi.org/10.1007/978-1-61779-252-6_6

Caplow, M., & Shanks, J. (1996). Evidence that a single monolayer tubulin-GTP cap is both necessary and sufficient to stabilize microtubules. *Molecular Biology of the Cell*, 7(4), 663-675. <https://doi.org/10.1091/mbc.7.4.663>

Carlier, M. F., Didry, D., Melki, R., Chabre, M., & Pantaloni, D. (1988). Stabilization of microtubules by inorganic phosphate and its structural analogs, the fluoride complexes of aluminum and beryllium. *Biochemistry*, 27(10), 3555-3559. <https://doi.org/10.1021/bi00410a005>

Carlier, M. F., Didry, D., Simon, C., & Pantaloni, D. (1988). Mechanism of GTP hydrolysis in tubulin polymerization: characterization of the kinetic intermediate microtubule-GDP-Pi using phosphate analogs. *Biochemistry*, 28(4), 1783-1791. <https://doi.org/10.1021/bi00430a054>

Case, L. B., De Pasquale, M., Henry, L., & Rosen, M. K. (2022). Synergistic phase separation of two pathways promotes integrin clustering and nascent adhesion formation. *eLife*, 11, e72588. <https://doi.org/10.7554/eLife.72588>

Castle, B. T., McKibben, K. M., Rhoades, E., & Odde, D. J. (2020). Tau avoids the GTP cap at growing microtubule plus ends. *bioRxiv*. <https://doi.org/10.1101/2019.12.31.891234>

Castoldi, M., & Popov, A. V. (2003). Purification of brain tubulin through two cycles of polymerization-depolymerization in a high-molarity buffer. *Protein Expression & Purification*, 32(1), 83-88. [https://doi.org/10.1016/S1046-5928\(03\)00218-3](https://doi.org/10.1016/S1046-5928(03)00218-3)

Chazeau, A., Mehidi, A., Nair, D., Gautier, J. J., Leduc, C., Chamma, I., Kage, F., Kechkar, A., Thoumine, O., Rottner, K., Choquet, D., Gautreau, A., Sibarita, J. B., & Giannone, G. (2014). Nanoscale segregation of actin nucleation and elongation factors determines dendritic spine protrusion. *The EMBO Journal*, 33(23), 2745-2764. <https://doi.org/https://doi.org/10.15252/emj.201488837>

Che, D. L., Duan, L., Zhang, K., & Cui, B. (2015). The Dual Characteristics of Light-Induced Cryptochrome 2, Homo-oligomerization and Heterodimerization, for Optogenetic Manipulation in Mammalian Cells. *ACS Synth Biol*, 4(10), 1124-1135. <https://doi.org/10.1021/acssynbio.5b00048>

- Chen, D., & Huang, S. (2001). Nucleolar Components Involved in Ribosome Biogenesis Cycle between the Nucleolus and Nucleoplasm in Interphase Cells. *The Journal of Cell Biology*, 153(1), 169-176. <https://doi.org/10.1083/jcb.153.1.169>
- Chen, G., Cleary, J. M., Asenjo, A. B., Chen, Y., Mascaro, J. A., Arginteanu, D. F. J., Sosa, H., & Hancock, W. O. (2019). Kinesin-5 Promotes Microtubule Nucleation and Assembly by Stabilizing a Lattice-Competent Conformation of Tubulin. *Current Biology*, 29(14), 2259-2269.e2254. <https://doi.org/10.1016/j.cub.2019.05.075>
- Chen, L., Stone, M. C., Tao, J., & Rolls, M. M. (2012). Axon injury and stress trigger a microtubule-based neuroprotective pathway. *Proc Natl Acad Sci U S A*, 109(29), 11842-11847. <https://doi.org/10.1073/pnas.1121180109>
- Chen, X., Jia, B., Zhu, S., & Zhang, M. (2023). Phase separation-mediated actin bundling by the postsynaptic density condensates. *eLife*, 12, e84446. <https://doi.org/10.7554/eLife.84446>
- Cheng, Z.-Y., He, T.-T., Gao, X.-M., Zhao, Y., & Wang, J. (2021). ZBTB Transcription Factors: Key Regulators of the Development, Differentiation and Effector Function of T Cells [Review]. *Frontiers in Immunology*, 12. <https://doi.org/10.3389/fimmu.2021.713294>
- Chislock, E. M., & Pendergast, A. M. (2013). Abl family kinases regulate endothelial barrier function in vitro and in mice. *PLoS One*, 8(12), e85231. <https://doi.org/10.1371/journal.pone.0085231>
- Choi, Y.-K., Liu, P., Sze, S. K., Dai, C., & Qi, R. Z. (2010). CDK5RAP2 stimulates microtubule nucleation by the γ -tubulin ring complex. *Journal of Cell Biology*, 191(6), 1089-1095. <https://doi.org/10.1083/jcb.201007030>
- Chrétien, D., & Fuller, S. D. (2000). Microtubules switch occasionally into unfavorable configurations during elongation. *Journal of Molecular Biology*, 298(4), 663-676. <https://doi.org/https://doi.org/10.1006/jmbi.2000.3696>
- Chrétien, D., Metoz, F., Verde, F., Karsenti, E., & Wade, R. H. (1992). Lattice defects in microtubules: Protofilament numbers vary within individual microtubules. *Journal of Cell Biology*, 117(5), 1031-1040. <https://www.scopus.com/inward/record.uri?eid=2-s2.0-0026667023&partnerID=40&md5=7ce3a48642f01adc079535666f4855ea>

Cohen, R. S., Blomberg, F., Berzins, K., & Siekevitz, P. (1977). The structure of postsynaptic densities isolated from dog cerebral cortex. I. Overall morphology and protein composition. *J Cell Biol*, 74(1), 181-203. <https://doi.org/10.1083/jcb.74.1.181>

Colicelli, J. (2010). ABL Tyrosine Kinases: Evolution of Function, Regulation, and Specificity. *Science Signaling*, 3(139), re6-re6. <https://doi.org/doi:10.1126/scisignal.3139re6>

Compton, L. A., & Johnson Jr, W. C. (1986). Analysis of protein circular dichroism spectra for secondary structure using a simple matrix multiplication. *Analytical Biochemistry*, 155(1), 155-167. [https://doi.org/10.1016/0003-2697\(86\)90241-1](https://doi.org/10.1016/0003-2697(86)90241-1)

Courtemanche, N., Gifford, S. M., Simpson, M. A., Pollard, T. D., & Koleske, A. J. (2015). Abl2/Abl-related Gene Stabilizes Actin Filaments, Stimulates Actin Branching by Actin-related Protein 2/3 Complex, and Promotes Actin Filament Severing by Cofilin. *Journal of Biological Chemistry*, 290(7), 4038-4046. <https://doi.org/10.1074/jbc.M114.608117>

Cunningham, K. S., & Gotlieb, A. I. (2005). The role of shear stress in the pathogenesis of atherosclerosis. *Laboratory Investigation*, 85(1), 9-23. <https://doi.org/https://doi.org/10.1038/labinvest.3700215>

Dale, J. M., & Garcia, M. L. (2012). Neurofilament Phosphorylation during Development and Disease: Which Came First, the Phosphorylation or the Accumulation? *J Amino Acids*, 2012, 382107. <https://doi.org/10.1155/2012/382107>

de Forges, H., Pilon, A., Cantaloube, I., Pallandre, A., Haghiri-Gosnet, A., Perez, F., & Poüs, C. (2016). Localized Mechanical Stress Promotes Microtubule Rescue. *Current Biology*, 26(24), 3399-3406. <https://doi.org/10.1016/j.cub.2016.10.048>

de Jager, L., Jansen, K. I., Kapitein, L. C., Förster, F., & Howes, S. C. (2022). Increased microtubule lattice spacing correlates with selective binding of kinesin-1 in cells. *bioRxiv*. <https://doi.org/10.1101/2022.05.25.493428>

Debs, G. E., Cha, M., Liu, X., Huehn, A. R., & Sindelar, C. V. (2020). Dynamic and asymmetric fluctuations in the microtubule wall captured by high-resolution cryoelectron microscopy. *Proc Natl Acad Sci U S A*, 117(29), 16976-16984. <https://doi.org/10.1073/pnas.2001546117>

Dederer, V., Murillo, M. S., Karasmanis, E. P., Hatch, K. S., Chatterjee, D., Preuss, F., Azeez, K. R. A., Nguyen, L. V., Galicia, C., Dreier, B., Plückthun, A., Versees, W., Mathea, S., Leschziner, A. E., Reck-Peterson, S. L., & Knapp, S. (2023). Development of LRRK2 designed ankyrin-repeat proteins. *bioRxiv*, 2023.2011.2014.567123. <https://doi.org/10.1101/2023.11.14.567123>

Deniston, C. K., Salogiannis, J., Mathea, S., Snead, D. M., Lahiri, I., Matyszewski, M., Donosa, O., Watanabe, R., Böhning, J., Shiau, A. K., Knapp, S., Villa, E., Reck-Peterson, S. L., & Leschziner, A. E. (2020). Structure of LRRK2 in Parkinson's disease and model for microtubule interaction. *Nature*, 588(7837), 344-349. <https://doi.org/10.1038/s41586-020-2673-2>

Dent, E. W. (2017). Of microtubules and memory: implications for microtubule dynamics in dendrites and spines. *Molecular Biology of the Cell*, 28(1), 1-8. <https://doi.org/10.1091/mbc.E15-11-0769>

Dent, E. W. (2020). Dynamic microtubules at the synapse. *Current Opinion in Neurobiology*, 63, 9-14. <https://doi.org/https://doi.org/10.1016/j.conb.2020.01.003>

Desai, A., & Mitchison, T. J. (1997). Microtubule Polymerization Dynamics. *Annual Review of Cell and Developmental Biology*, 13, 87-117. <https://doi.org/10.1146/annurev.cellbio.13.1.83>

Didiasova, M., Schaefer, L., & Wygrecka, M. (2019). When Place Matters: Shuttling of Enolase-1 Across Cellular Compartments. *Front Cell Dev Biol*, 7, 61. <https://doi.org/10.3389/fcell.2019.00061>

Dimitrov, A., Quesnoit, M., Moutel, S., Cantaloube, I., Poüs, C., & Perez, F. (2008). Detection of GTP-Tubulin Conformation in Vivo Reveals a Role for GTP Remnants in Microtubule Rescues. *Science*, 322(5906), 1353-1356. <https://doi.org/doi:10.1126/science.1165401>

Dixit, R., Ross, J. L., Goldman, Y. E., & Holzbaur, E. L. (2008). Differential regulation of dynein and kinesin motor proteins by tau. *Science*, 319(5866), 1086-1089. <https://doi.org/10.1126/science.1152993>

Dobin, A., Davis, C. A., Schlesinger, F., Drenkow, J., Zaleski, C., Jha, S., Batut, P., Chaisson, M., & Gingeras, T. R. (2013). STAR: ultrafast universal RNA-seq aligner. *Bioinformatics*, 29(1), 15-21. <https://doi.org/10.1093/bioinformatics/bts635>

Dogterom, M., & Koenderink, G. H. (2018). Actin–microtubule crosstalk in cell biology. *Nature Reviews Molecular Cell Biology*, 20, 38-54. <https://doi.org/10.1038/s41580-018-0067-1>

Drechsel, D. N., Hyman, A. A., Cobb, M. H., & Kirschner, M. W. (1992). Modulation of the dynamic instability of tubulin assembly by the microtubule-associated protein tau. *Molecular Biology of the Cell*, 3(10), 1141-1154. <https://doi.org/10.1091/mbc.3.10.1141>

Drechsel, D. N., & Kirschner, M. W. (1994). The minimum GTP cap required to stabilize microtubules. *Current Biology*, 4(12), 1053-1061. [https://doi.org/10.1016/S0960-9822\(00\)00243-8](https://doi.org/10.1016/S0960-9822(00)00243-8)

Druker, B. J., Sawyers, C. L., Kantarjian, H., Resta, D. J., Reese, S. F., M., F. J., Capdeville, R., & Talpaz, M. (2001). Activity of a specific inhibitor of the BCR-ABL tyrosine kinase in the blast crisis of chronic myeloid leukemia and acute lymphoblastic leukemia with the Philadelphia chromosome. *The New England Journal of Medicine*, 344, 1038-1042. <https://doi.org/10.1056/NEJM200104053441402>

Druker, B. J., Talpaz, M., Resta, D. J., Peng, B., Buchdunger, E., Ford, J. M., Lydon, N. B., Kantarjian, H., Capdeville, R., Ohno-Jones, S., & Sawyers, C. L. (2001). Efficacy and Safety of a Specific Inhibitor of the BCR-ABL Tyrosine Kinase in Chronic Myeloid Leukemia. *The New England Journal of Medicine*, 344, 1031-1037. <https://doi.org/10.1056/NEJM200104053441401>

Duan, D., Lyu, W., Chai, P., Ma, S., Wu, K., Wu, C., Xiong, Y., Sestan, N., Zhang, K., & Koleske, A. J. (2023). Abl2 repairs microtubules and phase separates with tubulin to promote microtubule nucleation. *Curr Biol*, 33(21), 4582-4598.e4510. <https://doi.org/10.1016/j.cub.2023.09.018>

Duelberg, C., Cade, N. I., Holmes, D., & Surrey, T. (2016). The size of the EB cap determines instantaneous microtubule stability. *eLife*, 5, e13470. <https://doi.org/10.7554/eLife.13470>

Duncan, P. I., Stojdl, D. F., Marius, R. M., Scheit, K. H., & Bell, J. C. (1998). The Clk2 and Clk3 dual-specificity protein kinases regulate the intranuclear distribution of SR proteins and influence pre-mRNA splicing. *Exp Cell Res*, 241(2), 300-308. <https://doi.org/10.1006/excr.1998.4083>

Efimov, A., Kharitonov, A., Efimova, N., Loncarek, J., Miller, P. M., Andreyeva, N., Gleeson, P., Galjart, N., Maia, A. R., McLeod, I. X., Yates, J. R., 3rd, Maiato, H., Khodjakov, A., Akhmanova, A., & Kaverina, I. (2007). Asymmetric CLASP-dependent nucleation of noncentrosomal

microtubules at the trans-Golgi network. *Dev Cell*, 12(6), 917-930.

<https://doi.org/10.1016/j.devcel.2007.04.002>

Elliott, D. A., Weickert, C. S., & Garner, B. (2010). Apolipoproteins in the brain: implications for neurological and psychiatric disorders. *Clin Lipidol*, 51(4), 555-573.

<https://doi.org/10.2217/clp.10.37>

Emperador-Melero, J., Wong, M. Y., Wang, S. S. H., de Nola, G., Nyitrai, H., Kirchhausen, T., & Kaeser, P. S. (2021). PKC-phosphorylation of Liprin- α 3 triggers phase separation and controls presynaptic active zone structure. *Nature Communications*, 12(1), 3057.

<https://doi.org/10.1038/s41467-021-23116-w>

Engel, U., Zhan, Y., Long, J. B., Boyle, S. N., Ballif, B. A., Dorey, K., Gygi, S. P., Koleske, A. J., & VanVactor, D. (2014). Abelson Phosphorylation of CLASP2 Modulates its Association With Microtubules and Actin. *Cytoskeleton (Hoboken)*, 71(3), 195-209.

<https://doi.org/10.1002/cm.21164>

Erickson, H. P., & O'Brien, E. T. (1992). Microtubule dynamic instability and GTP hydrolysis. *Annual Review of Biophysics and Biomolecular Structure*, 21, 145-166.

<https://doi.org/10.1146/annurev.bb.21.060192.001045>

Eshun-Wilson, L., Zhang, R., Portran, D., Nachury, M. V., Toso, D. B., Löhr, T., Vendruscolo, M., Bonomi, M., Fraser, J. S., & Nogales, E. (2019). Effects of α -tubulin acetylation on microtubule structure and stability. *Proceedings of the National Academy of Sciences*, 116(21), 10366-10371.

<https://doi.org/doi:10.1073/pnas.1900441116>

Estévez-Gallego, J., Josa-Prado, F., Ku, S., Buey, R. M., Balaguer, F. A., Prota, A. E., Lucena-Agell, D., Kamma-Lorger, C., Yagi, T., Iwamoto, H., Duchesne, L., Barasoain, I., Steinmetz, M. O., Chrétien, D., Kamimura, S., Díaz, J. F., & Oliva, M. A. (2020). Structural model for differential cap maturation at growing microtubule ends. *eLife*, 9(e50155), 1-26.

<https://doi.org/10.7554/eLife.50155>

Falinski, R., Nieborowska-Skorska, M., & Skorski, T. (2012). BCR-ABL1 kinase facilitates localization of acetylated histones 3 and 4 on DNA double-strand breaks. *Leuk Res*, 36(2), 241-244. <https://doi.org/10.1016/j.leukres.2011.10.007>

Farina, F., Gaillard, J., Guérin, C., Couté, Y., Sillibourne, J., Blanchoin, L., & Théry, M. (2016). The centrosome is an actin-organizing centre. *Nat Cell Biol*, *18*(1), 65-75.

<https://doi.org/10.1038/ncb3285>

Farmer, V. J., & Zanic, M. (2022). Beyond the GTP-cap: Elucidating the molecular mechanisms of microtubule catastrophe. *BioEssays*, *45*(1). <https://doi.org/10.1002/bies.202200081>

Feng, Z., Chen, X., Wu, X., & Zhang, M. (2019). Formation of biological condensates via phase separation: Characteristics, analytical methods, and physiological implications. *Journal of Biological Chemistry*, *294*(40), 14823-14835. <https://doi.org/10.1074/jbc.REV119.007895>

Ferro, L. S., Fang, Q., Eshun-Wilson, L., Fernandes, J., Jack, A., Farrell, D. P., Golcuk, M., Huijben, T., Costa, K., Gur, M., DiMaio, F., Nogales, E., & Yildiz, A. (2022). Structural and functional insight into regulation of kinesin-1 by microtubule-associated protein MAP7. *Science*, *375*(6578), 326-331. <https://doi.org/doi:10.1126/science.abf6154>

Fifková, E., & Anderson, C. L. (1981). Stimulation-induced changes in dimensions of stalks of dendritic spines in the dentate molecular layer. *Experimental Neurology*, *74*(2), 621-627.

[https://doi.org/https://doi.org/10.1016/0014-4886\(81\)90197-7](https://doi.org/https://doi.org/10.1016/0014-4886(81)90197-7)

Finka, A., & Goloubinoff, P. (2013). Proteomic data from human cell cultures refine mechanisms of chaperone-mediated protein homeostasis. *Cell Stress and Chaperones*, *18*, 591-605.

<https://doi.org/10.1007/s12192-013-0413-3>

Finn, A. J., Feng, G., & Pendergast, A. M. (2003). Postsynaptic requirement for Abl kinases in assembly of the neuromuscular junction. *Nature Neuroscience*, *6*, 717-723.

<https://doi.org/10.1038/nn1071>

Flyvbjerg, H., Jobs, E., & Leibler, S. (1996). Kinetics of self-assembling microtubules: An “inverse problem” in biochemistry. *Proceedings of the National Academy of Sciences*, *93*(12), 5975-5979.

<https://doi.org/10.1073/pnas.93.12.5975>

Fougerousse, F., Edom-Vovard, F., Merkulova, T., Ott, M. O., Durand, M., Butler-Browne, G., & Keller, A. (2001). The muscle-specific enolase is an early marker of human myogenesis. *J Muscle Res Cell Motil*, *22*(6), 535-544.

<https://doi.org/10.1023/a:1015008208007>

Fourniol, F., Perderiset, M., Houdusse, A., & Moores, C. (2013). Chapter 3 - Structural Studies of the Doublecortin Family of MAPs. In J. J. Correia & L. Wilson (Eds.), *Methods in Cell Biology* (Vol. 115, pp. 27-48). Academic Press. <https://doi.org/https://doi.org/10.1016/B978-0-12-407757-7.00003-7>

Fourniol, F. J., Sindelar, C. V., Amigues, B., Clare, D. K., Thomas, G., Perderiset, M., Francis, F., Houdusse, A., & Moores, C. A. (2010). Template-free 13-protofilament microtubule-MAP assembly visualized at 8 Å resolution. *J Cell Biol*, 191(3), 463-470. <https://doi.org/10.1083/jcb.201007081>

Fox, D. T., & Peifer, M. (2007). Abelson kinase (Abl) and RhoGEF2 regulate actin organization during cell constriction in *Drosophila*. *Development*, 134(3), 567-578. <https://doi.org/10.1242/dev.02748>

Freeley, M., Kelleher, D., & Long, A. (2011). Regulation of Protein Kinase C function by phosphorylation on conserved and non-conserved sites. *Cell Signal*, 23(5), 753-762. <https://doi.org/10.1016/j.cellsig.2010.10.013>

Frese, C. K., Mikhaylova, M., Stucchi, R., Gautier, V., Liu, Q., Mohammed, S., Heck, A. J. R., Altelaar, A. F. M., & Hoogenraad, C. C. (2017). Quantitative Map of Proteome Dynamics during Neuronal Differentiation. *Cell Rep*, 18(6), 1527-1542. <https://doi.org/10.1016/j.celrep.2017.01.025>

Gabriel, M., Delforge, Y., Deward, A., Habraken, Y., Henuy, B., Piette, J., Klinck, R., Chabot, B., Colige, A., & Lambert, C. (2015). Role of the splicing factor SRSF4 in cisplatin-induced modifications of pre-mRNA splicing and apoptosis. *BMC Cancer*, 15, 227. <https://doi.org/10.1186/s12885-015-1259-0>

Gazzola, M., Schaeffer, A., Butler-Hallisey, C., Friedl, K., Vianay, B., Gaillard, J., Leterrier, C., Blanchoin, L., & Théry, M. (2023). Microtubules self-repair in living cells. *Current Biology*, 33(1), 122-133. <https://doi.org/10.1016/j.cub.2022.11.060>

Geng, Q., Keya, J. J., Hotta, T., & Verhey, K. J. (2023). KIF1C, an RNA transporting kinesin-1, undergoes liquid-liquid phase separation through its C-terminal disordered domain. *bioRxiv*. <https://doi.org/10.1101/2023.10.23.563538>

Geraldo, S., Khanzada, U. K., Parsons, M., Chilton, J. K., & Gordon-Weeks, P. R. (2008). Targeting of the F-actin-binding protein drebrin by the microtubule plus-tip protein EB3 is required for neuritogenesis. *Nature Cell Biology*, *10*(10), 1181-1189. <https://doi.org/10.1038/ncb1778>

Gifford, S. M., Weizhi, L., Mader, C. C., Halo, T. L., Machida, K., Boggon, T. J., & Koleske, A. J. (2014). Two Amino Acid Residues Confer Different Binding Affinities of Abelson Family Kinase Src Homology 2 Domains for Phosphorylated Cortactin. *Journal of Biological Chemistry*, *289*(28), 19704-19713. <https://doi.org/10.1074/jbc.M114.556480>

Girão, H., Okada, N., Rodrigues, T. A., Silva, A. O., Figueiredo, A. C., Garcia, Z., Moutinho-Santos, T., Hayashi, I., Azevedo, J. E., Macedo-Ribeiro, S., & Maiato, H. (2019). CLASP2 binding to curved microtubule tips promotes flux and stabilizes kinetochore attachments. *Journal of Cell Biology*, *2019*(2), e201905080. <https://doi.org/10.1083/jcb.201905080>

Gleeson, J. G., Lin, P. T., Flanagan, L. A., & Walsh, C. A. (1999). Doublecortin is a microtubule-associated protein and is expressed widely by migrating neurons. *Neuron*, *23*(2), 257-271. [https://doi.org/10.1016/s0896-6273\(00\)80778-3](https://doi.org/10.1016/s0896-6273(00)80778-3)

Goddard, T. D., Huang, C. C., Meng, E. C., Pettersen, E. F., Couch, G. S., Morris, J. H., & Ferrin, T. E. (2018). UCSF ChimeraX: Meeting modern challenges in visualization and analysis. *Protein Sci*, *27*(1), 14-25. <https://doi.org/10.1002/pro.3235>

Goff, S. P., Gilboa, E., Witte, O. N., & Baltimore, D. (1980). Structure of the Abelson murine leukemia virus genome and the homologous cellular gene: Studies with cloned viral DNA. *Cell*, *22*(3), 777-785. [https://doi.org/10.1016/0092-8674\(80\)90554-1](https://doi.org/10.1016/0092-8674(80)90554-1)

Goodson, H. V., & Jonasson, E. M. (2018). Microtubules and Microtubule-Associated Proteins. *Cold Spring Harbor Perspectives in Biology*, *10*(6). <https://doi.org/10.1101/cshperspect.a022608>

Goodwin, S. S., & Vale, R. D. (2010). Patronin regulates the microtubule network by protecting microtubule minus ends. *Cell*, *143*(2), 263-274. <https://doi.org/10.1016/j.cell.2010.09.022>

Gourlay, C. W., & Ayscough, K. R. (2005). The actin cytoskeleton: a key regulator of apoptosis and ageing? *Nature Reviews Molecular Cell Biology*, *6*(7), 583-589. <https://doi.org/10.1038/nrm1682>

Gourley, S. L., Olevska, A., Warren, M. S., Taylor, J. R., & Koleske, A. J. (2012). Arg Kinase Regulates Prefrontal Dendritic Spine Refinement and Cocaine-Induced Plasticity. *The Journal of Neuroscience*, 32(7), 2314–2323. <https://doi.org/10.1523/JNEUROSCI.2730-11.2012>

Graham, M., Combe, C., Kolbowski, L., & Rappsilber, J. (2019). xiView: A common platform for the downstream analysis of Crosslinking Mass Spectrometry data. In: bioRxiv.

Greuber, E., Smith-Pearson, P., Wang, J., & Pendergast, A. M. (2013). Role of ABL family kinases in cancer: from leukemia to solid tumours. *Nature Reviews Cancer*, 13, 559-571. <https://doi.org/10.1038/nrc3563>

Grevengoed, E. E., Loureiro, J. J., Jesse, T. L., & Peifer, M. (2001). Abelson kinase regulates epithelial morphogenesis in *Drosophila*. *Journal of Cell Biology*, 155(7), 1185-1198. <https://doi.org/10.1083/jcb.200105102>

Gromova, K. V., Thies, E., Janiesch, P. C., Lützenkirchen, F. P., Zhu, Y., Stajano, D., Dürst, C. D., Schweizer, M., Konietzny, A., Mikhaylova, M., Gee, C. E., & Kneussel, M. (2023). The kinesin Kif21b binds myosin Va and mediates changes in actin dynamics underlying homeostatic synaptic downscaling. *Cell Rep*, 42(7), 112743. <https://doi.org/10.1016/j.celrep.2023.112743>

Gu, J., Firestein, B. L., & Zheng, J. Q. (2008). Microtubules in Dendritic Spine Development. *The Journal of Neuroscience*, 28(46), 12120-12124. <https://doi.org/10.1523/JNEUROSCI.2509-08.2008>

Guedes-Dias, P., Nirschl, J. J., Abreu, N., Tokito, M. K., Janke, C., Magiera, M. M., & Holzbaur, E. L. F. (2019). Kinesin-3 Responds to Local Microtubule Dynamics to Target Synaptic Cargo Delivery to the Presynapse. *Current Biology*, 29(2), 268-282.e268. <https://doi.org/https://doi.org/10.1016/j.cub.2018.11.065>

Guesdon, A., Bazile, F., Buey, R. M., Mohan, R., Monier, S., García, R. R., Angevin, M., Heichette, C., Wieneke, R., Tampé, R., Duchesne, L., Akhmanova, A., Steinmetz, M. O., & Chrétien, D. (2016). EB1 interacts with outwardly curved and straight regions of the microtubule lattice. *Nature Cell Biology*, 18, 1102-1108. <https://doi.org/10.1038/ncb3412>

- Guo, C., Alfaro-Aco, R., Zhang, C., Russell, R. W., Petry, S., & Polenova, T. (2023). Structural basis of protein condensation on microtubules underlying branching microtubule nucleation. *Nature Communications*, 14. <https://doi.org/10.1038/s41467-023-39176-z>
- Gupton, S. L., & Waterman-Storer, C. M. (2006). Spatiotemporal Feedback between Actomyosin and Focal-Adhesion Systems Optimizes Rapid Cell Migration. *Cell*, 125(7), 1361-1374. <https://doi.org/10.1016/j.cell.2006.05.029>
- Haahr, P., Hoffmann, S., Tollenaere, M. A. X., Ho, T., Toledo, L. I., Mann, M., Bekker-Jensen, S., Räschle, M., & Mailand, N. (2016). Activation of the ATR kinase by the RPA-binding protein ETAA1. *Nature Cell Biology*, 18(11), 1196-1207. <https://doi.org/10.1038/ncb3422>
- Hall, B., Cho, A., Limaye, A., Cho, K., Khillan, J., & Kulkarni, A. B. (2018). Genome Editing in Mice Using CRISPR/Cas9 Technology. *Curr Protoc Cell Biol*, 81(1), e57. <https://doi.org/10.1002/cpcb.57>
- Han, H., Schubert, H. L., McCullough, J., Monroe, N., Purdy, M. D., Yeager, M., Sundquist, W. I., & Hill, C. P. (2020). Structure of spastin bound to a glutamate-rich peptide implies a hand-over-hand mechanism of substrate translocation. *Journal of Biological Chemistry*, 295(2), 435-443. <https://doi.org/https://doi.org/10.1074/jbc.AC119.009890>
- Hanse, E. A., Ruan, C., Kachman, M., Wang, D., Lowman, X. H., & Kelekar, A. (2017). Cytosolic malate dehydrogenase activity helps support glycolysis in actively proliferating cells and cancer. *Oncogene*, 36(27), 3915-3924. <https://doi.org/10.1038/onc.2017.36>
- Harmon, B., Campbell, N., & Ratner, L. (2010). Role of Abl Kinase and the Wave2 Signaling Complex in HIV-1 Entry at a Post-Hemifusion Step. *PLOS Pathogens*, 6(6), e1000956. <https://doi.org/10.1371/journal.ppat.1000956>
- Harrison, S. C. (2003). Variation on an Src-like Theme. *Cell*, 112(6), 737-740. [https://doi.org/10.1016/S0092-8674\(03\)00196-X](https://doi.org/10.1016/S0092-8674(03)00196-X)
- Hehnl, H., & Doxsey, S. (2014). Rab11 Endosomes Contribute to Mitotic Spindle Organization and Orientation. *Developmental Cell*, 28(5), 497-507. <https://doi.org/10.1016/j.devcel.2014.01.014>

- Henty-Ridilla, J. L., Juanes, M. A., & Goode, B. L. (2017). Profilin Directly Promotes Microtubule Growth through Residues Mutated in Amyotrophic Lateral Sclerosis. *Curr Biol*, 27(22), 3535-3543.e3534. <https://doi.org/10.1016/j.cub.2017.10.002>
- Henty-Ridilla, J. L., Rankova, A., Eskin, J. A., Kenny, K., & Goode, B. L. (2016). Accelerated actin filament polymerization from microtubule plus ends. *Science*, 352(6288), 1004-1009. <https://doi.org/10.1126/science.aaf1709>
- Hernández, S. E., Settleman, J., & Koleske, A. J. (2004). Adhesion-Dependent Regulation of p190RhoGAP in the Developing Brain by the Abl-Related Gene Tyrosine Kinase. *Current Biology*, 14, 691-696. <https://doi.org/10.1016/j.cub.2004.03.062>
- Hernández-Candia, C. N., & Tucker, C. L. (2020). Optogenetic Control of Gene Expression Using Cryptochrome 2 and a Light-Activated Degron. In D. Niopak (Ed.), *Photoswitching Proteins : Methods and Protocols* (pp. 151-158). Springer US. https://doi.org/10.1007/978-1-0716-0755-8_10
- Hernández-Vega, A., Braun, M., Scharrel, L., Jahnel, M., Wegmann, S., Hyman, B. T., Alberti, S., Diez, S., & Hyman, A. A. (2017). Local Nucleation of Microtubule Bundles through Tubulin Concentration into a Condensed Tau Phase. *Cell Reports*, 20(10), 2304-2312. <https://doi.org/10.1016/j.celrep.2017.08.042>
- Hertzer, K. M., & Walczak, C. E. (2008). The C-termini of tubulin and the specific geometry of tubulin substrates influence the depolymerization activity of MCAK. *Cell Cycle*, 7(17), 2727-2737. <https://doi.org/10.4161/cc.7.17.6590>
- Hinrichs, M. H., Jalal, A., Brenner, B., Mandelkow, E., Kumar, S., & Scholz, T. (2012). Tau Protein Diffuses along the Microtubule Lattice. *Journal of Biological Chemistry*, 287(46), 38559-38568. <https://doi.org/10.1074/jbc.M112.369785>
- Hoj, J. P., Mayro, B., & Pendergast, A. M. (2020). The ABL2 kinase regulates an HSF1-dependent transcriptional program required for lung adenocarcinoma brain metastasis. *Proceedings of the National Academy of Sciences*, 117(52), 33486-33495. <https://doi.org/10.1073/pnas.2007991117>

- Hong, Y., Najafi, S., Casey, T., Shea, J.-E., Han, S.-I., & Hwang, D. S. (2022). Hydrophobicity of arginine leads to reentrant liquid-liquid phase separation behaviors of arginine-rich proteins. *Nature Communications*, 13(1), 7326. <https://doi.org/10.1038/s41467-022-35001-1>
- Honkura, N., Matsuzaki, M., Noguchi, J., Ellis-Davies, G. C. R., & Kasai, H. (2008). The Subspine Organization of Actin Fibers Regulates the Structure and Plasticity of Dendritic Spines. *Neuron*, 57(5), 719-729. <https://doi.org/https://doi.org/10.1016/j.neuron.2008.01.013>
- Höög, J. L., Huisman, S. M., Sebö-Lemke, Z., Sandblad, L., McIntosh, J. R., Antony, C., & Brunner, D. (2011). Electron tomography reveals a flared morphology on growing microtubule ends. *Journal of Cell Science*, 124(Pt 5), 693-698. <https://doi.org/10.1242/jcs.072967>
- Hoogenraad, C. C., & Bradke, F. (2009). Control of Neuronal Polarity and Plasticity—A Renaissance for Microtubules? *Trends in Cell Biology*, 19(12), 669-676. <https://doi.org/10.1016/j.tcb.2009.08.006>
- Hooikaas, P. J., Martin, M., Mühlethaler, T., Kuijntjes, G.-J., Peeters, C. A. E., Katrukha, E. A., Ferrari, L., Stucchi, R., Verhagen, D. G. F., van Riel, W. E., Grigoriev, I., Altelaar, A. F. M., Hoogenraad, C. C., Rüdiger, S. G. D., Steinmetz, M. O., Kapitein, L. C., & Akhmanova, A. (2019). MAP7 family proteins regulate kinesin-1 recruitment and activation. *Journal of Cell Biology*, 218(4), 1298-1318. <https://doi.org/10.1083/jcb.201808065>
- Howard, J., & Hyman, A. A. (2009). Growth, fluctuation and switching at microtubule plus ends. *Nature Reviews Molecular Cell Biology*, 10, 569-574. <https://doi.org/10.1038/nrm2713>
- Hu, X., Ballo, L., Pietila, L., Viesselmann, C., Ballweg, J., Lombard, D., Stevenson, M., Merriam, E., & Dent, E. W. (2011). BDNF-Induced Increase of PSD-95 in Dendritic Spines Requires Dynamic Microtubule Invasions. *The Journal of Neuroscience*, 31(43), 15597-15603. <https://doi.org/10.1523/JNEUROSCI.2445-11.2011>
- Hu, X., Viesselmann, C., Nam, S., Merriam, E., & Dent, E. W. (2008). Activity-Dependent Dynamic Microtubule Invasion of Dendritic Spines. *The Journal of Neuroscience*, 28(49), 13094-13105. <https://doi.org/10.1523/JNEUROSCI.3074-08.2008>

Hu, Y., Lyu, W., Lowery, L. A., & Koleske, A. J. (2019). Regulation of MT dynamics via direct binding of an Abl family kinase. *Journal of Cell Biology*, 218(12), 3986-3997. <https://doi.org/10.1083/jcb.201812144>

Hummel, J. J. A., & Hoogenraad, C. C. (2021). Specific KIF1A-adaptor interactions control selective cargo recognition. *J Cell Biol*, 220(10). <https://doi.org/10.1083/jcb.202105011>

Huppertz, I., Perez-Perri, J. I., Mantas, P., Sekaran, T., Schwarzl, T., Russo, F., Ferring-Appel, D., Koskova, Z., Dimitrova-Paternoga, L., Kafkia, E., Hennig, J., Neveu, P. A., Patil, K., & Hentze, M. W. (2022). Riboregulation of Enolase 1 activity controls glycolysis and embryonic stem cell differentiation. *Molecular Cell*, 82(14), 2666-2680.e2611. <https://doi.org/https://doi.org/10.1016/j.molcel.2022.05.019>

Hyman, A. A., Salsler, S., Drechsel, D. N., Unwin, N., & Mitchison, T. J. (1992). Role of GTP hydrolysis in microtubule dynamics: information from a slowly hydrolyzable analogue, GMPCPP. *Molecular Biology of the Cell*, 3(10), 1155-1167. <https://doi.org/10.1091/mbc.3.10.1155>

Ikegami, K., Mukai, M., Tsuchida, J., Heier, R. L., Macgregor, G. R., & Setou, M. (2006). TLL7 is a mammalian beta-tubulin polyglutamylase required for growth of MAP2-positive neurites. *J Biol Chem*, 281(41), 30707-30716. <https://doi.org/10.1074/jbc.M603984200>

Imasaki, T., Kikkawa, S., Niwa, S., Saijo-Hamano, Y., Shigematsu, H., Aoyama, K., Mitsuoka, K., Shimizu, T., Aoki, M., Sakamoto, A., Tomabechi, Y., Sakai, N., Shirouzu, M., Taguchi, S., Yamagishi, Y., Setsu, T., Sakihama, Y., Nitta, E., Takeichi, M., & Nitta, R. (2022). CAMSAP2 organizes a γ -tubulin-independent microtubule nucleation centre through phase separation. *eLife*, 11, e77365. <https://doi.org/10.7554/eLife.77365>

Irgen-Giorgio, S., Yoshida, S., Walling, V., & Chong, S. (2022). Fixation can change the appearance of phase separation in living cells. *eLife*, 11, e79903. <https://doi.org/10.7554/eLife.79903>

Jan, Y.-N., & Jan, L. Y. (2010). Branching out: mechanisms of dendritic arborization. *Nature Reviews Neuroscience*, 11(5), 316-328. <https://doi.org/10.1038/nrn2836>

Jang, H. N., Liu, Y., Choi, N., Oh, J., Ha, J., Zheng, X., & Shen, H. (2018). Binding of SRSF4 to a novel enhancer modulates splicing of exon 6 of Fas pre-mRNA. *Biochemical and Biophysical*

Research Communications, 506(3), 703-708.

<https://doi.org/https://doi.org/10.1016/j.bbrc.2018.10.123>

Janke, C., & Magiera, M. M. (2020). The tubulin code and its role in controlling microtubule properties and functions. *Nature Reviews Molecular Cell Biology*, 21(6), 307-326.

<https://doi.org/10.1038/s41580-020-0214-3>

Jaworski, J., Kapitein, L. C., Gouveia, S. M., Dortland, B. R., Wulf, P. S., Grigoriev, I., Camera, P., Spangler, S. A., Stefano, P. D., Demmers, J., Krugers, H., Defilippi, P., Akhmanova, A., & Hoogenraad, C. C. (2009). Dynamic Microtubules Regulate Dendritic Spine Morphology and Synaptic Plasticity. *Neuron*, 61, 85-100. <https://doi.org/10.1016/j.neuron.2008.11.013>

Jiang, K., Hua, S., Mohan, R., Grigoriev, I., Yau, Kah W., Liu, Q., Katrukha, Eugene A., Altelaar, A. F. M., Heck, Albert J. R., Hoogenraad, Casper C., & Akhmanova, A. (2014). Microtubule Minus-End Stabilization by Polymerization-Driven CAMSAP Deposition. *Developmental Cell*, 28(3), 295-309. <https://doi.org/https://doi.org/10.1016/j.devcel.2014.01.001>

Jijumon, A. S., Bodakuntla, S., Genova, M., Bangera, M., Sackett, V., Besse, L., Maksut, F., Henriot, V., Magiera, M. M., Sirajuddin, M., & Janke, C. (2022). Lysate-based pipeline to characterize microtubule-associated proteins uncovers unique microtubule behaviours. *Nature Cell Biology*, 24, 253-267. <https://doi.org/10.1038/s41556-021-00825-4>

Johnson-Chavarria, E. M., Tanyeri, M., & Schroeder, C. M. (2011). A Microfluidic-based Hydrodynamic Trap for Single Particles. *Journal of Visualized Experiments*, 21(47), 2517. <https://doi.org/10.3791/2517>

Jones, B. J., & Roberts, D. J. (2011). The quantitative measurement of motor inco-ordination in naive mice using an accelerating rotarod. *Journal of Pharmacy and Pharmacology*, 20(4), 302-304. <https://doi.org/10.1111/j.2042-7158.1968.tb09743.x>

Jones, D. T., & Cozzetto, D. (2014). DISOPRED3: precise disordered region predictions with annotated protein-binding activity. *Bioinformatics*, 31(6), 857–863. <https://doi.org/10.1093/bioinformatics/btu744>

Jumper, J., Evans, R., Pritzel, A., Green, T., Figurnov, M., Ronneberger, O., Tunyasuvunakool, K., Bates, R., Zidek, A., Potapenko, A., Bridgland, A., Meyer, C., Kohl, S. A. A., Ballard, A. J., Cowie,

A., Romera-Paredes, B., Nikolov, S., Jain, R., Adler, J., . . . Hassabis, D. (2021). Highly accurate protein structure prediction with AlphaFold. *Nature*, 596(7873), 583-589.

<https://doi.org/10.1038/s41586-021-03819-2>

Kadavath, H., Hofele, R. V., Biernat, J., Kumar, S., Tepper, K., Urlaub, H., Mandelkow, E., & Zweckstetter, M. (2015). Tau stabilizes microtubules by binding at the interface between tubulin heterodimers. *Proceedings of the National Academy of Sciences*, 112(24), 7501-7506.

<https://doi.org/doi:10.1073/pnas.1504081112>

Kain, K. H., & Klemke, R. L. (2001). Inhibition of Cell Migration by Abl Family Tyrosine Kinases through Uncoupling of Crk-CAS Complexes *. *Journal of Biological Chemistry*, 276(19), 16185-16192. <https://doi.org/10.1074/jbc.M100095200>

Kanaan, N. M., Hamel, C., Grabinski, T., & Combs, B. (2020). Liquid-liquid phase separation induces pathogenic tau conformations in vitro. *Nature Communications*, 11(2809).

<https://doi.org/10.1038/s41467-020-16580-3>

Kanaan, N. M., Morfini, G. A., LaPointe, N. E., Pigino, G. F., Patterson, K. R., Song, Y., Andreadis, A., Fu, Y., Brady, S. T., & Binder, L. I. (2011). Pathogenic forms of tau inhibit kinesin-dependent axonal transport through a mechanism involving activation of axonal phosphotransferases. *J Neurosci*, 31(27), 9858-9868. <https://doi.org/10.1523/jneurosci.0560-11.2011>

Kapitein, L. C., & Hoogenraad, C. C. (2011). Which way to go? Cytoskeletal organization and polarized transport in neurons. *Molecular and Cellular Neuroscience*, 46, 9-20.

<https://doi.org/10.1016/j.mcn.2010.08.015>

Kapitein, L. C., Yau, K. W., Gouveia, S. M., van der Zwan, W. A., Wulf, P. S., Keijzer, N., Demmers, J., Jaworski, J., Akhmanova, A., & Hoogenraad, C. C. (2011). NMDA Receptor Activation Suppresses Microtubule Growth and Spine Entry. *The Journal of Neuroscience*, 31(22), 8194-8209. <https://doi.org/10.1523/JNEUROSCI.6215-10.2011>

Kashiwagi, S., Fujioka, Y., Kondo, T., Satoh, A. O., Yoshida, A., Fujioka, M., Sasajima, H., Amano, M., Teshima, T., & Ohba, Y. (2019). Localization of BCR-ABL to Stress Granules Contributes to Its Oncogenic Function. *Cell Structure and Function*, 44(2), 195-204.

<https://doi.org/10.1247/csf.19033>

- Kellogg, E. H., Hejab, N. M. A., Poepsel, S., Downing, K. H., DiMaio, F., & Nogales, E. (2018). Near-atomic model of microtubule-tau interactions. *Science*, 360(6394), 1242-1246. <https://doi.org/10.1126/science.aat1780>
- Kerr, J. P., Robison, P., Shi, G., Bogush, A. I., Kempema, A. M., Hexum, J. K., Becerra, N., Harki, D. A., Martin, S. S., Raiteri, R., Prosser, B. L., & Ward, C. W. (2015). Detyrosinated microtubules modulate mechanotransduction in heart and skeletal muscle. *Nature Communications*, 6(1), 8526. <https://doi.org/10.1038/ncomms9526>
- Kerrisk, M. E., Greer, C. A., & Koleske, A. J. (2013). Integrin $\alpha 3$ Is Required for Late Postnatal Stability of Dendrite Arbors, Dendritic Spines and Synapses, and Mouse Behavior. *The Journal of Neuroscience*, 33(16), 6742-6752. <https://doi.org/10.1523/JNEUROSCI.0528-13.2013>
- Khatri, A., Wang, J., & Pendergast, A. M. (2016). Multifunctional Abl kinases in health and disease. *Journal of Cell Science*, 129(1), 9-16. <https://doi.org/10.1242/jcs.175521>
- King, M. R., & Petry, S. (2020). Phase separation of TPX2 enhances and spatially coordinates microtubule nucleation. *Nature Communications*, 11(270). <https://doi.org/10.1038/s41467-019-14087-0>
- Kirschner, M., & Mitchison, T. (1986). Beyond self-assembly: From microtubules to morphogenesis. *Cell*, 45(3), 329-342. [https://doi.org/10.1016/0092-8674\(86\)90318-1](https://doi.org/10.1016/0092-8674(86)90318-1)
- Kitamura, A., Oasa, S., Kawaguchi, H., Osaka, M., Vukojević, V., & Kinjo, M. (2023). Increased intracellular crowding during hyperosmotic stress. *Scientific Reports*, 13(1), 11834. <https://doi.org/10.1038/s41598-023-39090-w>
- Koleske, A. J. (2013). Molecular Mechanisms of Dendrite Stability. *Nature Reviews Neuroscience*, 14(8), 536-550. <https://doi.org/10.1038/nrn3486>
- Koleske, A. J., Gifford, A. M., Scott, M. L., Nee, M., Bronson, R. T., Miczek, K. A., & Baltimore, D. (1998). Essential Roles for the Abl and Arg Tyrosine Kinases in Neurulation. *Neuron*, 21(6), 1259-1272. [https://doi.org/10.1016/S0896-6273\(00\)80646-7](https://doi.org/10.1016/S0896-6273(00)80646-7)
- Konishi, H., Tanaka, M., Takemura, Y., Matsuzaki, H., Ono, Y., Kikkawa, U., & Nishizuka, Y. (1997). Activation of protein kinase C by tyrosine phosphorylation in

response;to;H₂O₂. *Proceedings of the National Academy of Sciences*, 94(21), 11233-11237. <https://doi.org/doi:10.1073/pnas.94.21.11233>

Kovar, D. R., Kuhn, J. R., Tichy, A. L., & Pollard, T. D. (2003). The fission yeast cytokinesis formin Cdc12p is a barbed end actin filament capping protein gated by profilin. *Journal of Cell Biology*, 161(5), 875-887. <https://doi.org/10.1083/jcb.200211078>

Kraus, J., Travis, S. M., King, M. R., & Petry, S. (2023). Augmin is a Ran-regulated spindle assembly factor. *Journal of Biological Chemistry*, 299(6). <https://doi.org/10.1016/j.jbc.2023.104736>

Kruh, G. D., Perego, R., Miki, T., & Aaronson, S. A. (1990). The complete coding sequence of arg defines the Abelson subfamily of cytoplasmic tyrosine kinases. *Proceedings of the National Academy of Sciences*, 87(15), 5802-5806. <https://doi.org/10.1073/pnas.87.15.5802>

Kuboyama, K., Fujikawa, A., Masumura, M., Suzuki, R., Matsumoto, M., & Noda, M. (2012). Protein Tyrosine Phosphatase Receptor Type Z Negatively Regulates Oligodendrocyte Differentiation and Myelination. *PLoS One*, 7(11), e48797. <https://doi.org/10.1371/journal.pone.0048797>

Kuchnir Fygenon, D., Flyvbjerg, H., Sneppen, K., Libchaber, A., & Leibler, S. (1995). Spontaneous nucleation of microtubules. *Physical Review E*, 51(5), 5058-5063. <https://doi.org/10.1103/PhysRevE.51.5058>

Kuo, Y., & Howard, J. (2021). Cutting, Amplifying, and Aligning Microtubules with Severing Enzymes. *Trends in Cell Biology*, 31(1), 50-61. <https://doi.org/10.1016/j.tcb.2020.10.004>

Kuo, Y.-W., Trottier, O., Mahamdeh, M., & Howard, J. (2019). Spastin is a dual-function enzyme that severs microtubules and promotes their regrowth to increase the number and mass of microtubules. *Proceedings of the National Academy of Sciences*, 116(12), 5533-5541. <https://doi.org/doi:10.1073/pnas.1818824116>

La Verde, V., Dominici, P., & Astegno, A. (2017). Determination of Hydrodynamic Radius of Proteins by Size Exclusion Chromatography. *Bio-Protocol*, 7(8). <https://doi.org/10.21769/BioProtoc.2230>

- LaFrance, B. J., Roostalu, J., Henkin, G., Greber, B. J., Zhang, R., Normanno, D., McCollum, C. O., Surrey, T., & Nogales, E. (2022). Structural transitions in the GTP cap visualized by cryo-electron microscopy of catalytically inactive microtubules. *Proceedings of the National Academy of Sciences*, *119*(2), e2114994119. <https://doi.org/10.1073/pnas.2114994119>
- Lansbergen, G., & Akhmanova, A. (2006). Microtubule Plus End: A Hub of Cellular Activities. *Traffic*, *7*(5), 499-507. <https://doi.org/10.1111/j.1600-0854.2006.00400.x>
- Lapetina, S., Mader, C. C., Machida, K., Mayer, B. J., & Koleske, A. J. (2009). Arg interacts with cortactin to promote adhesion-dependent cell edge protrusion. *Journal of Cell Biology*, *185*(3), 503-519. <https://doi.org/10.1083/jcb.200809085>
- Lasser, M., Tiber, J., & Lowery, L. A. (2018). The Role of the Microtubule Cytoskeleton in Neurodevelopmental Disorders. *Frontiers in Cellular Neuroscience*, *12*(165), 1-18. <https://doi.org/10.3389/fncel.2018.00165>
- Latremoliere, A., Cheng, L., DeLisle, M., Wu, C., Chew, S., Hutchinson, E. B., Sheridan, A., Alexandre, C., Latremoliere, F., Sheu, S. H., Golidy, S., Omura, T., Huebner, E. A., Fan, Y., Whitman, M. C., Nguyen, E., Hermawan, C., Pierpaoli, C., Tischfield, M. A., . . . Engle, E. C. (2018). Neuronal-Specific TUBB3 Is Not Required for Normal Neuronal Function but Is Essential for Timely Axon Regeneration. *Cell Rep*, *24*(7), 1865-1879.e1869. <https://doi.org/10.1016/j.celrep.2018.07.029>
- Lavrsen, K., Rajendraprasad, G., Leda, M., Eibes, S., Vitiello, E., Katopodis, V., Goryachev, A. B., & Barisic, M. (2023). Microtubule detyrosination drives symmetry breaking to polarize cells for directed cell migration. *Proceedings of the National Academy of Sciences*, *120*(22). <https://doi.org/10.1073/pnas.2300322120>
- Lawrence, E., Arpag, G., Norris, S. R., & Zanic, M. (2018). Human CLASP2 specifically regulates microtubule catastrophe and rescue. *Molecular Biology of the Cell*, *29*(10), 1168-1177. <https://doi.org/10.1091/mbc.E18-01-0016>
- Lawrence, E. J., Arpag, G., Arnaiz, C., & Zanic, M. (2021). SSNA1 stabilizes dynamic microtubules and detects microtubule damage. *eLife*, *10*, e67282. <https://doi.org/10.7554/eLife.67282>

- Lazarus, J. E., Moughamian, A. J., Tokito, M. K., & Holzbaur, E. L. F. (2013). Dynactin Subunit p150Glued Is a Neuron-Specific Anti-Catastrophe Factor. *PLOS Biology*, 11(7), e1001611. <https://doi.org/10.1371/journal.pbio.1001611>
- Lee, H., Engel, U., Rusch, J., Scherrer, S., Sheard, K., & Vactor, D. V. (2004). The Microtubule Plus End Tracking Protein Orbit/MAST/CLASP Acts Downstream of the Tyrosine Kinase Abl in Mediating Axon Guidance. *Neuron*, 42, 913-926. <https://doi.org/10.1016/j.neuron.2004.05.020>
- Lessard, D. V., Zinder, O. J., Hotta, T., Verhey, K. J., Ohi, R., & Berger, C. L. (2019). Polyglutamylation of tubulin's C-terminal tail controls pausing and motility of kinesin-3 family member KIF1A. *J Biol Chem*, 294(16), 6353-6363. <https://doi.org/10.1074/jbc.RA118.005765>
- Lewis, J. M., Baskaran, R., Taagepera, S., Schwartz, M. A., & Wang, J. Y. J. (1996). Integrin regulation of c-Abl tyrosine kinase activity and cytoplasmic-nuclear transport. *Proceedings of the National Academy of Sciences*, 93(26), 15174-15179. <https://doi.org/10.1073/pnas.93.26.15174>
- Li, B., & Dewey, C. N. (2011). RSEM: accurate transcript quantification from RNA-Seq data with or without a reference genome. *BMC Bioinformatics*, 12(323). <https://doi.org/10.1186/1471-2105-12-323>
- Liang, X., Kokes, M., Fetter, R. D., Sallee, M. D., Moore, A. W., Feldman, J. L., & Shen, K. (2020). Growth cone-localized microtubule organizing center establishes microtubule orientation in dendrites. *eLife*, 9, e56547. <https://doi.org/10.7554/eLife.56547>
- Lin, C. H., Tsai, P. I., Wu, R. M., & Chien, C. T. (2010). LRRK2 G2019S mutation induces dendrite degeneration through mislocalization and phosphorylation of tau by recruiting autoactivated GSK3 β . *J Neurosci*, 30(39), 13138-13149. <https://doi.org/10.1523/jneurosci.1737-10.2010>
- Lin, Y., Currie, S. L., & Rosen, M. K. (2017). Intrinsically disordered sequences enable modulation of protein phase separation through distributed tyrosine motifs. *Journal of Biological Chemistry*, 292(46), 19110-19120. <https://doi.org/10.1074/jbc.M117.800466>
- Lin, Y. C., Yeckel, M. F., & Koleske, A. J. (2013). Abl2/Arg Controls Dendritic Spine and Dendrite Arbor Stability via Distinct Cytoskeletal Control Pathways. *The Journal of Neuroscience*, 33(5), 1846-1857. <https://doi.org/10.1523/JNEUROSCI.4284-12.2013>

Lipka, J., Kapitein, L. C., Jaworski, J., & Hoogenraad, C. C. (2016). Microtubule-binding protein doublecortin-like kinase 1 (DCLK1) guides kinesin-3-mediated cargo transport to dendrites. *The EMBO Journal*, 35(3), 302-318. <https://doi.org/https://doi.org/10.15252/embj.201592929>

Liu, H., & Shima, T. (2023). Preference of CAMSAP3 for expanded microtubule lattice contributes to stabilization of the minus end. *Life Science Alliance*, 6(5). <https://doi.org/10.26508/lsa.202201714>

Lois, C., Hong, E. J., Pease, S., Brown, E. J., & Baltimore, D. (2002). Germline Transmission and Tissue-Specific Expression of Transgenes Delivered by Lentiviral Vectors. *Science*, 295(5556), 868-872. <https://doi.org/10.1126/science.1067081>

Longfield, S. F., Mollazade, M., & Wallis, T. P. (2023). Tau forms synaptic nano-biomolecular condensates controlling the dynamic clustering of recycling synaptic vesicles. *Nature Communications*, 14. <https://doi.org/10.1038/s41467-023-43130-4>

Lonsdale, J., Thomas, J., Salvatore, M., & al., e. (2013). The Genotype-Tissue Expression (GTEx) project. *Nature Genetics*, 45, 580-585. <https://doi.org/10.1038/ng.2653>

López-Palacios, T. P., & Andersen, J. L. (2023). Kinase regulation by liquid-liquid phase separation. *Trends in Cell Biology*, 33(8), 649-666. <https://doi.org/10.1016/j.tcb.2022.11.009>

Lowery, L. A., Lee, H., Lu, C., Murphy, R., Obar, R. A., Zhai, B., Schedl, M., Van Vactor, D., & Zhan, Y. (2010). Parallel Genetic and Proteomic Screens Identify Msps as a CLASP–Abl Pathway Interactor in Drosophila. *Genetics*, 185(4). <https://doi.org/10.1534/genetics.110.115626>

Luo, Y., Xiang, S., Hooikaas, P. J., van Bezouwen, L., Jijumon, A. S., Janke, C., Förster, F., Akhmanova, A., & Baldus, M. (2020). Direct observation of dynamic protein interactions involving human microtubules using solid-state NMR spectroscopy. *Nature Communications*, 11(18). <https://doi.org/10.1038/s41467-019-13876-x>

Luttman, J. H., Coleman, A., Mayro, B., & Pendergast, A. M. (2021). Role of the ABL tyrosine kinases in the epithelial–mesenchymal transition and the metastatic cascade. *Cell Communication and Signaling*, 19(59). <https://doi.org/10.1186/s12964-021-00739-6>

Lynch, Eric M., Grocock, Lynda M., Borek, Weronika E., & Sawin, Kenneth E. (2014). Activation of the γ -Tubulin Complex by the Mto1/2 Complex. *Current Biology*, 24(8), 896-903.

<https://doi.org/https://doi.org/10.1016/j.cub.2014.03.006>

Maan, R., Reese, L., Volkov, V. A., King, M. R., van der Sluis, E. O., Andrea, N., Evers, W. H., Jakobi, A. J., & Dogterom, M. (2022). Multivalent interactions facilitate motor-dependent protein accumulation at growing microtubule plus-ends. *Nature Cell Biology*, 25, 68-78.

<https://doi.org/10.1038/s41556-022-01035-2>

MacGrath, S. M., & Koleske, A. J. (2012). Arg/Abl2 Modulates the Affinity and Stoichiometry of Binding of Cortactin to F-Actin. *Biochemistry*, 51(33), 6644-6653.

<https://doi.org/10.1021/bi300722t>

Madeira, F., Pearce, M., Tivey, A. R. N., Basutkar, P., Lee, J., Edbali, O., Madhusoodanan, N., Kolesnikov, A., & Lopez, R. (2022). Search and sequence analysis tools services from EMBL-EBI in 2022. *Nucleic Acids Research*, 50(W1), W276-W279. <https://doi.org/10.1093/nar/gkac240>

Mader, C. C., Oser, M., Magalhaes, M. A. O., Bravo-Cordero, J. J., Condeelis, J., Koleske, A. J., & Gil-Henn, H. (2011). An EGFR-Src-Arg-Cortactin Pathway Mediates Functional Maturation of Invadopodia and Breast Cancer Cell Invasion. *Cancer Research*, 71(5), 1730-1741.

<https://doi.org/10.1158/0008-5472.CAN-10-1432>

Magiera, M. M., Singh, P., Gadadhar, S., & Janke, C. (2018). Tubulin Posttranslational Modifications and Emerging Links to Human Disease. *Cell*, 173(6), 1323-1327.

<https://doi.org/10.1016/j.cell.2018.05.018>

Majumdar, S., Kim, T., Chen, Z., Munyoki, S., Tso, S., Brautigam, C. A., & Rice, L. M. (2018). An isolated CLASP TOG domain suppresses microtubule catastrophe and promotes rescue.

Molecular Biology of the Cell, 29, 1359-1375. <https://doi.org/10.1091/mbc.E17-12-0748>

Manka, S. W., & Moores, C. A. (2018). The role of tubulin–tubulin lattice contacts in the mechanism of microtubule dynamic instability. *Nature Structural & Molecular Biology*, 25, 607-

615. <https://doi.org/10.1038/s41594-018-0087-8>

Marín, T., Dulcey, A. E., Campos, F., de la Fuente, C., Acuña, M., Castro, J., Pinto, C., Yañez, M. J., Cortez, C., McGrath, D. W., Sáez, P. J., Gorshkov, K., Zheng, W., Southall, N., Carmo-

Fonseca, M., Marugán, J., Alvarez, A. R., & Zanlungo, S. (2022). c-Abl Activation Linked to Autophagy-Lysosomal Dysfunction Contributes to Neurological Impairment in Niemann-Pick Type A Disease [Original Research]. *Frontiers in Cell and Developmental Biology*, 10.

<https://doi.org/10.3389/fcell.2022.844297>

Maurer, S. P., Bieling, P., Cope, J., Hoenger, A., & Surrey, T. (2011). GTPγS microtubules mimic the growing microtubule end structure recognized by end-binding proteins (EBs). *Proceedings of the National Academy of Sciences*, 108(10), 3988-3993.

<https://doi.org/10.1073/pnas.1014758108>

Maurer, S. P., Cade, N. I., Bohner, G., Gustafsson, N., Boutant, E., & Surrey, T. (2014). EB1 Accelerates Two Conformational Transitions Important for Microtubule Maturation and Dynamics. *Current Biology*, 24(4), 372-384. <https://doi.org/10.1016/j.cub.2013.12.042>

McDonald, N. A., Fetter, R. D., & Shen, K. (2020). Assembly of synaptic active zones requires phase separation of scaffold molecules. *Nature*, 588(7838), 454-458.

<https://doi.org/10.1038/s41586-020-2942-0>

McIntosh, J. R., O'Toole, E., Morgan, G., Austin, J., Ulyanov, E., Ataullakhanov, F., & Gudimchuk, N. (2018). Microtubules grow by the addition of bent guanosine triphosphate tubulin to the tips of curved protofilaments. *Journal of Cell Biology*, 217(8), 2691-2708.

<https://doi.org/10.1083/jcb.201802138>

McKenney, R. J., Huynh, W., Vale, R. D., & Sirajuddin, M. (2016). Tyrosination of α -tubulin controls the initiation of processive dynein-dynactin motility. *Embo j*, 35(11), 1175-1185.

<https://doi.org/10.15252/emj.201593071>

McVicker, D. P., Awe, A. M., Richters, K. E., Wilson, R. L., Cowdrey, D. A., Hu, X., Chapman, E. R., & Dent, E. W. (2016). Transport of a kinesin-cargo pair along microtubules into dendritic spines undergoing synaptic plasticity. *Nature Communications*, 7(1), 12741.

<https://doi.org/10.1038/ncomms12741>

McVicker, D. P., Hoepflich, G. J., Thompson, A. R., & Berger, C. L. (2014). Tau Interconverts Between Diffusive and Stable Populations on the Microtubule Surface in an Isoform and Lattice Specific Manner. *Cytoskeleton*, 71(3), 184-194. <https://doi.org/10.1002/cm.21163>

McWhirter, J. R., & Wang, J. Y. (1993). An actin-binding function contributes to transformation by the Bcr-Abl oncoprotein of Philadelphia chromosome-positive human leukemias. *Embo j*, 12(4), 1533-1546. <https://doi.org/10.1002/j.1460-2075.1993.tb05797.x>

Mehidi, A., & Aumeier, C. (2023). Regulation of the microtubule network; the shaft matters! *Current Opinion in Systems Biology*, 34, 100457. <https://doi.org/https://doi.org/10.1016/j.coisb.2023.100457>

Meier, S. M., Farcas, A., Kumar, A., Ijavi, M., Bill, R. T., Stelling, J., Dufresne, E. R., Steinmetz, M. O., & Barral, Y. (2022). Multivalency ensures persistence of a +TIP body at specialized microtubule ends. *Nature Cell Biology*, 25, 56-67. <https://doi.org/10.1038/s41556-022-01035-2>

Melková, K., Zapletal, V., Jansen, S., Nomilner, E., Zachrdla, M., Hritz, J., Nováček, J., Zweckstetter, M., Jensen, M. R., Blackledge, M., & Žídek, L. (2018). Functionally specific binding regions of microtubule-associated protein 2c exhibit distinct conformations and dynamics. *Journal of Biological Chemistry*, 293(34), 13297-13309. <https://doi.org/https://doi.org/10.1074/jbc.RA118.001769>

Merkley, E. D., Rysavy, S., Kahraman, A., Hafen, R. P., Daggett, V., & Adkins, J. N. (2014). Distance restraints from crosslinking mass spectrometry: mining a molecular dynamics simulation database to evaluate lysine-lysine distances. *Protein Sci*, 23(6), 747-759. <https://doi.org/10.1002/pro.2458>

Metzger, F., & Kapfhammer, J. P. (2000). Protein kinase C activity modulates dendritic differentiation of rat Purkinje cells in cerebellar slice cultures. *Eur J Neurosci*, 12(6), 1993-2005. <https://doi.org/10.1046/j.1460-9568.2000.00086.x>

Miao, Y., & Wang, J. Y. J. (1996). Binding of A/T-rich DNA by Three High Mobility Group-like Domains in c-Abl Tyrosine Kinase*. *The Journal of Biological Chemistry*, 271(37), 22823–22830. <https://doi.org/10.1074/jbc.271.37.22823>

Michaelsen-Preusse, K., Zessin, S., Grigoryan, G., Scharkowski, F., Feuge, J., Remus, A., & Korte, M. (2016). Neuronal profilins in health and disease: Relevance for spine plasticity and Fragile X syndrome. *Proceedings of the National Academy of Sciences*, 113(12), 3365-3370. <https://doi.org/doi:10.1073/pnas.1516697113>

- Miesch, J., Wimbish, R. T., Velluz, M., & Aumeier, C. (2023). Phase separation of +TIP-networks regulates microtubule dynamics. *Proceedings of the National Academy of Sciences*, 120(35).
<https://doi.org/10.1073/pnas.2301457120>
- Miller, A. L. M., Wang, Y., Mooseker, M. S., & Koleske, A. J. (2004). The Abl-related gene (Arg) requires its F-actin microtubule cross-linking activity to regulate lamellipodial dynamics during fibroblast adhesion. *Journal of Cell Biology*, 165(3), 407-420.
<https://doi.org/10.1083/jcb.200308055>
- Miller, K. E., DeProto, J., Kaufmann, N., Patel, B. N., Duckworth, A., & Van Vactor, D. (2005). Direct observation demonstrates that Liprin-alpha is required for trafficking of synaptic vesicles. *Curr Biol*, 15(7), 684-689. <https://doi.org/10.1016/j.cub.2005.02.061>
- Miller, M. M., Lapetina, S., MacGrath, S. M., Sfakianos, M. K., Pollard, T. D., & Koleske, A. J. (2010). Regulation of Actin Polymerization and Adhesion-Dependent Cell Edge Protrusion by the Abl-Related Gene (Arg) Tyrosine Kinase and N-WASp. *Biochemistry*, 49(10), 2227-2234.
<https://doi.org/10.1021/bi901721u>
- Min, S., Lim, Y. S., Shin, D., Park, C., Park, J. B., Kim, S., Windisch, M. P., & Hwang, S. B. (2017). Abl Tyrosine Kinase Regulates Hepatitis C Virus Entry. *Front Microbiol*, 8, 1129.
<https://doi.org/10.3389/fmicb.2017.01129>
- Mitchison, T., & Kirschner, M. (1984). Dynamic instability of microtubule growth. *Nature*, 312(15), 237-242. <https://doi.org/10.1038/312237a0>
- Mitra, A., & Sept, D. (2008). Taxol allosterically alters the dynamics of the tubulin dimer and increases the flexibility of microtubules. *Biophys J*, 95(7), 3252-3258.
<https://doi.org/10.1529/biophysj.108.133884>
- Mitra, S. K., Hanson, D. A., & Schlaepfer, D. D. (2005). Focal adhesion kinase: in command and control of cell motility. *Nature Reviews Molecular Cell Biology*, 6(1), 56-68.
<https://doi.org/10.1038/nrm1549>
- Miyamoto, D., Takeuchi, K., Chihara, K., Fujieda, S., & Sada, K. (2022). Protein tyrosine kinase Abl promotes hepatitis C virus particle assembly via interaction with viral substrate activator NS5A. *J Biol Chem*, 298(4), 101804. <https://doi.org/10.1016/j.jbc.2022.101804>

Monroy, B. Y., Sawyer, D. L., Ackermann, B. E., Borden, M. M., Tan, T. C., & Ori-McKenney, K. M. (2018). Competition between microtubule-associated proteins directs motor transport. *Nature Communications*, 9(1), 1487. <https://doi.org/10.1038/s41467-018-03909-2>

Moresco, E. M. Y., Donaldson, S., Williamson, A., & Koleske, A. J. (2005). Integrin-Mediated Dendrite Branch Maintenance Requires Abelson (Abl) Family Kinases. *The Journal of Neuroscience*, 25(26), 6105-6118. <https://doi.org/10.1523/JNEUROSCI.1432-05.2005>

Moresco, E. M. Y., & Koleske, A. J. (2003). Regulation of Neuronal Morphogenesis and Synaptic Function by Abl Family Kinases. *Current Opinion in Neurobiology*, 13(5), 535-544. <https://doi.org/10.1016/j.conb.2003.08.002>

Moresco, E. M. Y., Scheetz, A. J., Bornmann, W. G., Koleske, A. J., & Fitzsimonds, R. M. (2003). Abl Family Nonreceptor Tyrosine Kinases Modulate Short-Term Synaptic Plasticity. *Journal of Neurophysiology*, 89(3), 1678-1687. <https://doi.org/10.1152/jn.00892.2002>

Morfini, G., Szebenyi, G., Brown, H., Pant, H. C., Pigino, G., DeBoer, S., Beffert, U., & Brady, S. T. (2004). A novel CDK5-dependent pathway for regulating GSK3 activity and kinesin-driven motility in neurons. *Embo j*, 23(11), 2235-2245. <https://doi.org/10.1038/sj.emboj.7600237>

Morley, S. J., Qi, Y., Iovino, L., Andolfi, L., Guo, D., Kalebic, N., Castaldi, L., Tischer, C., Portulano, C., Bolasco, G., Shirlekar, K., Fusco, C. M., Asaro, A., Fermani, F., Sundukova, M., Matti, U., Reymond, L., De Ninno, A., Businaro, L., . . . Heppenstall, P. A. (2016). Acetylated tubulin is essential for touch sensation in mice. *eLife*, 5, e20813. <https://doi.org/10.7554/eLife.20813>

Mukherjee, A., Brooks, P. S., Bernard, F., Guichet, A., & Conduit, P. T. (2020). Microtubules originate asymmetrically at the somatic golgi and are guided via Kinesin2 to maintain polarity within neurons. *eLife*, 9, e58943. <https://doi.org/10.7554/eLife.58943>

Mullins, R. D., Kelleher, J. F., Xu, J., & Pollard, T. D. (1998). Arp2/3 complex from *Acanthamoeba* binds profilin and cross-links actin filaments. *Mol Biol Cell*, 9(4), 841-852. <https://doi.org/10.1091/mbc.9.4.841>

Musacchio, A. (2022). On the role of phase separation in the biogenesis of membraneless compartments. *The EMBO Journal*, 41, e109952. <https://doi.org/10.15252/emj.2021109952>

Nagar, B., Hantschel, O., Young, M. A., Scheffzek, K., Veach, D., Bornmann, W., Clarkson, B., Superti-Furga, G., & Kuriyan, J. (2003). Structural Basis for the Autoinhibition of c-Abl Tyrosine Kinase. *Cell*, 112(6), 859-871. [https://doi.org/10.1016/S0092-8674\(03\)00194-6](https://doi.org/10.1016/S0092-8674(03)00194-6)

Naisbitt, S., Valtchanoff, J., Allison, D. W., Sala, C., Kim, E., Craig, A. M., Weinberg, R. J., & Sheng, M. (2000). Interaction of the postsynaptic density-95/guanylate kinase domain-associated protein complex with a light chain of myosin-V and dynein. *J Neurosci*, 20(12), 4524-4534. <https://doi.org/10.1523/jneurosci.20-12-04524.2000>

Neuhoff, H., Sassoè-Pognetto, M., Panzanelli, P., Maas, C., Witke, W., & Kneussel, M. (2005). The actin-binding protein profilin I is localized at synaptic sites in an activity-regulated manner. *European Journal of Neuroscience*, 21(1), 15-25. <https://doi.org/https://doi.org/10.1111/j.1460-9568.2004.03814.x>

Nguyen, M. M., McCracken, C. J., Milner, E. S., Goetschius, D. J., Weiner, A. T., Long, M. K., Michael, N. L., Munro, S., & Rolls, M. M. (2014). Γ -tubulin controls neuronal microtubule polarity independently of Golgi outposts. *Mol Biol Cell*, 25(13), 2039-2050. <https://doi.org/10.1091/mbc.E13-09-0515>

Nogales, E. (2000). Structural Insights Into Microtubule Function. *Annual Review of Biochemistry*, 69, 277-302. <https://doi.org/10.1146/annurev.biochem.69.1.277>

Nye, D. M. R., Albertson, R. M., Weiner, A. T., Hertzler, J. I., Shorey, M., Goberdhan, D. C. I., Wilson, C., Janes, K. A., & Rolls, M. M. (2020). The receptor tyrosine kinase Ror is required for dendrite regeneration in *Drosophila* neurons. *PLOS Biology*, 18(3), e3000657. <https://doi.org/10.1371/journal.pbio.3000657>

O'Brien, E. T., Voter, W. A., & Erickson, H. P. (1987). GTP Hydrolysis during Microtubule Assembly. *Biochemistry*, 26, 4148-4156. <https://doi.org/10.1021/bi00387a061>

O'Neill, A. J., Cotter, T. G., Russell, J. M., & Gaffney, E. F. (1997). Abl expression in human fetal and adult tissues, tumours, and tumour microvessels. *The Journal of Pathology*, 183(3), 325-329. [https://doi.org/10.1002/\(SICI\)1096-9896\(199711\)183:3<325::AID-PATH941>3.0.CO;2-A](https://doi.org/10.1002/(SICI)1096-9896(199711)183:3<325::AID-PATH941>3.0.CO;2-A)

Odde, D. J., Cassimeris, L., & Buettner, H. M. (1995). Kinetics of microtubule catastrophe assessed by probabilistic analysis. *Biophysical Journal*, 69(3), 796-802.

[https://doi.org/10.1016/S0006-3495\(95\)79953-2](https://doi.org/10.1016/S0006-3495(95)79953-2)

Ogami, T., Tamura, Y., Toss, K., Yuki, K., Morikawa, M., Tsutsumi, S., Aburatani, H., Miyazawa, K., Miyazono, K., & Koinuma, D. (2022). MAB21L4 regulates the TGF- β -induced expression of target genes in epidermal keratinocytes. *J Biochem*, 171(4), 399-410.

<https://doi.org/10.1093/jb/mvab141>

Ori-McKenney, K. M., Jan, L. Y., & Jan, Y. N. (2012). Golgi outposts shape dendrite morphology by functioning as sites of acentrosomal microtubule nucleation in neurons. *Neuron*, 76(5), 921-930. <https://doi.org/10.1016/j.neuron.2012.10.008>

Pan, X., Cao, Y., Stucchi, R., Hooikaas, P. J., Portegies, S., Will, L., Martin, M., Akhmanova, A., Harterink, M., & Hoogenraad, C. C. (2019). MAP7D2 Localizes to the Proximal Axon and Locally Promotes Kinesin-1-Mediated Cargo Transport into the Axon. *Cell Reports*, 26(8), 1988-1999.e1986. <https://doi.org/https://doi.org/10.1016/j.celrep.2019.01.084>

Pascua-Maestro, R., Corraliza-Gomez, M., Fadrique-Rojo, C., Ledesma, M. D., Schuchman, E. H., Sanchez, D., & Ganfornina, M. D. (2020). Apolipoprotein D-mediated preservation of lysosomal function promotes cell survival and delays motor impairment in Niemann-Pick type A disease. *Neurobiology of Disease*, 144, 105046.

<https://doi.org/https://doi.org/10.1016/j.nbd.2020.105046>

Payen, E., Verkerk, T., Michalovich, D., Dreyer, S. D., Winterpacht, A., Lee, B., De Zeeuw, C. I., Grosveld, F., & Galjart, N. (1998). The Centromeric/Nucleolar Chromatin Protein ZFP-37 May Function to Specify Neuronal Nuclear Domains*. *Journal of Biological Chemistry*, 273(15), 9099-9109. <https://doi.org/https://doi.org/10.1074/jbc.273.15.9099>

Peacock, J. C., Miller, A. L., Bradley, W. D., Rodriguez, O. C., Webb, D. J., & Koleske, A. J. (2007). The Abl-related Gene Tyrosine Kinase Acts Through p190RhoGAP to Inhibit Actomyosin Contractility and Regulate Focal Adhesion Dynamics Upon Adhesion to Fibronectin. *Molecular Biology of the Cell*, 18(10), 2860-2872. <https://doi.org/10.1091/mbc.e07-01-0075>

Peacock, J. G., Couch, B. A., & Koleske, A. J. (2010). The Abl and Arg non-receptor tyrosine kinases regulate different zones of stress fiber, focal adhesion, and contractile network localization in spreading fibroblasts. *Cytoskeleton*, 67(10), 666-675.

<https://doi.org/https://doi.org/10.1002/cm.20479>

Pear, W. S., Nolan, G. P., Scott, M. L., & Baltimore, D. (1993). Production of high-titer helper-free retroviruses by transient transfection. *Proceedings of the National Academy of Sciences*, 90(18), 8392-8396. <https://doi.org/10.1073/pnas.90.18.8392>

Peloquin, J., Komarova, Y., & Borisy, G. (2005). Conjugation of fluorophores to tubulin. *Nature Methods*, 2(4), 299-303. <https://doi.org/10.1038/nmeth0405-299>

Pendergast, A. M. (2002). The Abl family kinases: mechanisms of regulation and signaling. *Advances in Cancer Research*, 85, 51-53, 53a-55a, 54-100. [https://doi.org/10.1016/S0065-230X\(02\)85003-5](https://doi.org/10.1016/S0065-230X(02)85003-5)

Petry, S., Groen, Aaron C., Ishihara, K., Mitchison, Timothy J., & Vale, Ronald D. (2013). Branching Microtubule Nucleation in Xenopus Egg Extracts Mediated by Augmin and TPX2. *Cell*, 152(4), 768-777. <https://doi.org/https://doi.org/10.1016/j.cell.2012.12.044>

Plattner, R., Kadlec, L., DeMali, K. A., Kazlauskas, A., & Pendergast, A. M. (1999). c-Abl is activated by growth factors and Src family kinases and has a role in the cellular responses to PDGF. *Genes & Development*, 13(18), 2400-2411. <https://doi.org/10.1101/gad.13.18.2400>

Plattner, R., Koleske, A. J., Kazlauskas, A., & Pendergast, A. M. (2004). Bidirectional Signaling Links the Abelson Kinases to the Platelet-Derived Growth Factor Receptor. *Molecular and Cellular Biology*, 24(6). <https://doi.org/10.1128/MCB.24.6.2573-2583.2004>

Pluk, H., Dorey, K., & Superti-Furga, G. (2001). Autoinhibition of c-Abl. *Cell*, 108(2), 247-259. [https://doi.org/10.1016/S0092-8674\(02\)00623-2](https://doi.org/10.1016/S0092-8674(02)00623-2)

Pollard, T. D. (2010). A Guide to Simple and Informative Binding Assays. *Molecular Biology of the Cell*, 21(23), 4061-4067. <https://doi.org/10.1091/mbc.e10-08-0683>

Pollard, T. D., & Borisy, G. G. (2003). Cellular motility driven by assembly and disassembly of actin filaments. *Cell*, 112(4), 453-465. [https://doi.org/10.1016/s0092-8674\(03\)00120-x](https://doi.org/10.1016/s0092-8674(03)00120-x)

Pollard, T. D., & Cooper, J. A. (1984). Quantitative analysis of the effect of Acanthamoeba profilin on actin filament nucleation and elongation. *Biochemistry*, 23(26), 6631-6641.

<https://doi.org/10.1021/bi00321a054>

Pongrakhananon, V., Saito, H., Hiver, S., Abe, T., Shioi, G., Meng, W., & Takeichi, M. (2018).

CAMSAP3 maintains neuronal polarity through regulation of microtubule stability. *Proc Natl Acad Sci U S A*, 115(39), 9750-9755. <https://doi.org/10.1073/pnas.1803875115>

Portran, D., Schaedel, L., Xu, Z., Théry, M., & Nachury, M. V. (2017). Tubulin acetylation protects long-lived microtubules against mechanical ageing. *Nat Cell Biol*, 19(4), 391-398.

<https://doi.org/10.1038/ncb3481>

Prota, A. E., Lucena-Agell, D., Ma, Y., Estevez-Gallego, J., Li, S., Bargsten, K., Josa-Prado, F., Altmann, K.-H., Gaillard, N., Kamimura, S., Mühlethaler, T., Gago, F., Oliva, M. A., Steinmetz, M. O., Fang, W.-S., & Díaz, J. F. (2023). Structural insight into the stabilization of microtubules by taxanes. *eLife*, 12, e84791. <https://doi.org/10.7554/eLife.84791>

Provencher, S. W., & Glöckner, J. (1981). Estimation of Globular Protein Secondary Structure from Circular Dichroism. *Biochemistry*, 20(1), 33-37. <https://doi.org/10.1021/bi00504a006>

Punjani, A., Rubinstein, J. L., Fleet, D. J., & Brubaker, M. A. (2017). cryoSPARC: algorithms for rapid unsupervised cryo-EM structure determination. *Nat Methods*, 14(3), 290-296.

<https://doi.org/10.1038/nmeth.4169>

Qu, X., Kumar, A., Blockus, H., Waites, C., & Bartolini, F. (2019). Activity-Dependent Nucleation of Dynamic Microtubules at Presynaptic Boutons Controls Neurotransmission. *Curr Biol*, 29(24), 4231-4240.e4235. <https://doi.org/10.1016/j.cub.2019.10.049>

Reid, T. A., Coombes, C., & Gardner, M. K. (2017). Manipulation and quantification of microtubule lattice integrity. *Biology Open*, 6, 1245-1256. <https://doi.org/10.1242/bio.025320>

Reid, T. A., Coombes, C., Mukherjee, S., Goldblum, R. R., White, K., Parmar, S., McClellan, M., Zanic, M., Courtemanche, N., & Gardner, M. K. (2019). Structural state recognition facilitates tip tracking of EB1 at growing microtubule ends. *eLife*, 8, e48117. <https://doi.org/10.7554/eLife.48117>

Rice, L. M., Moritz, M., & Agard, D. A. (2021). Microtubules form by progressively faster tubulin accretion, not by nucleation-elongation. *Journal of Cell Biology*, 220(5), e202012079.

<https://doi.org/10.1083/jcb.202012079>

Rickman, J., Duellberg, C., & Cade, N. I. (2017). Steady-state EB cap size fluctuations are determined by stochastic microtubule growth and maturation. *Proceedings of the National Academy of Sciences*, 114(13), 3427-3432. <https://doi.org/10.1073/pnas.1620274114>

Robison, P., Caporizzo, M. A., Ahmadzadeh, H., Bogush, A. I., Chen, C. Y., Margulies, K. B., Shenoy, V. B., & Prosser, B. L. (2016). Detyrosinated microtubules buckle and bear load in contracting cardiomyocytes. *Science*, 352(6284), aaf0659.

<https://doi.org/doi:10.1126/science.aaf0659>

Rodríguez-Martín, T., Cuchillo-Ibáñez, I., Noble, W., Nyenya, F., Anderton, B. H., & Hanger, D. P. (2013). Tau phosphorylation affects its axonal transport and degradation. *Neurobiol Aging*, 34(9), 2146-2157. <https://doi.org/10.1016/j.neurobiolaging.2013.03.015>

Roger, B., Al-Bassam, J., Dehmelt, L., Milligan, R. A., & Halpain, S. (2004). MAP2c, but Not Tau, Binds and Bundles F-Actin via Its Microtubule Binding Domain. *Current Biology*, 14(5), 363-371. <https://doi.org/10.1016/j.cub.2004.01.058>

Rogers, E. M., Allred, S. C., & Peifer, M. (2021). Abelson kinase's intrinsically disordered region plays essential roles in protein function and protein stability. *Cell Communication and Signaling*, 19(1), 27. <https://doi.org/10.1186/s12964-020-00703-w>

Rogers, E. M., Spracklen, A. J., Bilancia, C. G., Sumigray, K. D., Allred, S. C., Nowotarski, S. H., Schaefer, K. N., Ritchie, B. J., & Peifer, M. (2016). Abelson kinase acts as a robust, multifunctional scaffold in regulating embryonic morphogenesis. *Molecular Biology of the Cell*, 27(16), 2613-2631. <https://doi.org/10.1091/mbc.E16-05-0292>

Roll-Mecak, A. (2020). The Tubulin Code in Microtubule Dynamics and Information Encoding. *Dev Cell*, 54(1), 7-20. <https://doi.org/10.1016/j.devcel.2020.06.008>

Roll-Mecak, A., & Vale, R. D. (2006). Making more microtubules by severing: a common theme of noncentrosomal microtubule arrays? *J Cell Biol*, 175(6), 849-851.

<https://doi.org/10.1083/jcb.200611149>

Roostalu, J., & Surrey, T. (2017). Microtubule nucleation: beyond the template. *Nature Reviews Molecular Cell Biology*, 18(11), 702-710. <https://doi.org/10.1038/nrm.2017.75>

Roostalu, J., Thomas, C., Cade, N. I., Kunzelmann, S., Taylor, I. A., & Surrey, T. (2020). The speed of GTP hydrolysis determines GTP cap size controls microtubule stability. *eLife*, 9, e51992. <https://doi.org/10.7554/eLife.51992>

Rostas, J. A. P., & Skelding, K. A. (2023). Calcium/Calmodulin-Stimulated Protein Kinase II (CaMKII): Different Functional Outcomes from Activation, Depending on the Cellular Microenvironment. *Cells*, 12(3), 401. <https://www.mdpi.com/2073-4409/12/3/401>

Rothe, F., Schmidt, W., & Wolf, G. (1983). Postnatal changes in the activity of glutamate dehydrogenase and aspartate aminotransferase in the rat nervous system with special reference to the glutamate transmitter metabolism. *Brain Res*, 313(1), 67-74. [https://doi.org/10.1016/0165-3806\(83\)90202-x](https://doi.org/10.1016/0165-3806(83)90202-x)

Safari, M. S., King, M. R., Brangwynne, C. P., & Petry, S. (2021). Interaction of spindle assembly factor TPX2 with importins- α/β inhibits protein phase separation. *Journal of Biological Chemistry*, 297(3), 100998. <https://doi.org/10.1016/j.jbc.2021.100998>

Sánchez-Huertas, C., Freixo, F., Viais, R., Lacasa, C., Soriano, E., & Lüders, J. (2016). Non-centrosomal nucleation mediated by augmin organizes microtubules in post-mitotic neurons and controls axonal microtubule polarity. *Nature Communications*, 7(1), 12187. <https://doi.org/10.1038/ncomms12187>

Sanz Murillo, M., Villagran Suarez, A., Dederer, V., Chatterjee, D., Alegrio Louro, J., Knapp, S., Mathea, S., & Leschziner, A. E. (2023). Inhibition of Parkinson's disease-related LRRK2 by type I and type II kinase inhibitors: Activity and structures. *Science Advances*, 9(48), eadk6191. <https://doi.org/doi:10.1126/sciadv.adk6191>

Schaedel, L., John, K., Gaillard, J., Nachury, M. V., Blanchoin, L., & Théry, M. (2015). Microtubules self-repair in response to mechanical stress. *Nature Materials*, 14(11), 1156-1163. <https://doi.org/10.1038/nmat4396>

Schaedel, L., Triclin, S., Chrétien, D., Abrieu, A., Aumeier, C., Gaillard, J., Blanchoin, L., Théry, M., & John, K. (2019). Lattice defects induce microtubule self-renewal. *Nature Physics*, *15*(8), 830-838. <https://doi.org/10.1038/s41567-019-0542-4>

Schaefer, A. W., Kabir, N., & Forscher, P. (2002). Filopodia and actin arcs guide the assembly and transport of two populations of microtubules with unique dynamic parameters in neuronal growth cones. *Journal of Cell Biology*, *158*(1), 139-152. <https://doi.org/10.1083/jcb.200203038>

Schätzle, P., da Silva, M. E., Tas, R. P., Katrukha, E. A., Hu, H. Y., Wierenga, C. J., Kapitein, L. C., & Hoogenraad, C. C. (2018). Activity-Dependent Actin Remodeling at the Base of Dendritic Spines Promotes Microtubule Entry. *Current Biology*, *13*(13), 2081-2093.e2086. <https://doi.org/10.1016/j.cub.2018.05.004>

Schaum, N., Karkanas, J., Neff, N. F., May, A. P., Quake, S. R., Wyss-Coray, T., Darmanis, S., Batson, J., Botvinnik, O., Chen, M. B., Chen, S., Green, F., Jones, R. C., Maynard, A., Penland, L., Pisco, A. O., Sit, R. V., Stanley, G. M., Webber, J. T., . . . Wyss-Coray, T. (2018). Single-cell transcriptomics of 20 mouse organs creates a Tabula Muris. *Nature*, *562*(7727), 367-372. <https://doi.org/10.1038/s41586-018-0590-4>

Schindelin, J., Arganda-Carreras, I., Frise, E., Kaynig, V., Longair, M., Pietzsch, T., Preibisch, S., Rueden, C., Saalfeld, S., Schmid, B., Tinevez, J.-Y., White, D. J., Hartenstein, V., Eliceiri, K., Tomancak, P., & Cardona, A. (2012). Fiji: an open-source platform for biological-image analysis. *Nature Methods*, *9*(7), 676-682. <https://doi.org/10.1038/nmeth.2019>

Schorb, M., Haberbosch, I., Hagen, W. J. H., Schwab, Y., & Mastrorarde, D. N. (2019). Software tools for automated transmission electron microscopy. *Nature Methods*, *16*, 471-477. <https://doi.org/10.1038/s41592-019-0396-9>

Sears, R. M., May, D. G., & Roux, K. J. (2019). BioID as a Tool for Protein-Proximity Labeling in Living Cells. In T. Nuijens & M. Schmidt (Eds.), *Enzyme-Mediated Ligation Methods* (pp. 299-313). Springer New York. https://doi.org/10.1007/978-1-4939-9546-2_15

Seetapun, D., Castle, Brian T., McIntyre, Alistair J., Tran, Phong T., & Odde, David J. (2012). Estimating the Microtubule GTP Cap Size In Vivo. *Current Biology*, *22*(18), 1681-1687. <https://doi.org/https://doi.org/10.1016/j.cub.2012.06.068>

Sfakianos, M. K., Eisman, A., Gourley, S. L., Bradley, W. D., Scheetz, A. J., Settleman, J., Taylor, J. R., Greer, C. A., Williamson, A., & Koleske, A. J. (2007). Inhibition of Rho via Arg and p190RhoGAP in the Postnatal Mouse Hippocampus Regulates Dendritic Spine Maturation, Synapse and Dendrite Stability, and Behavior. *The Journal of Neuroscience*, 27(41), 10982-10992. <https://doi.org/10.1523/JNEUROSCI.0793-07.2007>

Shah, N. P., Nicoll, J. M., Nagar, B., Gorre, M. E., Paquette, R. L., Kuriyan, J., & Sawyers, C. L. (2002). Multiple BCR-ABL kinase domain mutations confer polyclonal resistance to the tyrosine kinase inhibitor imatinib (STI571) in chronic phase and blast crisis chronic myeloid leukemia. *Cancer Cell*, 2(2), 117-125. [https://doi.org/10.1016/s1535-6108\(02\)00096-x](https://doi.org/10.1016/s1535-6108(02)00096-x)

Shaw, J. E., Kilander, M. B. C., Lin, Y., & Koleske, A. J. (2021). Abl2:Cortactin Interactions Regulate Dendritic Spine Stability via Control of a Stable Filamentous Actin Pool. *Journal of Neuroscience*, 41(14), 3068-3081. <https://doi.org/10.1523/JNEUROSCI.2472-20.2021>

Shima, T., Morikawa, M., Kaneshiro, J., Kambara, T., Kamimura, S., Yagi, T., Iwamoto, H., Uemura, S., Shigematsu, H., Shirouzu, M., Ichimura, T., Watanabe, T. M., Nitta, R., Okada, Y., & Hirokawa, N. (2018). Kinesin-binding-triggered conformation switching of microtubules contributes to polarized transport. *J Cell Biol*, 217(12), 4164-4183. <https://doi.org/10.1083/jcb.201711178>

Shin, Y., Berry, J., Pannucci, N., Haataja, M. P., Toettcher, J. E., & Brangwynne, C. P. (2017). Spatiotemporal Control of Intracellular Phase Transitions Using Light-Activated optoDroplets. *Cell*, 168, 159-171. <https://doi.org/10.1016/j.cell.2016.11.054>

Siahaan, V., Krattenmacher, J., Hyman, A. A., Diez, S., Hernández-Vega, A., Diez, S., Hernández-Vega, A., Lansky, Z., & Braun, M. (2019). Kinetically distinct phases of tau on microtubules regulate kinesin motors and severing enzymes. *Nature Cell Biology*, 21, 1086-1092. <https://doi.org/10.1038/s41556-019-0374-6>

Siahaan, V., Tan, R., Humhalova, T., Libusova, L., Lacey, S. E., Tan, T., Dacy, M., Ori-McKenney, K. M., McKenney, R. J., Braun, M., & Lansky, Z. (2022). Microtubule lattice spacing governs cohesive envelope formation of tau family proteins. *Nature Chemical Biology*, 18, 1224-1235. <https://doi.org/10.1038/s41589-022-01096-2>

Simpson, M. A., Bradley, W. D., Harburger, D., Parsons, M., Calderwood, D. A., & Koleske, A. J. (2015). Direct Interactions with the Integrin β 1 Cytoplasmic Tail Activate the Abl2/Arg Kinase. *Journal of Biological Chemistry*, 290(13), 8360-8372. <https://doi.org/10.1074/jbc.M115.638874>

Sirajuddin, M., Rice, L. M., & Vale, R. D. (2014). Regulation of microtubule motors by tubulin isotypes and post-translational modifications. *Nat Cell Biol*, 16(4), 335-344. <https://doi.org/10.1038/ncb2920>

Snead, D. M., Matyszewski, M., Dickey, A. M., Lin, Y. X., Leschziner, A. E., & Reck-Peterson, S. L. (2022). Structural basis for Parkinson's disease-linked LRRK2's binding to microtubules. *Nature Structural & Molecular Biology*, 29, 1196-1207. <https://doi.org/10.1038/s41594-022-00863-y>

Song, X., Yang, F., yang, T., Wang, Y., Ding, M., Li, L., Xu, P., Liu, S., Dai, M., Chi, C., Xiang, S., Xu, C., Li, D., Wang, Z., Li, L., Hill, D. L., Fu, C., Yuan, K., Li, P., . . . Yao, X. (2022). Phase separation of EB1 guides microtubule plus-ends dynamics. *Nature Cell Biology*, 25, 79-91. <https://doi.org/10.1038/s41556-022-01033-4>

Spector, J. O., Vemu, A., & Roll-Mecak, A. (2020). *In Vitro Microtubule Dynamics Assays Using Dark-Field Microscopy* (Vol. 2101). https://doi.org/10.1007/978-1-0716-0219-5_4

Speer, S. L., Stewart, C. J., Sapir, L., Harries, D., & Plelak, G. J. (2022). Macromolecular Crowding Is More than Hard-Core Repulsions. *Annual Review of Biophysics*, 51, 267-300. <https://doi.org/10.1146/annurev-biophys-091321-071829>

Spiering, D., & Hodgson, L. (2011). Dynamics of the Rho-family small GTPases in actin regulation and motility. *Cell Adhesion & Migration*, 5(2), 170-180. <https://doi.org/10.4161/cam.5.2.14403>

Sreerama, N., & Woody, R. W. (2000). Estimation of Protein Secondary Structure from Circular Dichroism Spectra: Comparison of CONTIN, SELCON, and CDSSTR Methods with an Expanded Reference Set. *Analytical Biochemistry*, 287, 252-260. <https://doi.org/10.1006/abio.2000.4880>

Stark, H. (2010). GraFix: stabilization of fragile macromolecular complexes for single particle cryo-EM. *Methods Enzymol*, 481, 109-126. [https://doi.org/10.1016/s0076-6879\(10\)81005-5](https://doi.org/10.1016/s0076-6879(10)81005-5)

Stiess, M., Maghelli, N., Kapitein, L. C., Gomis-Rüth, S., Wilsch-Bräuninger, M., Hoogenraad, C. C., Tolić-Nørrelykke, I. M., & Bradke, F. (2010). Axon Extension Occurs Independently of

Centrosomal Microtubule Nucleation. *Science*, 327(5966), 704-707.

<https://doi.org/doi:10.1126/science.1182179>

Strothman, C., Farmer, V., Arpag, G., Rodgers, N., Podolski, M., Norris, S., Ohi, R., & Zanic, M. (2019). Microtubule minus-end stability is dictated by the tubulin off-rate. *Journal of Cell Biology*, 218(9), 2841-2853. <https://doi.org/10.1083/jcb.201905019>

Stucchi, R., Plucińska, G., Hummel, J. J. A., Zahavi, E. E., Guerra San Juan, I., Klykov, O., Scheltema, R. A., Altelaar, A. F. M., & Hoogenraad, C. C. (2018). Regulation of KIF1A-Driven Dense Core Vesicle Transport: Ca²⁺/CaM Controls DCV Binding and Liprin- α /TANC2 Recruits DCVs to Postsynaptic Sites. *Cell Rep*, 24(3), 685-700.

<https://doi.org/10.1016/j.celrep.2018.06.071>

Südhof, T. C. (2012). The presynaptic active zone. *Neuron*, 75(1), 11-25.

<https://doi.org/10.1016/j.neuron.2012.06.012>

Suetsugu, S., Miki, H., & Takenawa, T. (1998). The essential role of profilin in the assembly of actin for microspike formation. *Embo j*, 17(22), 6516-6526.

<https://doi.org/10.1093/emboj/17.22.6516>

Sun, L., Xu, X., Chen, Y., Zhou, Y., Tan, R., Qiu, H., Jin, L., Zhang, W., Fan, R., Hong, W., & Wang, T. (2018). Rab34 regulates adhesion, migration, and invasion of breast cancer cells.

Oncogene, 37(27), 3698-3714. <https://doi.org/10.1038/s41388-018-0202-7>

Sweet, E. S., Previtara, M. L., Fernández, J. R., Charych, E. I., Tseng, C.-Y., Kwon, M., Starovoytov, V., Zheng, J. Q., & Firestein, B. L. (2011). PSD-95 Alters Microtubule Dynamics via an Association With EB3. *The Journal of Neuroscience*, 31(3), 1038-1047.

<https://doi.org/10.1523/jneurosci.1205-10.2011>

Szczesna, E., Zehr, E. A., Cummings, S. W., Szyk, A., Mahalingan, K. K., Li, Y., & Roll-Mecak, A. (2022). Combinatorial and antagonistic effects of tubulin glutamylation and glycylation on katanin microtubule severing. *Developmental Cell*, 57(21), 2497-2513.e2496.

<https://doi.org/https://doi.org/10.1016/j.devcel.2022.10.003>

Tamada, H., Blanc, J., Korogod, N., Petersen, C. C. H., & Knott, G. W. (2020). Ultrastructural comparison of dendritic spine morphology preserved with cryo and chemical fixation. *eLife*, 9, e56384. <https://doi.org/10.7554/eLife.56384>

Tan, R., Lam, A. J., Tan, T., Han, J., Nowakowski, D. W., Vershinin, M., Simó, S., Ori-McKenney, K. M., & McKenney, R. J. (2019). Microtubules gate tau condensation to spatially regulate microtubule functions. *Nature Cell Biology*, 21, 1078-1085. <https://doi.org/10.1038/s41556-019-0375-5>

Tan, Z., Yue, Y., Leprevost, F., Haynes, S., Basrur, V., Nesvizhskii, A. I., Verhey, K. J., & Cianfrocco, M. A. (2023). Autoinhibited kinesin-1 adopts a hierarchical folding pattern. *eLife*, 12, RP86776. <https://doi.org/10.7554/eLife.86776>

Tanis, K. Q., Veach, D., Duewel, H. S., Bornmann, W. G., & Koleske, A. J. (2003). Two distinct phosphorylation pathways have additive effects on Abl family kinase activation. *Molecular and Cellular Biology*, 23(11), 3884-3896. <https://doi.org/10.1128/mcb.23.11.3884-3896.2003>

Tasic, B., Yao, Z., Graybuck, L. T., Smith, K. A., Nguyen, T. N., Bertagnolli, D., Goldy, J., Garren, E., Economo, M. N., Viswanathan, S., Penn, O., Bakken, T., Menon, V., Miller, J., Fong, O., Hirokawa, K. E., Lathia, K., Rimorin, C., Tieu, M., . . . Zeng, H. (2018). Shared and distinct transcriptomic cell types across neocortical areas. *Nature*, 563(7729), 72-78. <https://doi.org/10.1038/s41586-018-0654-5>

Taylor, N. O., Wei, M., Stone, H. A., & Brangwynne, C. P. (2019). Quantifying Dynamics in Phase-Separated Condensates Using Fluorescence Recovery After Photobleaching. *Biophysical Journal*, 117, 1285-1300. <https://doi.org/10.1016/j.bpj.2019.08.030>

Thawani, A., Kadzik, R. S., & Petry, S. (2018). XMAP215 is a microtubule nucleation factor that functions synergistically with the γ -tubulin ring complex. *Nature Cell Biology*, 20(5), 575-585. <https://doi.org/10.1038/s41556-018-0091-6>

Theillet, F. X., Kalmar, L., Tompa, P., Han, K. H., Selenko, P., Dunker, A. K., Daughdrill, G. W., & Uversky, V. N. (2013). The alphabet of intrinsic disorder: I. Act like a Pro: On the abundance and roles of proline residues in intrinsically disordered proteins. *Intrinsically Disord Proteins*, 1(1), e24360. <https://doi.org/10.4161/idp.24360>

- Théry, M., & Blanchoin, L. (2021). Microtubule self-repair. *Current Opinion in Cell Biology*, 68, 144-154. <https://doi.org/https://doi.org/10.1016/j.ceb.2020.10.012>
- Ti, S.-C., Wieczorek, M., & Kapoor, T. M. (2020). Purification of Affinity Tag-free Recombinant Tubulin from Insect Cells. *STAR Protocols*, 1(1), 100011. <https://doi.org/https://doi.org/10.1016/j.xpro.2019.100011>
- Topham, M. K., Bunting, M., Zimmerman, G. A., McIntyre, T. M., Blackshear, P. J., & Prescott, S. M. (1998). Protein kinase C regulates the nuclear localization of diacylglycerol kinase- ζ . *Nature*, 394(6694), 697-700. <https://doi.org/10.1038/29337>
- Topham, M. K., & Epand, R. M. (2009). Mammalian diacylglycerol kinases: molecular interactions and biological functions of selected isoforms. *Biochim Biophys Acta*, 1790(6), 416-424. <https://doi.org/10.1016/j.bbagen.2009.01.010>
- Tran, P. T., Walker, R. A., & Salmon, E. D. (1997). A Metastable Intermediate State of Microtubule Dynamic Instability That Differs Significantly between Plus and Minus Ends. *Journal of Cell Biology*, 138(1), 105-117. <https://doi.org/10.1083/jcb.138.1.105>
- Tremblay, M. A., Acker, C. M., & Davies, P. (2010). Tau Phosphorylated at Tyrosine 394 is Found in Alzheimer's Disease Tangles and can be a Product of the Abl-Related Kinase, Arg. *Journal of Alzheimer's Disease*, 19(2), 721-733. <https://doi.org/10.3233/JAD-2010-1271>
- Triclin, S., Inoue, D., Gaillard, J., Htet, Z. M., DeSantis, M. E., Portran, D., Derivery, E., Aumeier, C., Schaedel, L., John, K., Leterrier, C., Reck-Peterson, S. L., Blanchoin, L., & Théry, M. (2021). Self-repair protects microtubules from destruction by molecular motors. *Nature Materials*, 20(6), 883-891. <https://doi.org/10.1038/s41563-020-00905-0>
- Trivedi, P., Palomba, F., Niedzialkowska, E., Digman, M. A., Gratton, E., & Stukenberg, P. T. (2019). The inner centromere is a biomolecular condensate scaffolded by the chromosomal passenger complex. *Nature Cell Biology*, 21(9), 1127-1137. <https://doi.org/10.1038/s41556-019-0376-4>
- Tropini, C., Roth, E. A., Zanic, M., Gardner, M. K., & Howard, J. (2012). Islands Containing Slowly Hydrolyzable GTP Analogs Promote Microtubule Rescues. *PLoS One*, 7(1), e30103. <https://doi.org/10.1371/journal.pone.0030103>

- Tymanskyj, S. R., & Ma, L. (2019). MAP7 Prevents Axonal Branch Retraction by Creating a Stable Microtubule Boundary to Rescue Polymerization. *The Journal of Neuroscience*, 39(36), 7118-7131. <https://doi.org/10.1523/jneurosci.0775-19.2019>
- Tymanskyj, S. R., Yang, B. H., Verhey, K. J., & Ma, L. (2018). MAP7 regulates axon morphogenesis by recruiting kinesin-1 to microtubules and modulating organelle transport. *eLife*, 7, e36374. <https://doi.org/10.7554/eLife.36374>
- Umemori, H., Satot, S., Yagi, T., Aizawal, S., & Yamamoto, T. (1994). Initial events of myelination involve Fyn tyrosine kinase signalling. *Nature*, 367(6463), 572-576. <https://doi.org/10.1038/367572a0>
- Urano, T., Liu, J., Zhang, P., Fan, Y.-x., Egile, C., Li, R., Mueller, S. C., & Zhan, X. (2001). Activation of Arp2/3 complex-mediated actin polymerization by cortactin. *Nature Cell Biology*, 3(3), 259-266. <https://doi.org/10.1038/35060051>
- Utsumi, T., Sakurai, N., Nakano, K., & Ishisaka, R. (2003). C-terminal 15 kDa fragment of cytoskeletal actin is posttranslationally N-myristoylated upon caspase-mediated cleavage and targeted to mitochondria. *FEBS Lett*, 539(1-3), 37-44. [https://doi.org/10.1016/s0014-5793\(03\)00180-7](https://doi.org/10.1016/s0014-5793(03)00180-7)
- Uversky, V. N., Kuznetsova, I. M., Turoverov, K. K., & Zaslavsky, B. (2015). Intrinsically disordered proteins as crucial constituents of cellular aqueous two phase systems and coacervates. *FEBS Letters*, 589(1), 15-22. <https://doi.org/https://doi.org/10.1016/j.febslet.2014.11.028>
- van den Berg, C. M., Volkov, V. A., Schnorrenberg, S., Huang, Z., Stecker, K. E., Grigoriev, I., Gilani, S., Frikstad, K. M., Patzke, S., Zimmerman, T., Dogterom, M., & Akhmanova, A. (2023). CSPP1 stabilizes growing microtubule ends and damaged lattices from the luminal side. *Journal of Cell Biology*, 222(4), e202208062. <https://doi.org/10.1083/jcb.202208062>
- Van Etten, R. A., Jackson, P., Baltimore, D., Sanders, M. C., Matsudaira, P. T., & Janmey, P. A. (1994). The COOH Terminus of the c-Abl Tyrosine Kinase Contains Distinct F- and G-Actin Binding Domains with Bundling Activity. *Journal of Cell Biology*, 124(3), 325-340. <https://doi.org/10.1083/jcb.124.3.325>

- VanBuren, V., Odde, D. J., & Cassimeris, L. (2002). Estimates of lateral and longitudinal bond energies within the microtubule lattice. *Proceedings of the National Academy of Sciences*, 99(9), 6035-6040. <https://doi.org/10.1073/pnas.092504999>
- Vandecandelaere, A., Brune, M., Webb, M. R., Martin, S. R., & Bayley, P. M. (1999). Phosphate Release during Microtubule Assembly: What Stabilizes Growing Microtubules? *Biochemistry*, 38(25), 8179-8188. <https://doi.org/10.1021/bi9830765>
- Vemu, A., Atherton, J., Spector, J. O., Szyk, A., Moores, C. A., & Roll-Mecak, A. (2016). Structure and Dynamics of Single-isoform Recombinant Neuronal Human Tubulin. *Journal of Biological Chemistry*, 291(25), 12907–12915. <https://doi.org/10.1074/jbc.C116.731133>
- Vitre, B., Coquelle, F. M., Heichette, C., Garnier, C., Chrétien, D., & Arnal, I. (2008). EB1 regulates microtubule dynamics and tubulin sheet closure in vitro. *Nature Cell Biology*, 10(4), 415-421. <https://doi.org/10.1038/ncb1703>
- Voter, W. A., & Erickson, H. P. (1984). The kinetics of microtubule assembly. Evidence for a two-stage nucleation mechanism. *Journal of Biological Chemistry*, 259(16), 10430-10438. [https://doi.org/10.1016/S0021-9258\(18\)90982-8](https://doi.org/10.1016/S0021-9258(18)90982-8)
- Walker, R. A., Inoué, S., & Salmon, E. D. (1989). Asymmetric behavior of severed microtubule ends after ultraviolet-microbeam irradiation of individual microtubules in vitro. *Journal of Cell Biology*, 108(3), 931-937. <https://doi.org/10.1083/jcb.108.3.931>
- Walker, R. A., O'Brien, E. T., Pryer, N. K., Soboeiro, M. F., Voter, W. A., Erickson, H. P., & Salmon, E. D. (1988). Dynamic Instability of Individual Microtubules Analyzed by Video Light Microscopy: Rate Constants and Transition Frequencies. *Journal of Cell Biology*, 107(4), 1437-1448. <https://doi.org/10.1083/jcb.107.4.1437>
- Walker, R. A., Pryer, N. K., & Salmon, E. D. (1991). Dilution of individual microtubules observed in real time in vitro: evidence that cap size is small and independent of elongation rate. *Journal of Cell Biology*, 114(1), 73-81. <https://doi.org/10.1083/jcb.114.1.73>
- Wang, J., Choi, J., Holehouse, A. S., Lee, H. O., Zhang, X., Jahnel, M., Maharana, S., Lemaitre, R., Pozniakovsky, A., Drechsel, D., Poser, I., Pappu, R. V., Alberti, S., & Hyman, A. A. (2018). A

Molecular Grammar Governing the Driving Forces for Phase Separation of Prion-like RNA Binding Proteins. *Cell*, 174(3), 688-699. <https://doi.org/10.1016/j.cell.2018.06.006>

Wang, Y., Miller, A. L., Mooseker, M. S., & Koleske, A. J. (2001). The Abl-related gene (Arg) nonreceptor tyrosine kinase uses two F-actin-binding domains to bundle F-actin. *Proceedings of the National Academy of Sciences*, 98(26), 14865-14870. <https://doi.org/10.1073/pnas.251249298>

Warren, M. S., Bradley, W. D., Gourley, S. L., Lin, Y., Simpson, M. A., Reichardt, L. F., Greer, C. A., Taylor, J. R., & Koleske, A. J. (2012). Integrin $\beta 1$ Signals through Arg to Regulate Postnatal Dendritic Arborization, Synapse Density, and Behavior. *The Journal of Neuroscience*, 32(8), 2824-2834. <https://doi.org/10.1523/JNEUROSCI.3942-11.2012>

Waschbüsch, D., & Khan, A. R. (2020). Phosphorylation of Rab GTPases in the regulation of membrane trafficking. *Traffic*, 21(11), 712-719. <https://doi.org/10.1111/tra.12765>

Watanabe, R., Buschauer, R., Böhning, J., Audagnotto, M., Lasker, K., Lu, T. W., Boassa, D., Taylor, S., & Villa, E. (2020). The In Situ Structure of Parkinson's Disease-Linked LRRK2. *Cell*, 182(6), 1508-1518.e1516. <https://doi.org/10.1016/j.cell.2020.08.004>

Wegmann, S., Eftekhazadeh, B., Tepper, K., Zoltowska, K. M., Bennett, R. E., Dujardin, S., Laskowski, P. R., MacKenzie, D., Kamath, T., Commins, C., Vanderburg, C., Roe, A. D., Fan, Z., Mollie, A. M., Hernandez-Vega, A., Muller, D., Hyman, A. A., Mandelkow, E., Taylor, J. P., & Hyman, B. T. (2018). Tau protein liquid-liquid phase separation can initiate tau aggregation. *Embo j*, 37(7). <https://doi.org/10.15252/emboj.201798049>

Weiner, A. T., Seebold, D. Y., Torres-Gutierrez, P., Folker, C., Swope, R. D., Kothe, G. O., Stoltz, J. G., Zalenski, M. K., Kozłowski, C., Barbera, D. J., Patel, M. A., Thyagarajan, P., Shorey, M., Nye, D. M. R., Keegan, M., Behari, K., Song, S., Axelrod, J. D., & Rolls, M. M. (2020). Endosomal Wnt signaling proteins control microtubule nucleation in dendrites. *PLOS Biology*, 18(3), e3000647. <https://doi.org/10.1371/journal.pbio.3000647>

Weiner, A. T., Thyagarajan, P., Shen, Y., & Rolls, M. M. (2021). To nucleate or not, that is the question in neurons. *Neurosci Lett*, 751, 135806. <https://doi.org/10.1016/j.neulet.2021.135806>

Wen, S. T., Jackson, P. K., & Van Etten, R. A. (1996). The cytostatic function of c-Abl is controlled by multiple nuclear localization signals and requires the p53 and Rb tumor suppressor gene products. *The EMBO Journal*, 15(7), 1583-1595.

Wertheim, J. A., Perera, S. A., Hammer, D. A., Ren, R., Boettiger, D., & Pear, W. S. (2003). Localization of BCR-ABL to F-actin regulates cell adhesion but does not attenuate CML development. *Blood*, 102(6), 2220-2228. <https://doi.org/10.1182/blood-2003-01-0062>

Wethekam, L. C., & Moore, J. K. (2023). Tubulin isotype regulation maintains asymmetric requirement for α -tubulin over β -tubulin. *Journal of Cell Biology*, 222(3). <https://doi.org/10.1083/jcb.202202102>

Widlund, P. O., Stear, J. H., Pozniakovsky, A., Zanic, M., Reber, S., Brouhard, G. J., Hyman, A. A., & Howard, J. (2011). XMAP215 polymerase activity is built by combining multiple tubulin-binding TOG domains and a basic lattice-binding region. *Proceedings of the National Academy of Sciences*, 108(7), 2741-2746. <https://doi.org/doi:10.1073/pnas.1016498108>

Wills, Z., Bateman, J., Korey, C. A., Comer, A., & Van Vactor, D. (1999). The Tyrosine Kinase Abl and Its Substrate Enabled Collaborate with the Receptor Phosphatase Dlar to Control Motor Axon Guidance. *Neuron*, 22(2), 301-312. [https://doi.org/10.1016/S0896-6273\(00\)81091-0](https://doi.org/10.1016/S0896-6273(00)81091-0)

Wills, Z., Marr, L., Zinn, K., Goodman, C. S., & Van Vactor, D. (1999). Profilin and the Abl Tyrosine Kinase Are Required for Motor Axon Outgrowth in the *Drosophila* Embryo. *Neuron*, 22(2), 291-299. [https://doi.org/10.1016/S0896-6273\(00\)81090-9](https://doi.org/10.1016/S0896-6273(00)81090-9)

Wiredja, D. D., Koyutürk, M., & Chance, M. R. (2017). The KSEA App: a web-based tool for kinase activity inference from quantitative phosphoproteomics. *Bioinformatics*, 33(21), 3489-3491. <https://doi.org/10.1093/bioinformatics/btx415>

Wong, S., & Witte, O. N. (2004). The BCR-ABL Story: Bench to Bedside and Back. *Annual Review of Immunology*, 22(1), 247-306. <https://doi.org/10.1146/annurev.immunol.22.012703.104753>

Woodring, P. J., Hunter, T., & Wang, J. Y. J. (2001). Inhibition of c-Abl Tyrosine Kinase Activity by Filamentous Actin. *The Journal of Biological Chemistry*, 276(29), 27104–27110. <https://doi.org/10.1074/jbc.M100559200>

Woodring, P. J., Hunter, T., & Wang, J. Y. J. (2003). Regulation of F-actin-dependent processes by the Abl family of tyrosine kinases. *Journal of Cell Science*, 116(13), 2613–2626.

<https://doi.org/10.1242/jcs.00622>

Wu, K., Wu, H., Lyu, W., Kim, Y., Furdui, C. M., Anderson, K. S., & Koleske, A. J. (2021). Platelet-derived growth factor receptor beta activates Abl2 via direct binding and phosphorylation. *Journal of Biological Chemistry*, 297(1), 100883. <https://doi.org/10.1016/j.jbc.2021.100883>

Wu, X., Cai, Q., Feng, Z., & Zhang, M. (2020). Liquid-Liquid Phase Separation in Neuronal Development and Synaptic Signaling. *Dev Cell*, 55(1), 18-29.

<https://doi.org/10.1016/j.devcel.2020.06.012>

Xiao, H., Verdier-Pinard, P., Fernandez-Fuentes, N., Burd, B., Angeletti, R., Fiser, A., Horwitz, S. B., & Orr, G. A. (2006). Insights into the mechanism of microtubule stabilization by Taxol. *Proc Natl Acad Sci U S A*, 103(27), 10166-10173. <https://doi.org/10.1073/pnas.0603704103>

Xiao, X., Levy, A. D., Rosenberg, B. J., Higley, M. J., & Koleske, A. J. (2016). Disruption of Coordinated Presynaptic and Postsynaptic Maturation Underlies the Defects in Hippocampal Synapse Stability and Plasticity in Abl2/Arg-Deficient Mice. *The Journal of Neuroscience*, 36(25), 6778-6791. <https://doi.org/10.1523/JNEUROSCI.4092-15.2016>

Xie, X., Liang, M., Yu, C., & Wei, Z. (2021). Liprin- α -Mediated Assemblies and Their Roles in Synapse Formation [Review]. *Frontiers in Cell and Developmental Biology*, 9.

<https://doi.org/10.3389/fcell.2021.653381>

Xu, Z., Schaedel, L., Portran, D., Aguilar, A., Gaillard, J., Marinkovich, M. P., Théry, M., & Nachury, M. V. (2017). Microtubules acquire resistance from mechanical breakage through intraluminal acetylation. *Science*, 356(6335), 328-332.

<https://doi.org/doi:10.1126/science.aai8764>

Xue, B., Dunbrack, R. L., Williams, R. W., Dunker, A. K., & Uversky, V. N. (2010). PONDR-FIT: A Meta-Predictor of Intrinsically Disordered Amino Acids. *Biochimica et Biophysica Acta*, 1804(4), 996-1010. <https://doi.org/10.1016/j.bbapap.2010.01.011>

Yang, S., Liu, C., Guo, Y., Li, G., Li, D., Yan, X., & Zhu, X. (2022). Self-construction of actin networks through phase separation–induced abLIM1 condensates. *Proceedings of the National Academy of Sciences*, 119(29), e2122420119. <https://doi.org/doi:10.1073/pnas.2122420119>

Yau, K. W., van Beuningen, S. F., Cunha-Ferreira, I., Cloin, B. M., van Battum, E. Y., Will, L., Schätzle, P., Tas, R. P., van Krugten, J., Katrukha, E. A., Jiang, K., Wulf, P. S., Mikhaylova, M., Harterink, M., Pasterkamp, R. J., Akhmanova, A., Kapitein, L. C., & Hoogenraad, C. C. (2014). Microtubule minus-end binding protein CAMSAP2 controls axon specification and dendrite development. *Neuron*, 82(5), 1058-1073. <https://doi.org/10.1016/j.neuron.2014.04.019>

Yeo, G., & Burge, C. B. (2004). Maximum entropy modeling of short sequence motifs with applications to RNA splicing signals. *J Comput Biol*, 11(2-3), 377-394. <https://doi.org/10.1089/1066527041410418>

Yonekawa, Y., Harada, A., Okada, Y., Funakoshi, T., Kanai, Y., Takei, Y., Terada, S., Noda, T., & Hirokawa, N. (1998). Defect in Synaptic Vesicle Precursor Transport and Neuronal Cell Death in KIF1A Motor Protein–deficient Mice. *Journal of Cell Biology*, 141(2), 431-441. <https://doi.org/10.1083/jcb.141.2.431>

Zandy, N. L., & Pendergast, A. M. (2008). Abl Tyrosine Kinases Modulate Cadherin-dependent Adhesion Upstream and Downstream of Rho Family GTPases. *Cell Cycle*, 7(4), 444-448. <https://doi.org/10.4161/cc.7.4.5452>

Zandy, N. L., Playford, M., & Pendergast, A. M. (2007). Abl tyrosine kinases regulate cell-cell adhesion through Rho GTPases. *Proceedings of the National Academy of Sciences*, 104(45), 17686-17691. <https://doi.org/10.1073/pnas.0703077104>

Zanic, M., Stear, J. H., Hyman, A. A., & Howard, J. (2009). EB1 recognizes the nucleotide state of tubulin in the microtubule lattice. *PLoS One*, 4(10), e7585. <https://doi.org/10.1371/journal.pone.0007585>

Zbinden, A., Pérez-Berlanga, M., De Rossi, P., & Polymenidou, M. (2020). Phase Separation and Neurodegenerative Diseases: A Disturbance in the Force. *Developmental Cell*, 55(1), 45-68. <https://doi.org/https://doi.org/10.1016/j.devcel.2020.09.014>

- Zhang, J., Sun, J. G., Xing, X., Wu, R., Zhou, L., Zhang, Y., Yuan, F., Wang, S., & Yuan, Z. (2022). c-Abl-induced Olig2 phosphorylation regulates the proliferation of oligodendrocyte precursor cells. *Glia*, 70(6), 1084-1099. <https://doi.org/10.1002/glia.24157>
- Zhang, K., Lyu, W., Yu, J., & Koleske, A. J. (2018). Abl2 is recruited to ventral actin waves through cytoskeletal interactions to promote lamellipodium extension. *Molecular Biology of the Cell*, 29(23), 2863-2873. <https://doi.org/10.1091/mbc.E18-01-0044>
- Zhang, R., Alushin, G. M., Brown, A., & Nogales, E. (2015). Mechanistic Origin of Microtubule Dynamic Instability and Its Modulation by EB Proteins. *Cell*, 162(2), 849-859. <https://doi.org/10.1016/j.cell.2015.07.012>
- Zhang, R., Roostalu, J., Surrey, T., & Nogales, E. (2017). Structural insight into TPX2-stimulated microtubule assembly. *eLife*, 6, e30959. <https://doi.org/10.7554/eLife.30959>
- Zhang, X., Vigers, M., McCarty, J., Rauch, J. N., Fredrickson, G. H., Wilson, M. Z., Shea, J.-E., Han, S., & Kosik, K. S. (2020). The proline-rich domain promotes Tau liquid–liquid phase separation in cells. *Journal of Cell Biology*, 219(11). <https://doi.org/10.1083/jcb.202006054>
- Zhang, Z., Dmitrieva, N. I., Park, J. H., Levine, R. L., & Burg, M. B. (2004). High urea and NaCl carbonylate proteins in renal cells in culture and in vivo, and high urea causes 8-oxoguanine lesions in their DNA. *Proc Natl Acad Sci U S A*, 101(25), 9491-9496. <https://doi.org/10.1073/pnas.0402961101>